Development and Applications of Mechanics- and Data-based Capacity Models for Intact/Corroded Prestressed Concrete Bridge Girders

by

Jiadaren Liu

A thesis submitted in partial fulfillment of the requirements for the degree of

Doctor of Philosophy

in

Structural Engineering

Department of Civil and Environmental Engineering

University of Alberta

ABSTRACT

Prestressed concrete (PC) highway bridges represent an integral part of the transportation network and contribute significantly to socio-economic development. However, highway bridges are susceptible to Deterioration and thus exhibit structural deficiency after years of service, especially in the cold climate of North America (e.g., Alberta, Canada) where the de-icing salt is used seasonally and can heavily corrode roads and bridges. To facilitate the reliability-based safety assessment for both intact (e.g., as-built) and corroded PC bridge girders, reliable load-carrying capacity prediction models are required as a fundamental ingredient including both mechanics-based and data-based models.

Firstly, a mechanics-based load-carrying capacity prediction model (i.e., a flexure-shear coupled fibre beam element) for intact PC girders was developed based on Timoshenko beam theory combined with multi-axial material models, as complementary to the conventional fibre beam elements without considering shear. The developed element was validated through a classic test series of shear-critical reinforced concrete (RC) beams from the literature and a PC girder recently tested under both shear-critical and flexure-dominated scenarios. Then, the developed element was applied to a representative nine-girder PC bridge in Alberta, Canada to study the bridge system behavior and load sharing of multi-girder bridges.

Data-based shear capacity models for intact PC girders were then developed by adding probabilistic correction terms to existing deterministic design code models. In this research task, an experimental database containing 369 PC girders that failed in shear was compiled. Using the experimental database, shear capacity models from five concrete structure and bridge design codes were assessed, including ACI 318-19, AASHTO LRFD 2017, CSA A23.3:19, CSA S6:19 and *fib* MC 2010. Probabilistic correction terms were then calibrated and added to the design code models via Bayesian linear regression and Gaussian process regression approaches. The resulted models can benefit shear capacity predictions with better accuracy and precision, as well as reliability/fragility analysis of PC girders with the model error considered.

Data-based load-carrying capacity models were also developed for corroded PC voided girders which are popular for short-span bridges in North America. Firstly, a 2D continuum-based FE model for corroded PC girders was developed and validated by existing experimental tests. Then, a virtual experimental database of 4,165 PC girder tests considering various design, loading, and corrosion conditions was generated based on the developed FE model. With the generated virtual experimental database, the probabilistic capacity reduction factor model and the load-carrying capacity model were developed via Gaussian process regression to study the corrosion effects on capacity reduction and failure probability of corroded PC girders, respectively.

PREFACE

This thesis includes original research conducted by Jiadaren Liu. Five journal papers have been published/under review/in preparation for publication on the basis of this thesis. The details of the corresponding chapters are summarized below:

A version of Chapter 3 has been published as ***Liu, J., Huang, L., Wu, Z., Tomlinson, D., Cruz-Noguez, C., Alexander, J., Adeeb, S., & Li, Y., "Development of enhanced fibre beam element with multi-axial material constitutive models for reinforced/prestressed concrete beams", Engineering Structures, 248: 113289, 2021.*** For the consistency and coherence of this thesis, contents have been modified, removed, or added from the published paper. Jiadaren Liu was responsible for conceptualization, methodology development, model development, analysis implementation, and paper composition. Liying Huang and Zhaohan Wu were in charge of paper composition and paper revision. Douglas Tomlinson, Carlos Cruz-Noguez, John Alexander, and Samer Adeeb were in charge of supervision and paper revision. Yong Li was in charge of conceptualization, supervision, funding acquisition, and paper revision.

A version of Chapter 4 is under review as ***Liu, J., Alexander, J., Song, S., & Li, Y., "Study of load-sharing of shear-connected multi-girder prestressed concrete bridges using newly developed nonlinear beam elements", ASCE Journal of Bridge Engineering.*** For the consistency and coherence of this thesis, contents have been modified, removed, or added from the prepared manuscript. Jiadaren Liu was responsible for conceptualization, methodology development, model development, analysis implementation, and paper composition. John Alexander was in charge of conceptualization, supervision and paper revision. Shasha Song was in charge of analysis implementation and paper revision. Yong Li was in charge of conceptualization, supervision, funding acquisition, and paper revision.

A version of Chapter 5 is under review as ***Liu, J., Alexander, J., & Li, Y., "Probabilistic error assessment and correction of design code-based shear strength prediction models for reliability analysis of prestressed concrete girders", Engineering Structures.*** For the consistency and coherence of this thesis, contents have been modified, removed, or added from the submitted paper. Jiadaren Liu was responsible for conceptualization, methodology development, model development, analysis implementation, and paper composition. John Alexander was in charge of supervision and paper revision. Yong Li was in charge of conceptualization, supervision, funding acquisition, and paper revision.

A version of Chapter 6 is under review as ***Liu, J., Alexander, J., & Li, Y., "Integrating existing models and experimental data via gaussian process regression for probabilistic model development: shear capacity of prestressed concrete beams", Soft Computing.*** For the consistency and coherence of this thesis, contents have been modified, removed, or added from the submitted paper. Jiadaren Liu was responsible for conceptualization, methodology development, model development, analysis implementation, and paper composition. John Alexander was in charge of supervision and paper revision. Yong Li was in charge of conceptualization, supervision, funding acquisition, and paper revision.

A version of Chapter 7 is under review as ***Liu, J., Alexander, J., & Li, Y., "Load-carrying capacity models of prestressed concrete bridge girders for fast-screening and reliability-based evaluation", Construction and Building Materials.*** For the consistency and coherence of this thesis, contents have been modified, removed, or added from the prepared manuscript. Jiadaren Liu was responsible for conceptualization, methodology development, model development, analysis implementation, and paper composition. John Alexander was in charge of supervision and paper revision. Yong Li was in charge of conceptualization, supervision, funding acquisition, and paper revision.

ACKNOWLDEGEMENTS

The completion of this thesis would not have been possible without the support and guidance from numerous people and organizations. First and foremost, I would like to express my deepest appreciation and gratitude to my supervisor Dr. Yong Li, for his guidance and encouragement throughout my doctoral studies. He taught me many important lessons that shaped and widened my engineering vision during all the years we worked together. It is always my pleasure working with and learning from him. Next, I would like to acknowledge the supervisory committee members: Dr. Samer Adeeb and Dr. Douglas Tomlinson for their precious time and constructive comments for my research project.

The work described in this thesis is financially supported by Alberta Transportation (AT). I would like to acknowledge John Alexander, the Director of Bridge Engineering at AT, Mike Tokar, the Structural Engineering Specialist at AT, Rubiat Islam, the Structural Engineering Specialist at AT, and Nolan Rettie, the Structural Engineering Specialist at AT, for their valuable technical support and insightful feedback on my research work.

I would also like to give my thanks to my colleagues and classmates during my PhD study at the University of Alberta, including, but not limited to, Shaghayegh Abtahi, Liying Huang, Zhenning Liu, Durlabh Bartaula, Bowen Zeng, Odin Guzman Sanchez, Vahid Zamani, Pouya Taraghi, Mohammadali Ameri Fard Nasrand, Zeyad Nabil Shaban, Wanyan Liu, and Junbo Yang.

Finally, I would like to give my special thanks to my parents and family for all their love and endless support. They are always my strongest backup and give me courage to get through all challenges.

TABLE OF CONTENTS

LIST OF FIGURES

LIST OF TABLES

CHAPTER 1: INTRODUCTION

This research project focuses on the development and applications of mechanics- and data-based capacity models for intact/corroded prestressed concrete (PC) bridge girders. This chapter provides an overview of this research project by outlining the project background, problem statement and motivation, objective and methodology, novelty and significance, research assumptions, and thesis organization.

1.1 Background

Precast PC highway bridge girders have been extensively used as an integral part of the transportation network and contributed significantly to socio-economic development. It was reported that PC girder bridges constitute more than 50 percent of the bridge inventory in North America (Dunker and Rabbat 1993). This is mainly due to their great stiffness, ease of fabrication, and fast construction. Their safety and functionality have been a critical concern for bridge engineers and owners for years during bridge design, inspection, condition evaluation, and repair processes. To ensure safety of PC bridge girders, reliable capacity prediction, considering flexural failure, shear failure and a combination of two, plays an important role in engineering practice for structural design of new bridges and maintenance of existing ones.

In design of new bridge girders, the flexural and shear capacities, which are defined as the ability of PC girders to resist failure in bending and shear, respectively, need to be checked under flexure-dominated and shear-critical load conditions. The mechanism of flexural failure has been well understood and the flexure capacity can be predicted with sufficient accuracy nowadays. On the contrary, shear failure mechanism is more complicated especially after the initiation of cracks, and thus is less understood; furthermore, accurate shear capacity prediction of concrete members remains a challenge and thus models with large prediction scatter/errors are commonly used with conservation. The shear failure mechanisms can be broadly categorized into five types as shown in Figure. 1-1 mainly depending on the shear span to effective depth ratios (*a*/*d*). The five shear failure types are tied-arch action for deep beams with struts, shear compression failure mainly due to insufficient concrete strength, shear tension failure mainly due to insufficient anchorage/bond, diagonal tension failure mainly due to insufficient shear reinforcement, and web-crushing failure for thin-web girders.

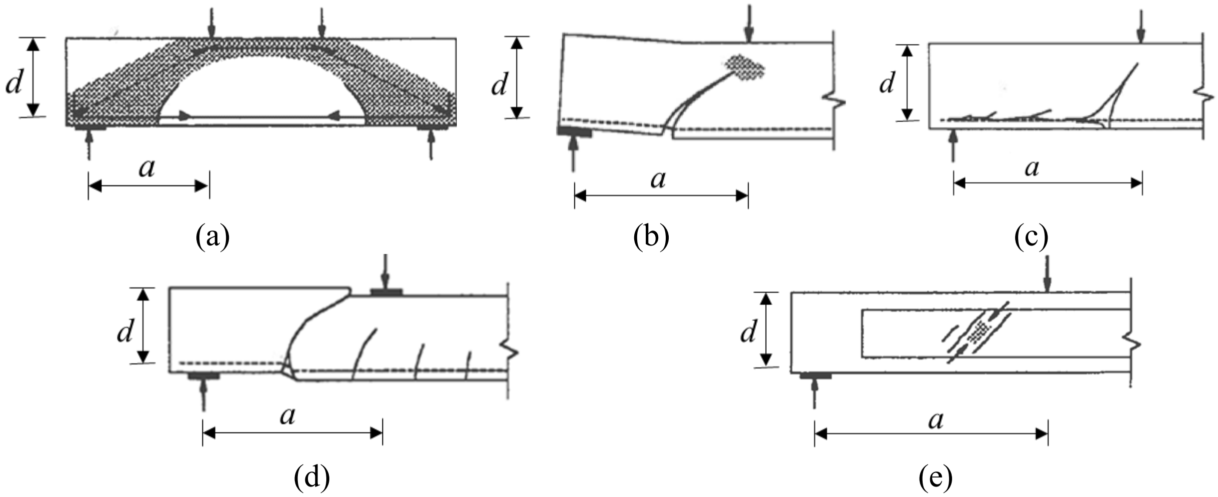

(a) (b) (c)

(d) (e)

Figure 1-1: Shear failure mechanisms (ASCE-ACI 426, 1973): (a) tied-arch action (*a*/*d* <1), (b) shear compression failure (1< *a*/*d* <2.5), (c) shear tension failure (1< *a*/*d* <2.5), (d) diagonal tension failure (2.5< *a*/*d* <6), and (e) web-crushing failure

Even though PC girders were design with sufficient capacity, aging PC girders with possible Deterioration can lead to capacity degradation and it is not uncommon in engineering practice. Canadian Infrastructure Report Card (2019) reported that 38% of bridges in Canada were in fair/poor/very poor physical conditions compared with 60% in good/very good conditions. ASCE (2021) reported that 42% of all bridges in the United States are at least 50 years old, and 7.5% of the nation’s bridge are considered structurally deficient. BRIME (2001) estimated that a significant portion of the concrete highway bridges were affected by deterioration and thus considered to be substandard in Europe, e.g., 39% in France, 37% in Germany, 26% in Norway and 30% in the United Kingdom. There were also many reported catastrophic failure events of bridges due to deterioration effects, such as the collapse of the Lake View Drive Bridge in the US in 2005 (Harries 2009), the Saint Stefano Bridge in Italy in 1999 (Darmawan 2009), the Ynys-y-Gwas Bridge in the UK in 1985 (Woodward and Williams 1988), and the Melle Bridge in Belgium in 1992 (Mathy et al. 1996).

Among various causes of Deterioration for concrete bridge girders, chloride-induced steel corrosion has been identified as one of the most predominant reasons (Bhargava et al. 2011; Wang et al. 2014; Zhang et al. 2017a). During the corrosion process, steel turns into rust which has a relatively lower density, primarily leading to (1) cross-sectional area reduction in steel reinforcement and weakened material properties, (2) cracking and spalling of the concrete cover due to volume expansion that generates splitting stresses in concrete and altered material properties, and (3) bond deterioration between steel reinforcement and the surrounding concrete. As a result of these factors, corrosion can eventually lead to load-carrying capacity degradation and possible failure mechanism change under the same loading condition, as evidenced in many experimental and numerical studies (Darmawan and Stewart 2007; Coronelli et al. 2009; Guo et al. 2011; Wang et al. 2014; Zhang et al. 2017b).

To provide reliable guidance for the design and management of both intact and corroded bridges, the prediction of load-carrying capacity with prevailing uncertainties considered is of significant importance since uncertainties are inevitable for safety assessment. Uncertainties may arise from material property randomness (Nowak and the Szerszen 2003), geometric defects, corrosion-induced defects for corroded structures, and more importantly, prediction model inaccuracy that is often ignored assuming models are perfect (Yang et al. 2021). By developing probabilistic capacity prediction models with prevailing uncertainty considered, reliability analysis (considering the uncertainty in both loads/demands and resistance/capacity) or conditional reliability analysis at a given load level (without considering the uncertainty in loads/demands) can provide useful information in terms of probability of failure, which can help making rational decisions for bridge design and maintenance, repair or replacement.

1.2 Problem Statement and Motivation

To facilitate reliability-based safety assessment for both intact and corroded PC bridge girders, reliable capacity prediction models with prediction uncertainty/error probabilistically quantified are required as a fundamental ingredient. As mentioned earlier, for intact PC girders, the load-carrying capacity is usually related to the flexure and shear capacities; the flexural capacity can be well predicted with satisfactory accuracy nowadays, while shear capacity prediction still remains as a challenging problem and is worth further investigation. For corroded PC girders, the load-carrying capacity prediction become more difficult due to the possible corrosion-induced failure mode change. That is to say, a girder, which fails in shear under shear-critical loading in the pristine condition, can fail after years of corrosion due to reduced flexure capacity, or vise versa. Thus, the central problem to address in this thesis is to develop reliable capacity prediction models for intact/corroded PC bridge girders with particular emphasis on shear failure for intact PC girders and corrosion effect for corroded PC girders.

Capacity prediction models can be broadly classified into mechanics-based (e.g., finite element models, analytical procedures with engineering simplifications) and data-based models (e.g., machine learning based models or some empirical models based on limited test data). More details on the classification and illustration of different model types can be referred to the literature review in Chapter 2. Based on the literature review, the following three research gaps have been discovered for capacity prediction of intact/corroded PC girders that motivated the research work in this thesis:

(1) Fibre beam element model represents a good balance between prediction accuracy and computational efficiency for frame elements, including PC girders. The performance of fibre beam element models has been verified by many researchers for flexure-dominated concrete members, while most of the existing fibre beam element are based on Euler-Bernoulli beam theory and fail to consider the flexure-shear coupling effect. This means that they are not applicable to PC girders under shear-critical loading scenarios. To this end, new flexure-shear coupled fibre beam element needs to be developed to better model PC girders. Such elements would be particularly useful for bridge system modeling, such as shear-connected multi-girder systems, and thus can be used to study the load-sharing behavior of multi-girder systems.

(2) The capacity prediction models from design codes are well-suited for reliability-based safety assessment, in particular, for reliability-based code calibration and development, of PC girders due to their computational efficiency and wide use in engineering practice. However, the shear capacity prediction models from design codes were observed to exhibit large conservative bias and prediction scatter based on the preliminary accuracy assessment conducted in this thesis. Although being conservative should not be criticized for structural design purposes, the model error/uncertainty needs to be quantified for transparency and considered to benefit reliability analysis. In addition, previous studies on probabilistic shear capacity prediction only focus on reinforced concrete (RC) members, while more research work is needed for the probabilistic shear capacity prediction of PC girder.

(3) Despite the limited efforts in experimental and numerical studies of corroded PC girders as reported in the literature, no probabilistic capacity models have been developed. This is in contrast to probabilistic capacity model development for corroded RC members, which is mainly due to the limited experimental work on corroded PC girders compared to relevant work on corroded RC members. The lack of capacity models for corroded PC girders hinders the quantitative condition assessment based on corrosion-induced reduction in load-carrying capacity and increase in probability of failure. To this end, further studies are required to address this gap for corroded PC girders.

1.3 Objectives and Methodology

The overall goal of this research project is to develop capacity prediction models for both intact and corroded PC girders with particular emphasis on shear failure for intact PC girders and corrosion effect for corroded PC girders. This can be divided into three sub-objectives with methodologies as detailed below:

(1) Sub-objective #1: Mechanics-based shear capacity model using newly developed beam element for intact PC girders

For this sub-objective, a new flexure-shear coupled fibre beam element is developed in an open-source finite element platform (i.e., *OpenSees*) to benefit the analysis of PC girders under shear-critical loading scenarios. To accomplish this sub-objective, relevant research work is conducted as follows: (a) implementing new multi-axial material model in *OpenSees*; (b) developing and implementing the new flexure-shear coupled fibre beam element in *OpenSees*; (c) validating the newly developed element using classical shear tests of RC beams in the literature and experimental tested PC girders at the University of Alberta; and (d) demonstrating its use by applying it to multi-girder bridge analysis to study the bridge system behavior and load sharing.

(2) Sub-objective #2: Experimental data-based shear capacity model for intact PC girders using probabilistic machine learning

For this sub-objective, probabilistic shear capacity models are developed by taking advantage of experimental test data compiled from the literature and existing design code models, which will facilitate the future use of developed models. To accomplish this sub-objective, relevant research work is conducted as follows: (a) reviewing existing deterministic design code models; (b) compiling experimental database of intact PC girders that failed in shear; (c) assessing the accuracy of existing design code models probabilistically; (d) developing probabilistic models by adding probabilistic correction terms to existing deterministic models (i.e., design code models); and (e) demonstrating their use by applying the developed probabilistic models to conditional reliability (fragility) analysis of PC girders. Note that two probabilistic machine learning methods, including Bayesian linear regression and Gaussian process regression, are considered in this research project to construct the probabilistic models, which allow probabilistic description of remaining model errors.

(3) Sub-objective #3: Simulated data-based load-carrying capacity model for corroded PC girder using Gaussian process regression (GPR)

For this sub-objective, probabilistic load-carrying capacity prediction models are developed for corroded PC girders using simulated data from validated finite element models. To accomplish this sub-objective, relevant research work is conducted as follows: (a) developing and validating two-dimensional (2D) mechanics-based nonlinear finite element models for corroded PC girders; (b) generating virtual experimental database for corroded PC girders based on the developed finite element model considering different design, corrosion, and loading conditions (with both flexural-dominated and shear-critical loading scenarios considered); (c) developing probabilistic load-carrying capacity prediction models for corroded PC girders based on the generated database; and (d) demonstrate its use by applying the developed probabilistic models to study how corrosion reduces the load-carrying capacity and increases the probability of failure for corroded PC girders.

1.4 Novelty and Significance of Research

In the sub-objective #1, a new flexure-shear coupled fibre beam element is developed as complementary to the conventional fibre beam elements which neglect the shear (deformation) and are thus not applicable to PC girders under shear-critical loading scenarios. The new beam element is then applied to comprehensively study the system behavior and load sharing of multi-girder bridges under both flexure-dominated and shear-critical loading scenarios, where existing studies only focus on the bridge system behavior under flexure-dominated loading.

In the sub-objective #2, experimental data-based shear capacity models for intact PC girders are developed using probabilistic machine learning. Despite the efforts devoted to RC members in terms of the probabilistic shear capacity model development, no existing model is available for PC girders. The developed probabilistic models in this thesis can fill this research gap and benefit shear capacity predictions with better accuracy and precision, as well as reliability/fragility analysis of PC girders with the model error considered.

In the sub-objective #3, simulated data-based load-carrying capacity models for corroded PC girders are developed using Gaussian process regression. Due to the limited experimental data on the load-carrying capacity of corroded PC girders especially under shear-critical loading scenarios, no relevant work aimed to develop probabilistic models with prediction error quantified for corroded PC girders. The developed probabilistic models in this thesis can fill this research gap and quantify the corrosion effect on PC girders in terms of reduction in load-carrying capacity and increase in probability of failure.

1.5 Research Scope and Assumptions

This thesis aims at developing reliable capacity prediction models for intact/corroded PC bridge girders with particular emphasis on shear failure for intact PC girders and corrosion effect for corroded PC girders. Main assumptions/limitations in this thesis are summarised as follows:

1. The developed mechanics-based finite element (FE) models for intact and corroded PC girders are only appliable to bonded (pre-tensioned or post-tensioned) PC girders, since either perfect bonding (e.g., in the new flexure-shear coupled fibre beam element) or detailed bond-slip relationship (e.g., in the FE model for corroded PC girders) is utilized for the model development.

2. The developed data-based models in this thesis are also only appliable to bonded (intact or corroded) PC girders, since unbonded PC girders are not included in both the experimental and simulated databases for intact and corroded PC girders, respectively.

3. In the study of multi-girder PC bridge system, the torsion effects are neglected while the focuses are put on the flexural and shear behavior of girders and bridge systems.

1.6 Organization of Thesis

This thesis consists of eight chapters as follows:

- Chapter 1 of this thesis is a brief introduction into the background, problem statement, motivation, objectives and methodology, novelty and significance of this research.
- Chapter 2 provides a literature review regarding the relevant aspects related to the overall goal of developing probabilistic capacity prediction models for concrete girders.
- Chapter 3 presents the development of mechanics-based shear capacity models for intact PC girders, i.e., the new flexure-shear coupled fibre beam element.

- Chapter 4 presents the application of the newly developed flexure-shear coupled fibre beam element to multi-girder bridge analysis.
- Chapter 5 presents the development and demonstration of the experimental data-based shear capacity models for intact PC girders based on Bayesian linear regression.
- Chapter 6 presents the development and demonstration of the experimental data-based shear capacity models for intact PC girders based on Gaussian process regression.
- Chapter 7 presents the development and demonstration of the simulated data-based load-carrying capacity models for corroded PC girders based on Gaussian process regression.
- Chapter 8 concludes the thesis work with summary, conclusions, contributions, and highlights of this research, as well as the recommendation for future work.

CHAPTER 2: LITERATURE REVIEW

This chapter provides a literature review regarding the relevant aspects related to the overall goal of developing probabilistic capacity prediction models for prestressed concrete (PC) girders. Both deterministic and probabilistic capacity prediction models for PC girders are reviewed in this chapter with particular emphasis on shear capacity for intact PC girders and corrosion effect for corroded PC girders.

2.1 Deterministic Capacity Prediction Models for PC Girders

2.1.1 Flexural Capacity Prediction Models

Reliable capacity prediction is of significant importance for bridge girder evaluation to ensure structural safety and make proper management decisions, which mainly contains flexural and shear capacity prediction for PC girders. It was shown that nowadays the flexural capacity of concrete members can be well predicted with reasonable accuracy over a wide range of cases (Tošić et al. 2016). Thus, literature review on the flexural capacity prediction models is only briefly introduced as follows in this thesis.

Existing flexural capacity prediction model can be broadly categorized into mechanics-based finite element (FE) models (Coronelli and Gambarova 2004; Elghazy et al. 2018), and mechanics-based analytical models. FE models can be classified into models based on beam elements or continuum (e.g., quadrilateral/triangular and brick/tetrahedron) elements. For mechanics-based analytical models, the strain compatibility approach can be considered as the most well-received one, which has been adopted in many concrete structure and bridge design codes worldwide, e.g., ACI 318-19 (ACI 2019), AASHTO LRFD 2017 (AASHTO 2017), CSA A23.3:19 (CSA 2019), CSA S6:19 (CSA 2019), *fib* MC 2010 (*fib* 2010) and GB 50010-2010

(MOHURD 2010). This approach is based on the sectional analysis by satisfying stress equilibrium and strain compatibility conditions. For well-designed flexural-dominated concrete members that fail by concrete crushing after steel yielding, this approach has been validated by many researchers, which can provide satisfactory prediction results of flexural capacity (Tošić et al. 2016; Mast et al. 2018). As such, prediction of the flexure capacity of PC girders rarely needs finite element models.

2.1.2 Shear Capacity Prediction Models

2.1.2.1 Intact PC girders

Significant efforts have been devoted to the shear capacity prediction of concrete members among decades, leading to a wide variety of shear capacity prediction models, which can be broadly categorized into data-based (e.g., design code models) and mechanics-based models (e.g., finite element models). Generally, mechanics-based models are more functionally versatile with the ability to provide the structural behavior information during the whole loading process. In contrast, data-based models conventionally focus on only one quantity of interest. For example, the data-based shear capacity prediction model is only capable to provide shear capacity prediction, while it is incapable to provide predictions on deformation or stress-strain state. However, data-based models are computationally more efficient compared with mechanics-based models, which is especially beneficial in reliability or probabilistic studies.

Data-based models refer to those models mainly developed based on experimental database via regression approaches. Typical examples are the shear capacity prediction models from design codes which are also referred to as semi-empirical or simplified-mechanical equation models, e.g., ACI 318-19 (ACI 2019), AASHTO LRFD 2017 (AASHTO 2017), CSA A23.3:19 (CSA 2019), CSA S6:19 (CSA 2019), *fib* MC 2010 (*fib* 2010) and GB 50010-2010 (MOHURD 2010). Due to the simplified mechanics theories and elegant formulations, these models are readily comprehensible to engineers and have been widely utilized in engineering practice. However, it was found that (Nakamura et al. 2013) these models conventionally exhibit inherent conservative bias and large prediction scatters. Although being conservative should not be criticized for structural design purposes, several research/engineering areas requires models with quantitative information about the conservatism or the model error (e.g., bias and scatter), such as more realistic/confident reliability analysis and performance-based design (Gardoni et al. 2002). Thus, the model error of these design code models needs to be quantified and improved.

Mechanics-based models can be categorized into mechanics-based analytical models and FE models. Mechanics-based analytical models are generally more sophisticated than semi-empirical equation models. Examples are the modified compression field theory (MCFT) family (Vecchio and Collins 1986; Vecchio 2000) and the soften truss model (STM) family (Hsu 1988; Belarbi and Hsu 1994; Pang and Hus 1996; Hsu and Zhu 2002). These models have been widely used for concrete members under shear-critical loadings because of their accurate predictability for the shear capacity. Specifically, based on the MCFT, the general method for shear design in CSA A23.3:19 (CSA 2019), CSA S6:19 (CSA 2019) and AASHTO LRDF 2017 (AASHTO 2017) are developed and well accepted in engineering practice. For instance, the design expressions based on MCFT were shown by Nakamura et al. (2013) to yield the most accurate shear capacity estimations for PC members that failed in typical shear failure modes compared with other design expressions.

The abovementioned mechanics-based analytical models were mainly used to develop material stress-strain relationships of RC/PC panels/membrane elements. Thus, when applied to the shear capacity prediction of RC/PC girders, they are usually adopted as the concrete material models in FE models. Based on these mechanics-based analytical models, several nonlinear FE software/platforms have been developed such as *VecTor2* (Wong et al. 2013) based on the MCFT family and the *SCS* (Hsu and Mo 2010) based on the STM family. Additionally, mechanics-based analytical models can also be simplified to semi-empirical models for shear capacity prediction of RC/PC girders. For example, the shear capacity models from CSA A23.3:19 (CSA 2019) and AASHTO LRFD 2017 (AASHTO 2017) are developed based on the simplified MCFT.

FE models can be broadly categorized into 1D fibre beam element models (Spacone et al. 1996a, 1996b) and 2D/3D continuum-based solid element models (Vecchio 1989; Jnaid and Aboutaha 2016). 2D/3D continuum-based FE models are generally considered as more accurate than the analytical models and 1D fibre beam element models while relatively more computationally costly. When probabilistic/reliability analysis of large-scale structures is involved, 2D/3D continuum-based FE models can be impractical due to their computational cost. In contrast to the 2D/3D continuum FE approach, one distinguishing feature of the 1D fibre beam element approach is the use of simple material constitutive models (i.e., uniaxial stress-strain). Specifically, in the widely used 1D fibre beam element formulation (Spacone et al. 1996a, 1996b), the cross-section is discretized into concrete and steel fibres, and each fibre is assigned with a uniaxial stress-strain model. The fibre section compatibility is derived based on Euler-Bernoulli beam theory, in which a plane cross-section perpendicular to the neutral axis before deformation is assumed to remain perpendicular after deformation (i.e., shear deformation is neglected). As such, the coupled axial and flexural effects in slender beam members can be well captured with satisfactory numerical accuracy and high computational efficiency. In contrast, for members that involve non-negligible shear deformation, conventional fibre beam elements are not applicable and flexure-shear coupling effect need to be taken into account.

2.1.2.2 Corroded PC girders

Compared with studies on flexural capacity prediction of corroded PC girders (Coronelli et al. 2009; Castel et al. 2011; Wang et al. 2017a), research on shear capacity prediction of corroded PC girders is scarce. Belletti et al. (2020) developed nonlinear FE models for corroded PC girders without shear reinforcement based on the membrane elements in ABAQUS. Corrosion degree was defined as the average cross-sectional area reduction in steel bars due to corrosion. Based on the defined corrosion degree, key corrosion effects were modelled, i.e., reduced concrete compressive strength, deteriorated mechanical properties of prestressing strand, prestress force loss and bond degradation. An experimental test on naturally corroded PC girder was utilized to validate the developed FE model.

Several studies have been conducted on shear capacity prediction models of corroded reinforcement concrete (RC) beams, mainly including data-based models (Lu et al. 2018; Fu and Feng 2021) and mechanics-based FE models (Potisuk et al. 2011). Fu and Feng (2021) developed a machine leaning based shear capacity model for corroded RC beams based on the gradient boosting regression tree method and the compiled experimental database of 158 shear tests of corroded RC beams. Based on the same experimental database, Lu et al. (2018) developed an empirical model for predicting the residual shear capacity of corroded RC beams. Potisuk et al. (2011) developed 2D continuum-based FE models for corroded RC beams with shear-dominated behavior, in which corrosion induced damages were considered including concrete cover spalling, uniform stirrup cross-sectional loss, localized stirrup cross-sectional loss and debonding of corrosion-damaged stirrups. Although PC girders and RC beams are similar in terms of structural behavior to some extent, the shear capacity prediction of PC girders differs from that of RC beams due to the utilization of high-tensile-strength strands and prestressing force. Thus, studies on shear capacity prediction are required for corroded PC girders with well-consideration of unique features for PC girders.

2.2 Uncertainty and Structural Reliability

2.2.1 Aleatory and Epistemic Uncertainties

For shear capacity prediction of both intact and corroded PC girders, uncertainties are inevitable. Hacking (1975) classified the source of uncertainties as either aleatory or epistemic. Aleatory uncertainty is due to the natural randomness and inherent variability of complex phenomena. As a result, these are uncertainties that cannot be reduced. Examples are the uncertainties inside material properties, geometric dimensions and loads. On the contrary, epistemic uncertainty arises from the lack of knowledge or the finite size of observation samples, which is also referred to as model uncertainty or model error. This type of uncertainty can be reduced with improved mathematical modeling or collection of additional samples.

The aleatory uncertainty for PC girders has been studied and considered in reliability analysis by many researchers. Nowak and the Szerszen (2003) studied the uncertainties in material properties including the strength of concrete, reinforcing steel bars and prestressing strands. The bias factor (i.e., the ratio of mean strength to nominal value) and the coefficient of variation (COV) were summarized based on material test data provided by the industry. Ellingwood et al. (1980) studied the uncertainties in dimensions and geometry of PC girders, including sectional width and effective depth. MacGregor et al. (1997) summarized the typical statistical distributions to consider uncertainties in dead load, live load and impact load for PC girders.

The epistemic uncertainty is another important aspect of uncertainties. It was shown that the approach of only considering the aleatory uncertainty may greatly underestimate the probability of failure (Gokkaya et al. 2016; Yang et al. 2021). For structural analysis of concrete girders, the epistemic uncertainty mainly refers to the model uncertainty/error due to model inexactness (e.g., adopted idealizations and approximations, inexact model parameters due to finite size of experimental tests). The model uncertainty is conventionally considered as a multiplicative random variable, which can be obtained from comparison of experimental and model results. Somo and Hong (2005) analyzed the model uncertainties of several commonly referred models for predicting shear capacity of RC beams based on a compiled experimental database. Statistics of the model uncertainties (i.e., mean and COV) were obtained and compared based on the ratio of the test to predicted shear capacity. Similarly, Sykora et al. (2013, 2018) studied the model uncertainties in shear resistance models of RC beams from *fib* MC 2010 (*fib* 2010) and EN 1992-1-1 (Eurocode 2 2004).

2.2.2 Reliability Analysis

In the presence of uncertainties, neither the load effects nor component/system resistance can be treated as deterministic for safety assessment. The probability of failure is always greater than zero and absolute safety for structures is impossible to achieve. With prevailing uncertainties considered, reliability analysis can be conducted to predict the failure probability of PC girders/bridges, based on which constructive guidance can be provided for design and maintenance purpose.

Thoft-Christensen and Baker (2012) defined structural reliability as the probability that a structure will attain each specified limit state during a reference period. The limit state is the boundary between safety and failure. For a structural component or system, the load-carrying capacity, R, and the load effect, S, formulate the basic limit state function, g, as shown in Eq. (2-1).

$$g\left(R,S\right)=R-S \tag{2-1}$$

Thus, the negative value of g indicates the violation of the limit state, namely failure. The probability of failure, P_F, can be expressed as shown in Eq. (2-2).

$$P_F=P\left(g<0\right) \tag{2-2}$$

Significant efforts have been devoted to reliability analysis of both intact (Nowak and Zhou 1990; Tabsh and Nowak 1991; Du and Au 2005; Hamutçuoğlu and Scott 2009) and corroded (Stewart and Rosowsky 1998, Darmawan and Stewart 2007) concrete girders. Most of the studies focused on the flexural capacity limit state of concrete girders, while only a few took into account the moment-shear interaction (Hamutçuoğlu and Scott 2009). It was shown that the interaction of moment and shear plays an important role for failure states (Hamutçuoğlu and Scott 2009).

2.3 Probabilistic Capacity Prediction Models for PC Girders

To facilitate the consideration of both aleatory and epistemic uncertainties in reliability-based bridge assessment, probabilistic load-carrying capacity prediction models are required. To this end, several research were conducted for probabilistic capacity prediction of intact and corroded concrete members.

2.3.1 Intact PC Girders

Several studies on probabilistic shear capacity model development are existing for RC members. Yu et al. (2019) developed probabilistic shear capacity models for RC columns. New deterministic models for shear capacity were developed first based on some well-recognized shear mechanical theories (i.e., the variable angle truss-arch theory). Then the probabilistic distributions of unknown model parameters were estimated by Bayesian inference based on a compiled database of experimental tests. Ning and Li (2017, 2018) proposed probabilistic shear capacity models for reinforced concrete (RC) beams without stirrups and squat walls, also following the scheme of first developing new deterministic models and then calibrating probabilistic models.

To facilitate the use of the developed probabilistic models, instead of developing new deterministic shear capacity models, probabilistic correction terms can be added to existing models. One typical approach is to quantify the model error (i.e., prediction bias and scatter) of existing models as an independent random variable and use it as a probabilistic corrective factor (MacGregor et al. 1997; Del Vecchio et al. 2017; Sykora et al. 2018). However, this approach is based on the assumption that there is no systematic correlation between the model error and model parameters, but the model can actually be improved by correcting the potentially existing systematic error. Gardoni et al. (2002) developed probabilistic correction terms to the existing deterministic shear capacity models of RC columns. A polynomial function form containing a suitable set of model parameters was adopted for the probabilistic correction terms. Song et al. (2010) implemented and improved this probabilistic model framework to develop probabilistic shear capacity models for RC beams without stirrups. It was shown that the developed models not only corrected the inherent bias inside the existing models, but also decrease the prediction scatter significantly.

Despite the aforementioned efforts on probabilistic shear capacity models of RC members, no relevant literature is available for PC girders. The shear behavior of PC girders differs from RC members due to the utilization of high-tensile-strength strands and higher-strength concrete in bridge girder constructions, as well as the application of prestressing force. Thus, probabilistic shear capacity models with quantified model uncertainties are required to be developed for PC girders.

2.3.2 Corroded PC Girders

Similarly, despite the limited efforts devoted to probabilistic load-carrying capacity models for corroded RC members, no available research has been found for corroded PC girders. Choe et al (2008) developed a probabilistic shear capacity prediction model for corroded RC columns based on a compiled experimental database, which was used to estimate seismic fragility of corroded structures. Ma et al. (2013) developed a probabilistic flexural capacity prediction model for corroded RC beams on the basis of a compiled experimental database. Recognizing the limited data available from systematically tested corroded RC beams experimentally, Aslani and Dehestani (2020) developed a probabilistic model to predict the flexural capacity reduction as a function of corrosion degree, using the database generated from FE simulations. Note that these efforts were mainly devoted to corroded RC members, while no relevant work aimed to develop probabilistic models with prediction error quantified for corroded PC girders. This is possibly due to the limited experimental work on corroded PC girders especially for shear-critical loading test (Belletti et al. 2020; Wang et al. 2020), since the calibration of probabilistic models conventionally requires a large set of data. Thus, further studies are required to address this gap for corroded PC girders.

CHAPTER 3: DEVELOPMENT OF MECHANICS-BASED FIBRE BEAM ELEMENT FOR PRESTRESSED CONCRETE BEAMS CONSIDERING FLEXURE-SHEAR COUPLING

In order to consider the interactive behavior of flexure and shear, an enhanced displacement-based fibre beam element is developed by utilizing multi-axial material constitutive models for fibres, in particular, with the Modified Compression Field Theory (MCFT) for fibres representing concrete with smeared stirrups in reinforced and prestressed concrete (RC/PC) beams/girders. The potential shear-locking problem is avoided by adopting a mixed interpolation form with a bubble term for the displacement field, and the validity of the approach is verified by a classic example. The proposed element is first validated through a classic test series of shear-critical RC beams from the literature and then applied to a PC girder recently tested under both shear-critical and flexure-dominated scenarios. It is shown that the proposed element can be used to predict the structural behavior of RC beams and PC girders satisfactorily, after enhancing the conventional fibre beam element by considering the coupling of flexure and shear. In addition, the proposed element provides a tool to predict both flexure and shear capacities of concrete beams with adequate accuracy.

3.1 Introduction

Reinforced and prestressed concrete (RC/PC) beams or girders are widely used structural components in building and bridge engineering. Under in-plane loading, their flexure and shear behaviors are of concern to structural engineers and analysts. A variety of engineering models for flexural and shear capacity predictions have been developed and used for design purposes (ACI 2019; CSA 2019a; CSA 2019b; *fib* 2013). Compared to flexural behavior, shear behavior is more complex and less understood due to the complex shear transfer mechanism, especially after concrete cracks. In addition, shear failure is typically more brittle compared with flexural failure and considered as a more consequential limit state. As such, accurate prediction of the nonlinear behavior of RC/PC beams considering the coupling or interactive behavior of flexure and shear is of significant value for reliable engineering design and assessment, e.g., particularly for newly designed beams with smaller shear span to depth ratios and/or existing beams with insufficient transverse reinforcement (e.g., due to inappropriate design or construction errors).

To understand the nonlinear behavior of concrete beams, finite element (FE) analysis has been shown to be a viable alternative to physical experiments. Different FE approaches have been proposed, including modeling using three-dimensional (3-D) or two-dimensional (2-D) continuum elements (Vecchio 1989; Belletti et al. 2013; Jnaid and Aboutaha 2016) and one-dimensional (1-D) fibre beam elements (Spacone et al. 1996a; Spacone et al. 1996b). Among these types of elements, the 1D fibre beam element has been proved to be computational efficient with adequate accuracy (Ferreira et al. 2015) for flexure-behavior-dominated members, and can be used for finite element analysis (FEA) of large-scale frame-type structural systems and FEA-based probabilistic structural analysis. Furthermore, in contrast to the continuum FE approach, one distinguishing feature of the fibre beam element approach is the use of simple material constitutive models (i.e., uniaxial). Specifically, in the widely used 1-D fibre beam element formulation, the cross-section is discretized into material fibres, and each fibre is assigned with a uniaxial concrete or steel stress-strain model. The fibre section compatibility is derived based on Euler-Bernoulli beam theory, in which a plane cross-section perpendicular to the neutral axis before deformation is assumed to remain perpendicular after deformation (i.e., shear deformation is neglected). As such, the coupled axial and flexural effects in slender beam members can be well captured with satisfactory numerical accuracy and high computational efficiency. However, for members that involve non-negligible shear deformation, the finite shear flexibility and strength need to be taken into account.

One approach to consider shear deformation is to use a predefined shear force-deformation model, which is aggregated to the conventional fibre-section or lumped in the ends of fibre beam elements (D'Ambrisi and Filippou 1999; Marini and Spacone 2006; Xu and Zhang 2012). However, this approach relies on the prior knowledge of the shear force-deformation relationship and oversimplifies coupling between shear and flexure. Besides this approach to consider the coupling effect in RC/PC beams, a variety of modified fibre beam elements have been proposed based on Timoshenko beam theory (i.e., considering uniform shear strain over the cross-section) or even generalized beam theories (i.e., considering torsion and warping). Filippou and Saritas (2006) proposed a mixed-formulation for fibre beam element based on Timoshenko beam theory to simulate the response of RC beams under the interaction of axial force, shear force, and bending moment. Mixed fibre beam elements, similar to force-based fibre beam elements, require fewer elements per beam compared with displacement-based beam elements and are free from the common problem of shear locking, i.e., underestimation of deformation due to spurious stiffness contribution in the beam element formulation (Bitar et al. 2018). However, additional iterations are needed for element state determination in mixed and force-based fibre beam elements; this can lead to additional computational cost and convergence issues (Saritas 2006). Ceresa et al. (2009) and Li et al (2016) utilized the displacement-based beam element based on Timoshenko beam theory with a focus on the nonlinear cyclic behavior of RC members. The FE formulation utilized in their fibre beam elements are based on the total form using secant stiffness, instead of the incremental form using tangent stiffness which is more efficient for general FE codes. In addition, Stramandinoli and Rovere (2012) and Feng et al. (2017; 2018) studied displacement-based

Timoshenko beam elements for nonlinear analysis of shear-critical RC beams within the context of tangent stiffness FE formulation. The basic idea behind these fibre beam element formulations is to incorporate a multi-axial constitutive model for concrete fibres, instead of the uniaxial constitutive laws in conventional fibre beam elements. As such, the coupling effect of flexure and shear can be obtained not only at the element level, but also at the material and section levels. For example, Feng et al. (2017) used a softened damage-plasticity model to represent the multi-axial constitutive behavior of concrete fibres, which shows the improvement for simulating the behavior of shear-critical RC beams compared with the conventional fibre beam element developed based on Euler-Bernoulli beam theory.

When integrating multi-axial constitutive models with 1-D fibre beam element formulations, a wide variety of constitutive models for plain or reinforced concrete can be used. Multi-axial concrete constitutive models of different degrees of sophistication include plasticity-based models (e.g., Yu et al. 2010a), damage-plasticity models (e.g., Yu et al. 2010b), fracture-based models (e.g., Bažant and Oh 1983), fracture-plasticity models (e.g., Červenka and Papanikolaou 2008; ATENA 2020), and smeared crack models such as the softened truss model (STM) (Hsu and Zhu 2002) and the modified compression field theory (MCFT) (Vecchio and Collins 1986; Vecchio 2000). These smeared crack models have been widely used for shear-critical members because of their simple interpretability and accurate predictability for the shear capacity of both RC and PC members. Specifically, based on the MCFT, the general method for shear design in CSA A23.3:19 (CSA 2019a) and AASHTO LRFD 2017 (AASHTO 2017) are developed and well accepted by engineering practice. For instance, the design expressions based on MCFT were shown by Nakamura et al. (2013) to yield the most accurate shear capacity estimations for PC members that failed in typical shear failure modes compared with other design expressions. It is also worth mentioning that the MCFT family forms the basis for a widely used nonlinear FE analysis software, *VecTor2*, which was developed for reinforced concrete membrane structures (Wong et al. 2013). The *DIANA* FEA software also adopted MCFT as the basis of the Total Strain Crack Models for concrete constitutive models (DIANA 2021).

Motivated by the robustness of the MCFT theory for shear-critical components (e.g., in *VecTor2*) and the efficiency of the conventional 1-D fibre beam elements (e.g., in *OpenSees*), this study aims to develop a new flexure-shear coupled fibre beam element , by integrating the benefits of these two modeling techniques. This novel element can capture both flexure and shear deformations of RC/PC girders and thus is particularly useful for analyzing girders under shear-critical loading. Compared with the widely used fibre beam element that accounts for flexure deformation only, the proposed element is capable of considering both flexure and shear deformations. Thus, it provides analysts and engineers with a reliable numerical tool for concrete girder behavior/failure analysis, particularly for girders under shear-critical loading. Compared with 2D/3D continuum FE elements currently used to capture both flexure and shear deformations, the proposed element is computationally more efficient, from which the FE-based reliability analysis and FE analysis of large-scale structures can benefit. To sum up, this new element enables more accurate and efficient capacity/performance assessment of RC/PC girders in engineering practice, particularly for shear-critical ones.

To this end, as complementary to the conventional fibre beam elements without considering shear in *OpenSees*, which is adopted as the reference element for comparison purpose in this study, a new displacement-based fibre beam element is developed to consider the coupling effect of flexure and shear using the tangent stiffness formulation. The common issue of shear locking, associated with classic displacement-based elements, is also discussed by comparing the mixed interpolation method and the reduced integration method. The proposed element is first validated through a classic test series of shear-critical RC beams obtained from the literature, and then applied to a bridge girder recently tested under both flexure-dominated and shear-critical loading conditions. Comparisons with numerical results from the reference element are also included to demonstrate the advantage of the proposed element.

3.2 Flexural Shear Coupled Fibre Beam Element

3.2.1 Element Formulation

Under in-plane loading conditions, a straight concrete beam can be modeled using two-node beam elements. Each node contains three degrees of freedom (DOFs) as shown in Figure 3-1: the axial displacement along the beam axis (e.g., DOFs u_1, u_2), the transverse displacement perpendicular to the beam axis (e.g., DOFs v_1, v_2), and the rotation (e.g., DOFs α_1, α_2). The conventional fibre beam element, which is formulated based on Euler-Bernoulli beam theory, can be described by the displacement field vector, $\mathbf{u}(x)$, consisting of the longitudinal displacement field, $u(x)$, and the transverse displacement field, $v(x)$. In contrast, to consider the shear flexibility or the shear failure mechanism, the proposed element, which is formulated based on Timoshenko beam theory, contains the cross-section rotation field, $\alpha(x)$, in addition to $u(x)$ and $v(x)$, as shown in Eq. (3-1). This is because of the difference between the slope of the transverse displacement and the cross-section rotation, which is resultant from the non-zero shear strain.

$$\mathbf{u}(x)=\{u(x),\alpha(x),v(x)\}^T \tag{3-1}$$

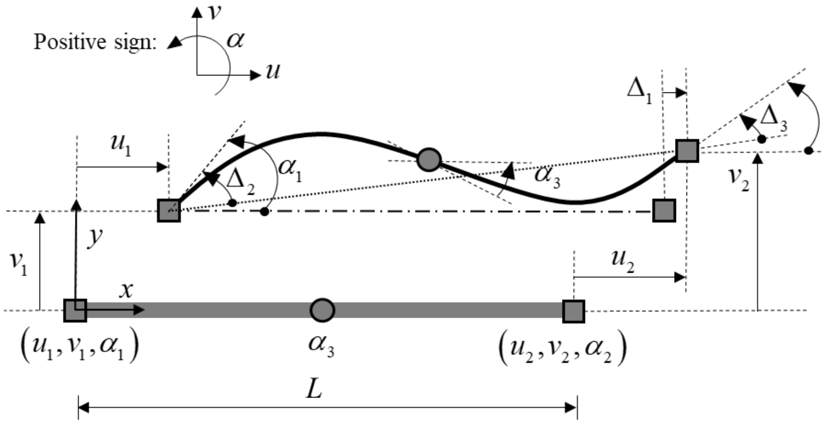

Figure 3-1: DOFs of the element in the local coordinate system and in the basic system

The description of the displacement field using the nodal displacement vector requires a set of well-behaved shape functions. However, the classic Hermite shape functions, which are used for conventional displacement-based fibre beam elements, can lead to shear locking problems. In order to remedy the possible shear-locking problem, different techniques can be used, such as reduced integration and advanced shape functions of mixed interpolation with bubble terms (Ehrlich and Armero 2005). In this study, the bubble term with an interior DOF, α_3 = rotation at the middle of the element as shown in Figure 3-1, is adopted and thus the displacement field is approximated per Eq. (3-2),

$$\begin{Bmatrix} u(x) \\ \alpha(x) \\ v(x) \end{Bmatrix} = \begin{bmatrix} 1-\frac{x}{L} & 0 & 0 & \frac{x}{L} & 0 & 0 & 0 \\ 0 & 1-\frac{x}{L} & 0 & 0 & \frac{x}{L} & 0 & \frac{4x}{L}\left(1-\frac{x}{L}\right) \\ 0 & \frac{x}{2}\left(1-\frac{x}{L}\right) & 1-\frac{x}{L} & 0 & -\frac{x}{2}\left(1-\frac{x}{L}\right) & \frac{x}{L} & \frac{2x}{3}\left(\frac{2x}{L}-1\right)\left(1-\frac{x}{L}\right) \end{bmatrix} \begin{Bmatrix} u_1 \\ \alpha_1 \\ v_1 \\ u_2 \\ \alpha_2 \\ v_2 \\ \alpha_3 \end{Bmatrix} \quad (3\text{-}2)$$

where L is the undeformed element length. According to Timoshenko beam theory, which assumes that plane sections remain plane but not necessarily perpendicular to the neutral axis, the generalized section strain vector, $\boldsymbol{\varepsilon}^{s}\left(x\right)$, containing three components, can be derived from the displacement field through compatibility conditions according to Eq. (3-3).

$$\boldsymbol{\varepsilon}^{s}\left(x\right)=\begin{Bmatrix}\varepsilon\left(x\right)\\ \kappa\left(x\right)\\ \gamma\left(x\right)\end{Bmatrix}=\begin{bmatrix}\dfrac{\partial}{\partial x} & 0 & 0\\ 0 & \dfrac{\partial}{\partial x} & 0\\ 0 & -1 & \dfrac{\partial}{\partial x}\end{bmatrix}\begin{Bmatrix}u\left(x\right)\\ \alpha\left(x\right)\\ v\left(x\right)\end{Bmatrix} \tag{3-3}$$

where $\varepsilon\left(x\right)$ is the axial strain representing the longitudinal extension, $\kappa\left(x\right)$ is the section curvature representing the flexural deformation, and $\gamma\left(x\right)$ is the shear deformation. Substituting Eq. (2) into Eq. (3), the strain field can be expressed as Eq. (3-4).

$$\boldsymbol{\varepsilon}^{s}\left(x\right)=\begin{Bmatrix}\varepsilon\left(x\right)\\ \kappa\left(x\right)\\ \gamma\left(x\right)\end{Bmatrix}=\begin{bmatrix}-\dfrac{1}{L} & 0 & 0 & \dfrac{1}{L} & 0 & 0 & 0\\ 0 & -\dfrac{1}{L} & 0 & 0 & \dfrac{1}{L} & 0 & \dfrac{4}{L}-\dfrac{8x}{L^{2}}\\ 0 & -\dfrac{1}{2} & -\dfrac{1}{L} & 0 & -\dfrac{1}{2} & \dfrac{1}{L} & -\dfrac{2}{3}\end{bmatrix}\begin{Bmatrix}u_{1}\\ \alpha_{1}\\ v_{1}\\ u_{2}\\ \alpha_{2}\\ v_{2}\\ \alpha_{3}\end{Bmatrix}=\mathbf{B}^{L}\left(x\right)\mathbf{u}^{e} \tag{3-4}$$

where $\mathbf{B}^{L}\left(x\right)$ is the matrix relating the generalized section strain, $\boldsymbol{\varepsilon}^{s}\left(x\right)$, with the vector of element DOFs, $\mathbf{u}^{e}$, including the nodal DOFs in the local coordinate system and the interior DOF. Under the assumption of small deformation, the nodal DOFs in the basic system, $\boldsymbol{\Delta}^{e}$, with the rigid-body displacement modes eliminated, can be expressed as Eq. (3-5).

$$\boldsymbol{\Delta}^{e}=\begin{Bmatrix}\Delta_{1}\\ \Delta_{2}\\ \Delta_{3}\\ \alpha_{3}\end{Bmatrix}=\begin{bmatrix}-1 & 0 & 0 & 1 & 0 & 0 & 0\\ 0 & 1 & 1/L & 0 & 0 & -1/L & 0\\ 0 & 0 & 1/L & 0 & 1 & -1/L & 0\\ 0 & 0 & 0 & 0 & 0 & 0 & 1\end{bmatrix}\mathbf{u}^{e} \tag{3-5}$$

Based on Eq. (3-4) and Eq. (3-5), the generalized section strain field can be expressed as Eq. (3-6).

$$\boldsymbol{\varepsilon}^s(x)=\begin{Bmatrix}\varepsilon(x)\\ \kappa(x)\\ \gamma(x)\end{Bmatrix}=\begin{bmatrix}\frac{1}{L} & 0 & 0 & 0\\ 0 & -\frac{1}{L} & \frac{1}{L} & \frac{4}{L}-\frac{8x}{L^2}\\ 0 & -\frac{1}{2} & -\frac{1}{2} & -\frac{2}{3}\end{bmatrix}\begin{Bmatrix}\Delta_1\\ \Delta_2\\ \Delta_3\\ \alpha_3\end{Bmatrix}=\mathbf{B}(x)\boldsymbol{\Delta}^e \tag{3-6}$$

According to the principle of virtual work, the element stiffness matrix $\mathbf{K}^e$ and element force vector $\mathbf{F}^e$ in the basic system can be obtained as Eq. (3-7) and Eq. (3-8), respectively,

$$\mathbf{K}^e=\int_L \mathbf{B}^T(x)\mathbf{K}^s(x)\mathbf{B}(x)dx \tag{3-7}$$

$$\mathbf{F}^e=\int_L \mathbf{B}^T(x)\mathbf{F}^s(x)dx \tag{3-8}$$

where $\mathbf{K}^s(x)$ is the section stiffness matrix, and $\mathbf{F}^s(x)$ is the section force vector, which will be determined in the following section state determination as follows.

In the proposed fibre beam element, the fibre section is divided into uniaxial steel fibres representing the longitudinal steel reinforcement and multi-axial concrete fibres with uniform shear strain for 2-D concrete with smeared transverse steel reinforcement. The fibre strain vector at section height y, $\boldsymbol{\varepsilon}^{fib}(x,y)=\{\varepsilon_{xx},\gamma_{xy}\}^T$, is obtained based on the plane section assumption, see Eq. (3-9),

$$\boldsymbol{\varepsilon}^{fib}(x,y)=\mathbf{I}(y)\boldsymbol{\varepsilon}^s(x)==\begin{Bmatrix}1 & -y & 0\\ 0 & 0 & \psi\end{Bmatrix}\begin{Bmatrix}\varepsilon(x)\\ \kappa(x)\\ \gamma(x)\end{Bmatrix} \tag{3-9}$$

where $\mathbf{I}(y)$ is the section kinematic (compatibility) vector, ψ is the shear coefficient (e.g., $\psi = 5/6$ for rectangular cross-section of elastic beams). The section stiffness matrix $\mathbf{K}^s(x)$ and section force vector $\mathbf{F}^s(x)$ are determined according to Eq. (3-10) and (3-11), respectively,

$$\mathbf{K}^s(x) = \int_{A(x)} \mathbf{I}^T(y)\mathbf{D}^{fib}(x,y)\mathbf{I}(y)dA \tag{3-10}$$

$$\mathbf{F}^s(x) = \int_{A(x)} \mathbf{I}^T(y)\boldsymbol{\sigma}^{fib}(x,y)dA \tag{3-11}$$

where $\mathbf{D}^{fib}(x,y)$ and $\boldsymbol{\sigma}^{fib}(x,y)$ are the tangent stiffness matrix and stress vector of the material fibre at location (*x*, *y*), respectively. Note that $\boldsymbol{\sigma}^{fib}(x,y) = \{\sigma_{xx}, \tau_{xy}\}^T$ contains the normal stress (σ_{xx}) and shear stress component (τ_{xy}), which is different from the uniaxial material fibre in conventional fibre sections, where only the normal stress (σ_{xx}) is involved.

3.2.2 Material Modeling

As in continuum FE modeling of plane problems, the proposed fibre beam element requires 2-D material constitutive models for concrete in multi-axial fibre sections, instead of uniaxial material models for concrete as used in conventional fibre sections. They can be either reduced from classic 3-D plasticity-based models (e.g., under the plane stress condition) or specialized 2-D models, such as the modified compression field theory (MCFT) for concrete structures. MCFT considers cracked concrete as an orthotropic material, which can be defined based on average stresses and strains in the principal directions over areas or distances large enough to include several cracks. The principal strain axes are assumed to coincide with the principal stress axes for concrete, and steel is perfectly bonded to concrete. A concise summary is presented here to provide context for the integration of the theory with the new element. Additional details can be found in Vecchio and

Collins (1986). Note that the crack checking procedure introduced in MCFT, which was to account the local stress variations across cracks, is avoided by utilizing average steel stresses and strains for reinforcement as recommended by Stevens et al. (1991). Note that the validation on the implementation of MCFT is conducted and summarized in Appendix A.

3.2.2.1 Modified compression field theory

In MCFT, given a strain state $\boldsymbol{\varepsilon}=\left(\varepsilon_{xx},\varepsilon_{yy},\gamma_{xy}\right)^T$, the principal strain vector $\boldsymbol{\varepsilon}^*=\left(\varepsilon_1,\varepsilon_2,\gamma_{12}\right)^T$ with $\gamma_{12}=0$ can be obtained, as per Eq. (3-12),

$$\boldsymbol{\varepsilon}^*=\mathbf{T}\boldsymbol{\varepsilon},\ \text{in which}\ \mathbf{T}=\begin{bmatrix} \cos^2\varphi & \sin^2\varphi & \sin\varphi\cos\varphi \\ \sin^2\varphi & \cos^2\varphi & -\sin\varphi\cos\varphi \\ -2\sin\varphi\cos\varphi & 2\sin\varphi\cos\varphi & \cos^2\varphi-\sin^2\varphi \end{bmatrix} \tag{3-12}$$

where φ is the angle between the first principal-axis and *x*-axis, which is obtained as shown in Eq. (3-13) by imposing $\gamma_{12}=0$ in Eq. (3-12).

$$\varphi=\frac{1}{2}\arctan\frac{\gamma_{xy}}{\varepsilon_{xx}-\varepsilon_{yy}} \tag{3-13}$$

With the principal strain vector $\boldsymbol{\varepsilon}^*=\left(\varepsilon_1,\varepsilon_2,\gamma_{12}\right)^T$, the stress vector and tangent stiffness matrix in the principal directions for concrete can be obtained based on the uniaxial stress-strain relationship $\sigma(\varepsilon)$ after considering effects of bi-axial stress states. As such, the following three different stress or strain states need to be considered: (1) *Tension-Compression (T-C)* state characterized by $\varepsilon_1>0$ and $\varepsilon_2<0$, (2) *Tension-Tension (T-T)* state characterized by $\varepsilon_1>0$ and $\varepsilon_2>0$, and (3) *Compression-Compression (C-C)* state characterized $\varepsilon_1<0$ and $\varepsilon_2<0$.

Under the strain states of *T-T* and *C-C*, concrete is assumed to behave independently in the two principal directions, and thus the principal stress components, σ_1^c and σ_2^c (with the superscript *c* denoting concrete), can be determined by Eq (3-14) where $\sigma(\varepsilon)$ is the uniaxial stress-strain relationship of concrete.

$$\sigma_1^c = \sigma(\varepsilon_1); \qquad \sigma_2^c = \sigma(\varepsilon_2) \tag{3-14}$$

By contrast, under the strain state of *T-C*, compression-softening is introduced to account for the reduced principal compressive strength due to the co-existing principal tensile strain ($\varepsilon_1 > 0$) through a reduction factor β [30], as shown in Eq. (3-15),

$$\sigma_1^c = \sigma(\varepsilon_1); \qquad \sigma_2^c = \beta(\varepsilon_1, \varepsilon_c') \cdot \sigma(\varepsilon_2); \qquad \beta(\varepsilon_1, \varepsilon_c') = \frac{1}{1 - 0.27(\varepsilon_1/\varepsilon_c' + 0.37)} \tag{3-15}$$

in which, β is a function of the co-existing principal tensile strain $\varepsilon_1 > 0$ and the concrete compressive strain at peak stress ($\varepsilon_c' < 0$).

With $\sigma_1^c(\varepsilon_1)$ and $\sigma_2^c(\varepsilon_2)$ defined above, together with a common assumption that the stresses and strains due to the Poisson effect could be neglected in a biaxial stress and strain condition (Hsu and Zhu 2002; Filippou and Saritas 2006; Ceresa et al. 2009; Li et al. 2016) the tangent stiffness matrix of 2-D concrete in principal directions, $\mathbf{D}^{c*}$, can be defined as Eq. (3-16),

$$\mathbf{D}^{c*} = \begin{bmatrix} E_{11}^c & E_{12}^c & 0 \\ E_{21}^c & E_{22}^c & 0 \\ 0 & 0 & G_{12}^c \end{bmatrix} \tag{3-16}$$

where $E_{11}^c = \dfrac{d\sigma_1^c}{d\varepsilon_1}$, $E_{22}^c = \dfrac{d\sigma_2^c}{d\varepsilon_2}$, $E_{12}^c = E_{21}^c = 0$ and the shear modulus $G_{12}^c = \dfrac{\sigma_1^c - \sigma_2^c}{2(\varepsilon_1 - \varepsilon_2)}$ [39] for orthotropic materials (e.g., concrete). As such, the principal stress increment $\mathbf{d\sigma}^{c*}$ =

$\left(d\sigma_1^c, d\sigma_1^c, d\tau_{12}^c\right)^T$ can be related to the principal strain increment $\mathbf{d\varepsilon}^* = \left(d\varepsilon_1, d\varepsilon_2, d\gamma_{12}\right)^T$ according to the incremental tangent constitutive equation as shown in Eq. (3-17).

$$\mathbf{d\sigma}^{c*} = \mathbf{D}^{c*}\mathbf{d\varepsilon}^* \tag{3-17}$$

Thus, the material state determination for concrete can be conducted to obtain the stress vector $\boldsymbol{\sigma}^c = \left(\sigma_{xx}^c, \sigma_{yy}^c, \tau_{xy}^c\right)^T$ and the tangent stiffness matrix $\mathbf{D}^c$ of concrete in the local coordinate system by Eq. (3-18) and Eq. (3-19), respectively.

$$\boldsymbol{\sigma}^c = \mathbf{T}^T\boldsymbol{\sigma}^{c*} \tag{3-18}$$

$$\mathbf{D}^c = \mathbf{T}^T\mathbf{D}^{c*}\mathbf{T} \tag{3-19}$$

The stress vector $\boldsymbol{\sigma}$ and the tangent stiffness matrix $\mathbf{D}$ for concrete with smeared steel (e.g., transverse steel in beams) can be obtained using Eq. (3-20) and Eq. (3-21), respectively, by aggregating the contributions from concrete and transverse steel.

$$\boldsymbol{\sigma} = \boldsymbol{\sigma}^c + \boldsymbol{\sigma}^v = \boldsymbol{\sigma}^c + \begin{Bmatrix} 0 \\ \rho_y \sigma_{yv} \\ 0 \end{Bmatrix} \tag{3-20}$$

$$\mathbf{D} = \mathbf{D}^c + \mathbf{D}^v = \mathbf{D}^c + \begin{bmatrix} 0 & 0 & 0 \\ 0 & \rho_y E_{yv} & 0 \\ 0 & 0 & 0 \end{bmatrix} \tag{3-21}$$

where $\rho_y = A_{yv}/bs$ is the reinforcement ratio of transverse steel, defined as the ratio of the total area of transverse steel A_{yv} over the area formed by the cross-sectional width b and the stirrup spacing s; σ_{yv} and E_{yv} are the stress and tangent modulus of transverse steel. The stress vector increment $d\boldsymbol{\sigma} = \left(d\sigma_{xx}, d\sigma_{yy}, d\tau_{xy}\right)^T$ of reinforced concrete with smeared steel can be related to the strain vector increment $d\boldsymbol{\varepsilon} = \left(d\varepsilon_{xx}, d\varepsilon_{yy}, d\gamma_{xy}\right)^T$ via Eq. (3-22).

$$\mathrm{d}\boldsymbol{\sigma} = \mathbf{D}\mathrm{d}\boldsymbol{\varepsilon} \tag{3-22}$$

Note that in the aforementioned material strain vector $\boldsymbol{\varepsilon} = \left(\varepsilon_{xx}, \varepsilon_{yy}, \gamma_{xy}\right)^T$, the fibre strain components $\boldsymbol{\varepsilon}^{fib}\left(x, y\right) = \left\{\varepsilon_{xx}, \gamma_{xy}\right\}^T$ can be obtained for each multi-axial concrete fibre according to Eq. (3-9). The unknown transverse strain ε_{yy} can be obtained by imposing the internal equilibrium between stirrups and concrete in the transverse direction (*y*), namely $\sigma_{yy} = \sigma_{yy}^c + \rho_y \sigma_{yv} = 0$. Alternatively, imposing $d\sigma_{yy} = 0$ in Eq. (3-22) leads to the incremental transverse strain $d\varepsilon_{yy}$ in Eq. (3-23).

$$d\varepsilon_{yy} = -\frac{d\varepsilon_{xx} D_{21} + d\gamma_{xy} D_{23}}{D_{22}} \tag{3-23}$$

Accordingly, the condensed material constitutive relationship for multi-axial concrete fibres with smeared steel can be obtained as shown in Eq. (3-24) and Eq. (3-25).

$$\mathrm{d}\bar{\boldsymbol{\sigma}} = \bar{\mathbf{D}}\ \mathrm{d}\boldsymbol{\varepsilon}^{fib} \tag{3-24}$$

$$\bar{\mathbf{D}} = \begin{bmatrix} D_{11} - \dfrac{D_{12} D_{21}}{D_{22}} & D_{13} - \dfrac{D_{12} D_{23}}{D_{22}} \\ D_{31} - \dfrac{D_{32} D_{21}}{D_{22}} & D_{33} - \dfrac{D_{32} D_{23}}{D_{22}} \end{bmatrix} \tag{3-25}$$

where $\mathrm{d}\bar{\boldsymbol{\sigma}} = \left\{\mathrm{d}\sigma_{xx}, \mathrm{d}\tau_{xy}\right\}^T$ and $\mathrm{d}\boldsymbol{\varepsilon}^{fib} = \left\{\mathrm{d}\varepsilon_{xx}, \mathrm{d}\varepsilon_{xy}\right\}^T$ represent the fibre stress increment and fibre strain increment, respectively, and $\bar{\mathbf{D}}$ is the condensed stiffness matrix for multi-axial concrete fibres with smeared steel.

In contrast to transverse reinforcement, longitudinal reinforcement in the multi-axial fibre sections for the proposed fibre beam element is modeled by uniaxial fibres in a discrete manner in the same way as in conventional fibre sections. Hence, the section stiffness matrix $\mathbf{K}^s(x)$ and section force vector $\mathbf{F}^s(x)$ in Eq. (3-10) and (3-11), can be rewritten as Eq. (3-26) and Eq. (3-27), respectively, by considering the contributions of longitudinal steel fibres (i.e., $\mathbf{D}^l$ and $\boldsymbol{\sigma}^l$) and the multi-axial concrete fibres (i.e., $\bar{\mathbf{D}}$ and $\bar{\boldsymbol{\sigma}}$) to $\mathbf{D}^{fib}(x,y)$ and $\boldsymbol{\sigma}^{fib}(x,y)$.

$$\mathbf{K}^s(x)=\int_{A(x)}\mathbf{I}^T(y)\bar{\mathbf{D}}(x,y)\mathbf{I}(y)dA+\sum_{i=1}^{n^l}\mathbf{I}^T(y_i)\mathbf{D}^l\mathbf{I}(y_i)A_i^l \tag{3-26}$$

$$\mathbf{F}^s(x)=\int_{A(x)}\mathbf{I}^T(y)\bar{\boldsymbol{\sigma}}(x,y)dA+\sum_{i=1}^{n^l}\mathbf{I}^T(y_i)\boldsymbol{\sigma}^l A_i^l \tag{3-27}$$

Here, $\boldsymbol{\sigma}^l=\begin{Bmatrix}\sigma^l\\0\end{Bmatrix}$ and $\mathbf{D}^l=\begin{bmatrix}E^l & 0\\0 & 0\end{bmatrix}$ represent the stress vector and tangent stiffness matrix for the longitudinal reinforcement in the expanded form with σ^l and $E^l=d\sigma^l/d\varepsilon$ representing the stress and tangent modulus of longitudinal steel. A_i^l represents the cross-sectional area of the *i*-th longitudinal reinforcement (*i* = 1, 2, …, n^l, which indicates the number of longitudinal reinforcing bars).

To summarize, in the context of MCFT, uniaxial constitutive material laws for concrete and steel are needed. This allows to take advantage of existing uniaxial material models or user-defined stress-strain curve provided by material coupon tests. A short summary of the uniaxial models used in this study for the concrete beams/girders are presented next.

3.2.2.2 *Uniaxial constitutive laws for concrete and steel*

A wide variety of uniaxial stress-strain behaviors of concrete under compression and tension are available in the literature. When no stress-strain (σ_c - ε_c) curve is provided by concrete compression tests, the constitutive equation for concrete stress-strain under compression suggested by Vecchio and Collins (1993), see Eq. (3-28), is adopted in this study,

$$\sigma_c = f_c' \frac{\eta\left(\varepsilon_c/\varepsilon_c'\right)}{\eta - 1 + \left(\varepsilon_c/\varepsilon_c'\right)^{\eta\xi}}, \text{ with}$$
$$\eta = 0.80 - f_c'(\text{MPa})/17, \text{ and, } \xi = \begin{cases} 1, & \varepsilon_c' < \varepsilon_c < 0 \\ 0.67 - f_c'(\text{MPa})/62, & \varepsilon_c < \varepsilon_c' \end{cases} \tag{3-28}$$

where f_c' is the concrete compressive strength ($f_c' < 0$). For concrete subjected to tension, the stress-strain curve (σ_t - ε_t) is commonly assumed linear prior to cracking, followed by a linear decay curve to consider the tension-stiffening effect (Ian Gilbert 2007), see Eq. (3-29),

$$\sigma_t = \begin{cases} E_c \varepsilon_t & \varepsilon_t \le \varepsilon_{cr} \\ f_{cr} - \dfrac{E_c}{n_t}\left(\varepsilon_t - \varepsilon_{cr}\right) & \varepsilon_t > \varepsilon_{cr} \end{cases} \tag{3-29}$$

where $\varepsilon_{cr} = f_{cr}/E_c$ is the cracking strain corresponding to the tensile stress at cracking $f_{cr} = 0.33\sqrt{|f_c'|}$ (f_c' in MPa), and n_t (e.g., = 10) is the factor to consider the tension-stiffening effect.

For reinforcing steel, a bilinear stress strain relationship (σ_s - ε_s) is assumed based on Eq. (3-30).

$$\sigma_s = \begin{cases} E_s \varepsilon_s & \varepsilon_s \le \varepsilon_y \\ \sigma_{yeff} + E_{sh}\left(\varepsilon_s - \varepsilon_y\right) & \varepsilon_s > \varepsilon_y \end{cases} \tag{3-30}$$

where E_s is the elastic modulus of steel; ε_y is the yield strain; E_{sh} is the tangent modulus of steel in the linear hardening stage, and σ_{yeff} is the reduced yield stress according to the average stress-strain technique (Stevens et al. 1991; Li et al. 2016) to avoid crack checking in MCFT, and is defined in Eq. (3-31),

$$\sigma_{yeff} = \sigma_y - \frac{75}{d} f_{cr} \tag{3-31}$$

where σ_y is the unreduced yield stress of steel, and d is the diameter of reinforcement in mm.

3.2.3 Finite Element Implementation

The proposed element is implemented in the open-source finite element software framework, *OpenSees*, as complementary to the conventional fibre beam elements without considering shear. Figure 3-2 summarizes the typical FE formulation procedure for fibre beam element, including the state determinations at the structure, element, section, and material levels for the proposed element. At each level, the stiffness matrix and resisting stress/force vector are determined. In contrast to the formulation of the conventional fibre beam element, each fibre for concrete with smeared stirrups is represented by a condensed multi-axial constitutive model (e.g., MFCT), with both the normal and shear stress components. As such, the coupling effect of flexure and shear can be eventually achieved at the structural level.

Specifically, at the fibre level, material state condensation is required for the multi-axial fibre of concrete with smeared steel to estimate the unknown transverse strain ε_{yy} by imposing the aforementioned internal equilibrium $\sigma_{yy} = \sigma_{yy}^c + \rho_y f_{yv} = 0$. To this end, an iterative procedure, the dynamic relaxation method (Rericha 1991), is used. In this method, the transverse strain committed in the last load step *n*–1 is selected as the initial guess (at iteration *k* = 1) of the unknown transverse strain, $\left(\varepsilon_{yy}^{n}\right)^{k=1}=\varepsilon_{yy}^{n-1}$. This initial guess is updated through the iterative equation $\left(\varepsilon_{yy}^{n}\right)^{k+1}=\left(\varepsilon_{yy}^{n}\right)^{k}-\left(\sigma_{yy}^{n}\right)^{k}/E_c$, until $\left|\left(\sigma_{yy}^{n}\right)^{k+1}\right|$ is significantly close to zero within a prescribed tolerance level. Here, E_c is the modulus of elasticity of plain concrete.

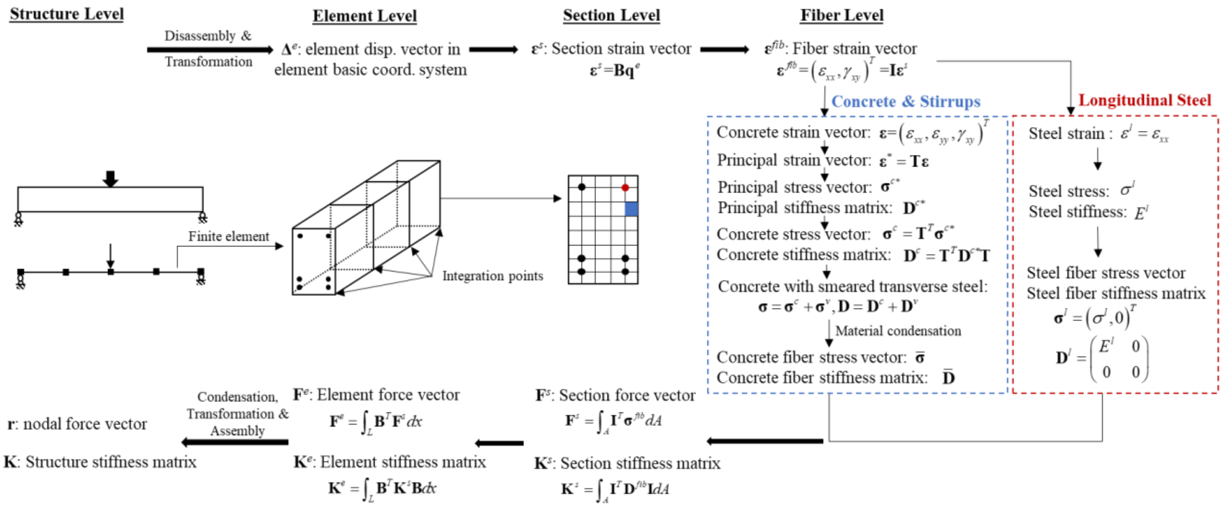

Figure 3-2: Schematic view of the FE formulation of the new fibre beam element considering shear: *DispBeamColumnFS*

Figure 3-3 shows the implementation of the proposed element in the *OpenSees* framework. With respect to the existing software architecture, a new sub-class of element (i.e., *DispBeamColumnFS*) is added for the proposed element. A new sub-class of *nDMaterial* in *OpenSees* (*TransverseCondensation*) is also added for the material state condensation. This new sub-class serves to interface 2-D material models, either newly added (i.e., *ConcreteMCFT*) or existing models, with the *NDFibreSection* that is used with the proposed element. Note that, the proposed element with the condensation procedure implemented, can work with other multi-axial material constitutive models (e.g., fracture-plasticity models and J2 plasticity models), in addition to the newly implemented MCFT material model.

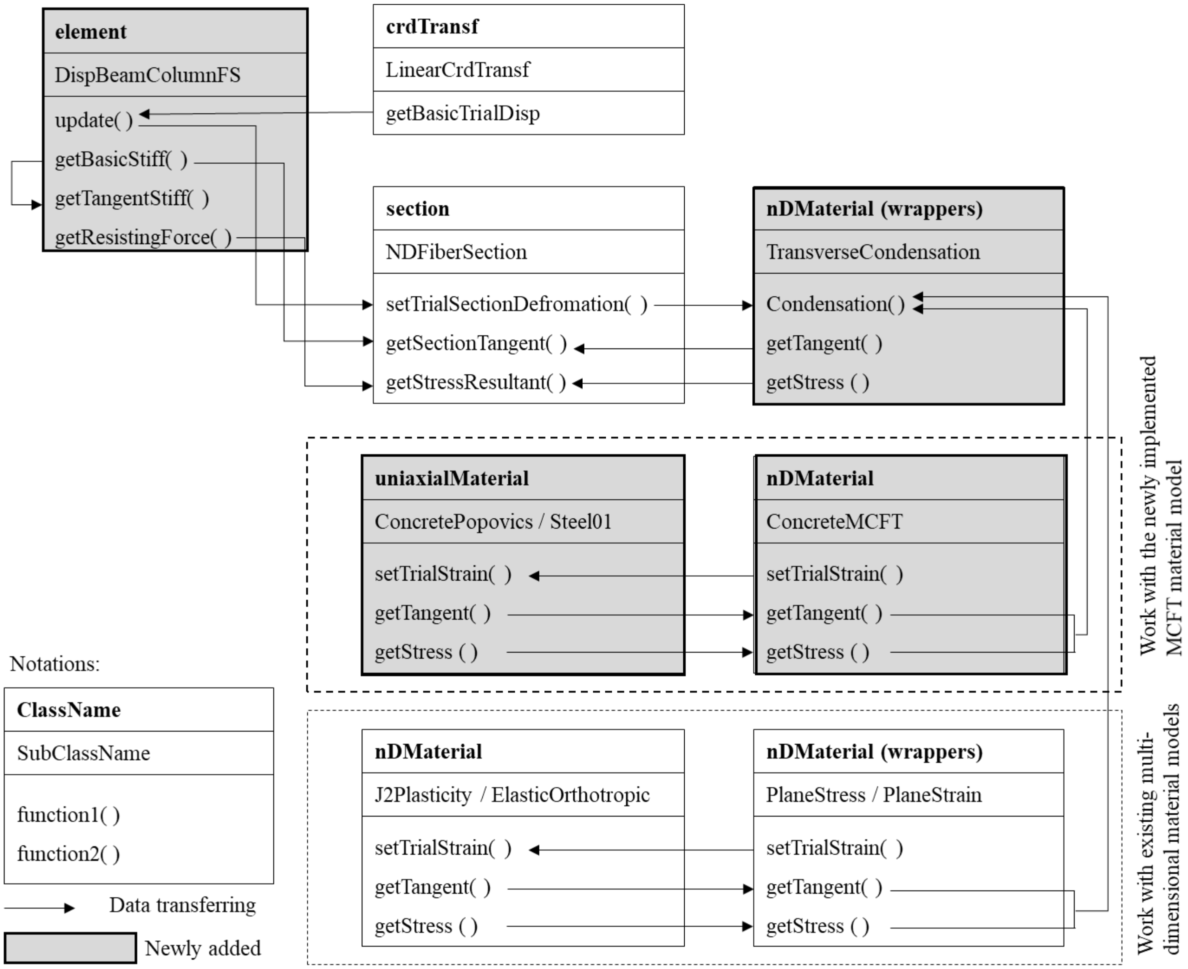

Figure 3-3: Flow chart for the implementation of the new fibre beam element (*DispBeamColumnFS*) in the *OpenSees* Framework

Additionally, as indicated in Figure 3-2, the interior DOF α_3 can be statically condensed out in the basic system at the element level before assembly for the structure stiffness matrix. This is accomplished by using the element stiffness matrix $\mathbf{K}^e$ in Eq. (3-7) together with Eq. (3-32),

$$\begin{bmatrix} K_{11}^e & K_{12}^e & K_{13}^e & K_{14}^e \\ K_{21}^e & K_{22}^e & K_{23}^e & K_{24}^e \\ K_{31}^e & K_{32}^e & K_{33}^e & K_{34}^e \\ K_{41}^e & K_{42}^e & K_{43}^e & K_{44}^e \end{bmatrix} \begin{Bmatrix} \mathrm{d}\Delta_1 \\ \mathrm{d}\Delta_2 \\ \mathrm{d}\Delta_3 \\ \mathrm{d}\alpha_3 \end{Bmatrix} = \begin{Bmatrix} \mathrm{d}F_1 \\ \mathrm{d}F_2 \\ \mathrm{d}F_3 \\ 0 \end{Bmatrix} \tag{3-32}$$

where F_i ($i = 1,2,3$) represents the non-trivial element end force associated to the *i*-th DOF of the beam in the basic system, and the imposed condition is that the force associated with the interior DOF equals to 0. As such, the condensed stiffness matrix can be obtained to relate nodal displacement increments and element force increments as shown in Eq. (3-33).

$$\begin{bmatrix} K_{11}^e - \dfrac{K_{14}^e K_{41}^e}{K_{44}^e} & K_{12}^e - \dfrac{K_{14}^e K_{42}^e}{K_{44}^e} & K_{13}^e - \dfrac{K_{14}^e K_{43}^e}{K_{44}^e} \\ K_{21}^e - \dfrac{K_{24}^e K_{41}^e}{K_{44}^e} & K_{22}^e - \dfrac{K_{24}^e K_{42}^e}{K_{44}^e} & K_{23}^e - \dfrac{K_{24}^e K_{43}^e}{K_{44}^e} \\ K_{31}^e - \dfrac{K_{34} K_{41}^e}{K_{44}^e} & K_{32}^e - \dfrac{K_{34}^e K_{42}^e}{K_{44}^e} & K_{33}^e - \dfrac{K_{34}^e K_{43}^e}{K_{44}^e} \end{bmatrix} \begin{Bmatrix} \mathrm{d}\Delta_1 \\ \mathrm{d}\Delta_2 \\ \mathrm{d}\Delta_3 \end{Bmatrix} = \begin{Bmatrix} \mathrm{d}F_1 \\ \mathrm{d}F_2 \\ \mathrm{d}F_3 \end{Bmatrix} \tag{3-33}$$

3.2.4 Verification of Shear Locking Free

Verification is an essential step for FE implementation. For the newly implemented displacement-based fibre beam element, the shear locking issue is examined here. For this purpose, the proposed element with mixed shape functions is used to model a classic example of a cantilever beam subjected to a transverse tip load. The material is considered as linear elastic orthotropic with an elastic modulus E = 200 GPa and zero Poisson’s ratio. According to Timoshenko beam theory, the exact analytical solution of the tip displacement is w_{eaxct} = 1.328mm.

Figure 3-4 shows the comparison between the normalized tip displacements, obtained using the proposed *DispBeamColumnFS* elements with mixed interpolation and linear interpolation. It is observed that beam elements using linear interpolation suffers from severe shear-locking, leading to significant underprediction of tip displacement when the number of elements is small. This shear-locking issue can be remedied by mesh refinement, but a large number of elements is required (e.g., larger than 16 even for such an elastic beam). By contrast, the mixed interpolation only requires one single element to predict the exact tip displacement for this classic numerical example, which verifies its effectivity in tackling shear locking issue.

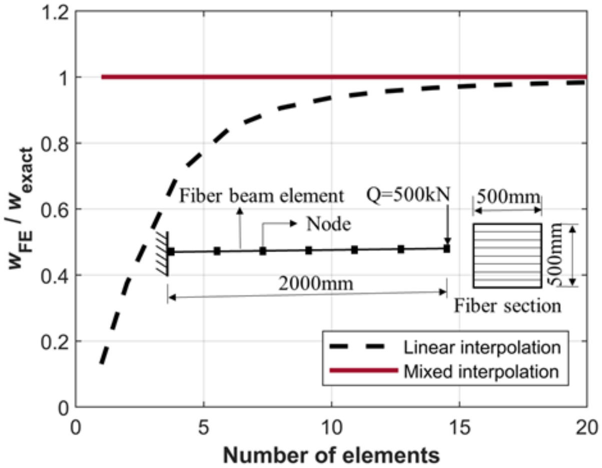

Figure 3-4: Comparison of normalized tip displacements for the classic numerical example of cantilever beam

3.3 Application to Concrete Beams/Girders

3.3.1 Shear-critical RC Beams

Bresler and Scordelis (1963) tested twelve shear-critical RC beams to investigate their shear behavior. This series of tests represents a challenge for the numerical modeling community, with many FE formulations failing to provide reliable simulations (Vecchio and Shim 2004). Therefore, it has served as a benchmark in the literature for the numerical modeling of shear-critical RC beams and are thus used in this study to validate the proposed element. A total of twelve simply supported beams were tested under a concentrated load at mid-span as shown in Figure 3-5. Note that there were three different span length, namely series 1, 2 and 3, and four sectional dimensions, namely OA, A, B and C. The concrete and the steel properties for each beam are summarized in Tables 3-1 and 3-2, respectively. The OA series did not contain transverse reinforcement, while the stirrup spacing for A, B and C series were 210 mm, 190 mm and 210 mm respectively.

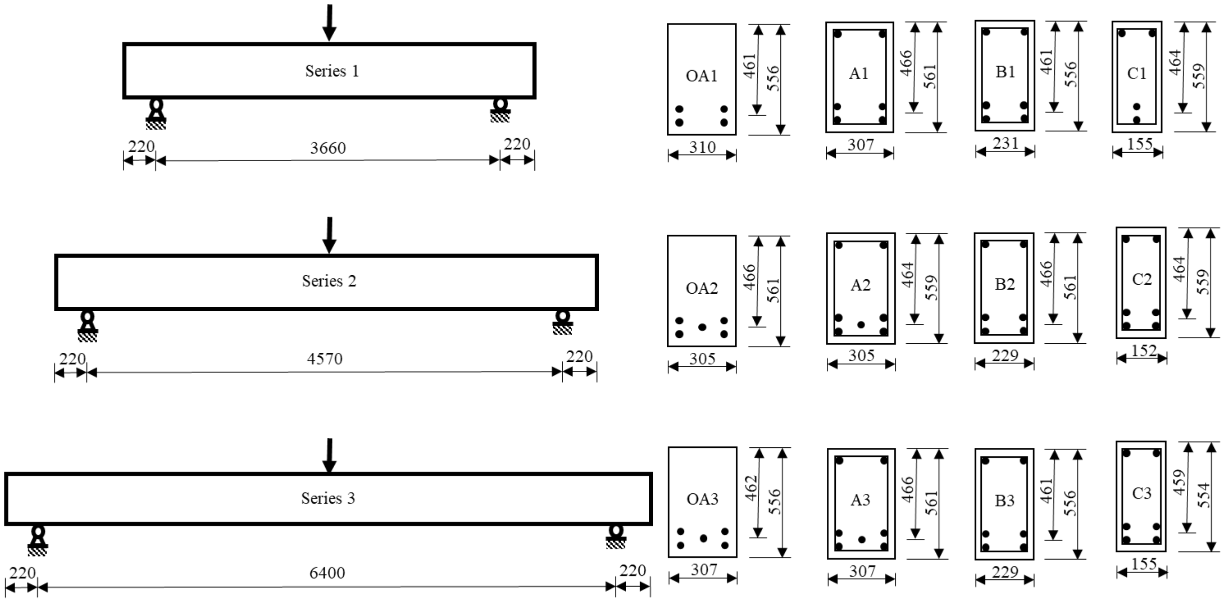

Figure 3-5: RC beams tested by Bresler and Scordelis (1963) (Unit: mm)

Table 3-1: Concrete properties in RC beams tested by Bresler and Scordelis (1963)

Beam	OA1	OA2	OA3	A1	A2	A3	B1	B2	B3	C1	C2	C3
f_c' (MPa)	22.6	23.7	37.6	24.1	24.3	35.1	24.8	23.2	38.8	29.6	23.8	35.1
ε_c'	0.002	0.002	0.002	0.002	0.002	0.002	0.002	0.002	0.002	0.002	0.002	0.002

Table 3-2: Steel properties in RC beams tested by Bresler and Scordelis (1963)

Bar type	d (mm)	A_s (mm^2)	f_y (MPa)	f_u (MPa)	E_s (MPa)	E_{sh}/E_s
	Nominal diameter	Nominal area	Yield strength	Ultimate strength	Elastic modulus	Hardening ratio
Stirrups	6.4	32	325	430	190,000	0.01
Top reinforcement	12.7	129	345	542	201,000	0.01
Bottom reinforcement	28.7	645	555	933	218,000	0.01

As shown in Figure 3-6, the proposed element is used to model these twelve shear-critical RC beams. Each beam is meshed into six *DispBeamColumnFS* elements with five Gauss-Lobatto integration points for each element, and the cross-section is discretized into 20 concrete fibres (layers) in the depth direction and longitudinal steel fibres defined according to the reinforcement details. Note that the mesh size employed in this study was determined based on convergence analysis. The multi-axial MCFT material is assigned to concrete layers, together with the uniaxial material models described before for concrete and stirrups. The FE analyses are carried out using displacement control and Newton–Raphson algorithm as the nonlinear solver. The numerical convergence criteria, *NormDispIncr* in *OpenSees*, is utilized by checking the Euclidean norm of the incremental displacement vector with a tolerance level of 0.001 based on convergence analysis.

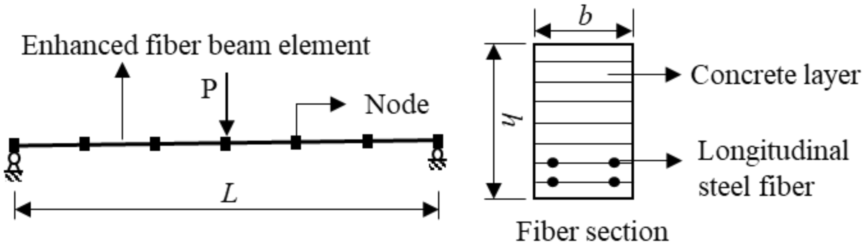

Figure 3-6: The developed fibre beam FE model for the RC beams

For the purpose of comparison, the conventional fibre beam element without shear (e.g., *DispBeamColumn* in *OpenSees*) was also utilized to model the twelve RC beams, and is referred to as the reference element in this study. Figure 3-7 shows the comparison of the load-deflection curves obtained from the FE models using the proposed element, counterparts from the FE models using the reference element, and the experimental tests. Note that deflection of beams refers to the vertical displacement as measured in the test.

It is shown that the proposed element with shear is capable of simulating the load-deflection behavior of all twelve tested RC beams with satisfactory accuracy, particularly in terms of load-carrying capacity. In contrast, the reference element overestimates the load-carrying capacity, especially for the OA series of beams without stirrups, which were the most shear-critical of these tests. Additionally, the load-deflection curves simulated by using the reference element are far more ductile than the experimental results, while the results from the newly developed fibre beam element considering shear do not exhibit such problems. This is because shear deformation is neglected in the conventional fibre beam element and thus the shear damage cannot be captured.

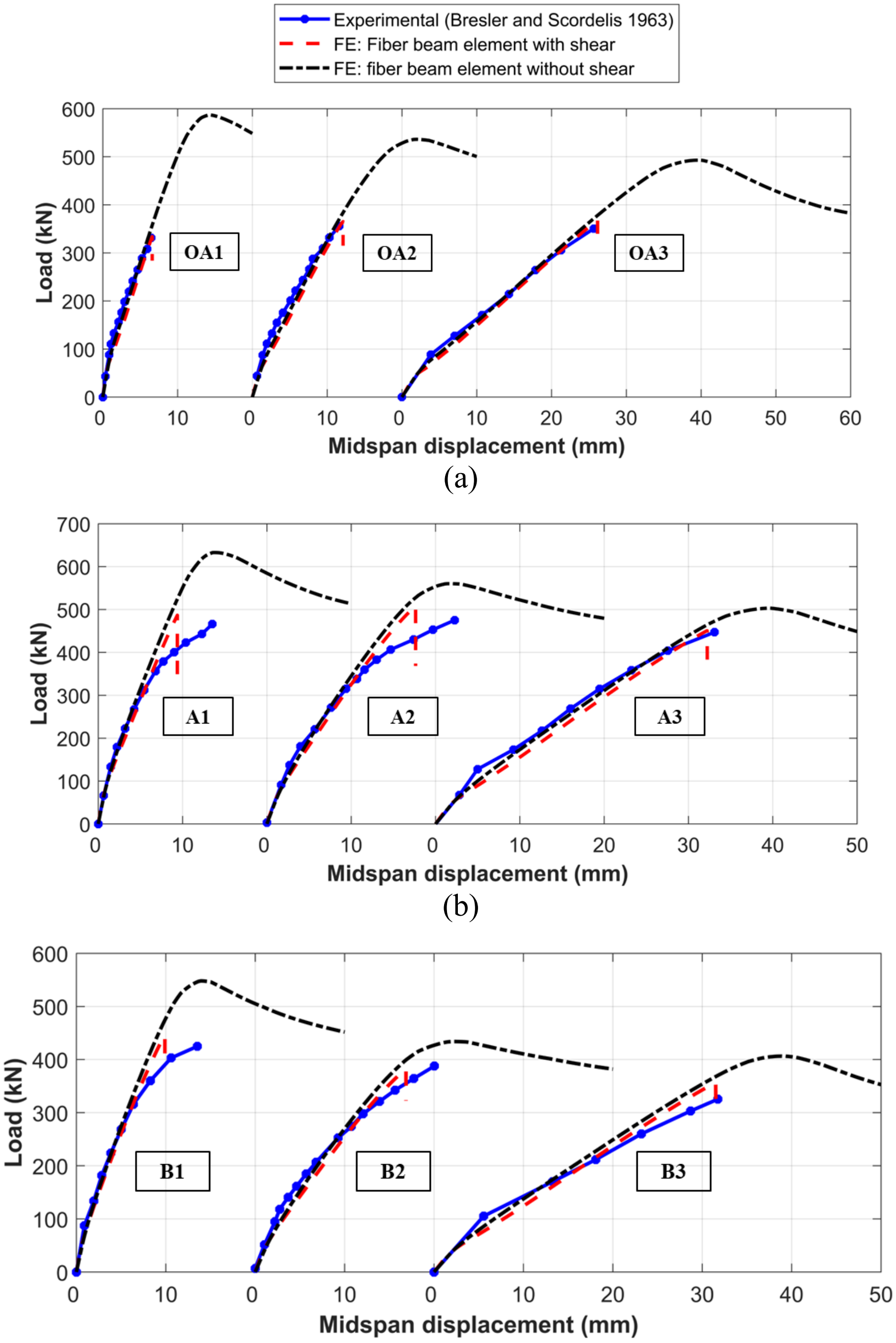

(a)

(b)

(c)

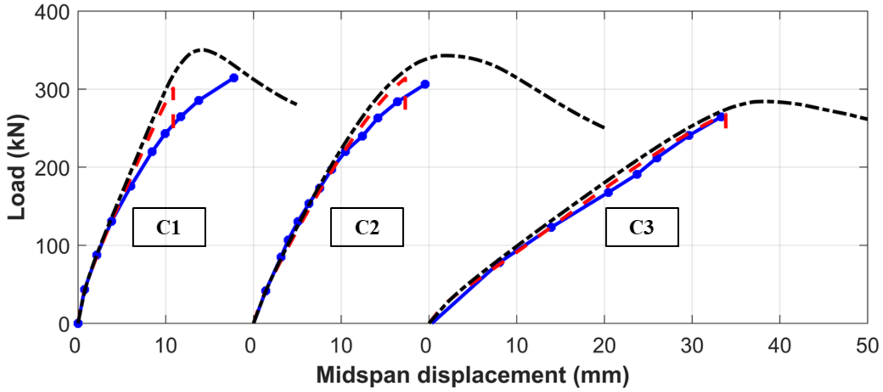

(d)

Figure 3-7: Comparison of the load-deflection curves: (a) OA series, (b) A series, (c) B series and (d) C series

In contrast, the newly proposed element considers shear deformation and damage by utilizing the material model of MCFT, leading to better capture of the failure point of shear-critical beams compared with the conventional fibre beam element. Such an application study based on shear-critical RC beams reveals that the proposed element outperforms the reference element, which is widely used primarily for flexure-dominated beams or columns. It is observed that the obtained load-deflection curves from the FE models are slightly stiffer than the experimental results, especially for the specimens from Series A as also reported in (Feng et al. 2017). This can be partially attributed to the uncertainties in the tests (e.g., construction and measurement errors) and the imperfection of FE models.

For each series of OA, A, B and C, the tested load-deflection curves become more flexure and ductile with the increasing shear span to depth ratios, namely, from series 1 to 3. The simulation results using the proposed element captured such a trend successfully as shown in Figure 3-7, indicating its capability as a reliable tool to simulate shear-critical RC beams with different shear span to depth ratios.

The accuracy of the predicted failure loads from the proposed element were also compared with some widely utilized shear capacity design code models, i.e., ACI 318-19 (ACI 2019), CSA A23.3:19 (CSA 2019a), *fib* MC 2010 (*fib* 2013) and GB 50010-2010 (MOHURD 2010). Specifically, the most advanced model from each code is utilized in this study, i.e., the general method in CSA A23.3:19, the Level Ⅱ approximation for members without shear reinforcement and the Level Ⅲ approximation for members with shear reinforcement in *fib* MC 2010. Note that the material strengths of steel and concrete use the tested values summarized in Tables 3-1 and 3-2 without material reduction factors or other safety factors (e.g., load and resistance factors) for fair comparison.

Table 3-3: Comparison of failure loads between tests, FE and analytical models

Beam	Failure Load (kN)						$V_{tested}/V_{predicted}$				
	Test	FE	ACI	CSA	*fib*	GB	FE	ACI	CSA	*fib*	GB
OA1	333.6	333.9	199.8	239.9	241.2	368.1	1.00	1.67	1.39	1.38	0.91
OA2	355.9	365.0	218.8	246.0	247.4	378.3	0.97	1.63	1.45	1.44	0.94
OA3	378.1	368.0	276.0	259.8	261.1	519.0	1.03	1.37	1.46	1.45	0.73
A1	467.1	486.6	337.9	347.2	315.4	333.7	0.96	1.38	1.35	1.48	1.40
A2	489.3	508.4	355.6	349.5	316.9	332.1	0.96	1.38	1.40	1.54	1.47
A3	467.1	450.3	411.4	334.2	326.6	405.0	1.04	1.14	1.40	1.43	1.15
B1	444.8	444.6	305.3	313.7	282.5	284.0	1.00	1.46	1.42	1.57	1.57
B2	400.3	382.7	299.9	295.7	268.0	277.2	1.05	1.33	1.35	1.49	1.44
B3	355.9	356.6	355.0	296.0	278.4	348.0	1.00	1.00	1.20	1.28	1.02
C1	311.4	262.4	228.8	222.2	206.9	232.1	1.19	1.36	1.40	1.50	1.34
C2	324.7	313.8	244.5	245.0	218.3	210.3	1.03	1.33	1.33	1.49	1.54
C3	271.3	267.6	277.1	241.9	224.0	246.8	1.01	0.98	1.12	1.21	1.10
Mean	-	-	-	-	-	-	1.02	1.34	1.35	1.44	1.22
CV	-	-	-	-	-	-	0.06	0.15	0.07	0.07	0.22

Table 3-3 summarizes the failure loads from the experiments and the predictions from various models. According to the test-to-prediction ratios of the shear capacity, $V_{tested}/V_{predicted}$, the proposed element can predict the shear capacity of these twelve beams with a bias factor of 1.02 and a coefficient of variation (CV) of 6%, which indicates better performance than those of the design code models. This implies that the proposed element is more accurate and reliable in shear capacity prediction, which can be used when higher accuracy prediction is required (e.g., accurate evaluation of existing RC beams). However, by no means should FE models replace the design code models for design purposes.

3.3.2 Flexure-dominated and Shear-critical PC Girders

One PC bridge girder salvaged from a decommissioned bridge (in service 1990 - 2017) located on central Alberta, Canada, was tested to failure. Compared to other girders salvaged from this bridge, this girder is considered as a control girder as it was visually intact with no concrete spalling or evidence of steel corrosion. It was first tested to failure under four-point bending to evaluate the flexural behavior. After the flexure test, the girder was cut near one end and further tested under a single point load to evaluate the girder's shear behavior. The proposed element is used to simulate the flexure and shear behavior of this girder with comparison to the tests in this section.

3.3.2.1 Testing Summary

The tested girder is 11000 mm long with a solid cross-section at both ends and a three-cell hollow cross-section in the middle (Figure 3-8). The cross-section is 1220 mm wide and 510 mm deep, and the diameter of the voids are 305 mm. Longitudinal reinforcement consisted of 20 prestressed seven-wire low-relaxation strands, seven 10M longitudinal reinforcement (5 G1012 and 2 G1013) and 4 25M reinforcement. The stirrups are made of 10M reinforcement. The nominal diameter of the 7-wire strands is 12.7 mm with a nominal area of 98.7 mm^2. Note that the prestressing force in each strand was not explicitly measured, but back-calculated by inverse modeling using 2-D continuum FE (Huang 2020) based on the tested cracking load. The evaluated effective prestress forces were 74.9 and 64.2 kN for the flexure and shear girders, respectively. This represents 30% and 40% prestress loss compared to the designed effective prestress force for the same girder.

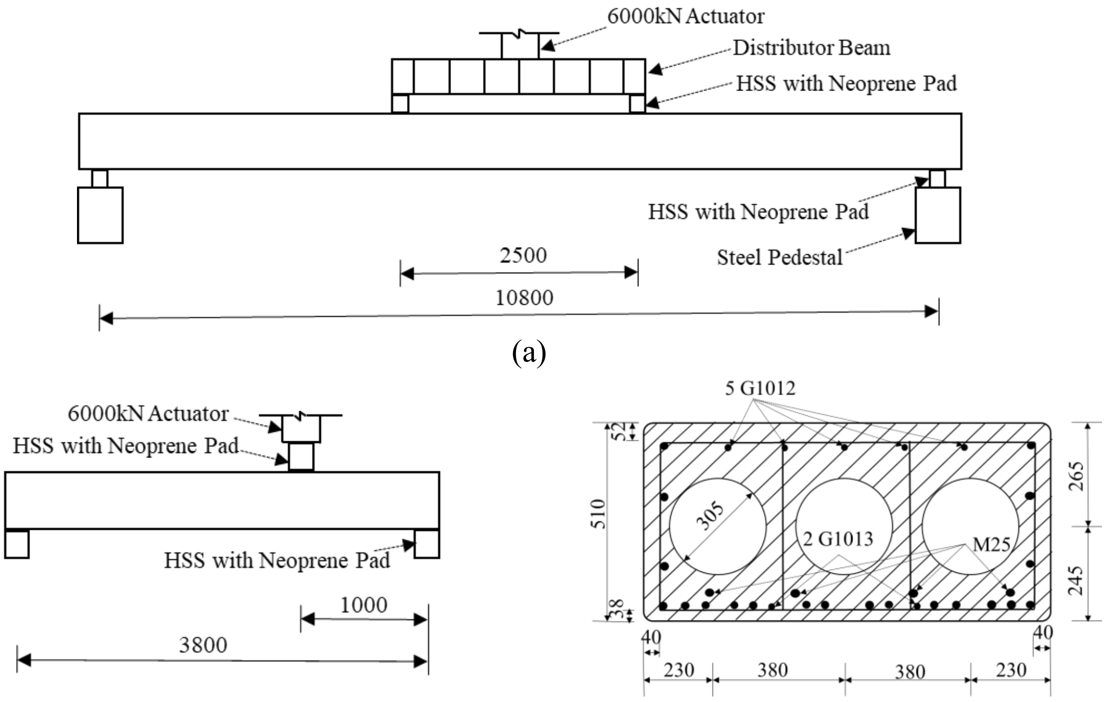

(a)

(b) (c)

Figure 3-8: Tested PC girder: (a) flexure test, (b) shear test, and (c) cross-section in the middle span (unit: mm)

The girder was first tested to failure in a four-point bending using a 6000 kN loading frame and actuator as shown in Figure 3-8(a). The tested girder was simply supported on steel pedestals. Hollow structural sections (HSS), filled with concrete, were used to distribute load along the width of the girder. At each support, a neoprene pad was placed on top of the HSS to imitate the true bridge girder's support conditions. The girder was tested to failure controlled by concrete crushing after reinforcement yielding as shown in Figure 3-9(a).

After the flexural test, since the damage caused by the flexural test was concentrated at midspan, the tested girder was cut into a smaller, 3900 mm long, end section. Then this shorter girder was simply supported with a span of 3800 mm and tested under a single point load applied 1000 mm away from one support, as shown in Figure 3-8(b). The failure was dominated by diagonal tension failure as shown in Figure 3-9(b). As such, these two girders well presented flexure-dominated and shear-critical PC girders, and will be simulated using the newly developed fibre beam element with comparison to the tests.

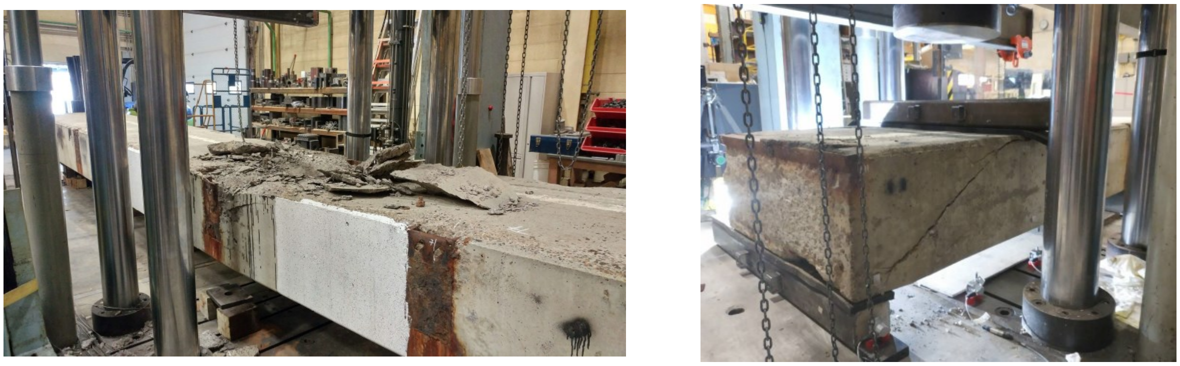
(a) (b)

Figure 3-9: Failure of the tested PC girder: (a) flexure test showing concrete crushing, and (b) shear test showing diagonal tension failure

3.3.2.2 FE modelling and simulation results

The proposed element is utilized to model both the flexural and shear test of this PC bridge girder. The PC girder is meshed into 36 and 38 beam elements respectively for the flexure and shear tests, with 5 integration points for each element, see Figure 3-10. Note that the variation of stirrup spacing along the length of the girder, i.e., $s = 150\,\text{mm}$ for region 1, $s = 200\,\text{mm}$ for region 2, $s = 250\,\text{mm}$ for region 3 and $s = 350\,\text{mm}$ for region 4, is considered in the MCFT model, which allows to consider smeared stirrups. As such, MCFT material models for these four regions are defined with different reinforcement ratios of transverse steel, $\rho_y = A_{yv}/bs$ used in Eq. (3-20) and (3-21) in the FE formulation, to consider four stirrup spacings. The cross-section is discretized into concrete fibres with an average mesh size of $10\,\text{mm} \times 10\,\text{mm}$ and steel fibres to represent the longitudinal steels including both non-prestressed reinforcement and prestressed strand as shown in Figure 3-10. The FE analyses are all carried out in displacement control using Newton–Raphson algorithm to solve nonlinear algebraic equations. The *NormDispIncr* in *OpenSees* is utilized to determine if convergence has been reached. The tolerance is set as 0.001 for all specimens based on convergence analysis.

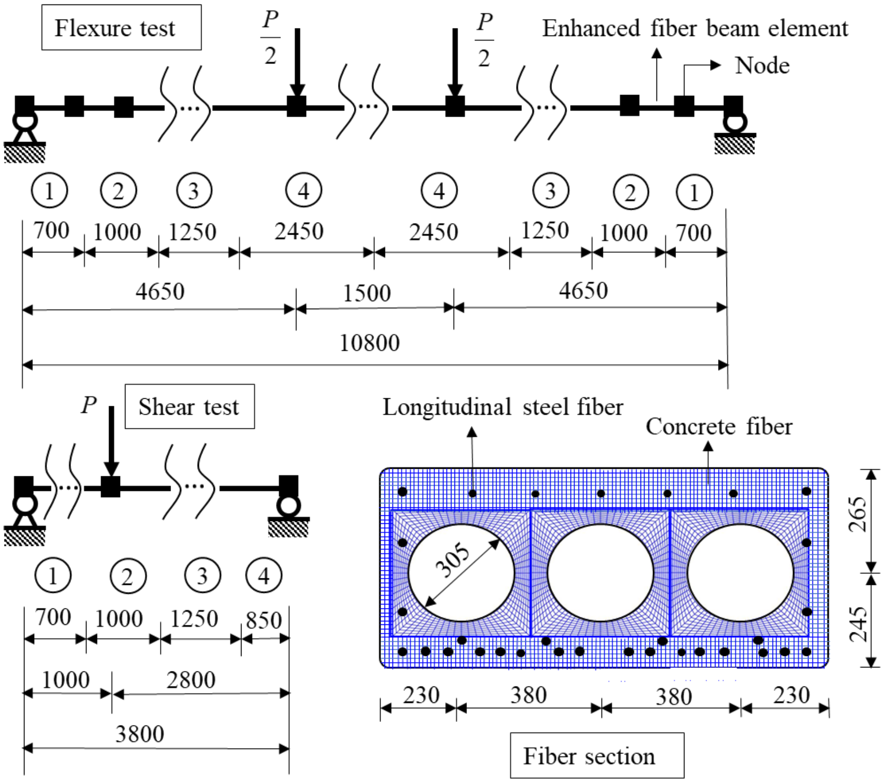

Figure 3-10: FE models for the tested PC girder (Unit: mm)

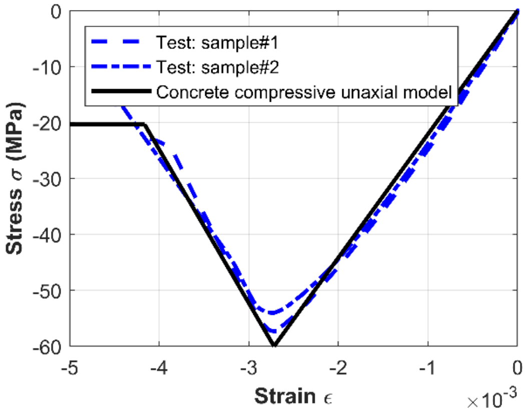

Figure 3-11: Stress-strain comparison between the material model and cylinder test for concrete in compression

The values of key material parameters for concrete and steel used in the MCFT are determined based on the material coupon tests. To be specific, concrete cylinders, non-prestressed steel coupons (e.g., M10, M25, stirrups), and prestressed strand coupons were extracted from the PC girder after the testing. As per ASTM C39/C39M-14 (ASTM 2014), ASTM A370-16 (ASTM 2016), and ASTM A1061/1061M-16 (ASTM 2016), their coupon sizes are 100 mm × 200 mm, 500 mm long (with the gauge length of 200 mm), 1000 mm long (with the gauge length of 610 mm), respectively. The tested material properties are summarized in Table 3-4.

Table 3-4: Tested material properties

Material	Symbol	Parameter	Longitudinal			Stirrups
			10M	25M	Strand	
Steel	f_y	Yield strength (MPa)	417	413	1676.5	424
	f_u	Ultimate strength (MPa)	670	640	1860	636
	ε_y	Yield strain (MPa)	0.0021	0.0022	0.0085	0.0022
	E_s	Elastic modulus (MPa)	198	203	196.5	196
	E_{sh}	Hardening modulus (MPa)	6.29	5.08	9.657	4.61
Concrete	f_c'	Peak compressive stress (MPa)	–55.5			
	f_u	Ultimate compressive stress (MPa)	–20.3			
	ε_c'	Strain at peak compressive stress	–0.0027			
	ε_u	Ultimate strain	–0.0042			

For concrete in compression, based on material tests on cylinders extracted from the tested girders as shown in Figure 3-11, it is reasonable to assume the pre-peak compressive behavior can be simulated by a linear relationship, followed by a linear post-peak branch. The peak compressive stress f_c' is set as –60 MPa to fit the material model well with the tested curves. The compressive strain (i.e., $\varepsilon_c' = -0.0027$) corresponding to the peak compressive stress is obtained by the average value of the two tested batches. The ultimate compressive stress and the corresponding strain are also obtained by the average value of the two tested batches as –20.3 MPa and –0.0042, respectively. For steel and concrete in tension, the typical uniaxial material models illustrated in previous section of uniaxial material models are employed.

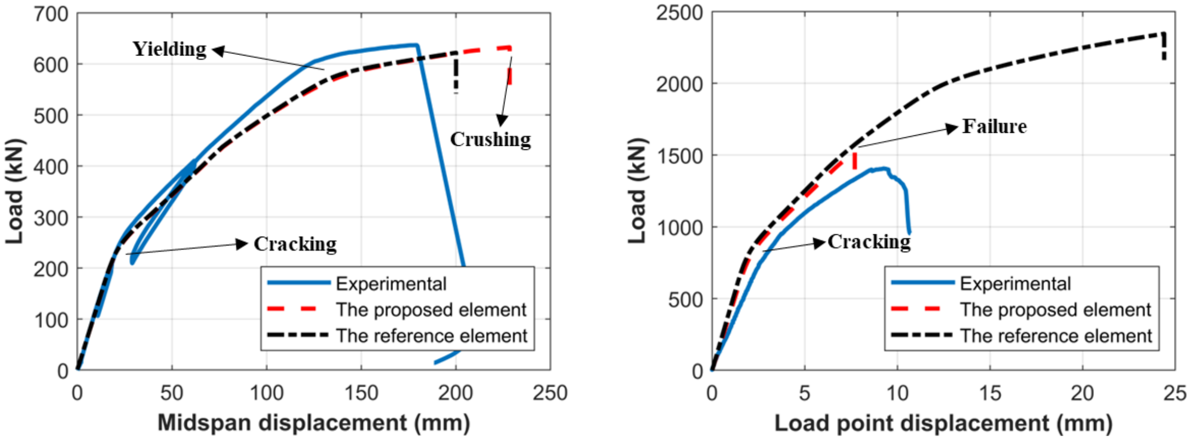

(a) (b)

Figure 3-12: Load-deflection curves for: (a) flexure test, and (b) shear test

For the purpose of comparison, the reference element is also utilized to model the PC girder for both flexure and shear tests, with the same uniaxial material models and mesh conditions as in the model using the proposed element. As shown by Figure 3-12, the simulation results from the proposed element agree well with the experimental results for both the flexure and shear tests. The cracking point, steel yield point, and ultimate strength are all captured well, indicating that the proposed element can be a reliable tool in predicting the behavior of PC girders for both shear-critical and flexure-dominated scenarios. Note that accurate prediction of ultimate displacements is a challenging task for concrete structures (Vecchio and Shim 2004). The proposed element is significantly more accurate in predicting the ultimate displacement for the shear test, see Figure 3-12(b). Compared with the error in predicting the ultimate displacement for the shear test using fibre beam element without shear, the small difference in the two predictions of the ultimate displacement for the flexure test in Figure 3-12(a) is considered as negligible. Note that only the monotonic loading behaviour is simulated and compared here. However, it is worth mentioning that the proposed element can potentially be used with cyclic MCFT to simulate the cyclic behaviour, which is outside the scope of this study.

Table 3-5: Comparison of failure loads between tests, FE and analytical models

	Models	Tested	FE	ACI	AASHTO	CSA	*fib*	GB
Flexure test	Failure Load (kN)	636.7	632.3	670.0	667.0	665.4	675.3	674.0
	Test-to-prediction ratio	-	1.01	0.95	0.95	0.96	0.94	0.94
Shear test	Failure Load (kN)	1406.2	1521.8	977.6	830.3	849.7	818.6	914.3
	Test-to-prediction ratio	-	0.92	1.44	1.69	1.66	1.72	1.54

The accuracy of the predicted failure loads from the proposed element is also compared with some widely utilized design code models as shown in Table 3-5. In addition to the concrete structure design codes, two highway bridge design codes, namely AASHTO LRFD 2017 (AASHTO 2017) and CSA S6:19 (CSA 2019b), are also adopted for comparison. For shear capacity prediction, the most advanced model from each code is utilized for the tested PC girders, i.e., the detailed method in ACI 318-19, the general procedure in AASHTO LRFD 2017, the general method in CSA A23.3:19 and CSA S6:19, and the Level III approximation in *fib* MC 2010. Note that the material strengths of steel and concrete take the tested values as summarized in Table 3-4 without material reduction factors or other safety factors for fair comparison. It is shown that the proposed element can predict load-carrying capacities well under both the flexure- and shear-critical scenarios. In contrast, the design code models can only obtain satisfactory predictions of load-carrying capacities for the flexure test, but poor predictions of the load-carrying capacities for the shear test. Thus, the proposed element is shown to be a simple but reliable tool to obtain satisfactory predictions for both tests.

3.4 Summary

In this study, an enhanced fibre beam element was developed and implemented considering flexure-shear coupling by utilizing multi-axial material constitutive models, as complementary to the conventional fibre beam elements using uniaxial material models. Particularly, the proposed element was integrated with modified compression field theory (MCFT) to model RC/PC girders in this study. The proposed element was first validated through a classic series of shear-critical RC beams tested in the literature, and then applied to a PC bridge girder recently tested under both flexure- and shear-critical loading conditions. Comparison with the reference element showed that the proposed element was superior in predicting the load-deflection behavior of RC/PC girders under shear-critical scenarios. Particularly, the FE model can be used to predict the shear capacity of RC/PC girders more accurately than commonly used code-based models. Based on the proposed element and its validation and application study, the main conclusions can be withdrawn as follows:

(1) The coupling of flexure and shear, achieved in MCFT at the material level and further considered at the fibre section and beam element levels, enables the proposed element to be used for simulating the structural behavior of both shear-critical and flexure-dominated RC/PC girders.

(2) This study provides analysts and engineers with a reliable numerical tool for structural behavior analysis of RC/PC girders, as complementary to the widely used conventional fibre beam element.

(3) The proposed element, with superior prediction of shear capacity for RC/PC girders compared to the design code models, provides an alternative model when high prediction accuracy is required.

Compared with flexure capacity prediction, the shear capacity prediction using the design code models is significantly less accurate, i.e., with strong bias and large variation. This further highlights the value and need of the proposed element.

CHAPTER 4: APPLICATION OF NEWLY DEVELOPED BEAM ELEMENT CONSIDERING FLEXURE-SHEAR COUPLING TO STUDY LOAD-SHARING BEHAVIOR OF MULTI-GIRDER PC BRIDGES

This chapter aims to study the load-sharing or system behavior of multi-girder prestressed concrete (PC) bridges, using an efficient nonlinear analysis tool based on finite element (FE) modeling. A newly developed nonlinear beam element, which considers flexure-shear coupling, was adopted to model each girder and macro nonlinear elements were adopted to model the shear connectors between adjacent girders. The nonlinear analysis tool for multi-girder bridge systems was applied to study the system behavior and load sharing of the studied bridge under both flexure-dominant and shear-critical loading scenarios. The influence of shear connectors on load-carrying capacity and load sharing was quantified by comparing the bridge system behavior of shear-connected girders and that of dis-connected girders (with isolated individual girders). It is found that shear connectors play a significant role, but less under shear-critical scenarios than under flexure-dominated scenarios. The influence of losing shear connectors (e.g., due to corrosion damage) and increasing shear connectors on the bridge system behavior was studied. The results indicated that one single shear connector loss can result in an overall load-carrying capacity loss up to 14.32% for the considered multi-girder bridge with five connectors between two adjacent girders, while adding more shear connectors between adjacent girders can improve the overall load-carrying capacity.

4.1 Introduction

Multi-girder concrete bridges, made from parallel precast girders/beams that are longitudinally connected to each other (AASHTO 2017; CSA 2019), represent a popular choice for short- to intermediate-span bridges in North America (Dunker and Rabbat 1993; Barker and Puckett 2013). This can be attributed to their unique advantages, including ease of fabrication, and fast construction, which requires minimum poured-in-place concrete for the bridge superstructure. In contrast to bridges with cast-in-place decks that behave as an integral structural component (e.g., slab), multi-girder bridges distribute vertical loads transversely through continuous or discrete shear connection joints at intervals along the girder. A variety of shear connection exist, including intermittent bolted shear connectors (Shah et al. 2007), continuous shear keys filled with grout (Hussein et al. 2018), transverse post-tensioning ties (Hansen et al. 2012), and an overlaid concrete structural slab (150 mm thick) (CSA 2019), depending on different girder types and design requirements. Multi-girder bridges offer convenience in construction and design, e.g., by treating the bridge superstructure as multiple bridge girders.

However, design and analysis of multi-girder bridges has been the subject of numerous studies in the past. The majority of those studies (Barr et al. 2001; Song et al. 2003; Hughs and Idriss 2006; Semendary et al. 2017; Huang and Davis 2018) used linear elastic models to provide the theoretical basis for the use of the live load distribution factor or truck load fraction factor (AASHTO 2017, CSA 2019). Moreover, existing works (Barr et al. 2001; Song et al. 2003; Hughs and Idriss 2006; Huang and Davis 2018) usually focused on composite girder-slab systems, in which the load distribution was considered to be solely dependent on the slab. This is different from multi-girder systems without an overlaid concrete structural slab, in which load-sharing depends on the shear connection joints. Only a few studies (Semendary et al. 2017) focused on the bridges without slabs/overlays by explicitly modelling the shear connection system (e.g., continuous shear keys filled with grout), while studies on more bridges with different shear connection types are limited.

During the routine design process of multi-girder system, the load distribution factor needs to be used with restrictions although it provides an approximate way to consider load sharing or distribution among girders in load effect calculation. For example, parallel beams must have approximately equal stiffness (AASHTO 2017; CSA 2019). Nonetheless, load sharing can be different when nonlinearity takes effect in the primarily loaded girder, which will experience more stiffness degradation in the inelastic stage than other girders (Tu et al. 2019; Wang et al. 2021). Similarly, the live load distribution factor approach is not appropriate for load evaluation or performance assessment of aged bridges, in which girders can deteriorate to different degrees. As such, instead of decreasing load effects (e.g., maximum moment and shear) in a girder considering load-sharing, an alternative perspective is to increase the load-carrying capacity of a girder due to contribution of other girders by studying the behavior of multi-girder systems.

To study the load-carrying capacity of multi-girder systems, nonlinear FE models can be adopted, which requires explicit modelling of multiple PC girders and the connection joints between adjacent girders. Existing FE models for multi-girder bridges include three-dimensional (3-D) or two-dimensional (2-D) continuum-based FE models (Hossain et al. 2014; Leng et al. 2020) and one-dimensional (1-D) fibre beam element models (Song et al. 2002; Tu et al. 2019; Wang et al. 2021). However, nonlinear bridge girder system models using continuum-based FE are computationally prohibitive, and demanding in efforts in constitutive material model calibrations and simulation results interpretation. In contrast, models using fibre beam elements are proved to be significantly more efficient and straightforward, and thus preferred by engineers for bridge girder system modeling (Ferreira et al. 2015). It is worth mentioning that existing FE-based analysis of bridge girder systems only focused on the bridge behavior under flexure-dominated loading scenarios. Nevertheless, the load-sharing behavior of multi-girder under shear-critical loading scenarios is worth investigation to obtain a comprehensive understanding of the bridge girder system behavior. For this purpose, the newly developed beam element, which considers flexure-shear coupling (Liu et al. 2021), is an appropriate analysis tool in lieu of the conventional fibre beam elements (Spacone et al. 1996), where the shear deformation and/or flexure-shear coupling is neglected.

Furthermore, impact of shear connection joints on the system behavior of multi-girder systems needs to be studied, particularly for multi-girder bridge systems without non-composite topping or a composite structural slab. This is because steel shear connectors can be severely damaged due to water and corrosive chemicals accumulated between girders (Leng et al. 2020), as evidenced from a recently decommissioned nine-girder PC bridge (Huang et al. 2022) and many others in Alberta, Canada, where the de-icing salt (Ramseyer and Kang 2012) is used seasonally. Frequent observation of shear connection damage/loss during regular bridge inspections has raised serious concerns about the overall performance of bridge girder systems (Yuan and Graybeal 2016).

To this end, the system behavior of a multi-girder PC bridge is studied based on nonlinear FE modeling using a recently developed nonlinear beam element that considers flexure-shear coupling. The multi-girder bridge system considered is based on a decommissioned nine-girder PC bridge, in which adjacent girders are connected by steel shear connectors. Its bridge girder system behavior is studied under both flexure-dominant and shear-critical loading scenarios. Additionally, the influence of shear connectors on load-carrying capacity and load sharing was studied considering two different settings: losing shear connectors in existing girders (e.g., due to corrosion damage) and increasing shear connectors in new designs.

4.2 Nonlinear FE Modelling of Multi-girder Bridge System

4.2.1 Bridge Description

A 27-year-old (in service from 1990 to 2017) single-span multi-girder bridge, called Tiger Lily bridge located near Barrhead in central Alberta, Canada, was decommissioned after failing a safety inspection. The bridge was 11m long, consisting of nine precast PC girders (referred to as G1 ~ G9) without additional wearing surface (e.g., concrete or asphalt overlay) simply supported on the abutments at both ends. Adjacent girders were tied to each other using five steel shear connectors located along the span as shown in Figure 4-1. The shear connects are denoted as C-G(n_1)-G2(n_2)-N, where n_1 and n_2 are the ID of adjacent girders and N is the ID of shear connectors along longitudinal direction of the bridge.

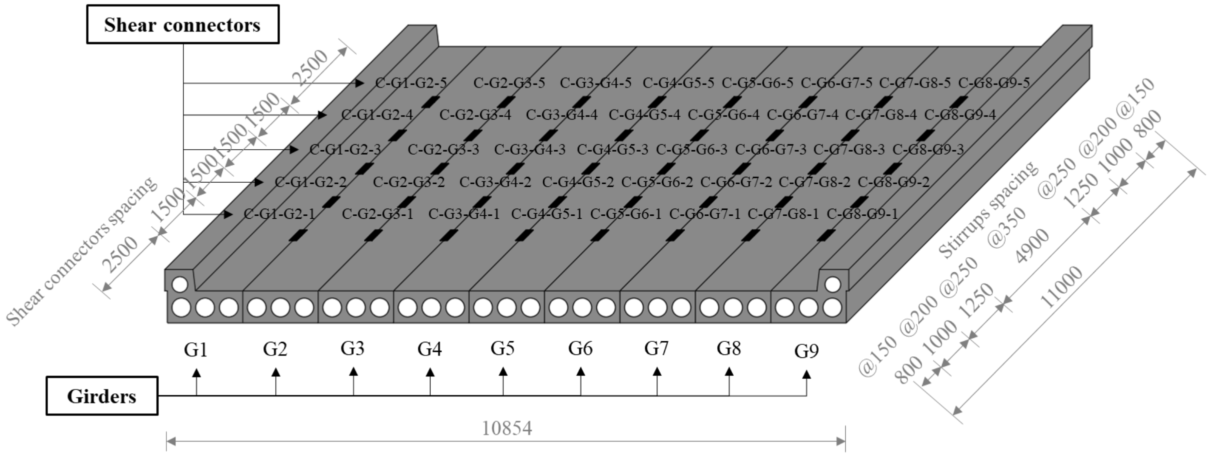

Figure 4-1: Schematic diagram of Tiger Lily bridge superstructure (dimension in mm)

This bridge can be considered as a representative of multi-girder PC bridges for short and intermediate spans in Alberta (Alberta Transportation 2019). Corrosion-induced damage of shear connectors was observed for this bridge, which raised serious concerns about bridge safety, in addition other girder Deterioration (e.g., concrete cracking and spalling). Thus, the residual structural performance of the individual bridge girders was studied experimentally and numerically by the authors (Liu et al. 2021; Huang et al. 2022; Wu 2021). This study will focus on the system behavior and load sharing of multi-girder systems with discrete shear connectors, with particular emphasis on the effect of shear connector damage/loss while assuming PC girders were in pristine conditions. The ultimate goal of this specific research scope is to provide insight into system behavior, potentially guiding maintenance and rehabilitation of similar multi-girder PC bridges associated with damage/loss of shear connectors.

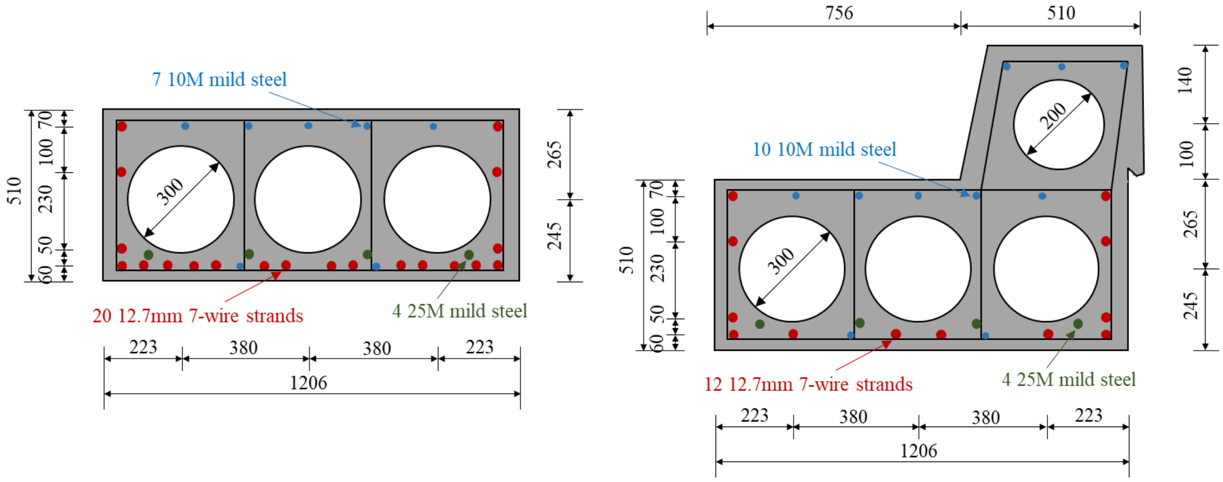

(a) (b)

Figure 4-2: Cross sections of SM-510: (a) interior girders, and (b) exterior girders (dimension in mm)

The interior and exterior girders are of type SM-510 (Alberta Transportation 2019) with the cross-section and reinforcement details as shown in Figure 4-2 (a) and (b). The interior girder consists of 20 prestressed seven-wire low-relaxation strands with a nominal area of 98.7 mm^2, seven 10M and four 25M longitudinal reinforcing bars with a nominal area of 100 mm^2 and 500 mm^2 respectively. The exterior girder consists of 12 prestressed seven-wire low-relaxation strands, 10 10M and four 25M longitudinal reinforcement. The effective prestress force is 107 kN per strand. The stirrups are made of 10M bars and their spacing varies along the longitudinal direction of the bridge as indicated in Figure 4-1. The steel and concrete material properties were tested after the bridge decommission and summarized in Table 4-1.

Table 4-1: Summary of tested material properties

Material	Parameter	10M	25M	Strands
Steel	Yield strength (MPa)	417	413	1677
	Ultimate strength (MPa)	670	640	1860
	Elastic modulus (GPa)	198	203	197
Concrete	Compressive strength (MPa)	55.5		
	Ultimate compressive strain (MPa)	20.3		
	Strain at compressive strength	0.0027		
	Ultimate strain	0.0042		
	Density (kg/m^3)	1980		

To study the system behavior and load sharing of the above multi-girder bridge, an efficient FE-based analysis model is developed as schematically shown in Figure 4-3. Modeling details are provided in the following two sub-sections.

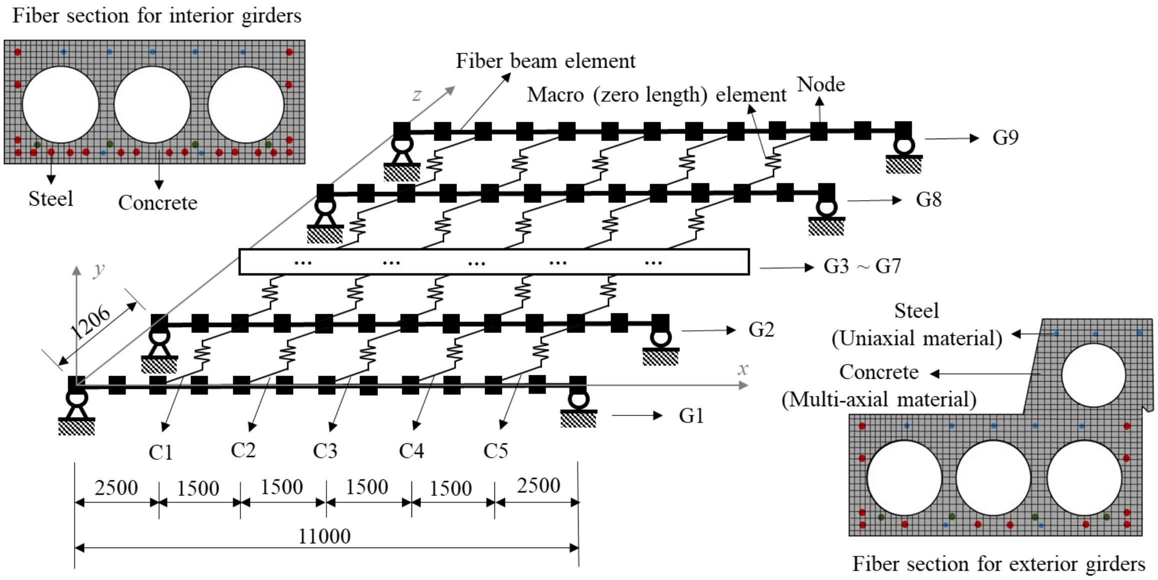

Figure 4-3: FE modelling for the Tiger Lily bridge (dimension in mm)

4.2.2 Girder Modelling

Both the newly developed flexure-shear coupled fibre beam element (i.e., the *dispBeamColumnFS*) in Chapter 3 and the conventional fibre beam element (i.e., the *dispBeamColumn*) are utilized to model the girders in this study. Each girder is meshed into 50 fibre beam elements with five Gauss-

Legendre integration points. The cross-section is discretized into concrete fibres with an average mesh size of 10 mm × 10 mm and steel fibres to represent the longitudinal steels including both non-prestressed mild steel and prestressed strands. Note that the mesh size employed in this study is determined based on convergence analysis. The FE analyses are all carried out in displacement control using Newton–Raphson algorithm to solve nonlinear algebraic equations. The *RelativeNormDispIncr* in *OpenSees* is utilized to determine if convergence has been reached. The tolerance is set as 0.01 for all FE simulations based on convergence analysis. Material models are the same as discussed in Chapter 3.

4.2.3 Shear Connector Modelling

Adjacent girders are tied to each other using five steel shear connectors along the longitudinal direction of the bridge to enable transverse load transferring/sharing. Each shear connector consisted of two ¾ A325 bolts and two A36 connector pockets as shown in Figure 4-4 (a) and (b). The connector pockets are embedded at the adjacent sides of two parallel girders and then bolted to each other. Severe deterioration and even complete damage/loss of shear connectors was observed for this bridge as shown in Figure 4-4 (c), which intrigued the study on load sharing analysis considering shear connector loss as presented later.

The shear connection joints are used primarily to transfer vertical shear forces, so that adjacent PC girders can share a portion of wheel loads that are applied to one girder. Thus, they can be mechanically equivalent to vertical springs and modeled by macro elements with only vertical force-deformation relationships, instead of detailed micro modeling of the joint in the multi-girder bridge system for simplicity. Thus, in the multi-girder bridge model, macro elements, i.e., the *zeroLength* elements in *OpenSees*, are adopted to model the shear connectors between adjacent girders.

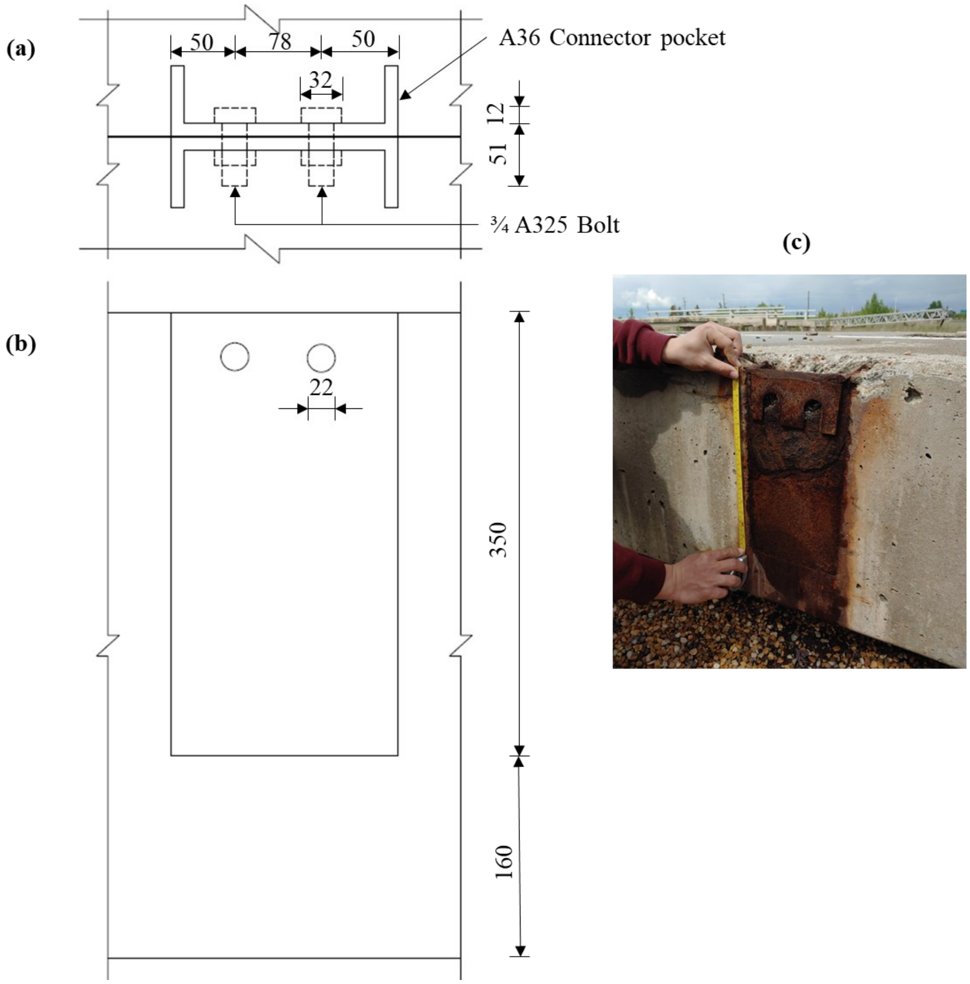

Figure 4-4: Shear connectors in: (a) plan view, (b) front view, and (c) engineering practice (deteriorated) (dimension in mm)

To obtain the vertical force-deformation relationship, a detailed 3-D continuum-based FE model is developed for the shear connection joint to simulate its mechanical behavior during vertical load transferring process in a commercial FE software *ABAQUS* (2014) widely used for detailed modeling of bolted connections and other similar joints (Kim and Kuwamura 2007). The eight-node brick element with reduced integration *C3D8R* is adopted to model the bolts and connector pockets. Figure 4-5 (a) shows the finite element mesh of the developed model. Based on mesh convergence analysis for a balance between accuracy and efficiency, a mesh size of 3 mm × 3 mm × 3 mm is assigned to the bolts and their neighborhood areas in the connector pockets;

the remaining part in the connector pockets is meshed with a relatively larger size of 6 mm × 6 mm × 6 mm. The material constitutive models for A325 bolt and A36 plate are the classical plasticity model with a von Mises yield surface, where the uniaxial stress-strain curves are obtained from the test results of other researchers (Kodur et al. 2012, Sajid et al. 2018) as shown in Figure 4-6 together with the summarized key properties. The contacts between bolts and pocket plates, bolts and nuts, and the two pocket plates are modeled by the 'general contact' in *ABAQUS* to allow free separation or contact. The normal behavior is defined by the hard contact (ABAQUS 2014), while the tangential behavior is defined by Coulomb friction model with a friction coefficient of 0.2 (Jiang et al. 2020).

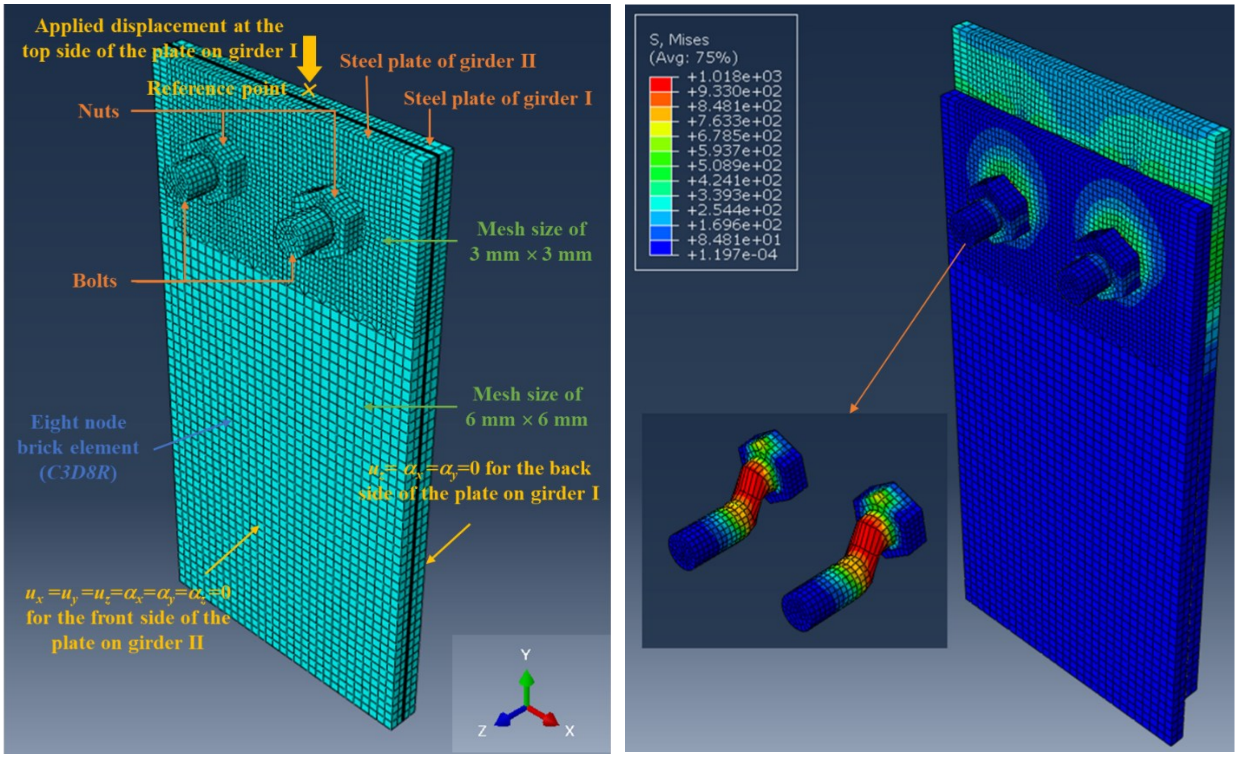

(a) (b)

Figure 4-5: Shear connector modeling: (a) 3D FE model, and (b) contour results on the Von Mises stress

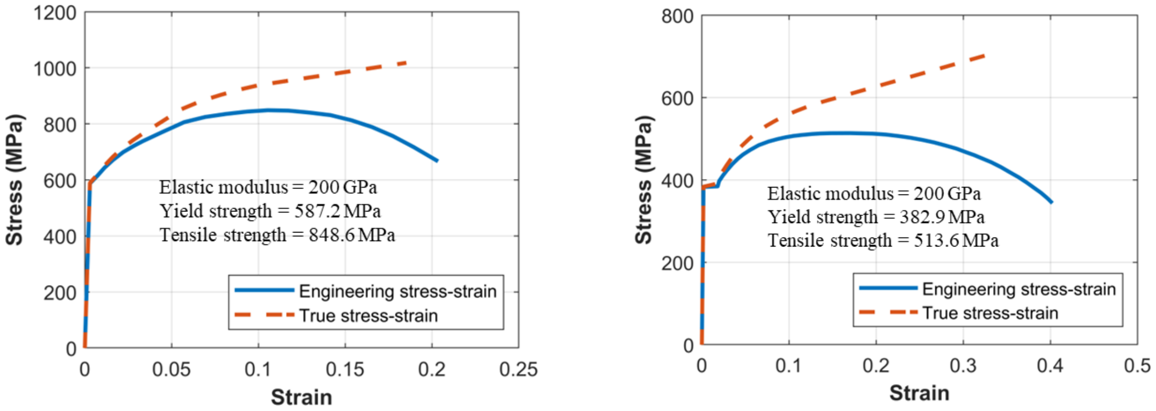

(a) (b)

Figure 4-6: Stress-strain curves of: (a) A325 bolt, and (b) A36 steel

The developed FE model for a shear connector is shown in Figure 4-5 (a), together with the loading and boundary conditions. The load is applied to a reference point, kinematically coupled to the nodes on the top side of the pocket plate on one girder (e.g., girder I), to simulate the vertical load transferred to the other girder (e.g., girder II). The out-of-plane deformations for the back of the pocket plate on girder I are constrained, i.e., $u_z = \alpha_x = \alpha_y = 0$, where u is the translation, α is the rotation, subscriptions of x, y and z indicate the directions as shown in Figure 4-5 (a). The front of the pocket plate on the girder II is fixed assuming that concrete restricts the deformation of steel pocket plate. This is to reflect the real boundary conditions of steel pockets provided by concrete when steel plates are embedded in concrete in engineering practice, i.e., the curling of thin-walled steel pockets will be restricted by the surrounding concrete.

Based on the developed 3D FE model for the shear connector, the obtained load-deformation relationship is shown in Figure 4-7. The contour results in terms of the Von Mises stress is also shown in Figure 4-5 (b). With the obtained load-deformation relationship (F - s), an analytical model described by Eq. (4-1) is developed and implemented as a uniaxial material in *OpenSees*, and used together with a macro element to model the vertical force-deformation relationship of shear connectors in the multi-girder system. Note that the curve fitting process follows the same principles as utilized in the uniaxial material model development by Menegotto and Pinto (1973).

$$F = \left(b_i \frac{s}{s_i} + \frac{(1-b_i)\frac{s}{s_i}}{\left[1+\left|\frac{s}{s_i}\right|^{R_i}\right]^{1/R_i}} \right) F_i + F_i^0,\ i=1\ (s \le s_0)\ or\ 2\ (s \ge s_0) \tag{4-1}$$

in which, $s_1 = 0.157\,\text{mm}$, $s_2 = 2.54\,\text{mm}$, $F_1 = 250.667\,\text{kN}$, $F_2 = 254\,\text{kN}$, and $b_1 = 0.0625$, $b_2 = 0$, $R_1 = 3$, $R_2 = 8$, $s_0 = 1.365\,\text{mm}$, $F_1^0 = 0$ kN and $F_2^0 = 235$ kN are fitted values.

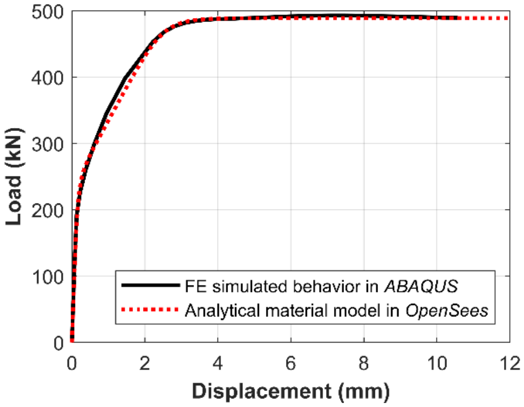

Figure 4-7: Comparison of the vertical load-deformation relationship obtained from 3D FE model and fitted for the macro element to represent a shear connector

4.3 Load-sharing Analysis of Multi-girder Bridge

With the developed FE model for the Tiger Lily bridge, the system behavior is studied in this section with a particular emphasis on load sharing under two scenarios: flexure-dominated and shear-critical loadings. The CL-625 truck load (CSA 2019), as shown in Figure 4-8, is used as a reference load and applied to the bridge with the two wheel-line loads on G2 and G3, which represents a realistic loading position in the transverse direction when a truck is in one lane. The truck position in the longitudinal direction differs for flexure-dominated and shear-critical loading scenarios as detailed later. After applying the dead load of self-weight calculated according to the tested concrete density of 1980 kg/m^3, the reference truck load is applied with an increasing multiplier of α in the FE simulation to determine the ultimate load-carrying capacity of the multi-girder system and to investigate load-sharing. For this purpose, in parallel, FE simulation is conducted for the multi-girder bridge without shear connectors, referred to as dis-connected girders (with isolated individual girders), and compared with the shear-connected multi-girder system.

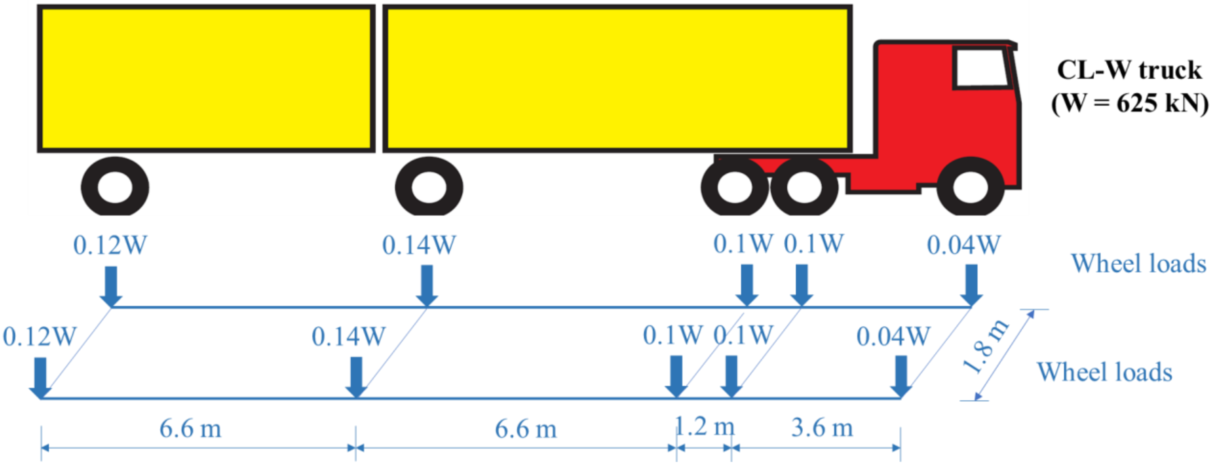

Figure 4-8: CL-625 truck load

4.3.1 Flexure-dominated Loading Scenario

The truck position in longitudinal direction for the considered flexure-dominated scenario is shown in Figure 4-9. This load position in this scenario is determined based on analysis of a single girder under CL-625 truck load to achieve the maximum bending moment. As such, the multiplier of α applied to the reference truck load can be used as a measure of the load level, and its peak value refers to the load-carrying capacity related to flexure failure. The obtained load-deflection curves, measured by the load multiplier and the midspan displacement of G3, are shown in Figure 4-10.

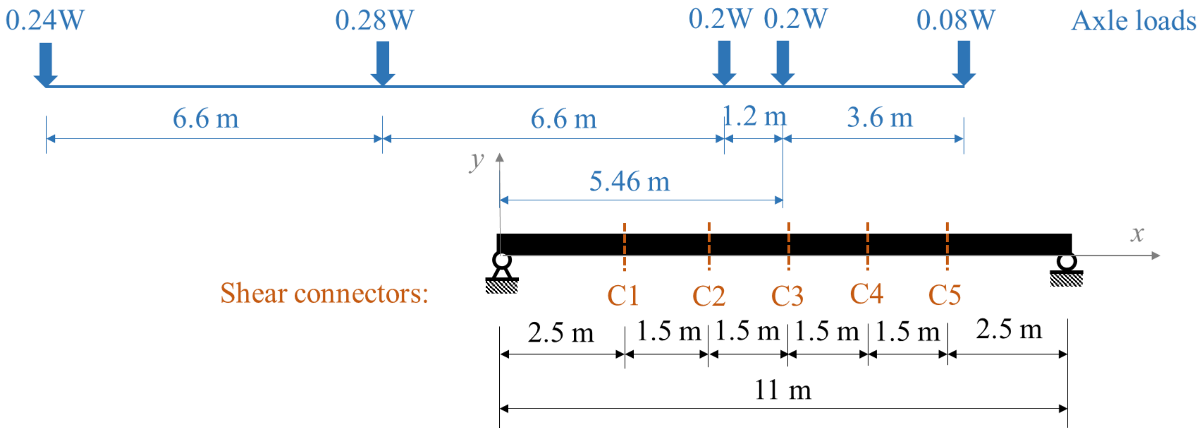

Figure 4-9: CL-625 truck position in longitudinal direction for the flexure-dominated scenario

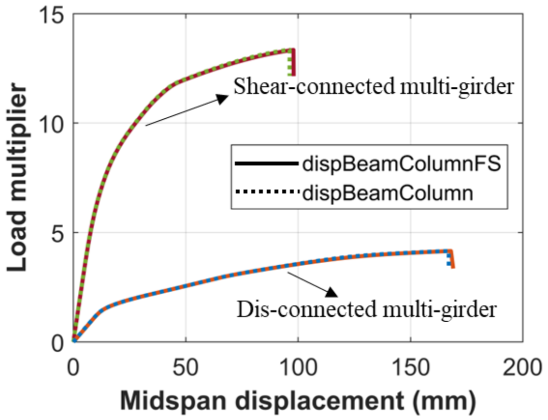

Figure 4-10: Load-deflection curves

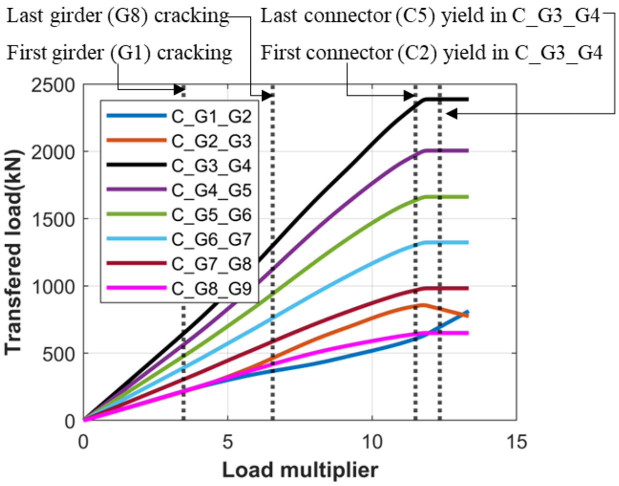

Figure 4-11: Transferred load by each line of shear connectors

It is shown that the load-carrying capacity of the shear-connected multi-girder system (P^{con}) is significantly higher than the load-carrying capacity of the dis-connected multi-girder system (P^{iso}), which indicates the important role of shear connectors for load-carrying capacity under the flexure-dominated loading scenario. The ratio $P^{con}/P^{iso} = 3.14$ quantifies the contribution of shear connectors or the other adjacent PC girders without being directly loaded by truck wheels. Note that in the multi-girder bridge model, the recently developed flexure-shear coupled fibre beam element (i.e., *dispBeamColumnFS*) was used. For the purpose of comparison, the conventional fibre beam element (i.e., *dispBeamColumn*) that neglects shear deformation is also used for the above analysis. It can be seen that under this flexure-dominated loading scenario, no visible difference can be observed in the simulation result when using the conventional fibre beam element, which is sufficient for FE modeling of girders under flexure-dominated loading.

For the shear-connected multi-girder system, the loads transferred by each line of shear connectors between two adjacent girders were obtained by summing up the forces transmitted in five shear connectors and summarized in Figure 4-11. It can be seen that the connectors between G3 and G4 transferred the highest load among all lines of connectors and thus most susceptible for structural damage due to repeated loading in this case. The plateau stage near the end of loading process in Figure 4-11 indicates that all shear connectors between G3 and G4 entered yielded. Note that after the sharp slope change, the transferred load still kept increasing (although it is neglectable) until the last connector yielded completely (i.e., entered the plateau stage as shown in Figure 4-7). The yield sequence of shear connectors between G3 and G4 follows C2, C3, C1, C4, and C5. This resulted in that afterwards no additional loads can be transferred from G3 to G4~G9 despite the increasingly applied external loads, indicating that the nonlinearity/plasticity plays an important role in the load transferring. In addition, the nonlinearity in terms of concrete cracking also influenced the load transferring as shown in Figure 4-11 by affecting the curve slope of C-G1-G2 and C-G2-G3. The sequence of girder cracking follows G1, G9, G2, G3, G4, G5, G6, G7, G8.

For the shear-connected multi-girder system, the load distributed to each girder was also obtained by summing up the vertical reaction forces at the end of each girder. The load percentage shared by each girder was summarized as shown in Figure 4-12 under different load levels, i.e., α = 1 (elastic stage), 3 (before any girder cracking), 7 (after all girder cracking), 11 (before any shear connector yielding) and 13.4 (failure state). It can be observed that the two exterior girders (G1 and G9) exhibit the largest load percentage due to their highest stiffness of exterior girders. With increasing load levels, the load percentage shared by each girder varies especially for G1 ~ G3 and G9, which is resulted from the nonlinearity(plasticity)-induced force redistribution. Specifically, among all interior girders that are identical, G2 and G3 take the most load share in the initial stage (α =1 and 3) and in the failure state (α = 13.4) after shear connecters between G3 and G4 yielded; in contrast, G2 and G3 take the least load percentage for α =7 and 11 due to the decreased stiffness with the increase of cracking formation.

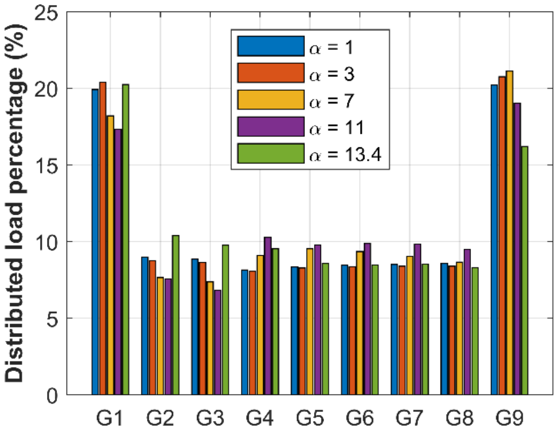

Figure 4-12: Distributed load percentage of each girder under different load levels

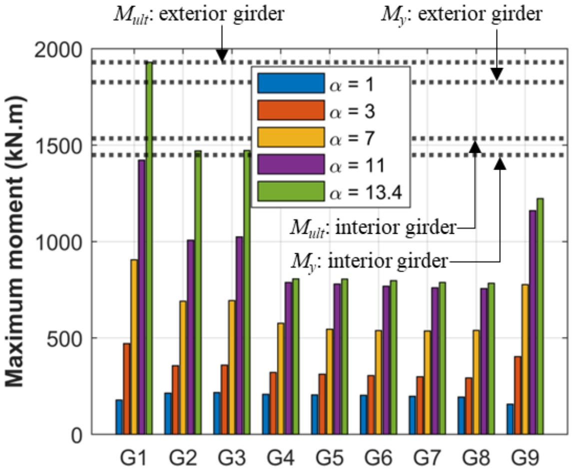

Figure 4-13: Maximum moment of each girder under different load levels

This redistribution effect can also be reflected in terms of the maximum moment in each girder as shown in Figure 4-13. When the load level is relatively low (e.g., α = 1), the maximum moment in G2 and G3 is largest among all the shear-connected girders, while with the increase of load levels, the differences between girders in terms of the maximum moment become significantly larger. This indicates that the nonlinearity plays an important role in internal force distribution and load sharing, while linear elastic assumption for load distribution factor can be unrealistic. This is because linear-elastic models underestimate the load-sharing capability of adjacent girders, considering the reduced stiffness of girders due to plastic deformation (e.g., concrete cracking and strands yielding), and the yielding of the shear connectors. Note that the ultimate and strands yielding moment capacities of PC girders are indicated in Figure 4-13, with the ultimate moment (M_{ult}) equal to1929 kN-m and 1534 kN-m and the strands yielding moment (M_y) equal to 1448 kN-m and 1825 kN-m for exterior and interior girders, respectively. Note that the M_{ult} and M_y were obtained by single girder analysis under the dead load and the increasing truck load with the same longitudinal location as shown in Figure 4-9. In the shear-connected multi-girder bridge system, G1 reached the ultimate moment, while the G2 and G3 reached the strands yielding moment but not reached the ultimate moment.

4.3.2 Shear-critical Loading Scenario

The truck position in longitudinal direction for the considered shear-critical scenario is shown in Figure 4-14. This loading scenario is equivalent to the single point loading with a shear span to effective depth ratio (*a*/*d*) of 2.25 (i.e., the same as the shear test on single interior girder discussed before). As such, the multiplier applied to the reference truck load can be used as a measure of the load level, and its peak value refers to the load-carrying capacity related to shear failure. The obtained load-deflection curves, measured by the load multiplier and the loading point displacement of G3, are shown in Figure 4-15.

It is shown that the load-carrying capacity of the shear-connected multi-girder system (P^{con}) is still higher than that of the dis-connected multi-girder system (P^{iso}) with the ratio P^{con}/P^{iso} = 1.47, while this ratio is relatively smaller compared with the ratio of 3.14 for the flexure-dominated loading scenario. This difference can be attributed to that the shear connectors play a less significant role for the considered shear-critical loading scenario. The bridge failed earlier due to shear under the shear-critical loading scenario without yielding of shear connectors. This can also be reflected in the transferred loads by each line of shear connectors as summarized in Figure 4-16. The connectors between G3 and G4 transferred the highest load among all lines of connectors similar to flexure-dominated loading scenario, all shear connectors remain elastic.

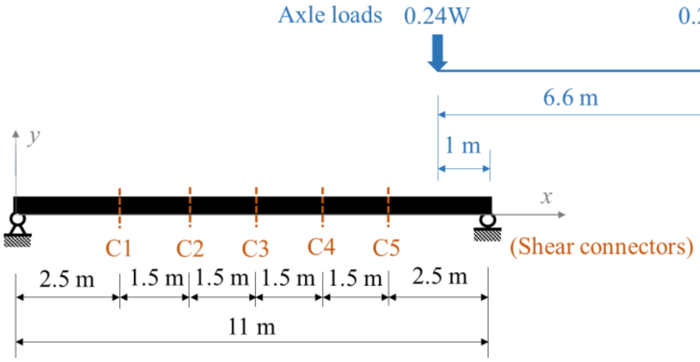

Figure 4-14: CL-625 truck position in longitudinal direction for the shear-critical scenario

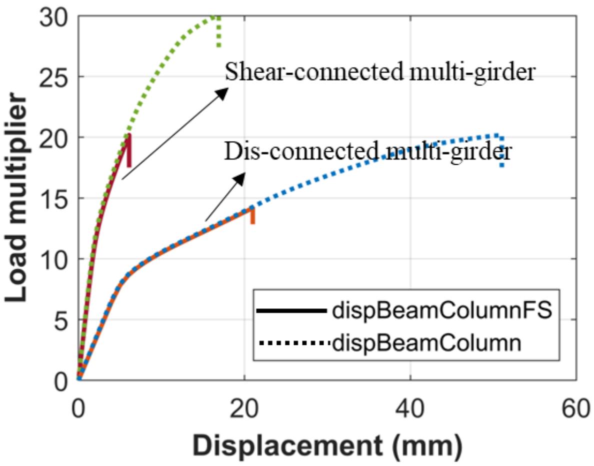

Figure 4-15: Load-deflection curves

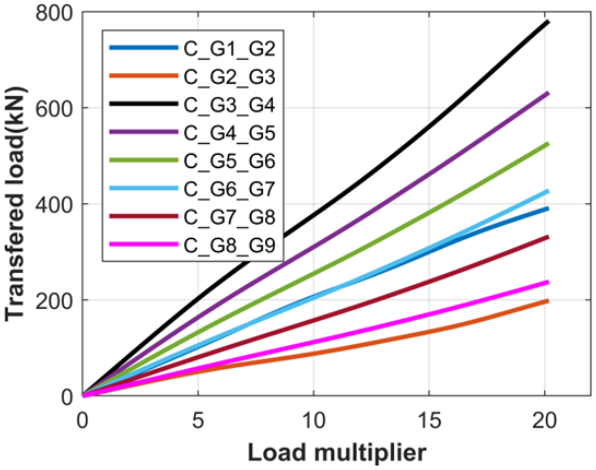

Figure 4-16: Transferred load by each line of shear connectors

Note that for the purpose of comparison, in addition to the multi-girder analysis using the recently developed flexure-shear coupled fibre beam element, the conventional fibre beam element that neglect shear deformation is also used. It can be seen that the FE models based on conventional fibre beam element overpredicted the load-carrying capacity for both the shear-connected multi-girder system and the dis-connected multi-girder system when loaded under a shear-critical loading scenario.

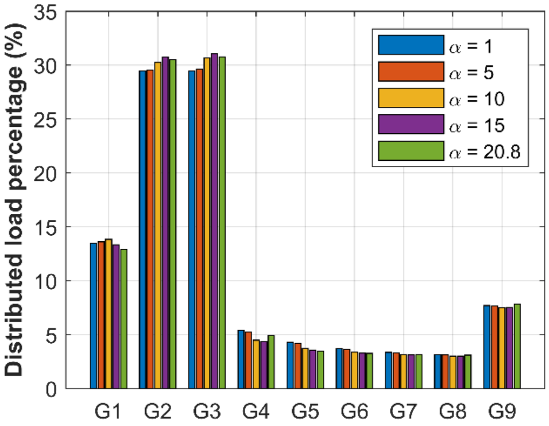

Figure 4-17: Distributed load percentage of each girder under different load levels

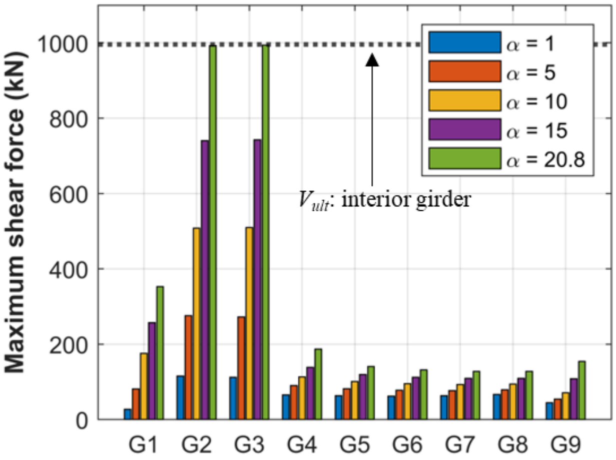

Figure 4-18: Maximum shear force of each girder under different load levels

The percentage of the load shared by each girder is summarized in Figure 4-17 under different load levels, i.e., α = 1, 5, 10, 15 and 20.8 (failure state). It can be seen that with the increasing load levels, the shared load percentage of each girder varies slightly, indicating that the nonlinearity-induced load redistribution plays a negligible role under shear-critical loading scenarios and thus models using linear elastic assumption is valid.

The maximum shear force of each girder under different load levels is also summarized in Figure 4-18. Different from the flexure-dominated loading scenario, with the increasing load levels, the maximum shear force in G2 and G3 increase significantly faster compared with other girders. The shear-connected multi-girder system eventually failed in that the G2 and G3 reached the ultimate shear force (V_{ult}) of the interior girder. This is because of the less significant role of shear connectors under this shear-critical loading scenario. Note that the V_{ult} was obtained by single girder analysis under the dead load and the increasing truck load with the same longitudinal location as shown in Figure 4-14.

4.4 Effects of Shear Connector Damage

Recognizing the importance of shear connectors on load sharing and load-carrying capacity of multi-girder bridges, this section studies the influence of single or multiple shear connector damage/loss (e.g., due to corrosion) on bridge system behavior. Since the connectors between G3 and G4 are shown to be critical in the system behavior of the multi-girder bridge for the two loading scenarios considered, the effects of shear connector damage/loss are studied.

4.4.1 Single Shear Connector Loss

By assuming one of the five connectors between G3 and G4 was damaged to complete loss, the multi-girder system is analyzed under the two loading scenarios. The loss in the load-carrying capacity due to shear-connector loss can be reflected by the change in the ratio (i.e., P^{con} / P^{iso}) between those of the shear-connected and dis-connected multi-girder systems. Table 4-2 summarizes P^{con} / P^{iso} for both flexure-dominated and shear-critical loading scenarios. It can be seen that shear connector loss has a more significant influence on bridges under flexure-dominated loading compared with those under shear-critical loading. The middle shear-connectors are more important for the flexure-dominated loading scenario, while the shear connector (C-G3-G4-5) close to wheel loading point for the shear-critical loading scenario considered is more important than others. One single shear connector loss out of the 40 shear connectors in this multi-girder bridge can result in a load-carrying capacity loss percentage (LP^c) up to 14.32%. This indicates that shear connectors can play an important role in the load sharing and thus load-carrying capacity of shear connected multi-girder bridges. Given the fact that corrosion-induced deterioration and damage/loss of shear connectors are widely observed for bridges during regular inspections, the potential safety issues resulted from shear connector damage/loss should raise concerns for evaluations of similar multi-girder bridges.

Table 4-2: Effects of complete loss of a single shear connector between G3 and G4

Loading scenarios		No connector loss	Loss of shear connectors of C-G3-G4-#				
			1	2	3	4	5
Flexure-dominated	P^{con} / P^{iso}	3.14	2.90	2.76	2.69	2.79	2.93
	LP^{c} (%)	–	7.47	12.16	14.32	10.93	6.64
Shear-critical	P^{con} / P^{iso}	1.47	1.47	1.47	1.47	1.44	1.36
	LP^{c} (%)	–	0	0	0	2.08	7.09

4.4.2 Multi Shear Connector Loss

Similarly, by assuming loss of more than one of the five connectors between G3 and G4, the complete loss of two, three, and four shear connectors between G3 and G4 are also studied. The ratios for P^{con} / P^{iso} under both flexure-dominated and shear-critical loadings are summarized in Tables 4-3, 4-4 and 4-5. As a result of the loss of two, three and four shear connectors between G2 and G3, the maximum load-carrying capacity loss percentage (LP^{c}) can be 26.01%, 37.06% and 44.42%, respectively, under the considered flexure-dominated loading scenario; while under the considered shear-critical loading scenario, the maximum load-carrying capacity loss percentage (LP^{c}) can be 10.41%, 12.38% and 14.09%, respectively. It is worth mentioning that the loss of shear connectors between G3 and G4 naturally increase the load shared by G1, which relies on the shear connectors between G1 and G2. If the shear connectors between G1 and G2 were also damaged, the load-carrying capacity loss would be more significant.

Table 4-3: Effects of complete loss of two shear connectors between G3 and G4

Loading scenarios		Loss of shear connectors of C-G3-G4- #									
		1 & 2	1 & 3	1 & 4	1 & 5	2 &3	2 & 4	2 & 5	3 & 4	3 & 5	4 & 5
Flexure-dominated	P^{con}/P^{iso}	2.48	2.47	2.57	2.69	2.32	2.42	2.55	2.34	2.48	2.58
	LP^{c} (%)	20.94	21.26	18.22	14.19	26.01	22.71	18.72	25.36	21.05	17.74
Shear-critical	P^{con}/P^{iso}	1.47	1.47	1.44	1.36	1.47	1.43	1.36	1.42	1.45	1.31
	LP^{c} (%)	0.05	0.01	2.11	7.10	0.01	2.27	7.07	3.43	1.07	10.41

Table 4-4: Effects of complete loss of three shear connectors between G3 and G4

Loading scenarios		Loss of shear connectors of C-G3-G4-#									
		1 & 2 & 3	1 & 2 & 4	1 & 2 & 5	1 & 3 & 4	1 & 3 & 5	1 & 4 & 5	2 & 3 & 4	2 & 3 & 5	2 & 4 & 5	3 & 4 & 5
Flexure-dominated	P^{con}/P^{iso}	2.08	2.17	2.30	2.12	2.26	2.34	1.97	2.11	2.20	2.13
	LP^{c} (%)	33.64	30.70	26.74	32.32	28.05	25.50	37.06	32.73	29.89	32.02
Shear-critical	P^{con}/P^{iso}	1.47	1.44	1.36	1.42	1.36	1.31	1.41	1.35	1.31	1.29
	LP^{c} (%)	0	1.70	7.10	3.04	7.26	11.02	3.99	7.96	10.69	12.38

Table 4-5: Effects of complete loss of four shear connectors between G3 and G4

Loading scenarios		Loss of shear connectors of C-G3-G4-#				
		1 & 2 & 3 & 4	1 & 2 & 3 & 5	1 & 2 & 4 & 5	1 & 3 & 4 & 5	2 & 3 & 4 & 5
Flexure-dominated	P^{con}/P^{iso}	1.74	1.87	1.95	1.90	1.76
	LP^{c} (%)	44.42	40.35	37.82	39.48	43.84
Shear-critical	P^{con}/P^{iso}	1.38	1.34	1.31	1.29	1.26
	LP^{c} (%)	5.82	8.91	10.84	12.25	14.09

4.5 Effect of Retrofit with More Shear Connectors

To further investigate the influence of shear connectors using the developed model for the multi-girder bridge, this section examines the benefits of retrofitting with more shear connectors. Specifically, 5, 7, 9, 19, and 29shear connectors between adjacent girders are considered. Note that shear connectors are assumed to be installed uniformly along the bridge longitudinal direction for simplicity. The increase of the load-carrying capacity due to more shear connectors can be reflected by the change in the ratio (i.e., P^{con}/P^{iso}) between those of the shear-connected and dis-connected multi-girder systems.

The influence of different amount of shear connectors on the ratio of P^{con}/P^{iso} is summarized as shown in Figure 4-19. With the increase of shear connector amount, the P^{con}/P^{iso}

increased and eventually converged for both flexure-dominated and shear-critical loading scenarios. This indicates that the load-carrying capacity of shear-connected girder system can be improved by increasing the shear connector amount. The P^{con}/P^{iso} for the shear-critical loading scenario was constantly much smaller than that for the flexure-dominated loading scenario, indicating again that the shear connector play a more significant role under flexure-dominated loading scenarios.

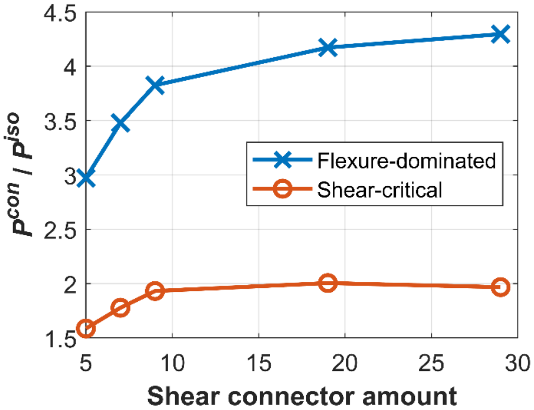

Figure 4-19: Influence of shear connector amount on the capacity ratio of P^{con}/P^{iso}

4.6 Summary

This chapter studied the system behavior and load sharing of multi-girder PC bridges based on a representative nine-girder PC bridge in Alberta, Canada. An efficient nonlinear analysis tool based on FE modeling was developed and applied to the considered bridge under both flexure-dominated and shear-critical loading scenarios. The influence of shear connectors on load-carrying capacity and load sharing was quantified by comparing the bridge system behavior of shear-connected girders and that of dis-connected girders. In the end, the influence of losing (e.g., due to corrosion damage) and increasing (e.g., due to retrofit) shear connectors were studied by parametric analyses. Main conclusions and results in this study are summarized below.

(1) The new flexure-shear coupled fibre beam element is shown to provide satisfactory prediction results for girders/bridges under both flexure-dominated and shear-critical loading scenarios. On the contrary, the conventional fibre beam element model can only obtain satisfactory results under flexure-dominated scenarios, while significantly overpredicts the ultimate load-carrying capacity under shear-critical scenarios due to the neglection of shear.

(2) The ratio between load-carrying capacities from the shear-connected multi-girder system and the dis-connected multi-girder system (P^{con} / P^{iso})are 3.14 and 1.47 for flexure-dominated and shear-critical loading scenarios respectively, which indicates that shear connectors and load sharing play more significant roles for flexure-dominated loading scenarios.

(3) It is shown that the nonlinearity (e.g., concrete cracking and connector yielding) plays an important role in internal force distribution and load sharing, while linear elastic assumption for load distribution factor can be unrealistic.

(4) Studies on the shear connector loss indicate that the shear connector loss has a greater influence on the shear-connected girder system under flexure-dominated loading compared with that under shear-critical loading. One single shear connector failure out of the 40 shear connectors in the studied bridge can result in a capacity loss up to 14.32%.

(5) Studies on increasing shear connectors indicate that the load-carrying capacity of shear-connected girder system can be improved by increasing the shear connector amount, while the shear connector still plays a less significant role under shear-critical loading with the increase of shear connectors.

CHAPTER 5:DATA-BASED SHEAR CAPACITY MODELS FOR INTACT PC GIRDERS BY BAYESIAN LINEAR REGRESSION

Aiming at probabilistic error assessment of design code models for shear capacity prediction of prestressed concrete (PC) girders, this chapter compiled an experimental database containing 369 PC girders that failed in shear. Using the experimental database, this chapter first assessed seven well-received shear capacity models from five concrete structure and bridge design codes, including ACI 318-19, AASHTO LRFD 2017, CSA A23.3:19, CSA S6:19 and *fib* MC 2010. In view of the fact that systematic error exists in those models, polynomial correction terms were calibrated for each model together with the remaining error quantified based on the compiled experimental database and Bayesian updating. The resulted models can be used for shear capacity predictions with better accuracy and, more importantly, with the model uncertainty quantified probabilistically. In the end, a case study of fragility analysis was conducted to show the benefits of the developed probabilistic models.

5.1 Introduction

Accurate capacity prediction of Prestressed concrete (PC) girders has been of a primary concern to structural engineers since they have been extensively used across the world and contribute significantly to the resilience of infrastructure system and socio-economic development. Compared with flexural capacity, predicting shear capacity remains a challenging task due to the complex load transfer and failure mechanism in concrete beam members under shear-critical loading, especially after concrete cracks are initiated (Tošic´ et al. 2016). To this end, significant efforts have been devoted to experimental and theoretical studies in the literature, leading to a wide variety of shear capacity prediction models for reinforced and prestressed concrete (RC/PC) members. Examples include finite element (FE) models (Metwally 2012; Feng et al. 2017), mechanics-based analytical models (Wang et al. 2008; Bernardo et al. 2018), and simplified-mechanical or semi-empirical models such as design code models (AASHTO 2017; ACI 2019; CSA 2019a; CSA 2019b; *fib* 2013). Compared with others, design code models are most widely utilized due to their simplicity and authority in engineering practice. However, unneglectable conservative bias and prediction scatter were observed for design code-based shear capacity prediction when compared to experimental database (Somo and Hong 2006; Nakamura et al. 2013; Tošic´ et al. 2016).

Although being conservative implies more safety margin in structural design, quantification of the model error is desired for better alignment with the reliability-based limit-state design philosophy (Holický et al. 2016). Based on the quantified model error, probabilistic shear capacity prediction model can be resulted by combing the original model and the quantified model error. This can benefit reliability analysis and probabilistic performance-based design (Gardoni et al. 2002) by enabling the consideration of all prevailing uncertainty/error sources. Compared with calibrating complete new probabilistic shear capacity models (Ning and Li 2018; Yu et al. 2019), the approach used in this study can take advantage of the prior knowledge on existing shear capacity models, and facilitate the utilization of resulted probabilistic models for engineers who are familiar with existing models, e.g., design code models.

The traditional approach to quantify model uncertainty is by using a professional/corrective factor as an independent random variable (MacGregor et al. 1997; Del Vecchio et al. 2017) to consider the model inaccuracy. In this approach, it is assumed that there exists no systematic correlation between the model error and model parameters. Additionally, the statistics (i.e., mean and coefficient of variation) and distribution type for the corrective factor were conventionally determined based on engineering judgment or limited experimental studies (Holický et al. 2016).

To remedy the aforementioned issues of the traditional corrective factor approach, Gardoni et al. (2002) proposed a Bayesian probabilistic correction approach, which expressed the model error as a function of model parameters with a residual term. This approach can benefit the correction of the systematic error inherent in an existing model and improve its prediction precision. More importantly, according to Gardoni et al. (2002), it takes advantage of the experimental data to improve the existing design code models of RC columns, which can facilitate the application of the developed models for reliability analysis. Song et al (2010) followed this Bayesian probabilistic correction approach and developed probabilistic shear capacity models for RC beams without shear reinforcement. In spite of the efforts developed to model error quantification as a function of model parameters to RC members, limited studies are available for PC girders. Chehab and Eamon (2018) developed a regression-based corrective factor as a function of model parameters for the shear capacity prediction of PC girders. However, no remaining model error is not quantified from a probabilistic point of view. In addition, the regression is based on a virtual experimental database generated by FE models rather than real experimental tests, which highly relies on the accuracy and versatility of the FE model.

Aiming at probabilistic error assessment and correction for shear capacity prediction of PC girders, this chapter compiled an experimental database containing 369 PC girders that failed in shear. Using the experimental data, this study first assessed the shear capacity models from five well-received concrete structure and bridge design codes using the conventional corrective factor approach. The design code models considered in this study include recommended models from ACI 318-19 (ACI 2019), AASHTO LRFD 2017 (AASHTO 2017), CSA A23.3:19 (CSA 2019a), CSA S6:19 (CSA 2019b) and *fib* MC 2010 (*fib* 2013). Based on the same experimental database, Bayesian probabilistic polynomial correction approach was then used to develop probabilistic shear capacity models for PC girders. Comparisons with the original design code models showed the superiority of the resulted probabilistic models with improved accuracy and precision. In the end, a case study of fragility analysis was conducted to show the benefits of the developed probabilistic models.

5.2 Experimental Database

To evaluate the model errors of the existing deterministic models, as well as to further develop probabilistic shear capacity models, a comprehensive literature review was conducted to compile an experimental database of shear tests on PC girders/beams. The following criteria were used to select the test specimens from the literature.

(1) The specimens are PC girders/beams that failed in shear. In other words, non-prestressed specimens and specimens that exhibit failure modes other than shear failure are not considered.

(2) The minimum shear span to effective depth ratio is 2.0. Specimens with shear span to effective depth ratio less than 2.0 are conventionally considered as deep beams and best designed by struct and tie models (AASHTO 2017). This is beyond the scope of this research project and thus not considered.

(3) The specimens were subjected to static loading. Specimens subjected to moving loads are not considered.

(4) The specimen information provided is sufficient for predicting the shear capacity by the design code models considered.

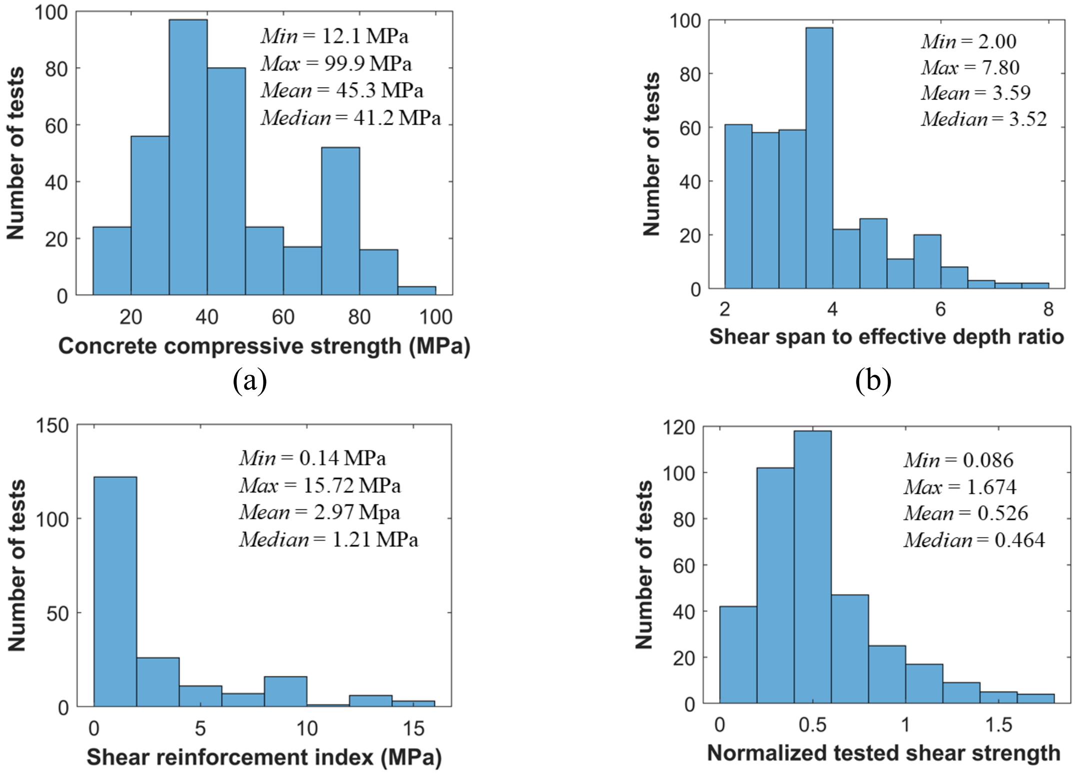

(a) (b)

(c) (d)

Figure 5-1: Distributions of four representative experimental variables: (a) concrete compressive strength for all girders, (b) shear span to effective depth ratio for all girders, (c) shear reinforcement index for PC girders with stirrups, and (d) normalized tested shear capacity for all girders

As a result of the literature review and the selection criteria, a total of 369 PC girders that failed in shear reported from 1954 to 2018 was compiled, including 192 girders with stirrups and 177 girders without stirrups. The detailed information of the 369 PC girders is provided in the the Appendix B. As a brief summary, Figure 5-1 presents the statistical information of the experimental database in terms of the four important quantities of shear-critical PC girders. They are the concrete compressive strength f_c', the shear span to effective depth ratio a/d, the shear reinforcement index defined as $\rho_v f_{yt} = A_v f_{yt} / (b_w s)$, and the normalized shear capacity defined as $V_{tested} / 0.25 f_c' b_w d$. Herein, a is the shear span, d is the effective depth, A_v is the area of shear reinforcement, f_{yt} is the yield strength of shear reinforcement, b_w is the web width, and s is the shear reinforcement spacing.

As seen from bar plots, the experimental database has a good coverage of concrete grade, with tested compressive strength ranging from 12.1 MPa to 99.9 MPa and the majority of them ranging from 30 MPa to 50 MPa. The majority of PC girders tested have a shear span to effective depth ratio ranging from 2.0 to 4.0, which is typical for shear critical loading scenarios. The shear reinforcement index reflects both the amount and strength of shear reinforcement and has a wide range from 0.14 MPa to 15.72 MPa. The majority of normalized shear capacity is less than 1.0, which is to be expected because the normalization factor of $0.25 f_c' b_w d$ is generally utilized as the upper limit of shear capacity by design code models. These imply that the compiled database is a good representation of shear-critical PC girders in engineering practice and thus can be used to assess the design code models for shear capacity predictions.

5.3 Shear Capacity Model Assessment

5.3.1 Shear Capacity Models

Shear capacity models from five concrete structure and bridge design codes are considered in this study, i.e., ACI 318-19 (ACI 2019), AASHTO LRFD 2017 (AASHTO 2017), CSA A23.3:19 (CSA 2019a), CSA S6:19 (CSA 2019b) and *fib* MC 2010 (*fib* 2013). The simplified procedure in AASHTO LRFD 2017 and the simplified method in CSA S6:19 for shear capacity calculation are not applicable to prestressed members, and thus not considered in this study. Note that for shear capacity prediction based on the models considered in this study, the tested values for the concrete and steel material properties are used without material reduction factors or other safety factors (e.g., resistance factors) for fair comparison with the test results. It should be mentioned that there are conventionally some restrictions for the application of simplified methods from design codes, such as the restriction on concrete and steel properties from ACI 318-19 and CSA A23.3:19. These restrictions are not considered in this study for existing design code model assessment and new probabilistic model development. This is to enable the development of probabilistic models without application restrictions to facilitate their application in engineering practice. The model error of existing design code models resulted from not following the application restrictions are expected to be learned and corrected in the following study of model error correction and probabilistic model development.

The calculation procedure of considered design code models and the related parameters are summarized in Appendix C. It is worth mentioning that each design code includes more than one shear capacity models with different levels of simplification. Shear capacity models from the five design codes have different theoretical bases. The models from AASHTO LRFD 2017, CSA A23.3:19 and CSA S6:19 are developed based on modified compression field theory (MCFT) (Vecchio and Collins 1986). For members without shear reinforcement, the models in *fib* MC 2010 are based on simplified modified compression field theory (SMCFT) (Bentz et al. 2006). While for members with shear reinforcement, the models in *fib* MC 2010 are based on a general stress field approach (Sigrist 2011) combined with SMCFT. The models from ACI 318-19 are based on a combination of truss analogy and empirical models (Zsutty 1968; Sigrist et al. 2013).

The influence of internal forces under design load combinations at critical sections (i.e., M_u, V_u and N_u) are considered in all the adopted design code models, i.e., the predicted shear capacity is a function of internal forces as $V_d = f(V_u, M_u, N_u)$. However, for those girders tested to failure in labs, the concept of design load combination is usually neglected. In this study, the related internal forces at critical sections are determined by imposing $V_u = V_d(V_u, M_u, N_u)$ for the tested load condition of each girder specimen.

5.3.2 Model Error Assessment

Based on the compiled experimental database in this study, the error (e.g., bias and scatter) of the design code models considered are assessed in terms of the test-to-prediction ratio $V_{tested}/V_{predicted}$, where V_{tested} and $V_{predicted}$ are the tested and predicted shear capacity, respectively. The mean value of $V_{tested}/V_{predicted}$ can represent the inherent bias while the coefficient of variation (COV) can reflect the prediction scatter. Note that for *fib* MC 2010, Level III approximation and Level II approximation methods are used for PC girders with and without stirrups, respectively.

Figure 5-2 summaries the histograms of $V_{tested}/V_{predicted}$ for the PC girders in the experimental database. It can be seen that although the detailed/general methods (see Figure 5-2 (b) and Figure 5-2 (e)) perform better than simplified methods (see Figure 5-2 (a) and Figure 5-2 (d)), all design code models exhibit significant conservative bias and relatively large prediction scatter. Detailed statistics, such as mean, COV, minimum, maximum, and the best-fitted distributions, of $V_{tested}/V_{predicted}$ are provided in Table 5-1. The least conservative model with the lowest mean value of $V_{tested}/V_{predicted}$ (1.535) is found to be the detailed method from ACI 318-19, which has a relatively low COV of 0.288. In contrast, the MCFT-based general procedure from AASHTO LRFD 2017 has the lowest COV value of 0.230. Note that the simplified methods in ACI 318-19 and CSA23.3:19 have large COV values, which indicate larger prediction scatter compared with other models.

The best fitted distribution of $V_{tested}/V_{predicted}$, which is conventionally utilized as the corrective factor or professional factor (MacGregor et al. 1997; Del Vecchio 2017) to consider the model error in reliability analysis, is also provided as shown in the column of ‘Best fitted distribution’ in Table 5-1. The best-fitted distribution type is determined based on Kolmogorov-Smirnov (K-S) tests (Massey 1951). It is shown that the lognormal and gamma distribution are the best two fitted distribution types. This is contradictory to the widely utilized normal distribution assumption for the professional factor (Nowak and Grouni 1983; MacGregor et al. 1997). The discrepancy between normal and the best fitted distribution can be significant as shown in Figure 5-2.

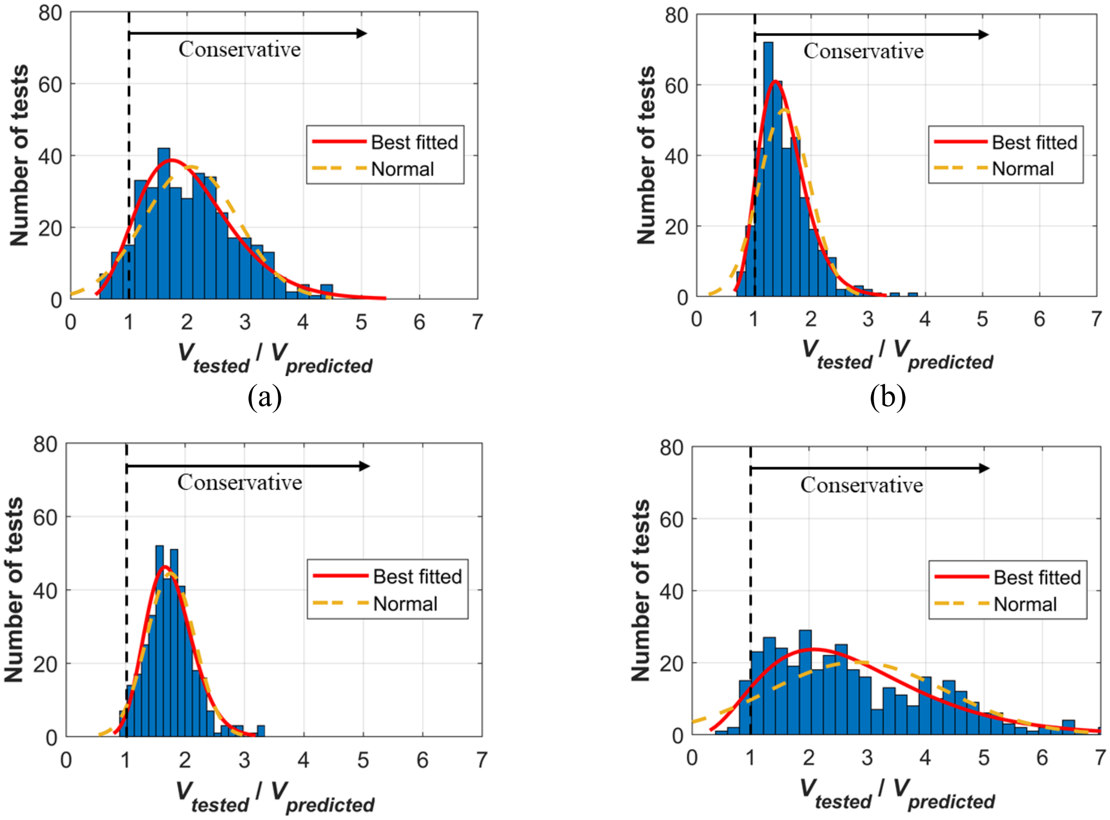

(a)

(b)

(c)

(d)

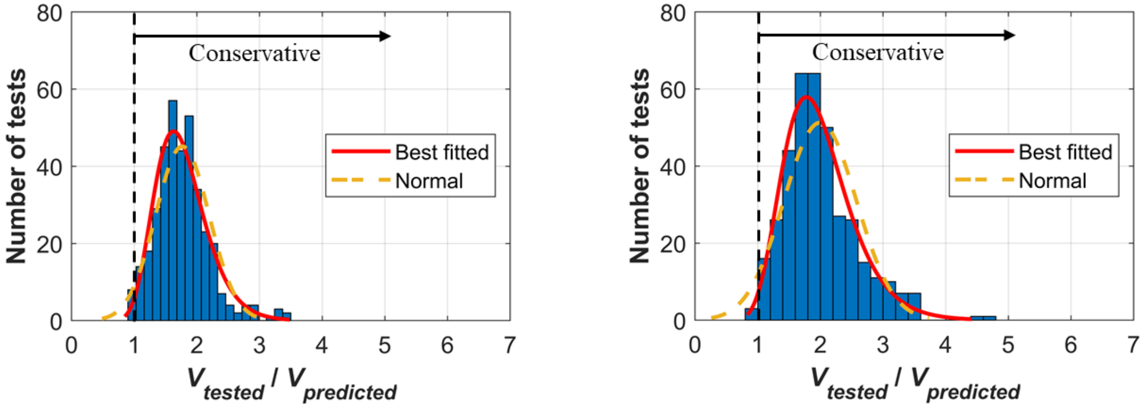

(e) (f)

Figure 5-2: Distributions of V_{tested} / $V_{predicted}$ for: (a) ACI 318-19 (Simplified method), (b) ACI 318-19 (Detailed method), (c) AASHTO LRFD 2017, (d) CSA A23.3:19 (Simplified method), (e) CSA A23.3:19/S6:19 (General method), and (f) *fib* MC 2010

Table 5-1: Assessment of different design code models in terms of V_{tested} / $V_{predicted}$

Model	Statistics				Best fitted distribution*	p-value	
	Min	*Max*	*Mean*	*COV*		Normal	Best fitted
ACI 318-19 (Simplified method)	0.538	4.440	2.068	0.389	$\Gamma(6.289, 0.329)$	0.101	0.640
ACI 318-19 (Detailed method)	0.793	3.855	1.535	0.288	$LN(0.391, 0.270^2)$	N/A	0.579
AASHTO LRFD 2017 (General procedure)	0.932	3.336	1.754	0.230	$\Gamma(19.542, 0.090)$	0.373	0.822
CSA A23.3:19 (Simplified method)	0.587	10.647	2.831	0.534	$\Gamma(3.787, 0.748)$	N/A	0.374
CSA A23.3:19/S6:19 (General method)	0.931	3.487	1.767	0.242	$LN(0.542, 0.235^2)$	0.083	0.719
fib MC 2010	0.884	4.709	1.995	0.289	$LN(0.652, 0.278^2)$	N/A	0.464

The p-values from K-S tests are also summarized in Table 5-1, which can represent the differences between the cumulative distribution functions from the observed samples and the assumed distribution type (i.e., normal, lognormal, gamma, Weibull distributions in this study), ranging from 0 to 1 (Massey 1951). The larger the p-value, the smaller the difference between the observed samples and the assumed distribution. If the p-value is less than a prescribed threshold (e.g., 0.01), usually referred to as the significance level, the hypothesis that the observed samples obey the assumed distribution type should be rejected. It can be seen from Table 5-1 that the normal distribution assumption performs poorly despite its wide use. The N/A represents that the $V_{tested}/V_{predicted}$ rejects the normal distribution assumption under a significance level of 0.01.

5.3.3 Correlation Between Test-to-prediction Ratios and Model Parameters

As shown in the previous section, the design code models considered exhibit significant conservative bias and prediction scatter. Although being conservative implies more safety margin in structural design, transparency in the model error is required. For example, unbiased strength prediction with quantified scatter (i.e., consideration of model error) is desired to benefit engineering practice for reliability analysis and probabilistic performance-based design. To this end, there are typically two approaches depending on whether the systematic correlation between the model error and model parameters exists. When this systematic correlation is not observed, the model error is typically considered as an independent random variable, such as the best fitted distribution provided for the $V_{tested}/V_{predicted}$ in Table 5-1. Otherwise, the relationship between the model error and model parameters can be modelled using stochastic regression models (Gardoni et al. 2002).

Taking the general method from CSA A23.3:19 for example, the model error observations ($V_{tested}/V_{predicted}$) is correlated to the shear span to effective depth ratio a/d and shear reinforcement index $\rho_v f_{yt} = A_v f_{yt}/(b_w s)$ as shown in Figure 5-3. It can be seen that the model error exhibits a functional relationship with both a/d and $\rho_v f_{yt}$. Similar systematic correlations have been observed for other design code models. Thus, such systematic error (trend) hidden can be learned as a regression function of model parameters and used to add correction terms to the code-based strength prediction models in this study.

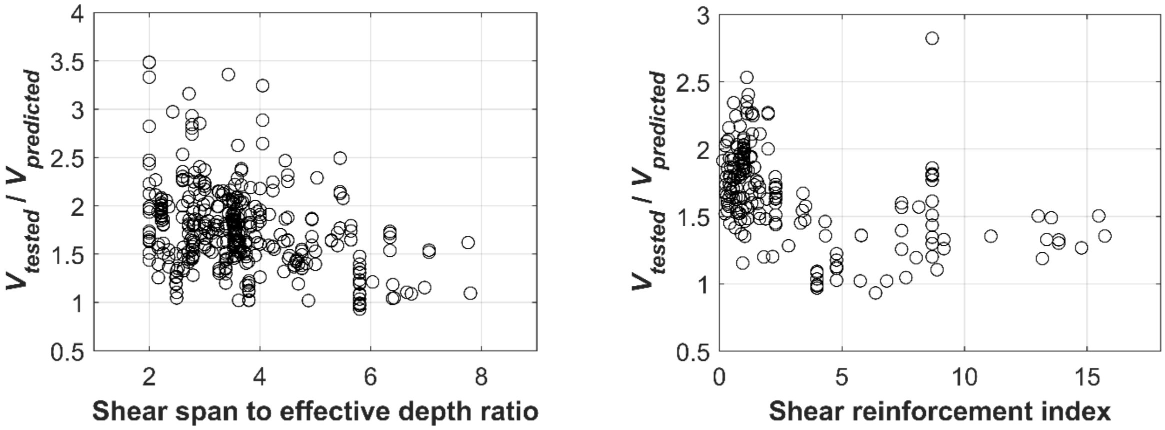

(a) (b)

Figure 5-3: Test-to-prediction ratios (V_{tested} / $V_{predicted}$) as a function of: (a) shear span to effective depth ratio a/d, and (b) shear reinforcement index $\rho_v f_{yt}$

5.4 Model Correction and Probabilistic Prediction Models

5.4.1 Model Development Procedure

In order to improve the model accuracy and precision (i.e., reducing bias and scatter) to facilitate reliability assessment or fragility analysis of PC girders, probabilistic correction terms can be added to the adopted deterministic shear capacity models (i.e., the design code models considered). To construct a dimensionless model for the shear capacity V, the normalized quantity $v = V/0.25 f_c' b_w d$ is adopted. The natural logarithmic transformation is applied to the normalized shear capacities to make the model homoscedastic. The model function form is shown as Eq. (5-1),

$$\ln\left[v(\mathbf{x},\mathbf{\Theta})\right] = \ln\left[v_d(\mathbf{x})\right] + \gamma(\mathbf{x},\boldsymbol{\theta}) + \sigma\varepsilon \tag{5-1}$$

where $v(\mathbf{x},\mathbf{\Theta})$ is the normalized shear capacity prediction from the developed probabilistic model, $v_d(\mathbf{x})$ is the normalized shear capacity prediction from the adopted deterministic design code model, $\gamma(\mathbf{x},\boldsymbol{\theta})$ is the correction term, ε is a random variable with zero mean and unit variance, and σ is the standard deviation (SD) of the remaining error in the shear capacity prediction model after correction. In this equation, $\mathbf{x}$ is the vector of input variables that can affect the shear capacity predictions, e.g., material properties and geometric dimensions as indicated in Table 5-2, $\boldsymbol{\Theta} = (\boldsymbol{\theta}, \sigma)$ denotes the set of unknown model parameters.

To construct the correction function $\gamma(\mathbf{x}, \boldsymbol{\theta})$, a suitable set of explanatory functions $h_i(\mathbf{x}), i = 1, ..., p$ are utilized to explore the sources of bias in the adopted deterministic model, where p is the total number of explanatory functions, see Eq. (5-2).

$$\gamma(\mathbf{x}, \boldsymbol{\theta}) = \sum_{i=1}^{p} \theta_i h_i(\mathbf{x}) \tag{5-2}$$

Song et al. (2010) found that the model error can be captured more effectively by applying natural logarithm transformation to the explanatory functions $h_i(\mathbf{x})$. This approach is adopted in this study and then a comprehensive set of explanatory functions to capture various possible sources of model error are selected as summarized in Table 5-2.

Table 5-2: Selection of explanatory functions

Explanatory functions	(Possible) Sources of model error
$h_1(\mathbf{x}) = \ln e = 1$	Independent of $\mathbf{x}$
$h_2(\mathbf{x}) = \ln(a/d)$	Shear span to depth ratio
$h_3(\mathbf{x}) = \ln(a/L)$	Loading position
$h_4(\mathbf{x}) = \ln(h/b_w)$	Sectional aspect ratio
$h_5(\mathbf{x}) = \ln(a_g/b_w)$	Maximum aggregate size
$h_6(\mathbf{x}) = \ln \rho_l = \ln((A_s + A_{ps})/b_w d)$	Tensile longitudinal steel ratio
$h_7(\mathbf{x}) = \ln(f_{se}/f_{pu})$	Percentage of effective prestress
$h_8(\mathbf{x}) = \ln(f_{yt}/f_c')$	Material strength
$h_9(\mathbf{x}) = \ln \rho_v = \ln(A_v/b_w s)$	Stirrups ratio

Bayesian parameter estimation is adopted in this study to learn the values of the unknown model parameters $\mathbf{\Theta} = (\boldsymbol{\theta}, \sigma)$. The well-known Bayesian updating rule is shown as Eq. (5-3),

$$f(\mathbf{\Theta}) = \kappa L(\mathbf{\Theta}) p(\mathbf{\Theta}) \tag{5-3}$$

where $f(\mathbf{\Theta})$ is the posterior probability distribution of unknown model parameters, $L(\mathbf{\Theta})$ is the likelihood function, $\kappa = \left[\int L(\mathbf{\Theta}) p(\mathbf{\Theta}) d\mathbf{\Theta}\right]^{-1}$ is the normalizing factor, $p(\Theta)$ is the prior probability distribution of unknown model parameters. It is not straightforward to compute the multifold integrals for obtaining the normalizing factor κ, thus Markov Chain Monte Carlo (MCMC) sampling is utilized to obtain the posterior probability distribution of unknown model parameters $f(\mathbf{\Theta})$. To be specific, the No-U-Turn Sampler (NUTS) (Hoffman and Gelman 2014; Salvatier et al. 2016) is utilized in this study, which is a variant of Hamiltonian Monte Carlo and can achieve dramatically faster convergence for problems with large data size compared with traditional sampling methods. In addition, a non-informative prior distribution that follows a uniform distribution from positive infinity to negative infinity is adopted for the unknown model parameters, which is usually referred to as the flat distribution (Salvatier et al. 2016).

In order to avoid loss of precision due to inclusion of unimportant explanatory functions and to avoid overfitting the data, Gardoni et al. (2002) proposed a stepwise procedure for removing insignificant explanatory terms from the bias-correction function $\gamma(\mathbf{x}, \boldsymbol{\theta})$. When an unknown model parameter θ_i has the largest posterior COV after a Bayesian updating, its related explanatory function $h_i(\mathbf{x})$ is considered the least informative and then dropped from the bias correction function. Bayesian updating is performed again using this updated bias-correction function with fewer terms. It is suggested that this process should be repeated until such a removal increases the posterior mean of σ by an unacceptable amount, e.g., larger than 1% in this study, or until the largest posterior COV from θ_i is smaller than the posterior mean of σ .

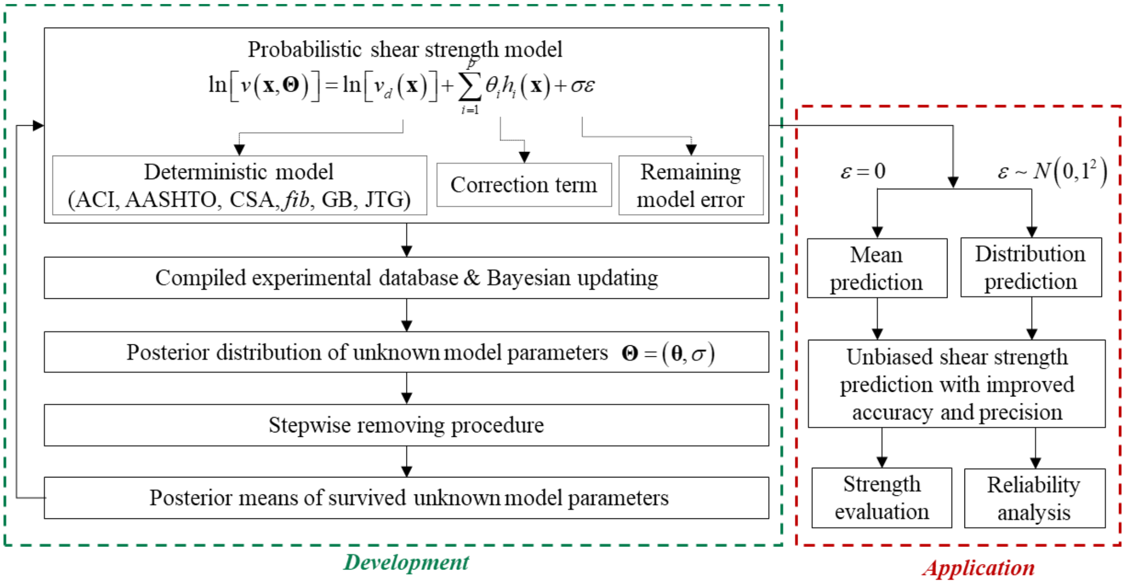

Figure 5-4: Flowchart for the development and application of the probabilistic models

The flowchart for the development and the potential applications of the probabilistic shear capacity models is shown in Figure 5-4. The posterior means of unknown model parameters $\mathbf{\Theta}=(\mathbf{\theta},\sigma)$ are considered as the best-fitting parameters and can be substituted into Eq. (5-1), which leads to deterministic and probabilistic shear capacity prediction models by neglecting or considering the remaining model error, respectively. The resulted model has an elegant formulation by adding a polynomial correction term to the existing deterministic model, which facilitate the use of newly developed models.

5.4.2 Model Correction Results

Following the procedure introduced in the previous section, Bayesian updating with stepwise removing process is performed using the experimental data compiled. The posterior means of unknown model parameters survived are listed in Table 5-3. By substituting the posterior means of survived unknow model parameters into Eq. (5-1), elegant probabilistic shear capacity models can be constructed and are summarized in Table 5-4.

Table 5-3: Posterior means of θ_i and σ after Bayesian updating with stepwise removing process

Model	θ_1	θ_2	θ_3	θ_4	θ_5	θ_6	θ_7	θ_8	θ_9	σ
ACI (Simplified)	1.263	−	−0.281	0.249	−	0.259	0.210	−0.324	−0.085	0.260
ACI (Detailed)	0.530	−0.171	−0.149	−	−	−	−	−0.087	−	0.246
AASHTO	0.873	−0.356	−	0.059	−	−	−0.080	−0.205	−0.056	0.192
CSA (Simplified)	−	−0.306	−0.299	0.570	−0.183	−	−	−0.533	−0.101	0.366
CSA (Detailed)	0.900	−0.371	−	0.063	−	−	−0.078	−0.178	−0.043	0.197
fib	−	−0.137	−0.324	0.147	−0.151	−	−	−0.230	−0.076	0.208

Table 5-4: The resulted probabilistic models with correction terms to the existing design code model and remaining error

Base model	Resulted probabilistic model
ACI (Simplified)	$\ln\left[v(\mathbf{x},\mathbf{\Theta})\right]=\ln\left[v_d(\mathbf{x})\right]+1.263-0.281\ln\frac{a}{L}+0.249\ln\frac{h}{b_w}+0.259\ln\rho_l+0.210\ln\frac{f_{se}}{f_{pu}}-0.324\ln\frac{f_{yt}}{f_c'}-0.085\ln\rho_v+0.260\varepsilon$
ACI (Detailed)	$\ln\left[v(\mathbf{x},\mathbf{\Theta})\right]=\ln\left[v_d(\mathbf{x})\right]+0.530-0.171\ln\frac{a}{d}-0.149\ln\frac{a}{L}-0.087\ln\frac{f_{yt}}{f_c'}+0.246\varepsilon$
AASHTO	$\ln\left[v(\mathbf{x},\mathbf{\Theta})\right]=\ln\left[v_d(\mathbf{x})\right]+0.873-0.356\ln\frac{a}{d}+0.059\ln\frac{h}{b_w}-0.080\ln\frac{f_{se}}{f_{pu}}-0.205\ln\frac{f_{yt}}{f_c'}-0.056\ln\rho_v+0.192\varepsilon$
CSA (Simplified)	$\ln\left[v(\mathbf{x},\mathbf{\Theta})\right]=\ln\left[v_d(\mathbf{x})\right]-0.306\ln\frac{a}{d}-0.299\ln\frac{a}{L}+0.570\ln\frac{h}{b_w}-0.183\ln\frac{a_g}{b_w}-0.533\ln\frac{f_{yt}}{f_c'}-0.101\ln\rho_v+0.366\varepsilon$
CSA (Detailed)	$\ln\left[v(\mathbf{x},\mathbf{\Theta})\right]=\ln\left[v_d(\mathbf{x})\right]+0.900-0.371\ln\frac{a}{d}+0.063\ln\frac{h}{b_w}-0.078\ln\frac{f_{se}}{f_{pu}}-0.178\ln\frac{f_{yt}}{f_c'}-0.043\ln\rho_v+0.197\varepsilon$
fib	$\ln\left[v(\mathbf{x},\mathbf{\Theta})\right]=\ln\left[v_d(\mathbf{x})\right]-0.137\ln\frac{a}{d}-0.324\ln\frac{a}{L}+0.147\ln\frac{h}{b_w}-0.151\ln\frac{a_g}{b_w}-0.230\ln\frac{f_{yt}}{f_c'}-0.076\ln\rho_v+0.208\varepsilon$

Table 5-5: Evaluation of the developed models in terms of $V_{tested} / V_{predicted}$

Model	Developed model		Original model (Table 2)	
	Mean	COV	Mean	COV
ACI (Simplified)	1.0343	0.2700	2.0678	0.3894
ACI (Detailed)	1.0304	0.2590	1.5346	0.2883
AASHTO	1.0183	0.1929	1.7544	0.2298
CSA (Simplified)	1.0662	0.3760	2.8308	0.5340
CSA (Detailed)	1.0189	0.1968	1.7672	0.2415
fib	1.0227	0.2175	1.9949	0.2899

The deterministic predictions from the newly developed models are compared with the predictions from the original design code models as shown in Table 5-5. It is shown that the developed models can not only correct the inherent bias successfully, but also decrease the prediction scatter significantly, indicating the improved accuracy and precision.

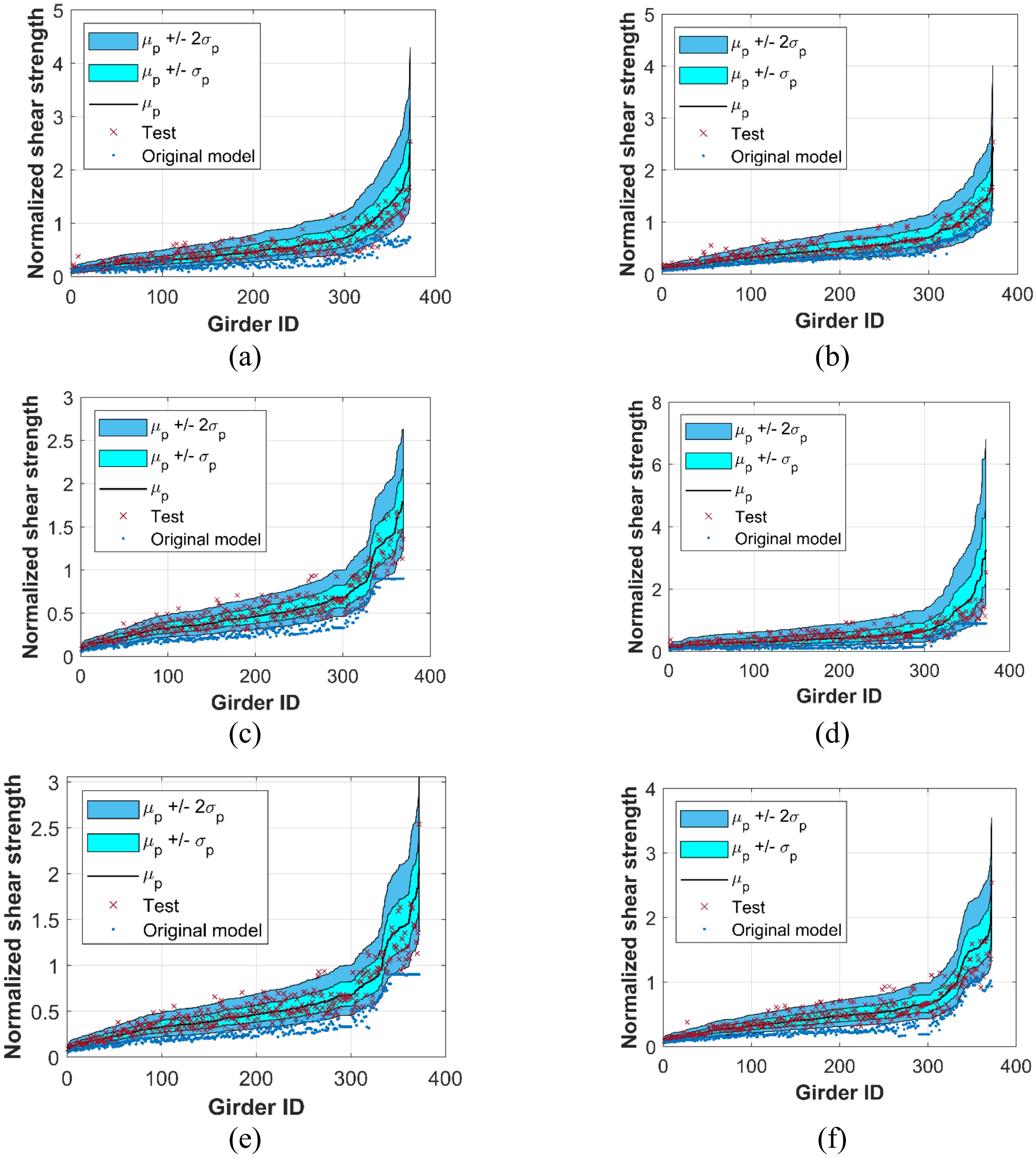

(a) (b) (c) (d) (e) (f)

Figure 5-5: Performance of the developed probabilistic models based on: (a) ACI 318-19 (Simplified method), (b) ACI 318-19 (Detailed method), (c) AASHTO LRFD 2017, (d) CSA A23.3:19 (Simplified method), (e) CSA A23.3:19/S6:19 (General method), and (f) *fib* MC 2010

The probabilistic predictions are also obtained for the PC girders in the compiled experimental database in order to further verify the performance of the developed probabilistic models. The mean values (i.e., μ_p) and confidence interval (i.e., $\mu_p \pm \sigma$, $\mu_p \pm 2\sigma$) predicted by the developed probabilistic models are shown in Figure 5-5. Note that, for the purpose of visualization, the girders from the experimental database are indexed with an increasing ID according to the mean prediction μ_p by each of the developed probabilistic models. It is observed that the predictions from original design code models show significantly conservative bias. By contrast, the mean prediction curves of all developed probabilistic models successfully represent the central tendencies of the tested shear capacity. Furthermore, the majority of the tested shear capacity fall within one or two SDs for all the models, indicating the remarkable performance of the developed probabilistic models.

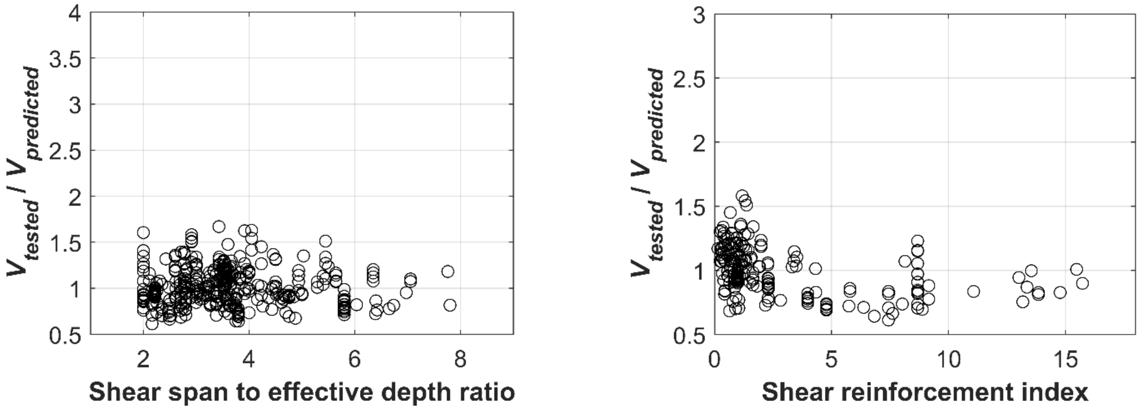

(a) (b)

Figure 5-6: Test-to-prediction ratios (V_{tested} / $V_{predicted}$) as a function of: (a) shear span to effective depth ratio a/d, and (b) shear reinforcement index $\rho_v f_{yt}$

The systematic correlations between test-to-prediction ratios $V_{tested}/V_{predicted}$ and model parameters are also studied for the developed models. Taking the developed mode based on the general method of CSA A23.3:19 for example, the test-to-prediction ratios as a function of the shear span to effective depth ratio a/d and shear reinforcement index $\rho_v f_{yt}$ are plotted as shown in Figure 5-6. It can be seen that no distinct systemic correlations can be observed, indicating that the systematic error hidden in the original design code models as shown in Figure 5-3 have been learned by the correction terms successfully.

5.5 Application to Fragility Analysis

The probabilistic shear capacity prediction models developed in this study can facilitate next-generation reliability-based code calibration and probabilistic performance assessment of PC girders. As a case study, the probabilistic model developed based on correcting the shear capacity prediction model in CSA A23.3:19 is applied to the fragility analysis of a PC girder recently tested under shear-critical loading at University of Alberta (Huang 2020; Liu et al. 2021).

This PC girder was tested with a span of 3800 mm under a single point load applied at 1000 mm from one support as shown in Figure 5-7(a). The cross section is 1220 mm in width and 510 mm in depth, having three voids with a diameter of 305 mm as shown in Figure 5-7(b). Longitudinal reinforcements consist of 20 prestressed seven-wire low relaxation strands with a diameter of 12.7 mm, seven 10M and four 25M mild steel bars. The stirrups are made of 10M reinforcement with a spacing of s = 200 mm. The effective prestress force was 64.2 kN per strand. In order to assess the probabilistic shear capacity of the PC girder considering pertinent uncertainties in material and geometric properties, fragility analysis is conducted here. The statistical parameters for the material and geometric properties of the PC girder considered are summarized in Table 5-6.

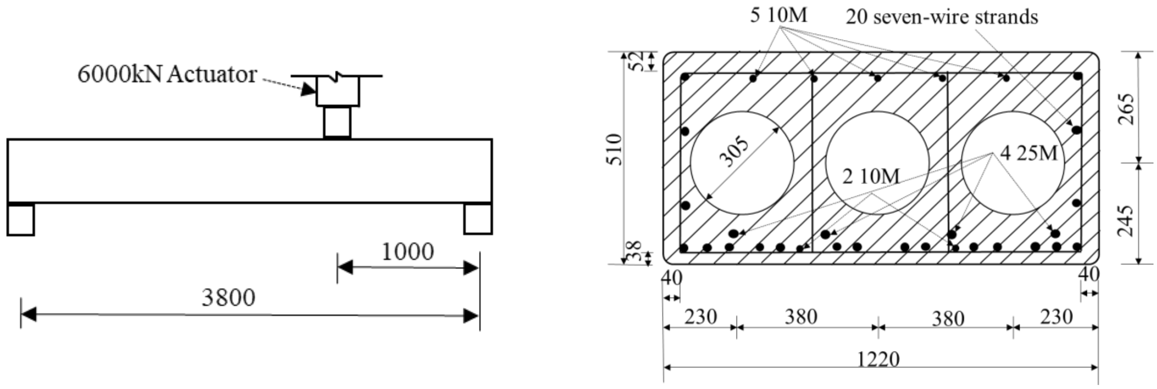

(a) (b)

Figure 5-7: Tested PC girder: (a) test setup, and (b) cross-section (units: mm)

For a structural component, fragility analysis is defined as calculating the conditional probability of attaining or exceeding a prescribed limit state for a given condition (Gardoni et al. 2002). Specifically, in this study the fragility is considered as the shear failure probability of the PC girder conditioned on a given shear demand; namely, the probability that the shear capacity $C(\mathbf{r})$ is less than or equal to a certain shear demand $D(\mathbf{s})$, as stated in Eq. (5-4),

$$F(\mathbf{s}) = P\left[\left\{C(\mathbf{r}) - D(\mathbf{s}) \le 0\right\} \middle| \mathbf{s}\right] \tag{5-4}$$

where $\mathbf{r}$ is a vector of material and geometrical variables, and $\mathbf{s}$ is an external load variable. As such, the fragility of the structural component can be used to interpret the probabilistic capacity of a PC girder.

Fragility analysis is conducted based on direct Monte Carlo simulation with a large number of samples (i.e., 10 million) for each shear demand level $D(\mathbf{s})$. For the purpose of comparison, the fragility analysis is also conducted using the original shear capacity model in CSA A23.3:19 without considering model error/uncertainty.

Table 5-6: Statistical parameters for the material and geometric properties of the PC girder considered

Parameters	Nominal	Mean	COV	Distribution	Reference
f'_c (MPa)	35	48.3	0.12	Normal	Nowak and Szerszen 2003
f_{yt} (MPa)	400	458	0.065	Normal	Nowak and Szerszen 2003
f_{pu} (MPa)	1860	1943	0.025	Normal	Nowak and Szerszen 2003
E_p (GPa)	-	195.8	0.02	Normal	Mirza et al. 1980
E_s_M10 (GPa)	-	200	0.033	Normal	Mirza et al. 1980
E_s_M25 (GPa)	-	200	0.033	Normal	Mirza et al. 1980
b_w	-	308	0.04	Normal	Nowak and Szerszen 2003
d	-	433	0.025	Normal	Nowak and Szerszen 2003

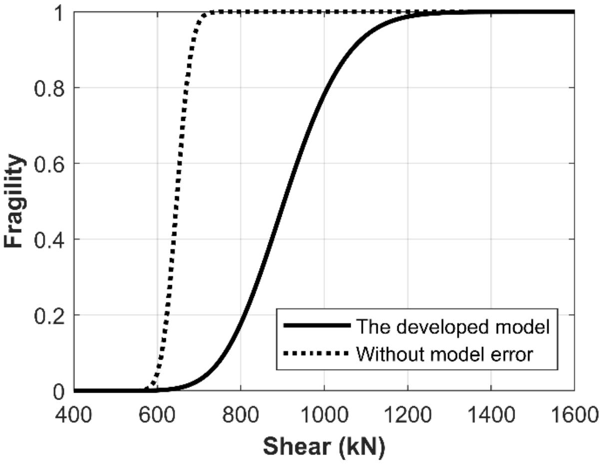

Figure 5-8: Fragility curves for shear failure of the PC girder considered

As shown in Figure 5-8, when model error/uncertainty is not considered, the shear failure probability of the PC girder considered for given loads (e.g., between 600 kN and 1200 kN) is significantly over-estimated due to the under-estimation of shear capacity. This is mainly because of the conservative bias inherent in the design code model. The comparison of the two fragility curves reveals the degree of conservatism related to the shear capacity prediction in the design code considered. To perform reliability-based code calibration and/or probabilistic performance assessment of PC girders, lack of inappropriate consideration of model error/uncertainty can lead to unreliable safety assessment. As such, model error needs to be taken into account for reliability assessment in the design and management of PC girders, and the probabilistic models developed in this study can be used for this purpose.

5.6 Summary

This chapter compiled an experimental database containing 369 PC girders that failed in shear and assessed the shear capacity models from five widely utilized concrete structure and bridge design codes, i.e., ACI 318-19, AASHTO LRFD 2017, CSA A23.3:19, CSA S6:19 and *fib* MC 2010. It is shown that although the detailed/general methods perform better than simplified methods, all design code models exhibit large conservative bias and prediction scatter. It is shown that the detailed method from ACI 318-19 exhibit the least conservatism, while the general procedure from AASHTO LRFD 2017 has the lowest prediction scatter. In addition, the best fitted distributions for professional factors of each design code models are provided in this study to facilitate its utilization in reliability analysis. It was also found that the normal distribution assumption for professional factors performs poorly despite its wide use.

In view of the fact that systematic error exists in those models, polynomial correction terms were calibrated for each design code model, together with the remaining model error quantification based on the compiled experimental database. The resulted probabilistic shear capacity prediction models have elegant formulations, which can facilitate their utilization in engineering practice. Both deterministic and probabilistic predictions can be obtained by neglecting and considering the remaining model error, respectively. Comparisons with original design code models showed that the developed models can not only correct the inherent bias successfully, but also decrease the prediction scatter significantly, indicating the improved accuracy and precision.

In the end, a case study of fragility analysis is conducted to show the benefit of the developed probabilistic models. It was shown that not considering the model error can lead to unreliable safety assessment in the design and management of PC girders and thus model error needs to be taken into account for reliability assessment, for which the probabilistic models developed can be used.

CHAPTER 6: DATA-BASED SHEAR CAPACITY MODELS FOR INTACT PC GIRDERS BY GAUSSIAN PROCESS REGRESSION

To facilitate rigorous reliability/probabilistic studies considering model uncertainty, this chapter proposed a method to quantify the error or uncertainty of existing design code models and develop probabilistic models based on Gaussian process regression (GPR). This method leverages prior knowledge inherent in existing models and high-fidelity data such as experimental observations, by modeling the discrepancy between model predictions and high-fidelity data using a Gaussian process. In this method, the discrepancy is modeled by a stochastic function of model parameters, where the model form is not restricted to a specific function class as in polynomial regression analysis. The proposed method was then applied to the shear capacity prediction of prestressed concrete (PC) girders. The model error of shear capacity models from five well-received concrete structure and bridge design codes, i.e., ACI 318-19, AASHTO LRFD 2017, CSA A23.3:19, CSA S6:19 and *fib* MC 2010, were quantified using an experimental database. Accordingly, probabilistic shear capacity prediction models were developed, whose mean predictions outperformed the corresponding deterministic design code models in both accuracy and precision. The prediction performance was further illustrated using five PC girder tests initially excluded from the experimental database used for GPR model development. The significance of the model error quantified was also demonstrated using a case study of fragility assessment of PC girders, where the model uncertainty played a significant role among all uncertainty sources.

6.1 Introduction

Various models have been developed in structural and mechanical engineering to predict responses of interest or capacities against a certain failure mode. Those models play important roles in engineering practice by providing guidance for design, maintenance, and retrofit. However, it is usually found that the developed models, particularly design code models, suffer from various degrees of inaccuracy when compared with high-fidelity model predictions or experimental results. Large prediction discrepancy (i.e., bias and scatter) can be expected for problems where the underlying physical mechanisms are complex or not well understood (Kennedy and O'Hagan 2001; Maupin and Swiler 2020), also known as model error or model uncertainty.

A typical example in structural engineering is the shear capacity prediction of concrete members, which remains as a challenging task due to the complex load transfer and failure mechanism compared with flexural capacity prediction. To address this issue, recent decades have witnessed significant efforts devoted to understanding the shear behavior of concrete, including the development of the modified compression field theory (MCFT) (Sadeghian and Vecchio 2018) and the softened truss model (STM) (Hsu and Mo 2010). However, there is still not yet a universally accepted mechanism or theory for shear capacity prediction. Especially for design code models, it was shown that shear capacity prediction suffers from non-negligible prediction discrepancy compared with high-fidelity data such as experimental observations (Tošic´ et al. 2016), which plays a significant role in the reliability analysis and code calibration of partial factors for semi-probabilistic design (Holický et al. 2016). In such instances, it is important to integrate existing models and high-fidelity data to develop probabilistic prediction models. It can leverage prior knowledge encoded in existing models and facilitate the utilization of well-received existing models (e.g., design code models) with model error considered, which can eventually benefit reliability-based studies by considering all prevailing uncertainty sources. Conventionally, this task of developing probabilistic models can be accomplished by quantifying the model error of existing models based on experimental data, while different approaches have been proposed by researchers.

One traditional approach in structural engineering is to use an independent multiplicative random variable defined as the test-to-prediction ratio (MacGregor et al. 1997; Del Vecchio et al. 2017; Sykora et al. 2018) to quantify the model error, which is also known as the professional factor. By adding this professional factor to the original model, probabilistic prediction models can be obtained to facilitate the consideration of model error. This approach assumes that the error is independent of model parameters and thus treated as random noise in model predictions. However, this assumption can be invalid and lead to unrealistic descriptions of model uncertainty. For example, it was shown that (Holický et al. 2016) the model error for design code-based shear capacity prediction of concrete sections can exhibit a functional relationship with several model parameters, such as the shear span to depth ratio and the amount of shear reinforcement.

With more high-fidelity data available from physical experiments, existing design code models can be further refined by exploring the inherent structure in the model error. As such, another modern approach to consider model error is to develop a corrector function of model parameters using polynomial regression (Kennedy and O'Hagan 2001; Maupin and Swiler 2020). To this end, Bayesian linear regression (Box and Tiao 1992) was adopted by researchers to calibrate the model error as a polynomial function of model parameters (Gardoni et al. 2002). The quantified model error was usually referred to as the correction term and added to the original model to construct a new probabilistic prediction model. It was shown that (Song et al. 2010) the resulted probabilistic model can not only correct the inherent bias, but also decrease the prediction scatter and giving insights into the sources of model error.

In the Bayesian linear regression-based approach, a series of basis functions is selected as explanatory variables or regressors. Although the simple linear function can facilitate the comprehension and application for engineers, it can not be guaranteed that the target function is well modelled by this pre-selected class. This issue can be remedied by increasing the number of model parameters considered, but the possibility of running into overfitting also increases. To avoid the restriction of the function class, alternative stochastic regression approaches such as Gaussian process regression (GPR) (Williams and Rasmussen 2006) can be adopted, where a stochastic process governs the properties of functions without assuming specific function classes.

Previous studies on GPR in structural engineering, as well as other machine learning approaches, mainly focused on developing prediction models based on data directly (Chou et al. 2020; Naderpour and Mirrashid 2020; Prayogo et al. 2020; Zhang et al. 2020; Jiang and Liang 2021; Yetilmezsoy et al. 2021). In contrast, this study developed a new method by combing existing models and experimental data based on GPR to develop probabilistic models with model error quantified. Namely, by adding the GPR-based quantified model error to the original model, the probabilistic prediction model was developed to benefit reliability analysis in engineering practice. The newly proposed method for probabilistic model development was then applied to the shear capacity prediction of prestressed concrete (PC) beams, which conventionally suffers from non-negligible prediction discrepancy and remains a challenging task. In the end, case studies of applications using the developed probabilistic model were performed to show the benefits of the developed models.

6.2 GPR-based Probabilistic Model

In many areas of scientific research, prediction models are widely utilized to describe processes and obtain quantities of interest as an efficient alternative to physical experiments. Those models can be essentially considered as explicit or implicit mathematical expressions relating one or more quantities of interest (e.g., structural responses) to a set of model parameters $\mathbf{x} = \{x_1, x_2, \cdots x_D\}^T$ (e.g., structural dimensions and material properties), where D is the total number of model parameters considered.

When comparing the model predictions with experimental observations, model errors (i.e., bias and scatter) can be expected due to the adopted simplifications and assumptions in the models, especially for the problems with complex underlying physical mechanisms. Conventionally, the model error can be considered as a random variable δ as shown in Eq. (6-1),

$$\delta = R(\mathbf{x}) / M(\mathbf{x}) \tag{6-1}$$

where $R(\mathbf{x})$ is the real structural response estimated from experimental observations, $M(\mathbf{x})$ is the predicted structural response from the existing model considered. Based on an experimental database, the statistic information for this random variable δ can be quantified, e.g., distribution type and parameters. By adding this quantified model error term to the original models as a multiplicative factor, probabilistic prediction models are obtained with quantified model error to benefit reliability-based studies.

This approach develops probabilistic prediction models by integrating existing deterministic models and the quantified model error. It can leverage prior knowledge encoded in existing models and facilitate the utilization of well-received existing models (e.g., design code models) with model error considered. However, this model error quantification approach highly relies on the assumption that there is no systematic correlation between the model error δ and model parameters $\mathbf{x}$. However, this assumption is often violated in engineering practice, especially when the models were developed empirically with limited observations or experimental data. Due to the imperfection of developed prediction models, the prediction residual δ can be correlated with model parameters $\mathbf{x}$ with different degrees. For example, it was shown that (Holický et al. 2016) the model error for design code-based shear capacity prediction can exhibit a functional relationship with several model parameters including shear span to depth ratio and the amount of shear reinforcement.

To consider the systematic correlation, in this study, the probabilistic model is also developed by combining existing models and the quantified model error but the model error $\delta(\mathbf{x})$ is considered as a function of model parameters based on GPR as shown in Eq. (6-2), where a stochastic process governs the properties of the function without assuming specific function classes.

$$\delta(\mathbf{x}) = R(\mathbf{x}) - M(\mathbf{x}) \sim GP\left(m(\mathbf{x}), k(\mathbf{x}, \mathbf{x}')\right) \tag{6-2}$$

Here, $m(\mathbf{x})$ and $k(\mathbf{x}, \mathbf{x}')$ are the mean and covariance function of a Gaussian process, based on which a Gaussian process is completely specified. The mean function is generally taken to be zero simplicity assuming that no prior information on the mean trend is available (Williams and Rasmussen 2006) as shown in Eq. (6-3) and squared exponential covariance function is adopted in this study as shown in Eq. (6-4).

$$m(\mathbf{x}) = 0 \tag{6-3}$$

$$k(\mathbf{x}_i, \mathbf{x}_j) = \sigma_f{}^2 \exp\left(-\frac{1}{2}(\mathbf{x}_i - \mathbf{x}_j)^T \mathbf{M}(\mathbf{x}_i - \mathbf{x}_j)\right) + \sigma_{\text{noise}}^2 \delta_{ij} \tag{6-4}$$

Here, $\mathbf{x}_i$ and $\mathbf{x}_j$ are input vector pairs, $i, j \in \{1, 2, \cdots, N\}$ where N is the total number of input vectors, $\sigma_f{}^2$, $\mathbf{M}$ and σ_{noise}^2 are the hyperparameters of the covariance function, $\sigma_f{}^2$ is the signal variance, $\mathbf{M} = \operatorname{diag}(\mathbf{l})^{-2}$ is a symmetric matrix, $\mathbf{l} = (l_1, \cdots, l_D)$ is a vector of characteristic length-scales, σ_{noise}^2 is the noise variance and δ_{ij} is a Kronecker delta, which is one if $i = j$ and zero otherwise. Note that considering σ_{noise}^2 in covariance functions enables the GPR to develop a model from training samples with random variations (e.g., the natural randomness in the compiled experimental database in this study), leading to a GPR-based model with more generalization capacities but without overfitting concerns.

For each existing model considered, the hyperparameter values can be learned based on a compiled experimental database (i.e., training samples). With the learned hyperparameters, a Gaussian process model is developed for quantifying the model error $\delta(\mathbf{x})$ as shown in Eqs. (6-2) ~ (6-4). This learning process is achieved by the maximum a posterior (MAP) estimation (Salvatier et al. 2016) in this study. Based on the quantified model error $\delta(\mathbf{x})$, the probabilistic prediction model $M_p(\mathbf{x})$ can be resulted by adding $\delta(\mathbf{x})$ to the original model prediction $M(\mathbf{x})$ as a correction term, see Eq. (6-5).

$$M_p(\mathbf{x}) = M(\mathbf{x}) + \delta(\mathbf{x}) \tag{6-5}$$

For structural response prediction of new PC girders beyond the experimental database (i.e., testing samples), the prediction of correction term $\boldsymbol{\delta}_*$ can be obtained as the conditional distribution in Eq. (6-6).

$$\boldsymbol{\delta}_* \,|\, \mathbf{X}, \boldsymbol{\delta}, \mathbf{X}_* \sim N\left(\overline{\boldsymbol{\delta}}_*, \operatorname{cov}(\boldsymbol{\delta}_*)\right) \tag{6-6}$$

where,

$$\overline{\boldsymbol{\delta}}_* = \mathbf{K}(\mathbf{X}_*, \mathbf{X})\left[\mathbf{K}(\mathbf{X}, \mathbf{X}) + \sigma_{\text{noise}}^2 \mathbf{I}\right]^{-1} \boldsymbol{\delta} \tag{6-7}$$

$$\operatorname{cov}\left(\boldsymbol{\delta}_*\right)=\mathbf{K}\left(\mathbf{X}_*,\mathbf{X}_*\right)-\mathbf{K}\left(\mathbf{X}_*,\mathbf{X}\right)\left[\mathbf{K}\left(\mathbf{X},\mathbf{X}\right)+\sigma_{\text{noise}}^2\mathbf{I}\right]^{-1}\mathbf{K}\left(\mathbf{X},\mathbf{X}_*\right) \tag{6-8}$$

Here, $\mathbf{X}$ and $\mathbf{X}_*$ are the input parameter matrices from training and testing samples, respectively, $\boldsymbol{\delta}$ and $\boldsymbol{\delta}_*$ are the vectors of correction term outputs for training and testing samples, respectively, $\mathbf{I}$ is the identity matrix, $\mathbf{K}\left(\mathbf{X}_*,\mathbf{X}\right)$ is the covariance matrix evaluated at all pairs of testing and training points, and similarly for the other entries $\mathbf{K}\left(\mathbf{X},\mathbf{X}\right)$, $\mathbf{K}\left(\mathbf{X},\mathbf{X}_*\right)$ and $\mathbf{K}\left(\mathbf{X}_*,\mathbf{X}_*\right)$.

With the obtained correction term prediction $\boldsymbol{\delta}_*$ for testing samples, the structural response prediction from the developed probabilistic model can be obtained as shown in Eq. (6-9),

$$\mathbf{M}_{p*}=\mathbf{M}_*+\boldsymbol{\delta}_* \tag{6-9}$$

where $\mathbf{M}_{p*}$ is the vector of structural response predictions for testing samples from the developed probabilistic model, $\mathbf{M}_*$ is the vector of structural response predictions for testing samples from the original model considered.

6.3 Probabilistic Model Development for Shear Capacity Prediction of PC Girders

Recent decades have witnessed significant efforts devoted to understanding shear behavior and/or predicting shear capacity of concrete beams. However, there is not yet a universally accepted mechanism or theory for shear capacity prediction. Compared with flexural capacity prediction, shear capacity prediction still remains a challenging task and suffers from non-negligible prediction model error nowadays.

Data-based shear capacity models using machine learning approaches can be an attractive alternative and have been successfully applied to reinforced concrete (RC) beams/walls in recent years (Chou et al. 2020; Naderpour and Mirrashid 2020; Prayogo et al. 2020; Zhang et al. 2020;

Jiang and Liang 2021), while there is still a gap in the relevant research area for PC girders. In addition, instead of developing new models purely based on data from the ground up, prior knowledge inherent in existing models can be utilized by combining with the quantified model error. To this end, the proposed GPR-based approach of developing probabilistic prediction models is applied to the shear capacity prediction of PC girders. Specifically, five existing shear capacity prediction models for PC girders were considered in this study. The model error of considered models were qualitatively diagnosis first and then quantified based on a compiled experimental database of PC girders that failed in shear. GPR-based probabilistic shear capacity prediction models were then developed by combining the original existing model and the quantified model error.

6.3.1 Shear Capacity Models and Experimental Database

Among various types of the developed shear capacity prediction models by researchers, design code models might possibly be the most widely utilized worldwide due to their comprehensible simplicity, high computational efficiency and well-recognised authority. Shear capacity models from five concrete structure and bridge design codes are considered in this study, i.e., ACI 318-19 (ACI 2019), AASHTO LRFD 2017 (AASHTO 2017), CSA A23.3:19 (CSA 2019a), CSA S6:19 (CSA 2019b) and *fib* MC 2010 (*fib* 2013). Note that each design code includes more than one shear capacity models with different levels of simplification, while only the most advanced models from each design code are considered in this study.

The compiled experimental database in Chapter 3 is utilized in this chapter to quantify the model error of considered shear capacity models and develop probabilistic prediction models based on Gaussian process regression. It is interesting to mention that some existing experimental databases are publicly available for RC beams that failed in shear such as the ACI-DAfStb database

(Reineck et al. 2013; Reineck et al. 2014). However, the shear behavior between RC and PC beams can differ from each other with the adoption of higher strength concrete and prestressed strands in PC girders. Thus, a new compiled experimental database in Chapter 3 for PC girders that failed in shear is utilized in this study.

6.3.2 Model Error Diagnosis

Based on the compiled experimental database, the performance of the considered shear capacity models is studied qualitatively in this section before the model error quantification. Note that the concrete and steel material properties are used as the tested values without material reduction factors or other safety factors for fair comparisons. The comparisons between tested and predicted shear capacity for each design code models are plotted in Figure 6-1. For the purpose of better visualization, a normalization factor of $0.25 f_c' b_w d$ is adopted to normalise the tested and predicted shear capacity in this study, where f_c' is the concrete compressive strength, b_w is the web width, d is the effective depth. It can be seen that all design code models exhibit significant conservative bias. Large prediction scatter is also observed, which can play an important role in reliability analysis among all sources of uncertainties.

To determine whether the model error can be considered as an independent random variable, the correlations between the model error and different model parameters are also studied. Correlation coefficients are first obtained and summarized in Table 6-1 to study the potential linear relationship between the model error observation $V_{tested}/V_{predicted}$ and model parameters, where a/d is the shear span to effective depth ratio, b_w/h is the ratio between web width and sectional height, f_c' is the concrete compressive strength, f_{yt} is the stirrups' yield strength, $\rho_l = \left(A_s + A_{ps}\right)/b_w d$ is the tensile longitudinal steel ratio, A_s and A_{ps} are the areas of non-prestressed and prestressed tensile longitudinal steel respectively, $\rho_v = A_v / b_w s$ is the stirrups ratio, A_v is the stirrups area, s is the stirrups spacing, f_{se} / f_{pu} is the ratio between effective stress and tensile strength of prestressed steel.

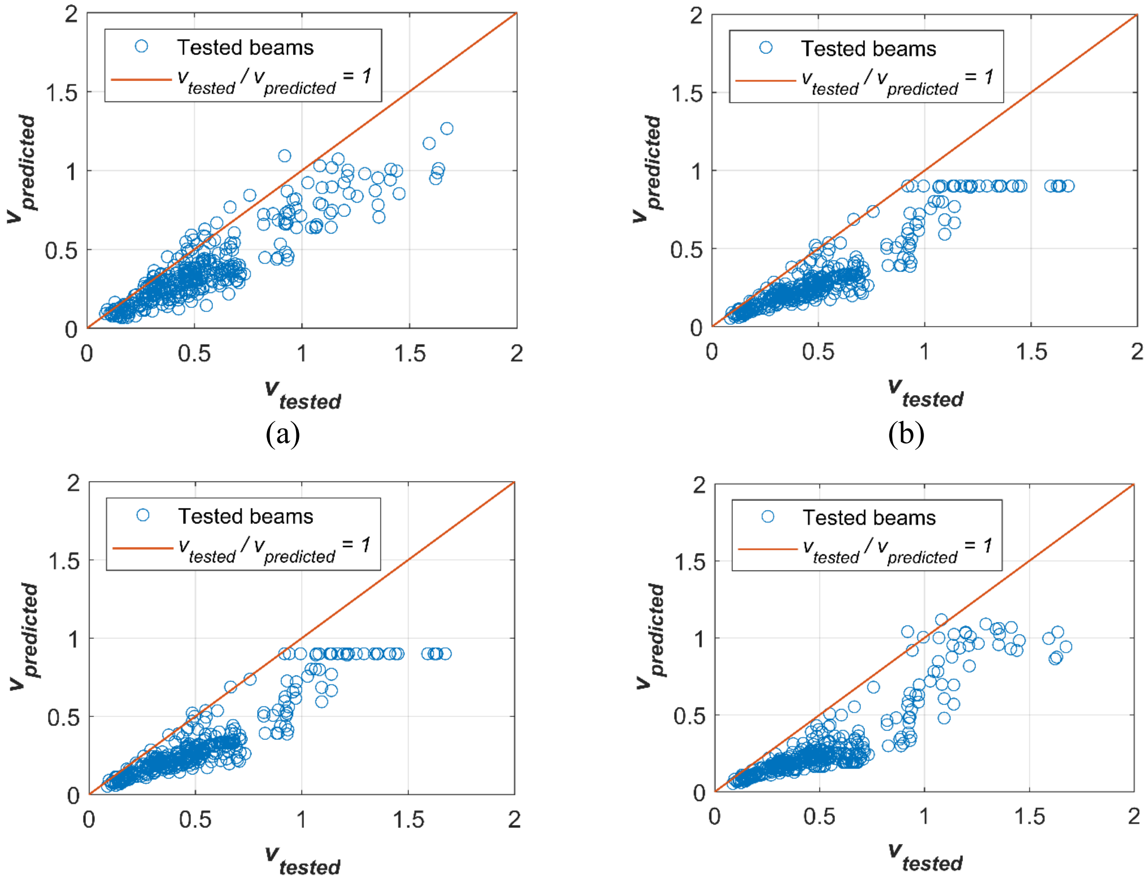

(a) (b)

(c) (d)

Figure 6-1: Comparison between tested and predicted normalized shear capacity based on: (a) ACI 318-19, (b) AASHTO LRFD 2017, (c) CSA A23.3:19/S6:19, and (d) *fib* MC 2010

Table 6-1: Correlation coefficients between $V_{tested} / V_{predicted}$ and model parameters

Parameter	a/d	b_w/h	f'_c	f_{yt}	ρ_l	ρ_v	f_{se}/f_{pu}
ACI	-0.166	0.095	-0.142	0.218	-0.022	-0.045	-0.103
AASHTO	-0.342	-0.104	-0.097	0.012	-0.154	-0.447	-0.121
CSA	-0.336	-0.104	-0.103	0.012	-0.150	-0.441	-0.127
fib	-0.343	-0.187	0.212	0.136	-0.077	-0.539	0.064

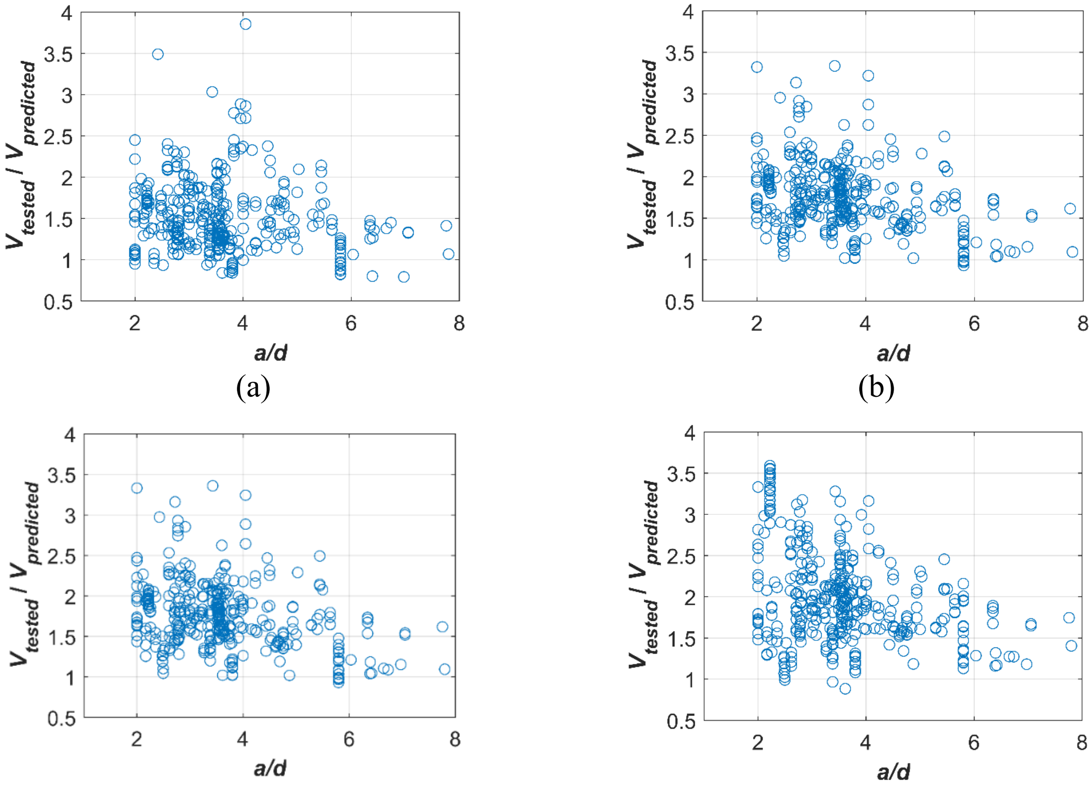

(a) (b)

(c) (d)

Figure 6-2: Test-to-prediction ratios V_{tested} / $V_{predicted}$ as a function of shear span to effective depth ratio a/d from the original model of: (a) ACI 318-19, (b) AASHTO LRFD 2017, (c) CSA A23.3:19/S6:19, and (d) *fib* MC 2010

It can be seen that the most two important influencing parameters are a/d and ρ_v, while other parameters exhibit relatively week linear correlations with the model error. Since the correlation coefficient only represents the linear correlation degree, scatter plots between the model error observation $V_{tested}/V_{predicted}$ and model parameters are also obtained as shown in Figure 6-2 and Figure 6-3 to study potential nonlinear correlations. It can be seen that the model error exhibits a functional relationship with both a/d and $\rho_v f_{yt}$. Thus, it is not reasonable to assume the model error as an independent random variable, and such systematic error (trend) hidden should be learned as a regression function of model parameters as discussed in this study.

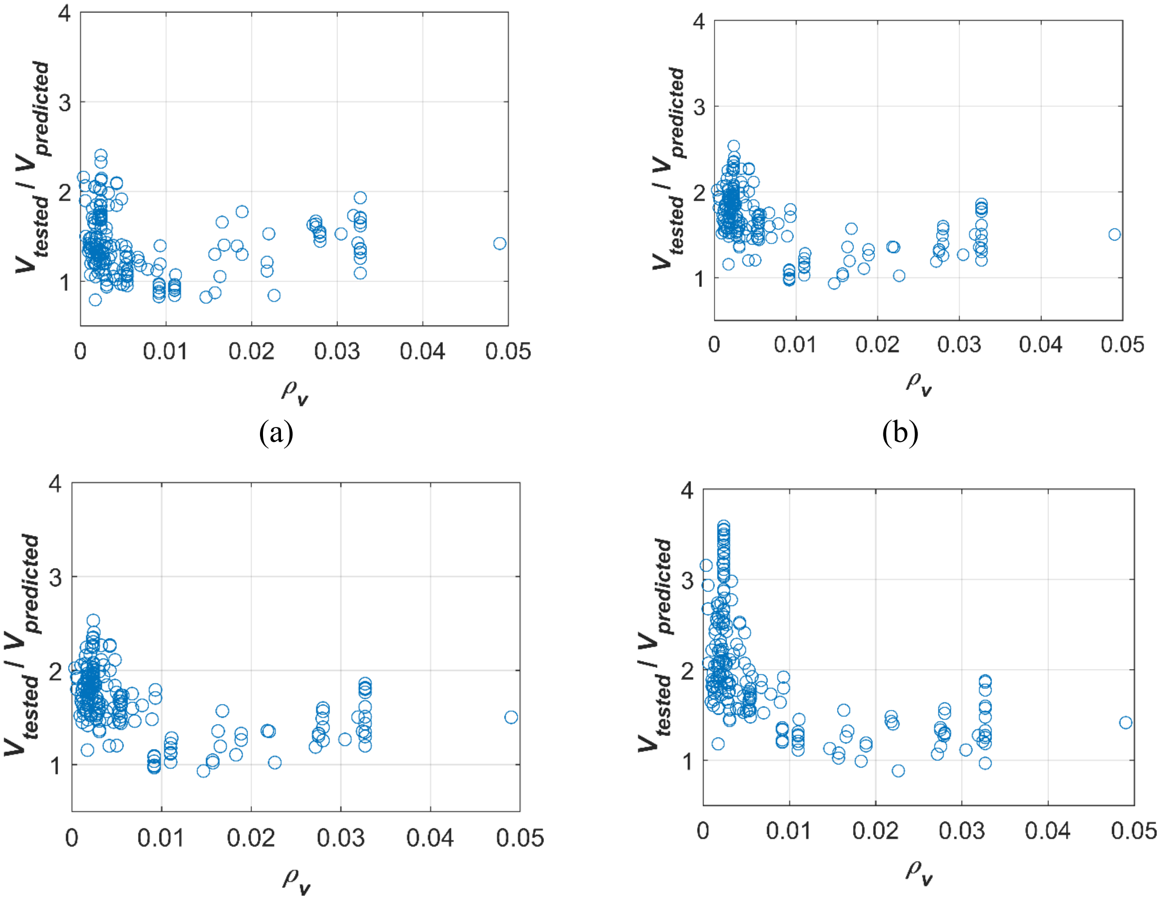

(a) (b) (c) (d)

Figure 6-3: Test-to-prediction ratios V_{tested} / $V_{predicted}$ as a function of stirrups ratio ρ_v from the original model of: (a) ACI 318-19, (b) AASHTO LRFD 2017, (c) CSA A23.3:19/S6:19, and (d) *fib* MC 2010

It is interesting to mention that although the correlation coefficient between $V_{tested}/V_{predicted}$ and ρ_v is relatively small for ACI 318-19, there is an evident functional relationship between them as shown in Figure 6-3 (a). This is because the correlation coefficient can only indicate linear correlation degree which fails to detect the potential nonlinear correlation.

6.3.3 Model Error Quantification

To quantify the model error of the considered shear capacity models, GPR is adopted as discussed, see Eq. (6-10),

$$\delta(\mathbf{x}) = v_t(\mathbf{x}) - v(\mathbf{x}) \sim GP\big(m(\mathbf{x}), k(\mathbf{x}, \mathbf{x}')\big) \tag{6-10}$$

where $v_t(\mathbf{x})$ is the normalized shear capacity estimated from the experimental test, $v(\mathbf{x})$ is the normalized shear capacity prediction from the shear capacity models considered. In this study, a comprehensive set of dimensionless model parameters are considered as shown in Eq. (6-11),

$$\mathbf{x} = \left\{a/d, b_w/h, f_c'/35, f_{yt}/415, \rho_l, \rho_v, f_{se}/f_{pu}\right\}^T \tag{6-11}$$

where the normalization factor for f_c' of 35 MPa is the minimum concrete strength value specified by CSA S6:19 for prestressed members, the normalization factor for f_{yt} of 415 MPa is a typical yield strength of steel, e.g., the ASTM A572 Grade 60 steel.

For each shear capacity model considered, based on the compiled experimental database (i.e., training samples), the optimal hyperparameters for each Gaussian process model are learned by the MAP estimation (Salvatier et al. 2016), and then the model error is quantified. The learned hyperparameters for each model are summarised in Table 6-2.

Table 6-2: Learned hyperparameters values

Models	σ_f	σ_{noise}	l_1	l_2	l_3	l_4	l_5	l_6	l_7
ACI 318-19	0.1966	0.0582	0.8793	0.2509	1.8073	6923.3	0.0465	0.0098	0.2460
AASHTO LRFD 2017	0.2277	0.0697	3.5577	0.2647	3.5540	0.2530	0.0223	0.1038	0.7813
CSA A23.3:19/S6:19	0.2422	0.0586	1.5354	0.8599	3.1666	6556.3	0.0277	0.0105	0.2433
fib MC 2010	0.2130	0.0555	0.7455	0.3678	2.4820	8.6932	0.0271	0.0093	0.1904

6.3.4 Probabilistic Prediction Models

Based on the quantified model error $\delta(\mathbf{x})$, the probabilistic shear capacity prediction model can be obtained by adding $\delta(\mathbf{x})$ as a probabilistic correction term to the corresponding deterministic design code model, see Eq. (6-12),

$$v_p(\mathbf{x}) = v(\mathbf{x}) + \delta(\mathbf{x}) \tag{6-12}$$

where $v_p(\mathbf{x})$ is the normalized shear capacity prediction from the developed probabilistic model.

It is interesting to note that both mean (deterministic) and distribution (probabilistic) predictions can be obtained by the developed model, which can benefit the shear capacity evaluation in engineering practice both deterministically and probabilistically. Based on the compiled experimental database, the mean predictions from the developed models are compared with the predictions from the original deterministic design code models in terms of test-to-prediction ratio $V_{tested}/V_{predicted}$ as shown in Table 6-3. It is shown that the developed models can not only correct the inherent bias of the original design code models successfully, but also decrease the prediction scatter significantly, i.e., the coefficient of variation (COV), indicating the improved accuracy and precision.

Table 6-3: Evaluation of the developed models in terms of $V_{tested} / V_{predicted}$

Models	Original model		Developed model	
	Mean	COV	Mean	COV
ACI 318-19	1.535	0.288	0.999	0.100
AASHTO LRFD 2017	1.754	0.230	0.998	0.111
CSA A23.3:19/S6:19	1.767	0.242	0.999	0.105
fib MC 2010	1.995	0.289	0.999	0.090

The distribution predictions from the developed models including both the mean prediction (i.e., μ_p) and confidence interval (i.e., $\mu_p \pm \sigma$) are also obtained and shown in Figure 6-4, together with the predictions from each original deterministic design code model and the tested shear capacity. It is shown that the predictions from the original deterministic design code models show significant conservative bias. By contrast, the mean prediction curves of all developed models successfully represent the central tendencies of the tested shear capacity. Also, the majority of the tested shear capacity fall within the mean ± 1 standard deviation (SD) intervals for all the models, indicating the capability of the developed models serving as reliable shear capacity prediction tool for PC girders.

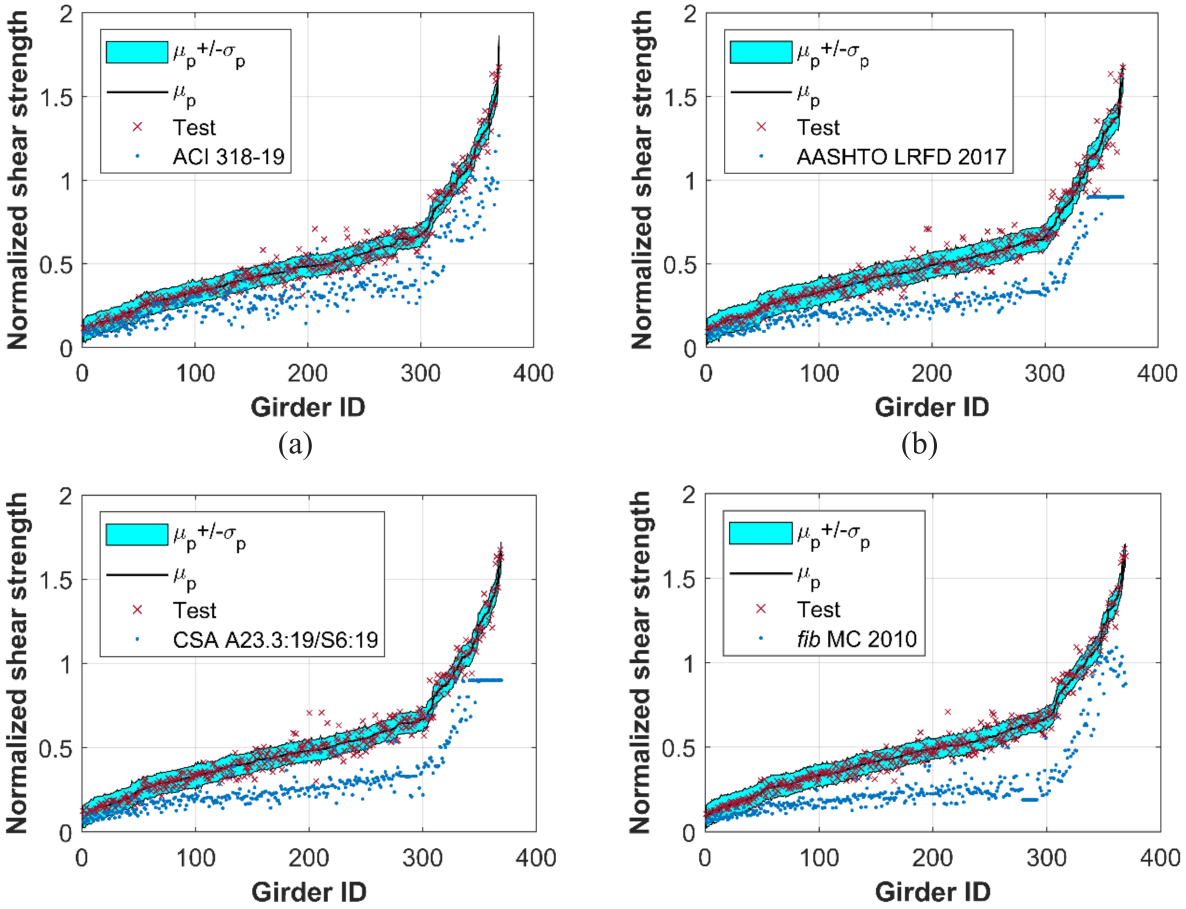

(c) (d)

Figure 6-4: Performance of the developed probabilistic models based on: (a) ACI 318-19, (b) AASHTO LRFD 2017, (c) CSA A23.3:19/S6:19, and (d) *fib* MC 2010

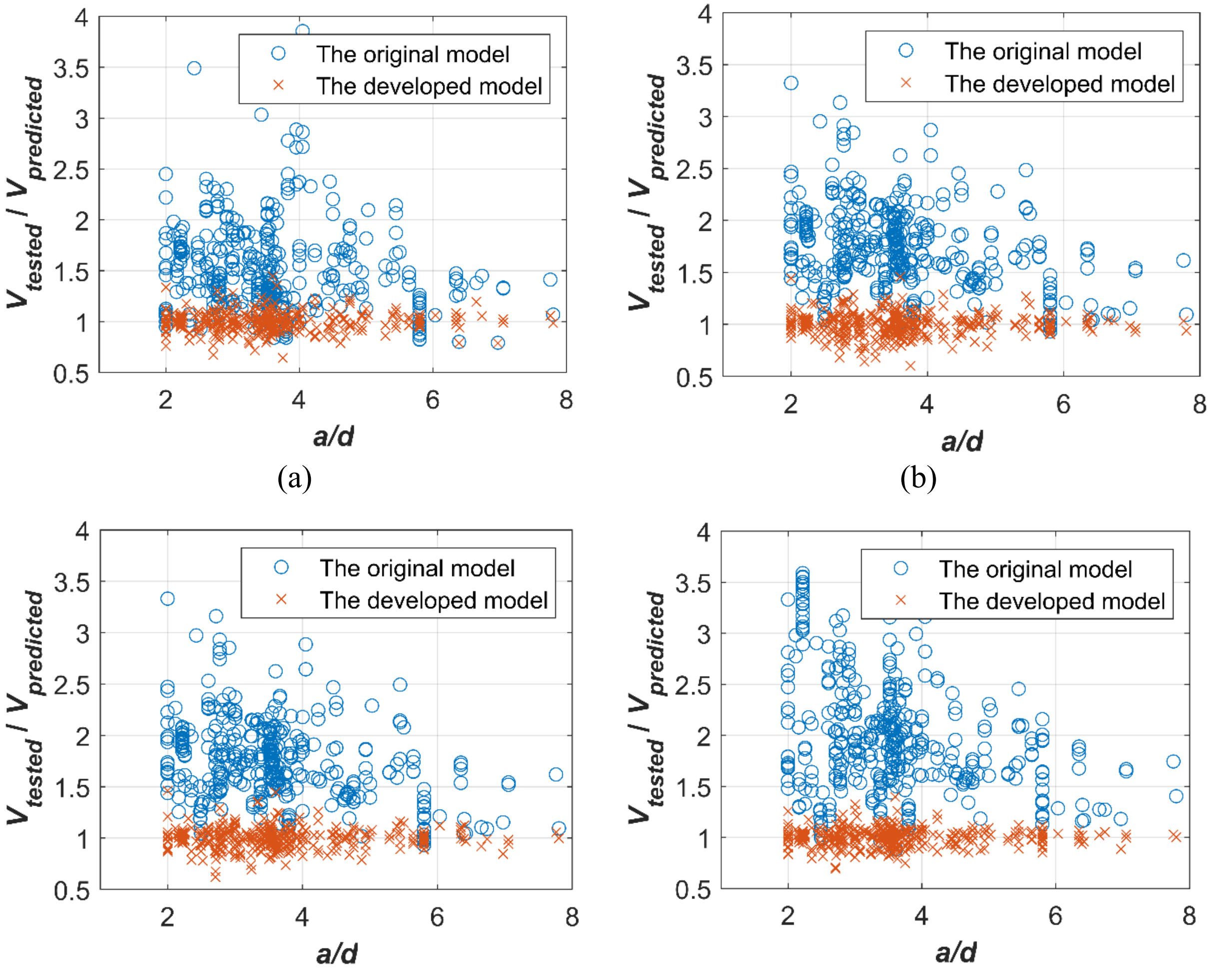

(a) (b) (c) (d)

Figure 6-5: Test-to-prediction ratios $V_{tested} / V_{predicted}$ as a function of shear span to effective depth ratio a/d from the original and developed models based on: (a) ACI 318-19, (b) AASHTO LRFD 2017, (c) CSA A23.3:19/S6:19, and (d) *fib* MC 2010

The systematic correlations between the model error observations (i.e., test-to-prediction ratios $V_{tested}/V_{predicted}$) and model parameters are also studied for the developed models. The test-to-prediction ratios as a function of the shear span to effective depth ratio a/d and stirrups ratio ρ_v are plotted as shown in Figure 6-5 and Figure 6-6, respectively. It can be seen that no distinct systemic correlations can be observed from the developed models, indicating that the systematic error hidden in the original design code models have been learned successfully by the correction terms. This also implies that the model errors of existing design code models for shear capacity prediction mainly arise from these two variables: the shear span to effective depth ratio a/d and stirrups ratio ρ_v, and more experimental tests in this regard should be conducted to further verify this.

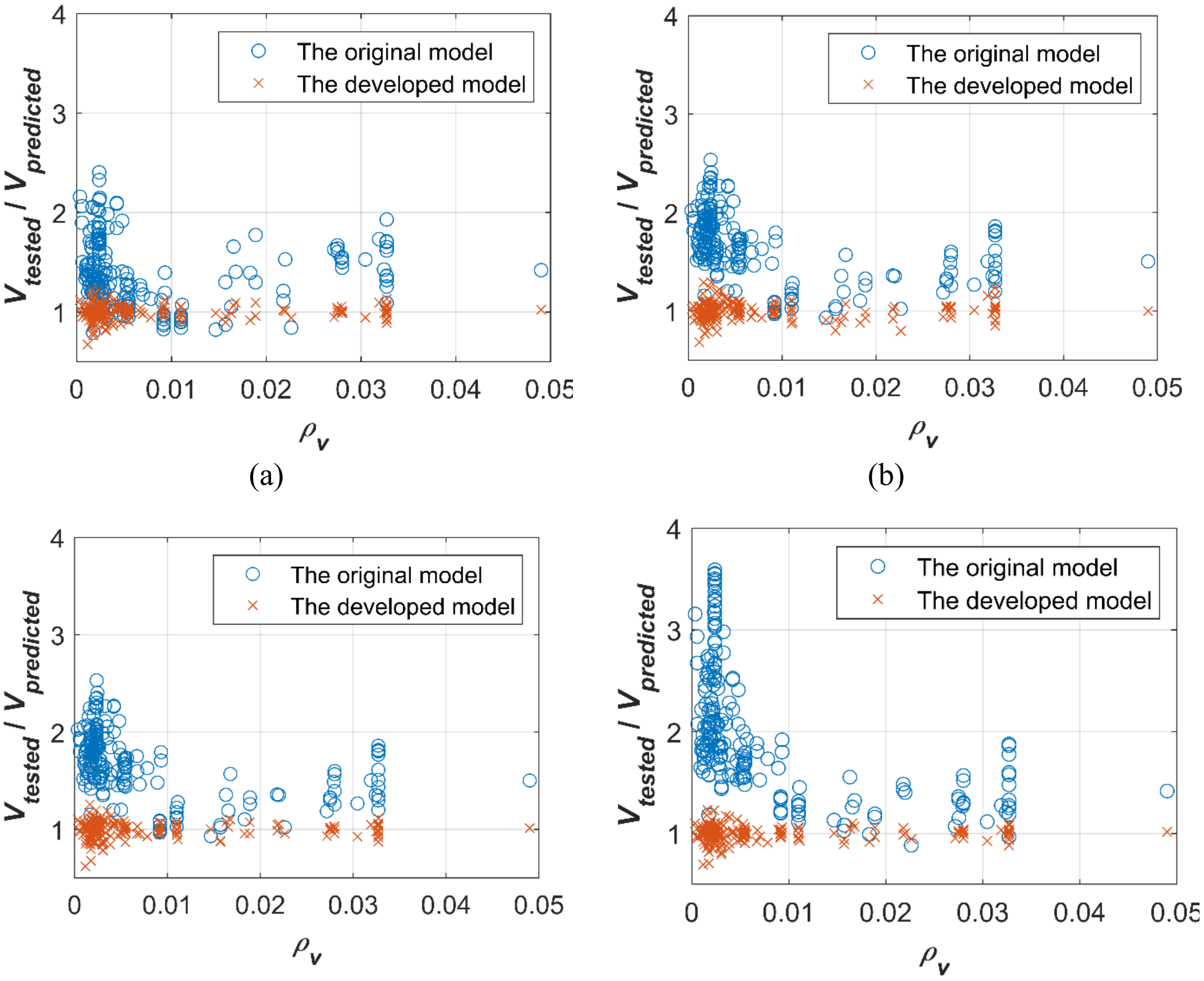

(a)

(b)

(c)

(d)

Figure 6-6: Test-to-prediction ratios V_{tested} / $V_{predicted}$ as a function of stirrups ratio ρ_v from the original and developed models based on: (a) ACI 318-19, (b) AASHTO LRFD 2017, (c) CSA A23.3:19/S6:19, and (d) *fib* MC 2010

6.4 Application of the Developed Probabilistic Models

To verify the benefits of the developed probabilistic shear capacity models, take the developed model based on *fib* MC 2010 for example, two case studies are conducted in this section, i.e., (1) shear capacity prediction for girders tested but not used earlier in the probabilistic model development and (2) fragility analysis to expose the importance of the model uncertainty in reliability analysis.

6.4.1 Shear Capacity Prediction

Five representative tested PC girders that failed in shear from three different research projects (Naito et al. 2005; Ramirez and Aguilar 2005; Liu et al. 2021) beyond the compiled experimental database are utilized as testing samples in this study. Note that these 5 girders are randomly selected from the available test dataset in the literature. A brief summary of the five PC girder tests is listed in Table 6-4. It can be seen that the five PC girders exhibit a good coverage of sectional and material properties, and thus can be considered as representative examples for shear capacity prediction. Note that the three research projects (Naito et al. 2005; Ramirez and Aguilar 2005; Liu et al. 2021) conducted more than five PC girder tests in total, while only PC girders that failed in shear are considered in this study.

Table 6-4: Summary of the five PC girder tests considered

No.	Reference	Specimen I.D.	Cross section	a/d	b_w/h	f'_c (MPa)	f_{yt} (MPa)	ρ_l	ρ_v	f_{se}/f_{pu}
1	Naito et al. (2005)	Test 2	I	2.37	0.16	61.6	454	1.47%	1.90%	0.56
2	Naito et al. (2005)	Test 4	I	2.37	0.16	63.3	454	1.47%	1.90%	0.54
3	Ramirez and Aguilar (2005)	13.3-5.1-326P	I	3.59	0.21	92.0	586	6.14%	0.37%	0.82
4	Ramirez and Aguilar (2005)	16.2-5.1-326P	I	3.59	0.21	111.4	586	6.14%	0.37%	0.82
5	Liu et al. (2021)	N/A	Box	2.31	0.60	55.5	424	3.01%	0.66%	0.35

The mean predictions from the developed model based on *fib* MC 2010 are listed in Table 6-5 and compared with the predictions from the original deterministic model. It can be seen that the original deterministic model significantly under-predicts the shear capacities for all tested PC girders, while the mean predictions from the developed model exhibit satisfactory accuracy. The distribution predictions from the developed model are also summarised in Table 6-5. It can be seen that the tested shear capacity all falls within the mean ± 1 SD interval predicted from the developed model.

Table 6-5: Shear capacity prediction comparison (kN)

No.	V_{tested}	Original model		Developed model		
		$V_{predicted}$	$V_{tested}/V_{predicted}$	$V_{predicted}$	$V_{tested}/V_{predicted}$	$\mu_p \pm \sigma_p$
1	2151.5	1427.0	1.508	2128.9	1.011	[1747.8, 2510.0]
2	2174.2	1413.1	1.539	2091.6	1.039	[1689.4, 2493.7]
3	800.2	449.8	1.779	824.3	0.971	[382.4, 1266.2]
4	955.9	455.0	2.101	793.1	1.205	[241.6, 1344.7]
5	1036.2	603.2	1.718	891.1	1.163	[604.9, 1177.3]

6.4.2 Fragility Analysis

The developed probabilistic models enable the consideration of model error/uncertainty, and thus can facilitate probabilistic performance assessment of PC girders. As a case study, the developed model based on *fib* MC 2010 is applied to the fragility analysis of the No. 1 PC girder considered in this study, i.e., the Test 2 from Naito et al. (2005).

Fragility analysis is conducted based on direct Monte Carlo simulation with a large number of samples (i.e., 10 million) for each shear demand level. For the purpose of comparison, the fragility analysis is also conducted using the original shear capacity model from *fib* MC 2010 without considering model error/uncertainty. The statistical parameters for the material and geometric properties of the PC girder considered are summarized in Table 6-6.

Table 6-6: Statistical parameters of the PC girder considered

Parameters	Tested	Nominal	Mean	CV	Distribution	Reference
f_c' (MPa)	61.6	55.1	60.3	0.09	Normal	Nowak and Szerszen (2003)
f_{yt} (MPa)	453.7	420	465.1	0.04	Normal	Nowak and Szerszen (2003)
f_{pu} (MPa)	1953.2	1860	1943	0.025	Normal	Nowak and Szerszen (2003)
E_p (GPa)	199.9	-	195.8	0.02	Normal	Mirza et al. (1980)
b_w	177.8	-	179.6	0.04	Normal	Nowak and Szerszen (2003)
d	986.3	-	986.3	0.025	Normal	Nowak and Szerszen (2003)

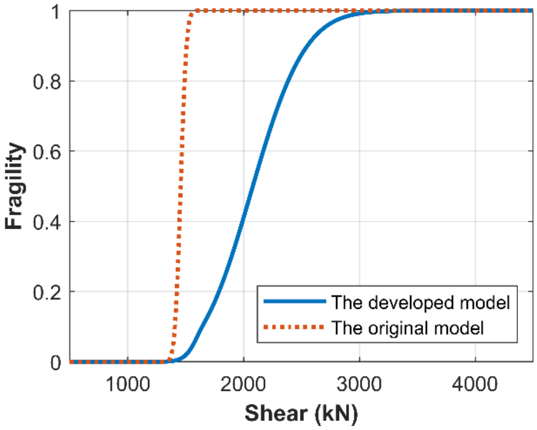

Figure 6-7: Fragility curves for shear failure of the PC girder considered

As shown in Figure 6-7, the shear failure probability curve obtained by the original design code model shows significant overestimation for given loads (e.g., between 1500 kN and 3000 kN) and exhibit narrower width compared with that of the developed model. This is due to the neglection of conservative bias and prediction scatter (i.e., model error/uncertainty) in the original design code model respectively, which plays a significant role among all uncertainty sources in this numerical example. In such cases, the neglection of model error can result in unrealistic reliability assessment results and eventually lead to inappropriate decision made for bridge design and management. Thus, the model error needs to be taken into account for reliability assessment of PC girders, and the developed probabilistic models in this study can be used for this purpose.

6.5 Summary

A methodology to develop probabilistic models was proposed by integrating existing models and experimental database based on GPR in this study. The proposed methodology represents the model error by a stochastic function of model parameters, where the model form is not restricted to a pre-selected function class as in polynomial regression analysis. The probabilistic model is then developed by adding the GPR-based quantified model error to the existing model to benefit reliability-based studies in engineering practice.

The proposed methodology was applied to developing probabilistic models for shear capacity prediction of PC girders. Firstly, the model errors from five concrete structure and bridge design codes were quantified, including ACI 318-19, AASHTO LRFD 2017, CSA A23.3:19, CSA S6:19 and *fib* MC 2010. Probabilistic shear capacity prediction models were then developed by combing the corresponding deterministic design code model and the GPR-based correction term. Comparison studies showed that the mean predictions from the developed probabilistic model outperformed the corresponding deterministic design code model in both accuracy and precision. It was also shown that the systemic correlation between the model error and model parameters in the original deterministic design code model has been learned successfully by the GPR-based correction term.

The prediction performance was further illustrated using five PC girder tests randomly selected but initially excluded from the experimental database used for GPR. It was shown that the original deterministic design code model significantly under-predicts the shear capacity for all PC girders considered, while the predictions from the developed probabilistic model exhibit satisfactory accuracy and precision. In the end, a case study of fragility analysis is conducted to show the benefit of the developed models in reliability assessment. It was shown that not considering the model error can lead to unreliable results in bridge design and management. Thus, model error needs to be taken into account for reliability assessment, for which the developed probabilistic models can be used.

CHAPTER 7:DATA-BASED LOAD-CARRYING CAPACITY MODELS FOR PC VOIDED GIRDERS UNDER VARIOUS CORROSION CONDITIONS

This chapter aims at developing data-based prediction models to quantify corrosion effects on load-carrying capacity of PC girders that are precast and standardized for short-span bridges. To develop data-based prediction models, generating sufficient data through physical experimental tests of full-scale corroded PC girders is prohibitively costly. Thus, a virtual experimental database is generated numerically using two-dimensional continuum-based finite element (FE) models for corroded PC girders, after being validated using 9 corroded PC girders tested in the literature with flexure or shear failure. To this end, a total of 4,165 PC girders under point loading are simulated to consider various design, loading, and corrosion conditions to estimate their load-carrying capacities. With this database, Gaussian process regression is used to develop (1) a capacity reduction model, and (2) load-carrying capacity prediction model. The application results of the two models enable engineers to quantify the corrosion effect on PC girders in terms of (1) reduction in load-carrying capacity and (2) increase in probability of failure.

7.1 Introduction

Highway bridges represent an integral part of the transportation network and contributes significantly to the resilience of infrastructure system and socio-economic development. The superstructure of bridges takes various forms, among which, prestress concrete (PC) girders have been commonly used and constitute more than 50% of the bridge inventory in North America (Dunker and Rabbat 1993). In particular, precast PC voided girders (with hollow cores) have been used extensively for short-span bridges in North America due to its ease of fabrication and fast speed of construction. This is well aligned with the concept of accelerated bridge construction and thus many of precast PC girders have been standardized with typical cross-section designs for various span ranges. These standardized girders have sectional dimensions and steel arrangement with similar standard drawings provided by Ministries of Transportation across North America (e.g., Alberta Transportation 2019, California Department of Transportation 2014).

However, compared to cast-in-place concrete girders, precast PC girders have shown more durability issues. For example, multi-girder bridges, which are made of parallel members with adjacent girders connected through grouted shear keys, are susceptible to Deterioration due to water and corrosive chemicals infiltration between girders. This issue is especially severe in the cold climate of North America (e.g., the province of Alberta in Canada) where de-icing salt (Ramseyer and Kang 2012) is used seasonally. Chloride-induced corrosion in stirrups, longitudinal mild steel bars and prestressed steel strands has been identified as one of the most predominant causes for bridge aging (Bhargava et al. 2011; Wang et al. 2014; Zhang et al. 2017a). During the corrosion process, steel turns into rust which has a relatively lower density, primarily leading to (1) cross-sectional area reduction in steel reinforcement and weakened material properties, (2) cracking and spalling of the concrete cover due to volume expansion that generates splitting stresses in concrete and altered material properties, and (3) bond deterioration between steel reinforcement and the surrounding concrete. As a result of these factors, corrosion can eventually lead to load-carrying capacity degradation and possible failure mechanism change, as evidenced in many experimental and numerical studies (Darmawan and Stewart 2007; Guo et al. 2011; Zhang et al. 2017b; Ye et al. 2018).

To support corroded bridge management, fast screening for safety assessment requires convenient and efficient capacity prediction models of corroded concrete girders in engineering practice. Unlike physics-based computational models (e.g., continuum finite element models), data-driven models based on simple empirical equations or machine learning are more well-received because they can be used to predict load-carrying capacity of corroded PC girders simply by feeding the models with information related to girder condition as inputs. For this purpose, several models of this kind have been developed for corroded reinforced concrete (RC) beams (Lu et al. 2018; Fu and Feng 2021; Soltani et al. 2021) and PC girders (Kioumarsi et al. 2021). These models were limited to either flexure or shear failure, as conventionally considered for design of new RC beams or PC girders for flexure- or shear-critical loading scenarios. Note that the model proposed for capacity reduction of corroded PC girders (Kioumarsi et al. 2021) only considered flexure failure, while no existing model available of this kind considers shear failure. More importantly, the failure mechanism for corroded members can be altered by corrosion as pointed out in the literature (Ye et al. 2018; Huang et al. 2022): as an example, a PC girder with corrosion can fail in a ductile mode when loaded under shear-critical loading condition with a relatively small shear-span-to-effective depth ratio. That said, it is desirable to use a load-carrying capacity model for safety assessment of corroded PC girders after considering both flexure and/or shear failure and other mechanisms (e.g., bond failure).

Models invariably suffer from prediction error, and this is true for empirical or machine learning models, which are usually developed to achieve an overall balance between the prediction bias (accuracy) and variance (precision). Compared with detailed mechanics-based finite element (FE) models, they are cheap-to-evaluate but generally less accurate. Thus, it is important to quantify the prediction error, which is essential when the model developed based on a limited database is used in a probabilistic context such as reliability-based evaluation. To this end, many studies quantified the prediction error probabilistically when a model was developed to facilitate its application in engineering practice. Choe et al (2008) developed a probabilistic shear capacity prediction model for corroded RC columns based on a compiled experimental database, which was used to estimate seismic fragility of corroded structures. Ma et al. (2013) developed a probabilistic flexural capacity prediction model for corroded RC beams on the basis of a compiled experimental database. Recognizing the limited data available from systematically tested corroded RC beams experimentally, Aslani and Dehestani (2020) developed a probabilistic model to predict the flexural capacity reduction as a function of corrosion degree, using the database generated from FE simulations. Note that these efforts were mainly devoted to corroded RC members, while no relevant work aimed to develop probabilistic models with prediction error quantified for corroded PC girders.

To address the aforementioned gaps and needs identified for corroded PC girders, this chapter developed prediction models for load-carrying capacity of corroded PC girders based on a virtual experimental database generated through computer models considering the fact that experimental data in this regard is limited in the literature (Belletti et al. 2020; Wang et al. 2020). To this end, two-dimensional (2D) continuum FE models for corroded PC girders were firstly developed and validated using 9 corroded PC girders tested in the literature under either flexure or shear critical loading scenarios. Next, using the validated FE models, a total of 4,165PC girders under point loading were simulated to consider various design, loading, and corrosion conditions to estimate their load-carrying capacities. Subsequently, based on the generated database, the probabilistic capacity reduction factor model and load-carrying capacity prediction model were developed. The former model was used to study the corrosion-induced reduction effects, and the later model was used to study the corrosion effects on the probability of failure of corroded PC girders at given load levels when capacity is affected by corrosion.

7.2 Computer Experiments for Corroded PC Girders

In many existing studies (Sharma et al. 2014; Su et al. 2017; Aslani and Dehestani 2020), computer experiments are used to generate data, which can be used to develop data-based prediction models, namely surrogate models relating the model output to input variables. In this section, the FE model strategy in *VecTor2*, a nonlinear analysis software for concrete structures based on the Modified Compression Field Theory and the Disturbed Stress Field Model (Wong et al. 2013) is first described for corrode PC girder modeling. Before performing computer experiments for virtual experimental database generation, the used modeling techniques are applied to nine experimentally tested PC girders, to confirm their capability in simulating corroded PC girder behavior with flexure or shear failure, particularly the ultimate load-carrying capacities.

7.2.1 FE modeling of Corroded PC Girders

In 2D FE modeling of PC girders in *VecTor2*, the concrete is modelled by four-node plane-stress rectangular elements. The longitudinal reinforcement is represented using two-node truss bar elements, and the stirrups are smeared in the concrete according to the Modified Compression Field Theory and the Disturbed Stress Field Model. The bond-slip relationship between steel and surrounding concrete is modeled by the two-node zero-length link element in *VecTor2*. For concrete, the pre-peak and post-peak behavior (i.e., before and after the strain ε_0 at the peak stress f_c') in compression are represented by the *Hognestad* model and the *Modified Park-Kent* model (Wong et al. 2013) as shown in Figure 7-1 (a), respectively. The tensile behavior of concrete is characterized by a linear branch before the cracking strain of ε_{cr}, and the *modified Bentz-2003* model (Wong et al. 2013) as shown in Figure 7-1 (a) is used to consider tension-stiffening in concrete after cracking. The cracking stress f_{cr} is estimated as $0.33\sqrt{f_c'}$ according to the concrete compressive strength f_c' in MPa (Wong et al. 2013). For longitudinal reinforcement and stirrups, the *Ductile Steel Reinforcement* model (Wong et al. 2013) as shown in Figure 7-1 (b) is adopted to simulate the uniaxial stress-strain relationship with two linear branches characterized by the elastic modulus and the strain hardening modulus respectively before and after the yield strain of ε_y. Relevant geometrical and material properties are determined according to the deterioration modeling proposed in the literature (Cairns et al. 2005; Castel et al. 2011; Zandi Hanjari et al. 2011; Kivell et al. 2015; Wang et al. 2017a; Wang et al. 2017b; Zhang et al. 2017a; Zhang et al. 2017b).

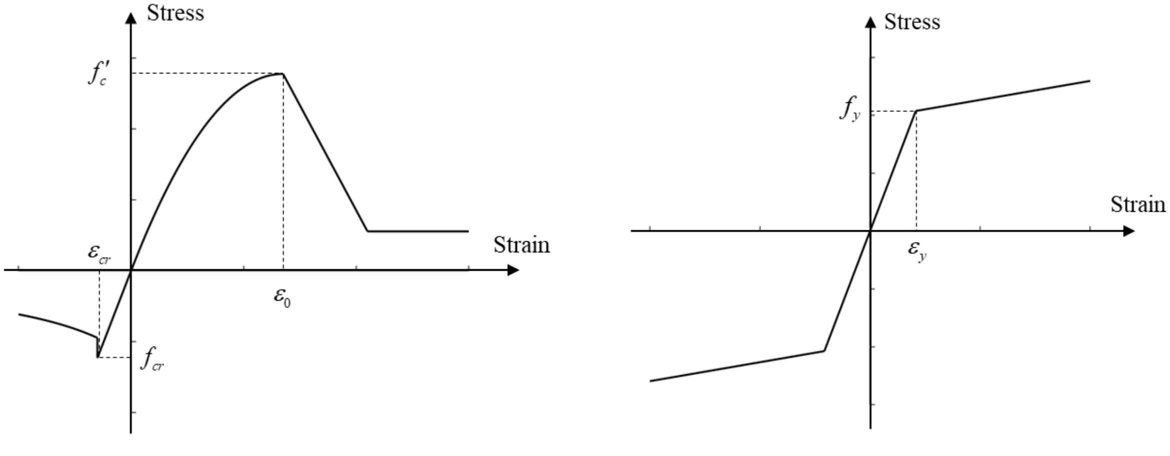

(a) (b)

Figure 7-1: Schematic diagrams of the considered uniaxial material model for: (1) concrete, and (2) steel

The corrosion-induced deterioration in mechanical properties of corroded RC/PC structures has been extensively studied over the past decades (Cairns et al. 2005; Castel et al. 2011; Zandi Hanjari et al. 2011; Kivell et al. 2015; Wang et al. 2017a; Wang et al. 2017b; Zhang et al. 2017a; Zhang et al. 2017b). Among various corrosion-induced Deterioration, the steel cross-sectional area loss, prestress loss, steel ductility reduction, and bond loss are the principal factors leading to the structural degradation of corroded PC girders (Huang et al. 2022), and thus are considered in the FE modelling of corroded PC girders in this chapter. According to the literature, the corrosion-induced modifications in these mechanical properties have been related to corrosion degree, which is defined as the average cross-sectional area loss η as shown in Eq. (7-1) .

$$\eta_{p,s,v} = \frac{A_{p,s,v} - A^c_{p,s,v}}{A_{p,s,v}} \times 100\% \tag{7-1}$$

where A is the initial cross-sectional area of steel under uncorroded condition, A^c is the remaining cross-sectional area of corroded steel, and the subscripts of *p*, *s* and *v* denote prestressed strands, non-prestressed longitudinal reinforcement and stirrups, respectively.

Corrosion in prestressed strands can lead to prestress force loss as a direct result of the strand area loss (Castel et al. 2011; Zhang et al. 2017a) and degradation of steel material properties, such as the yield strength, elastic modulus, and ductility (Zhang et al. 2017b). Based on previous experimental and numerical research (Castel et al. 2011; Zhang et al. 2017a), the remaining prestress force in corroded strands, F^c_p, was found to be proportional to the remaining cross-sectional area A^c_p per Eq. (7-2),

$$F^c_p = \sigma^{eff}_p A^c_p \tag{7-2}$$

where σ^{eff}_p is the effective prestress in uncorroded strands. Based on experimental studies (Zhang et al. 2017b; Wang et al. 2017a), corrosion has little effect on the yield strength and the elastic modulus, but can significantly decrease the ductility of strand. It was found that the ultimate strain for corroded strands (ε^c_{pu}) decreases linearly with the corrosion degree (η_p) when η_p is lower than a critical value (η_c= 11%), following $\varepsilon^c_{pu} = \varepsilon_{pu} - \left(\varepsilon_{pu} - \varepsilon_{py}\right)\eta_p / \eta_c$. Thus, the ultimate strength of corroded strands is reduced accordingly with $f^c_{pu} = f_{pu} - \left(f_{pu} - f_{py}\right)\eta_p / \eta_c$. To account for the ductility loss, the uniaxial stress-strain law proposed for corroded strand steel (Zhang et al. 2017b; Wang et al. 2017a), as shown in Eq. (7-3), is used in this study to relate its stress σ and strain ε ,

$$\sigma = \begin{cases} E_p \varepsilon, & \varepsilon \le \varepsilon_{py} \\ f_{py} + \left(\varepsilon - \varepsilon_{py}\right) \dfrac{f_{pu}^c - f_{py}}{\varepsilon_{pu}^c - \varepsilon_{py}}, & \varepsilon_{py} < \varepsilon \le \varepsilon_{pu}^c, \eta_p \le \eta_c \end{cases} \tag{7-3}$$

where E_p , ε_{py} , ε_{pu} , f_{py} and f_{pu} are the elastic modulus, yield strain, ultimate strain, yield strength, and ultimate strength of uncorroded strands. Note that when η_p exceeds η_c , the strands become brittle with the ultimate strain equal to the yield strain.

Corrosion also reduces the ductility of non-prestressed longitudinal reinforcement and stirrups (Cairns et al. 2005; Zandi Hanjari et al. 2011) and such effect can be considered by a well-received equation as shown in Eq. (7-4),

$$\varepsilon_{su,vu}^c = \varepsilon_{su,vu} - \alpha_1 \eta_{s,v} \cdot 100 \varepsilon_{su,vu} \tag{7-4}$$

where $\varepsilon_{su,vu}^c$ and $\varepsilon_{su,vu}$ denote the ultimate strain of corroded and uncorroded steel respectively, and the subscripts "*su*" and "*vu*" refer to longitudinal steel reinforcement and steel stirrups respectively. α_1 is an empirical coefficient taking a value of 0.017 as suggested by Zandi Hanjari et al. (2011).

Another principal factor causing structural degradation is the bond loss for prestressed steel strands and longitudinal steel bars. To consider the bond loss for prestressed strands, Wang et al. (2017b) improved the *fib* Model Code (*fib* 2010) for the bond stress-slip relationship prestressed strands, and proposed a model bonding between corroded strands and concrete, as shown in Eq. (7-5) .

$$\tau = \begin{cases} \tau_{p,\max}^{c}\left(s/s_2\right)^{0.4} & 0 \le s \le s_2 \\ \tau_{p,\max}^{c} - \left(\tau_{p,\max}^{c} - \tau_{p,f}^{c}\right)\dfrac{s-s_2}{s_3-s_2} & s_2 < s \le s_3 \\ \tau_{p,f}^{c} & s_3 < s \end{cases} \tag{7-5}$$

in which

$$\tau_{p,\max}^{c} = \begin{cases} \tau_{p,\max} & \eta_p \le 6\% \\ 2.03e^{-11.8\eta_p} \cdot \tau_{p,\max} & \eta_p > 6\% \end{cases} \tag{7-6}$$

$$\tau_{p,f}^{c} = 0.4\tau_{p,\max}^{c} \tag{7-7}$$

Here, $\tau_{p,max} = 1.25\sqrt{f_c'}$ (MPa) (Wang et al. 2017b; Belletti et al. 2020) and $\tau_{p,\max}^{c}$ represent the maximum bond stress for stands before and after corrosion; $\tau_{p,f}^{c}$ is the corrosion-affected residual bonding stress due to friction. The slip parameters (s_2 and s_3) are barely affected by corrosion and determined as $s_2 = 3$ mm, and s_3 = half of the distance between concrete gear and the adjacent wires (Wang et al. 2017b; Belletti et al. 2020), which is equivalent to the distance between ribs of the deformed bar.

Similarly, the bond stress-slip relationship $\tau\left(s\right)$ of corroded non-prestressed longitudinal steel bars (Kivell et al. 2015; Huang et al. 2022) is considered as shown in Eq. (7-8).

$$\tau = \begin{cases} \tau_{s,\max}^{c}\left(s/s_1\right)^{0.4} & 0 \le s \le s_1 \\ \tau_{s,\max}^{c} & s_1 \le s \le s_2 \\ \tau_{s,\max}^{c} - \left(\tau_{s,\max}^{c} - \tau_{s,f}^{c}\right)\dfrac{s-s_2}{s_3-s_2} & s_2 < s \le s_3 \\ \tau_{s,f}^{c} & s_3 < s \end{cases} \tag{7-8}$$

in which

$$\tau_{s,\max}^{c} = 1.2e^{-7.6\eta_s}\tau_{s,\max} \tag{7-9}$$

$$\tau_{s,f}^{c} = \begin{cases} \left(0.26+13\eta_s\right)\tau_{s,\max}^{c} & 0\% \le \eta_s < 3\% \\ 0.65\tau_{s,\max}^{c} & 3\% \le \eta_s < 13\% \\ \left[0.65-0.06\left(100\eta_s-13\right)\right]\tau_{s,\max}^{c} & 13\% \le \eta_s < 20\% \\ 0.23\tau_{s,\max}^{c} & 20\% \le \eta_s \end{cases} \tag{7-10}$$

Here, $\tau_{s,\max}$ and $\tau_{s,\max}^{c}$ represent the maximum bond stress for non-prestressed steel before and after corrosion; $\tau_{s,f}^{c}$ is the corrosion-affected residual bonding stress due to friction. Note that $\tau_{s,\max}$ can be estimated based on the reinforcement bar diameter (d_s) and the concrete compressive strength (f_c') as per, $\tau_{s,\max} = \left(20-d_s/4mm\right)\sqrt{f_c'/30MPa}$ (MPa). The slip parameters are estimated as $s_1 = \sqrt{f_c'/30MPa}$ (mm), $s_2 = 3$ mm , and s_3 = the lug spacing of deformed steel bars (Wong et al. 2013). It is worth mentioning that stirrups are smeared in the concrete assuming perfect bonding in this study.

7.2.2 Modeling and Validation of Tested Corroded PC Girders

7.2.2.1 Corroded PC girder with shear failure

Limited corroded PC girders were tested to shear failure in the literature (Belletti et al. 2020; Wang et al. 2020) and rarely sufficient information was provided for numerical modeling and model validation. After thorough review of the literature, a 10-year naturally-corroded pre-tensioned PC girder tested by Belletti et al. (2020) is studied in this section. The PC girder contained no shear reinforcement as shown in Figure 7-2(a), and it failed in shear during the experimental test. After the damaging test, the strands were extracted and the corrosion degrees were measured. The strands were corroded to different levels as grouped into five different categories with the corrosion distribution visually shown in Figure 7-2(b). The 2D continuum-based FE model is then developed, as shown in Figure 7-2(c), to simulate the structural behavior of this tested PC girder using the aforementioned modeling strategy. The tested material properties for steel and concrete before corrosion and the calculated material properties after corrosion are summarized in Table 7-1 and 7-2, respectively. The mesh size is determined as 25 mm × 25 mm based on a mesh sensitivity analysis to achieve a balance between computational accuracy and efficiency.

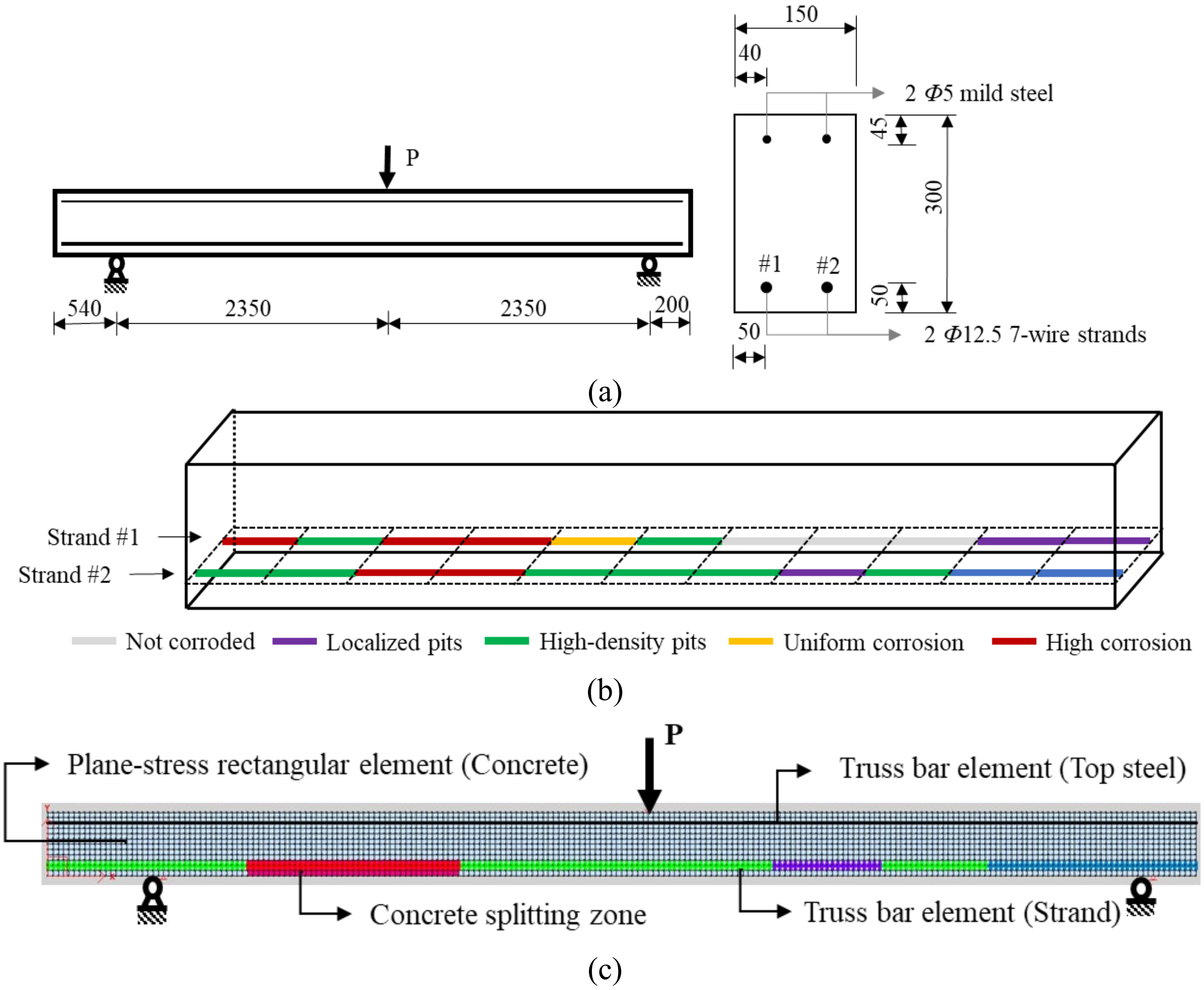

Figure 7-2: Tested PC girder (Belletti et al. 2020): (a) specimen under three-point bending and cross section, (b) strand corrosion distribution, and (c) 2D continuum-based FE model

The load-deflection curve of the corroded PC girder is simulated using the aforementioned corrosion-affected properties, and compared to the experimental results, as shown in Figure 7-3. To emphasize the corrosion-induced structural degradation, Figure 7-3(a) also reports the load-deflection curve simulated using the uncorroded material properties in Table 1 when assuming no corrosion. It is observed that corrosion greatly affects the structural behavior of the PC girder, particularly the ultimate load capacity and deformation capability. Moreover, the load-deflection curve predicted from the developed 2D FE model considering corrosion agrees well with the tested result. Note that average effective prestress $\sigma_p^{eff} = 1101.3\,\text{MPa}$ as estimated according to Belletti et al. (2020) is used in this study.

It is worth mentioning that the concrete splitting zone in the PC girder as indicated in Figure 7-2(c) has negligible influence on the PC girder behavior, as mentioned earlier regarding the principal corrosion-related factors leading to structural degradation. To further confirm this, corrosion-induced concrete splitting is considered in the FE model using the approach proposed by Coronelli and Gambarova (2004) by using a reduced concrete strength of 12.9MPa (Belletti et al. 2020). The simulated load-displacement curves with and without modelling this concrete splitting zone are compared as shown in Figure 7-3, confirming that corrosion-induced concrete splitting can be neglected.

Table 7-1: Tested material properties of uncorroded steel and concrete for PC girder tested in Belletti et al. (2020)

Material	Property	Bottom	Top
Steel	Nominal diameter d_p, d_s (mm)	12.5	5
	Nominal area A_p, A_s (mm^2)	93	19.6
	Yield strength f_{py}, f_{sy} (MPa)	1,580	435
	Ultimate strength f_{pu}, f_{su} (MPa)	1,860	500
	Elastic modulus E_p, E_s (MPa)	195,000	200,000
	Ultimate strain $\varepsilon_{pu}, \varepsilon_{su}$ (%)	5	18
	Average effective prestress σ_p^{eff} (MPa)	1,101.3	-
Concrete	Compressive strength f_c' (MPa)	43.65	
	Modulus of elasticity E_c (MPa)	35,137	

Table 7-2: Summary of strand corrosion degrees and material properties after corrosion for the PC girder tested in Belletti et al. (2020)

Corrosion category	Not corroded	Localized pits	High-density pits	Uniform corrosion	High corrosion
Tested average remaining area A_p^c (mm^2)	93.00	91.71	87.83	82.94	74.80
Tested corrosion degree η_p (%)	0	1.39	5.56	10.82	19.57
Calculated ultimate strain ε_{pu}^c (%)	5	4.47	2.88	0.88	0.81
Calculated ultimate strength f_{pu}^c (MPa)	1,860	1,825	1,718	1,584	1,580
Calculated maximum bond stress $\tau_{p,\max}^c$ (MPa)	8.26	8.26	8.26	4.68	1.67
Calculated residual friction stress $\tau_{p,f}^c$ (MPa)	3.30	3.30	3.30	1.87	0.67

In addition, Figure 7-4 shows the cracking pattern predicted from the 2D FE model and the experimental test, where the red zone in Figure 7-4 (a) represents the cracked region with the color depth indicating the crack width. Their comparison indicates that the developed 2D FE model can accurately simulate failure (i.e., typical shear tension failure) of the corroded PC girder, which is brittle instead of ductile when the girder is uncorded. Due to more severe corrosion in the left half-span, the failure initiated in the left half-span as expected. Overall, the FE model for the corroded PC girder can simulate the degraded behavior (e.g., stiffness, ultimate load capacity, and shear failure) reasonably well.

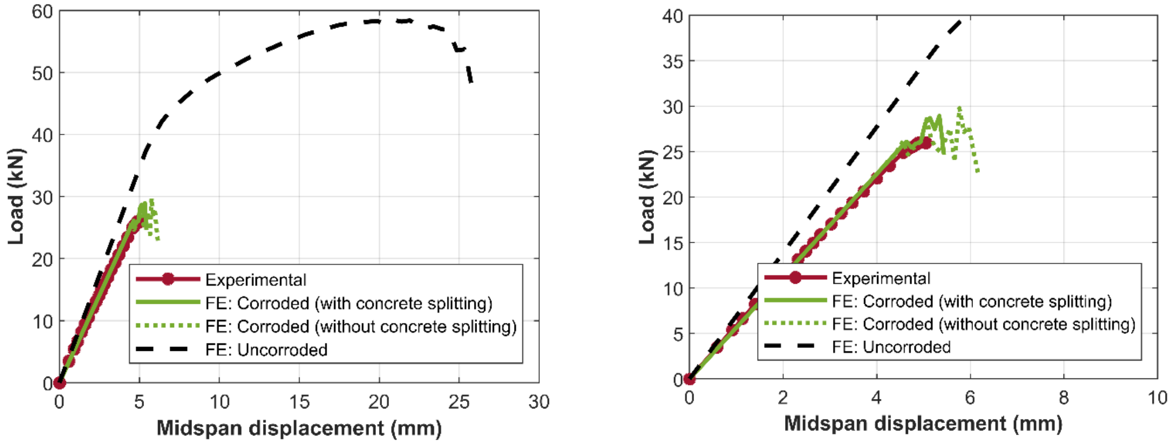

(a) (b)

Figure 7-3: Load-displacement curves at loading point: (a) full scale plot, and (b) zoom in plot

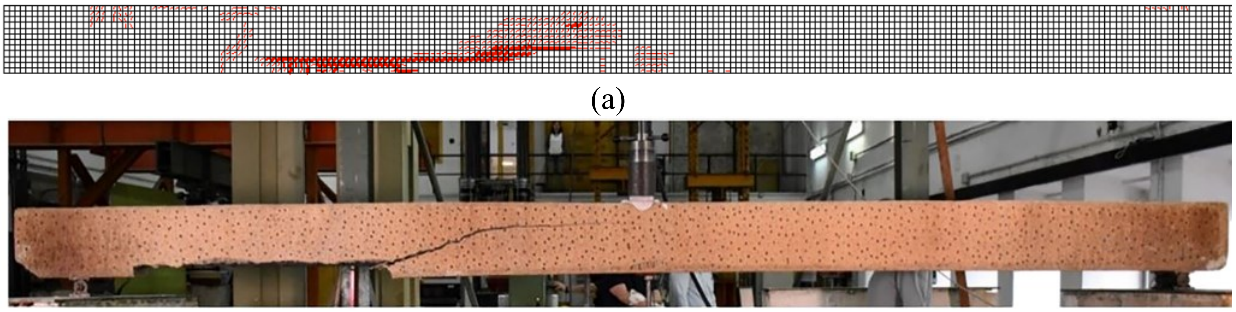

(a)

(b)

Figure 7-4: Cracking pattern of the corroded PC girder from: (a) FE prediction, and (b) experimental test (Belletti et al. 2020)

7.2.2.2 Corroded PC girder with flexure failure

Zhang et al. (2017a) tested eight nominally identical bonded post-tensioned PC girders, see Figure 7-5(a) for the specimen dimensions and loading position, under eight different strand corrosion degrees (i.e., 0%, 12.1%, 19.5%, 27.0%, 46.0%, 61.7%, 73.7%, 84.7%). These girders with increasing corrosion degrees are referred to as G1, G2, G3, G4, G5, G6, G7, and G8, respectively. The material properties for steel before corrosion was tested (Zhang et al. 2017a) and summarized in Table 7-3, and are used for modeling the PC girder under no corrosion (i.e., G1) and calculating the corrosion-affected properties in this study as summarized in Table 7-4. Note that the modulus of elasticity for concrete was not reported and is estimated by $E_c = 4500\sqrt{f_c'}$ (MPa) (CSA 2019) here. It is worth mentioning that the corrosion-induced prestress force loss was measured in the experiment (Zhang et al. 2017a) and the prestress force loss was proportional to the strand cross-sectional area reduction due to corrosion. This further confirms the accuracy of using Eq. (7-4) to consider the corrosion effect on prestress force in strands.

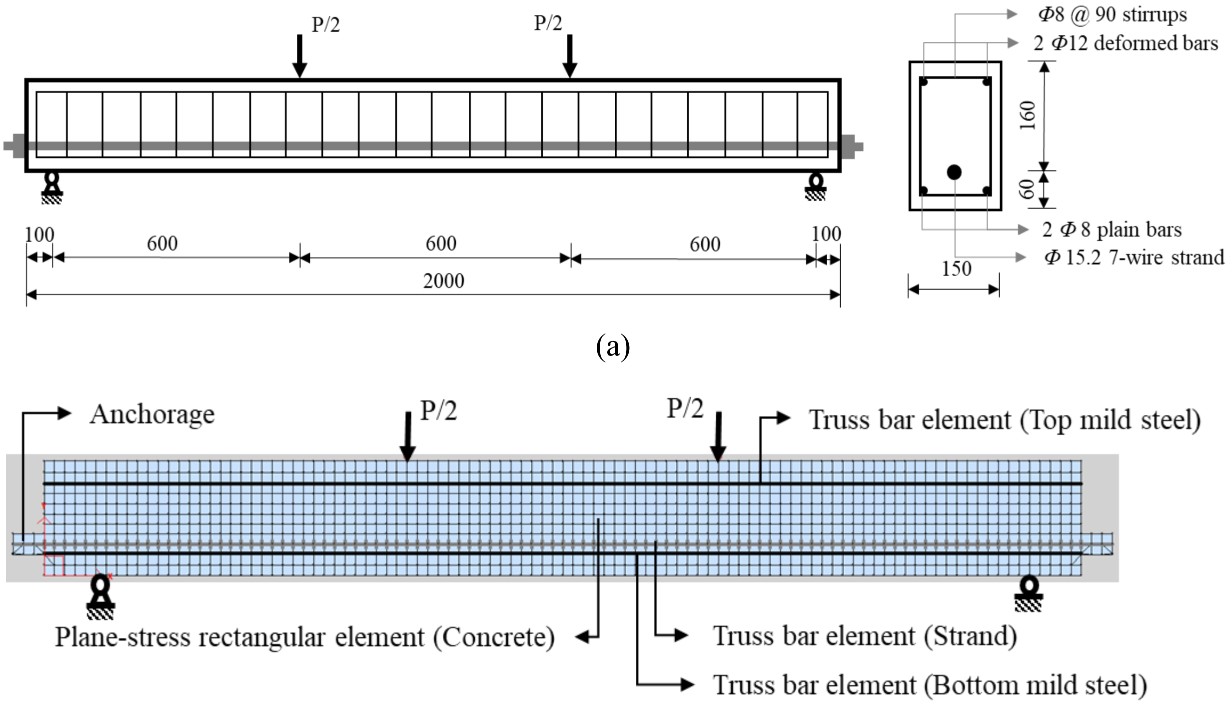

(a)

(b)

Figure 7-5: Tested PC girders (Zhang et al. 2017a): (a) specimen under four-point bending and cross section, and (b) 2D continuum-based FE model

The same FE modeling strategy as described and used earlier is employed to model these considered eight PC girders, as shown in Figure 7-5(b). Similarly, a mesh sensitivity analysis is conducted to determine the FE discretization size as 20 mm × 20 mm. Note that the anchorages for post-tensioned strands are modelled explicitly to ensure no slippage at anchorages using quasi-rigid (with high stiffness and strength) elements surrounding strands and perfect bonding. The developed 2D continuum-based FE model is used to simulate the structural behavior of these corroded PC girders.

Table 7-3: Tested material properties of uncorroded steel for PC girders tested in Zhang et al. (2017a)

Property	*Φ*15.2 Strands	*Φ*12 Mild steel	*Φ*8 Mild steel
Nominal diameter d_p, d_s (mm)	15.2	12	8
Nominal Area A_p, A_s (mm^2)	140	113	50.3
Yield strength f_{py}, f_{sy} (MPa)	1830	335	235
Ultimate strength f_{pu}, f_{su} (MPa)	1910	425	310
Elastic modulus E_p, E_s (MPa)	195000	210000	210000
Ultimate strain $\varepsilon_{pu}, \varepsilon_{su}$ (%)	2.9	20	20
Effective prestress σ_p (MPa)	1385.7	-	-

Table 7-4: Summary of the strand corrosion degrees and material properties after corrosion for PC girders tested in Zhang et al. (2017a)

Specimen	G1	G2	G3	G4	G5	G6	G7	G8
Tested corrosion degree η_p (%)	0	12.1	19.5	27.0	46.0	61.7	73.7	84.7
Tested concrete strength f_c' (MPa)	34.1	32.4	32.4	34.3	33.7	33.7	33.7	33.7
Tested effective prestress force F_p' (kN)	194	177	160	143	110	76	53	29.7
Calculated ultimate strain ε_{pu}^c (%)	2.9	0.94	0.94	0.94	0.94	0.94	0.94	0.94
Calculated ultimate strength f_{pu}^c (MPa)	1910	1830	1830	1830	1830	1830	1830	1830
Calculated maximum bond stress $\tau_{p,\max}^c$ (MPa)	7.2994	3.5538	1.4841	0.6125	0.0651	0.0102	0.0025	0.0007
Calculated residual friction stress $\tau_{p,f}^c$ (MPa)	2.9198	1.4215	0.5937	0.2450	0.0260	0.0041	0.0010	0.0003

Figure 7-6 presents the comparison between the FE-predicted and experimental load-deflection curves, with those for G1, G3, G5, G7 in Figure 7-6 (a) and G2, G4, G6, G8 in Figure 7-6 (b). The critical limit states (e.g., wire rupture, concrete crushing, yielding) are indicated on the curves as well.

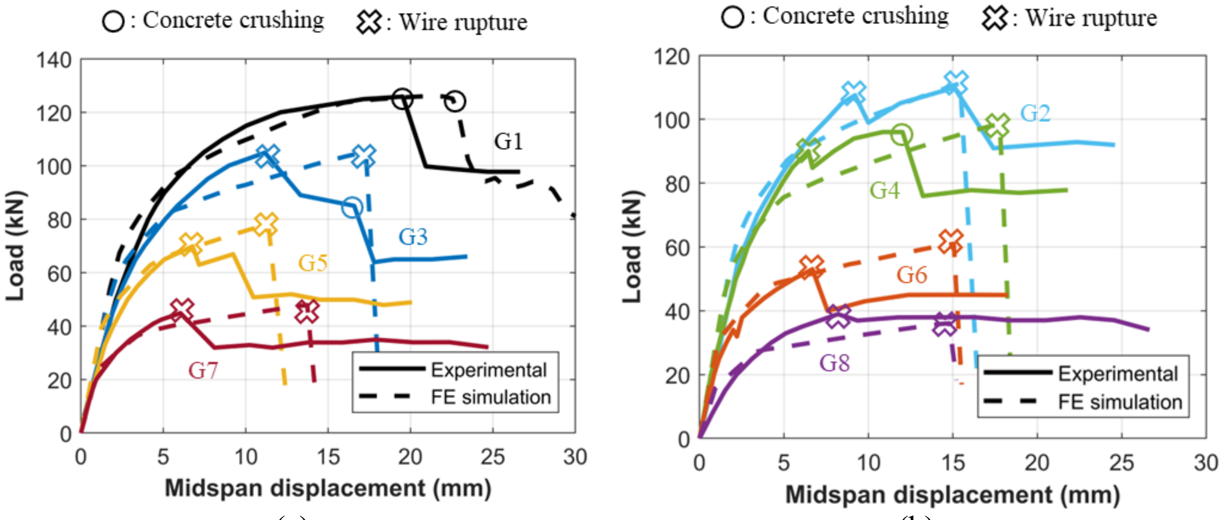

(a) (b)

Figure 7-6: Load-deflection curves at mid-span for: (a) G1, G3, G5 and G7, and (b) G2, G4, G6 and G8

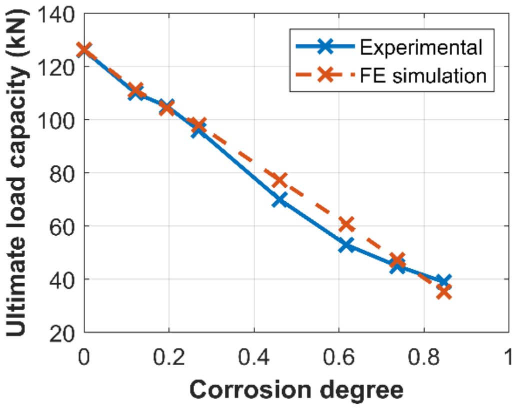

Figure 7-7: Comparison between the tested and predicted ultimate load capacities

Overall, the simulation results agree well with the experimental results. The degradation of post-cracking stiffness, ultimate load capacity, and failure mechanisms (or limit state exceedance) with the increasing strand corrosion degree is well captured. The deformation capability, as indicated by the ultimate displacements, is not as well captured as other quantities, especially for corroded PC girders with large corrosion degrees, which are dominated by strand rupture failure type. Accurate prediction of ultimate displacement is considered challenging due to the experiment uncertainties particularly inside the ultimate strain of corroded strands. Nevertheless, the ultimate load capacities of the tested corroded PC girders are predicted reasonably well as shown in Figure 7-7.

7.2.3 Virtual Experimental Database

The FE model strategy validated for corroded PC girders is used to simulate PC girders for a virtual experimental (numerical) database generation. A total of 4,165 corroded PC voided girders is simulated for the load-carrying capacity under a point load considering various design, loading, and corrosion conditions. Standardized precast PC voided girders that have been designed and used extensively for short-span bridges in North America are considered. Specifically, five girder types from the standard drawings archived for PC voided girders in Alberta (Alberta Transportation 2019) are used, namely 11m SM-510, 9.14m SL-510, 6m SL-510, 8.53m SC-510 and 6m SC-510 (see Table 7-5). The cross-sections for the standard PC voided girders considered are all 1206mm in width and 510mm in depth with three voids of 250~300mm in diameter, with the cross-section dimension and reinforcement details in Appendix D. They are regarded as representative voided girder cross-sections for precast PC bridge constructions; for example, the sectional type of SIV-48 from the standard drawings for PC voided girders in California, US (California Department of Transportation 2014) has similar sectional dimensions to these considered in this study.

Table 7-5: Summary of standardized PC girders considered in the database generation

Girder type	Nominal material properties			Tensile steel area		Compressive steel area		Stirrups	
	Concrete strength (f'_c) MPa	Tensile strength of strands (f_{pu}) MPa	Yield strength of mild steel ($f_{sy,vy}$) MPa	Strands (A_p) mm^2	Mild steel (A_s) mm^2	Strands (A_p) mm^2	Mild steel (A_s) mm^2	Area (A_v) mm^2	Spacing (s) (mm)
11m SM-510 (with 25M)	35	1860	400	1579.2	200 (2200)	394.8	500	400	150~350
9.14m SL-510	50	1860	400	1680	2200	560	500	400	150~300
6m SL-510	50	1860	400	1120	200	560	500	400	150~300
8.53m SC-510	35	1860	400	1381.8	200	394.8	500	400	150~350
6m SC-510	35	1860	400	789.6	200	394.8	500	400	150~350

Table 7-6: Summary of random material property considered in the database generation

Material property	Nominal (MPa)	Mean (MPa)	COV	Distribution	Reference
Concrete compressive strength (f_c')	35	48.3	0.12	Normal	Nowak and Szerszen (2003)
Tensile strength of strands (f_{pu})	1860	1943	0.025	Normal	Nowak and Szerszen (2003)
Yield strength of mild steel (f_y)	400	458	0.065	Normal	Nowak and Szerszen (2003)

Table 7-7: Summary of the corrosion degrees considered in the database generation

Corrosion degree		Corrosion degree for longitudinal steel η_v (%)								
		0	5	10	15	20	25	30	35	40
Corrosion degree for stirrups η_l (%)	0	√	√	√	√	√				
	5		√	√	√	√	√			
	10			√	√	√	√	√		
	15				√	√	√	√	√	
	20					√	√	√	√	√
	25						√	√	√	√
	30							√	√	√
	35								√	√
	40									√

The nominal tensile strength of prestressed strands and yield strength of mild steel are 1860MPa and 400MPa respectively for all the archived standard PC voided girders in Alberta. The effective prestress is typically around 60% of the tensile strength of strands for all the above standard girders considered. The nominal concrete compressive strength for these girders is either 35MPa (e.g., for SM-510 and SC-510) and 50MPa (e.g., SL-510). Note that the true values of concrete and steel strength differ from the nominal values in engineering practice, and thus the material variability (see Table 7-6) is considered in the virtual experimental design for 11m SM-510 to have a good coverage of different material properties according to Latin Hypercube Sampling (LHS) with 20 variants. While for the other girders, only the mean values of the material properties for the sake of data generation efficiency.

Different corrosion conditions are considered in terms of the corrosion degrees for longitudinal steel (i.e., prestressed strands and mild steel) and stirrups. In the real world, exact description of the corrosion levels of PC girders can be complicated; for practical reasons, corrosion is assumed uniform along the whole girder length, except that the corrosion degrees for longitudinal steel η_l and transverse steel η_v are distinguished from each other. This is to consider the fact that stirrups are critical for shear capacity and easier to get corroded. Thus, during the database generation, it is assumed that the corrosion degree of stirrups is larger than that of longitudinal steel, i.e., $\eta_v = \eta_l + \Delta\eta$ with $\Delta\eta$ ranging from 0 to 20% as shown in Table 7-7. This leads to 35 combinations of corrosion degrees for longitudinal and transverse steel (stirrups), which is applied to all PC girders simulated in the virtual experimental design.

Table 7-8: Summary of the simulated corroded PC girders in the virtual experimental design matrix

Girder type	Material properties (f_c', f_{pu}, f_y)	Corrosion degree combinations	Point load position	No. of girders
11m SM-510	20 variants	35	1m, 2m, 3m, 4m, 5m	3500
11m SM-510 (with 25M)	Mean values	35	1m, 2m, 3m, 4m, 5m	175
9.14m SL-510	Mean values	35	1m, 2m, 3m, 4m	140
6m SL-510	Mean values	35	1m, 2m, 3m	105
8.53m SC-510	Mean values	35	1m, 2m, 3m, 4m	140
6m SC-510	Mean values	35	1m, 2m, 3m	105

In addition to the consideration of different design and corrosion conditions, different loading positions are considered to cover both shear-critical and flexure-dominated loading scenarios. As such, the point load position varies from 1m away from the support to approximately the midspan for each girder, as summarized in the virtual experimental design matrix in Table 7-8.A summary on the input and output parameters of the generated virtual experimental database is included in Appendix E.

7.3 Probabilistic Capacity Reduction Factor Model

7.3.1 Model Development

To guide fast screening of bridge girder conditions, the knowledge about load-carrying capacity reduction due to corrosion can be beneficial. To this end, with the generated virtual experimental database, a probabilistic capacity reduction factor model is developed first, to predict the ratio between load-carrying capacities from the corroded and intact PC girders as shown in Eq. (7-11),

$$R(\mathbf{x}) = \frac{P(\mathbf{x})}{P(\mathbf{x};\eta_l = \eta_v = 0)} \tag{7-11}$$

where $R(\mathbf{x})$ is the load-carrying capacity reduction factor, $P(\mathbf{x})$ and $P(\mathbf{x};\eta_l = \eta_v = 0)$ are the load-carrying capacities from the corroded and uncorroded PC girders respectively, $\mathbf{x}$ is the vector of predictors, containing important influencing factors related to the design, corrosion and loading conditionsas shown in Eq. (7-12),

$$\mathbf{x} = \left\{ \eta_l, \eta_v, \frac{a}{d}, \frac{L}{h}, \rho_p, \rho_s, \rho_v, \frac{f_c'}{35MPa}, \frac{f_{pu}}{1860MPa}, \frac{f_y}{400MPa} \right\}^T \tag{7-12}$$

where η_l and η_v refer to corrosion degrees for longitudinal and transverse steel respectively; a/d is the shear span to effective depth ratio used to indicate the load position; and the other predictors are related to the girder design, such as L/h (h = 510mm) denoting the girder length to sectional height ratio, and $\rho_p = A_{ps}/b_w d$, $\rho_s = A_s/b_w d$, and $\rho_v = A_v/b_w s$ denoting the tensile strands ratio, tensile mild steel ratio and stirrups ratio, with b_w, d, and s indicating the web width, effective depth and stirrup spacing.

Among a wide variety of machine learning techniques, Gaussian process regression (Yetilmezsoy et al. 2021; Olalusi and Awoyera 2021) is adopted here for its probabilistic feature with prediction uncertainty and nice properties in nonlinear function representation (e.g., without specifying the function form explicitly). As shown in Eq. (7-13), the load-carrying capacity reduction factor is modeled by a stochastic Gaussian process,

$$R(\mathbf{x}) \sim GP\left(m(\mathbf{x}), k(\mathbf{x}, \mathbf{x}')\right) \tag{7-13}$$

where, $m(\mathbf{x})$ and $k(\mathbf{x}, \mathbf{x}')$ are the mean and covariance function of the Gaussian process. The mean function is used to represent the prior information about the general trend but is generally taken to be zero when no such information is available (Williams and Rasmussen 2006). The kernel covariance function specifies the statistical correlation between two points in the predictors' space and the squared exponential covariance function is a common use. Thus, a zero-mean function is used as shown in Eq. (7-14) and squared exponential covariance function is adopted in this study as shown in Eq. (7-15).

$$m(\mathbf{x}) = 0 \tag{7-14}$$

$$k\left(\mathbf{x}_i, \mathbf{x}_j\right) = {\sigma_f}^2 \exp\left(-\frac{1}{2}\left(\mathbf{x}_i - \mathbf{x}_j\right)^T \mathbf{M}\left(\mathbf{x}_i - \mathbf{x}_j\right)\right) + \sigma_{\text{noise}}^2 \delta_{ij} \tag{7-15}$$

in which, $\mathbf{x}$ and $\mathbf{x}'$ are input vector pairs; ${\sigma_f}^2$, $\mathbf{M}$ and σ_{noise}^2 are the hyperparameters of the covariance function to be estimated during the model training process. Specifically, ${\sigma_f}^2$ is the signal variance, $\mathbf{M} = \text{diag}(\mathbf{l})^{-2}$ is a symmetric matrix defined by a vector of characteristic length-scales $\mathbf{l} = \left(l_1, \cdots, l_N\right)$, σ_{noise}^2 is the noise variance and δ_{ij} is a Kronecker delta. Note that considering σ_{noise}^2 in covariance functions enables the GPR to develop a model from training data with random variations, leading to a GPR-based model with more generalization capacities but with little overfitting concerns. For more details about GPR modeling, readers of interest can refer to Williams and Rasmussen (2006).

To train and test the above GPR model, the generated database is split into two subsets for training and testing purpose, which composes 80% and 20% of the total database, respectively. Based on the training database, the unknown hyperparameters in the Gaussian process regression model are learned by the maximum a posterior (MAP) estimation (Salvatier et al. 2016) and summarized in Table 7-9.

Table 7-9: Summary of the learned hyperparameter values

Hyperparameter	σ_f	σ_{noise}	l_1	l_2	l_3	l_4	l_5	l_6	l_7	l_8	l_9	l_{10}
Value	0.311	0.023	0.123	0.981	3.158	65.9	9.379	3.680	0.685	0.273	0.081	2.693

Based on the obtained hyperparameter values, the probabilistic prediction of capacity reduction factor for PC girders not observed in the training set, $\mathbf{R}_*$ (e.g., PC girders from the testing database or others not in the database) can be obtained by the conditional Gaussian distribution in Eq. (7-16).

$$\mathbf{R}_* \left| \mathbf{X}, \mathbf{R}, \mathbf{X}_* \sim N\left(\bar{\mathbf{R}}_*, \operatorname{cov}\left(\mathbf{R}_*\right)\right)\right. \tag{7-16}$$

in which

$$\bar{\mathbf{R}}_* = \mathbf{K}\left(\mathbf{X}_*, \mathbf{X}\right)\left[\mathbf{K}\left(\mathbf{X}, \mathbf{X}\right) + \sigma_{\text{noise}}^2 \mathbf{I}\right]^{-1} \mathbf{R} \tag{7-17}$$

$$\operatorname{cov}\left(\mathbf{R}_*\right) = \mathbf{K}\left(\mathbf{X}_*, \mathbf{X}_*\right) - \mathbf{K}\left(\mathbf{X}_*, \mathbf{X}\right)\left[\mathbf{K}\left(\mathbf{X}, \mathbf{X}\right) + \sigma_{\text{noise}}^2 \mathbf{I}\right]^{-1} \mathbf{K}\left(\mathbf{X}, \mathbf{X}_*\right) \tag{7-18}$$

Here, $\mathbf{X}$ and $\mathbf{X}_*$ are the input parameter matrices for data points in the training dataset and unobserved points, respectively, $\mathbf{R}$ and $\mathbf{R}_*$ are their corresponding capacity reduction factors, respectively, $\mathbf{I}$ is the identity matrix, $\mathbf{K}\left(\mathbf{X}_*, \mathbf{X}\right)$ is the covariance matrix with its entries as $k\left(\mathbf{x}_*, \mathbf{x}\right)$ evaluated at all pairs of data points in $\mathbf{X}_*$ and $\mathbf{X}$, and similarly for the entries in

$\mathbf{K}(\mathbf{X},\mathbf{X})$, $\mathbf{K}(\mathbf{X},\mathbf{X}_*)$ and $\mathbf{K}(\mathbf{X}_*,\mathbf{X}_*)$. Thus, Eq. (7-16) can be used to predict the capacity reduction probabilistically given **x**, including the mean (i.e., μ_R) and standard deviation.

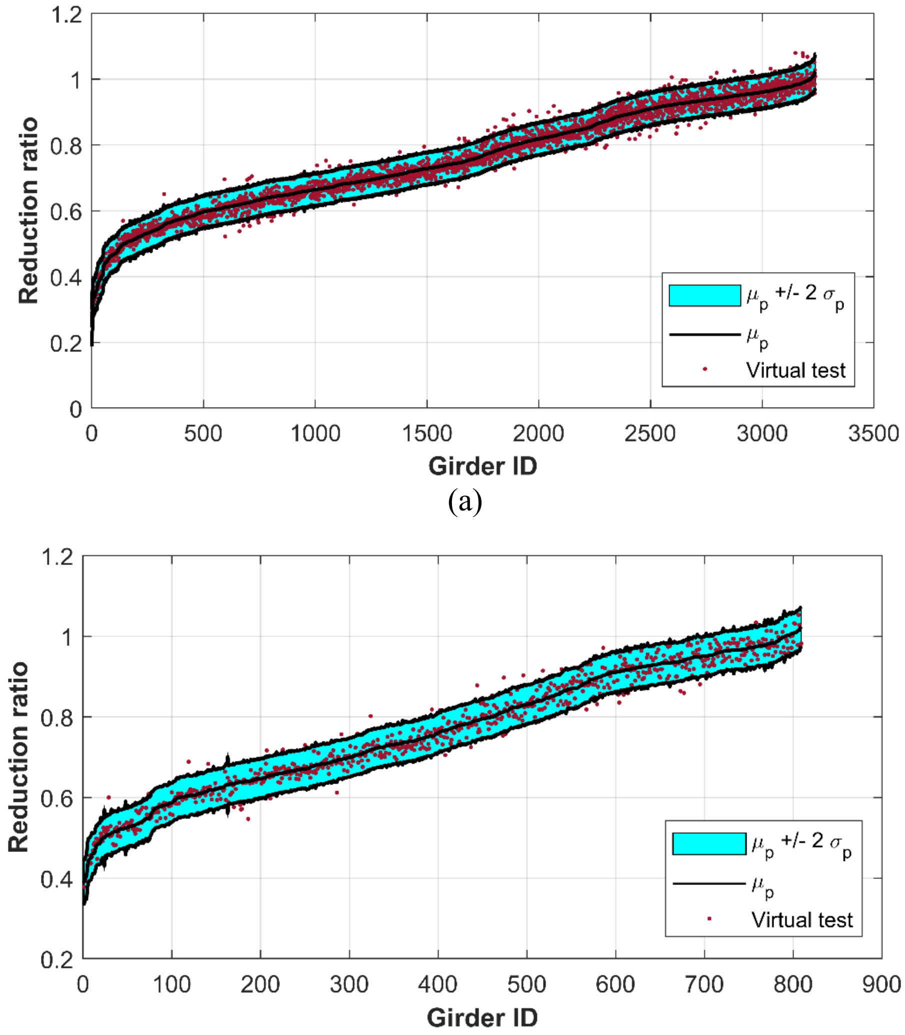

(a)

(b)

Figure 7-8: Performance of the developed capacity reduction factor model over: (a) training dataset, and (b) testing dataset

The developed probabilistic capacity reduction factor model is assessed against both training and testing databases as shown in Figure 7-8. Both the mean prediction (i.e., μ_R) and 95% confidence interval prediction (i.e., $\mu_R \pm 2\sigma_R$) are reported. Note that for visualization purpose in these plots, the PC girders from the virtual experimental database are indexed with an increasing

ID according to the mean prediction μ_R by the developed probabilistic model. It is shown that the developed model performs equally well for both training and testing datasets. The mean prediction curves obtained from the developed model successfully represent the central tendencies of the virtually tested results. Also, the majority of the virtually tested results fall within the mean ± 2 standard deviation (SD) intervals, indicating that the developed model can serve as a reliable capacity reduction factor prediction tool for corroded PC girders. Specifically, 3099 out of 3237 points (i.e., 95.7%) and 761 out of 809 points (i.e., 94.1%) fall within the 95% confidence interval for the training and testing database, respectively, which agrees well with the statistical significance of prediction uncertainty. For practical use, the mean + 2 standard deviation (SD) can be used for the capacity reduction to be conservative.

7.3.2 Application

Based on the developed capacity reduction factor model, parametric analysis is conducted in this section to study the effects of different model parameters on the capacity reduction factor through mean prediction approach. Take the simply supported 11m SM-510 girder under single point loading as a case study, the influence of different model parameters is studied in the one-at-a-time manner, i.e., varying the value of one model parameter while fixing the value of other parameters at a time. Unless otherwise specified, when studying the effects of other parameters, the fixed values for a/d, L/h, ρ_p, ρ_s, ρ_v, $f_c'/35$, $f_{pu}/1860$, and $f_y/1860$ are 2.25, 21.569, 1.161%, 0.147%, 0.373%, 1.38, 1.045, and 1.145 respectively based on the sectional properties and the mean value of material properties for the 11m SM-510 girder. Note that due to the length limitation, only representative parameters that have relatively large variability in engineering practice are discussed in this section. Studies on other parameters are included in Appendix F.

7.3.2.1 *Shear span to effective depth ratio*

The influence of shear span to effective depth ratio a/d is studied by varying its value from 2.25 to 11.25 with an increment of 2.25, which represents varying the shear span from 1m to 5m with an increment of 1m. Two corrosion scenarios are considered including $\eta_v = \eta_l$ and $\eta_v = \eta_l + 20\%$ to study the influence of a/d on the corrosion-induced capacity reduction factor of .., which is shown in Figure 7-9 (a) and Figure 7-9 (b), respectively.

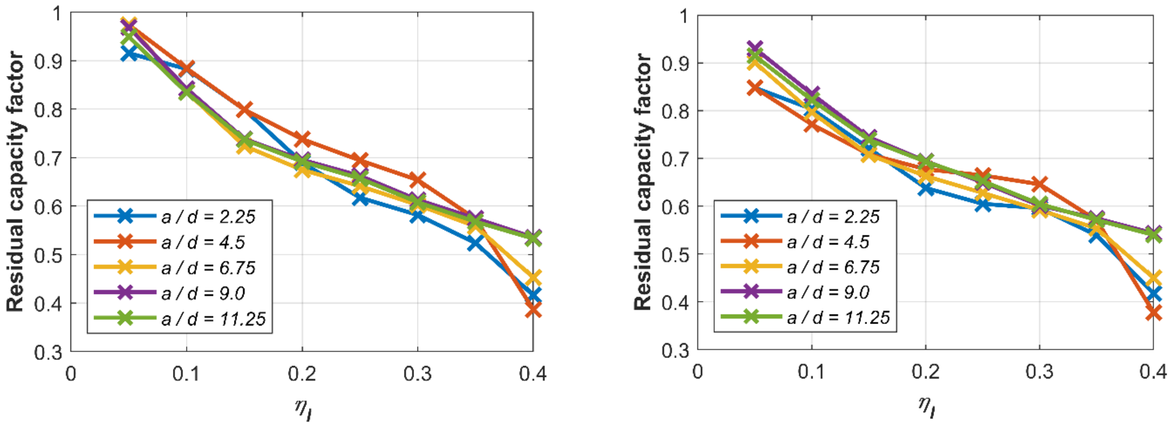

(a) (b)

Figure 7-9: The influence of shear span to effective depth ratio a/d on corrosion-induced capacity reduction: (a) $\eta_v = \eta_l$, and (b) $\eta_v = \eta_l + 20\%$

It is shown that the capacity reduction factor decreases (i.e., more reduction) with the increase of the corrosion degree (η_l, η_v) as expected. The influence of a/d on the capacity reduction is observed to be correlated with the corrosion degree without exhibiting an obvious tendency for both of the scenarios of $\eta_v = \eta_l$ and $\eta_v = \eta_l + 20\%$. In addition, by comparing Figure 7-9 (a) and Figure 7-9 (b), the capacity reduction from the corrosion scenario of $\eta_v = \eta_l + 20\%$ is larger than that from the corrosion scenario of $\eta_v = \eta_l$ especially for the loading scenarios of a/d = 2.25 and a/d = 4.5, where the shear failure dominates and the stirrups ratio plays an important role. This conclusion can also be observed in the following studies on other parameters, while repeated discussions are avoided in the following parametric studies due to the length limitation.

7.3.2.2 Tensile strands ratio

The influence of tensile strands ratio ρ_p is studied by varying its value from 0.6% to 1.3% with an increment of 0.175%, which covers the range of ρ_p for all virtually tested girders, i.e., from 0.573% to 1.260%. Two loading scenarios (i.e., $a/d = 2.25$ and $a/d = 11.25$ to represent shear-critical and flexure-dominated loadings) are considered to study the influence of ρ_p on the capacity reduction factor as shown in Figure 7-10 (a) ~ (b). The corrosion degrees for longitudinal steel and stirrups are considered to be the same.

It can be seen that for both the scenarios considered, the capacity reduction factor increases (i.e., less reduction) by increasing ρ_p without significant correlation effects with the corrosion degree (η_l, η_v). For the flexure-dominated loading scenario of $a/d = 11.25$, this indicates that increasing the tensile steel and the prestress force can reduce the corrosion-induced capacity loss. While for the shear-critical loading scenario of $a/d = 2.25$, this indicates that increasing the prestress force can reduce the corrosion-induced capacity loss, since it is shown in the following section that increasing the tensile steel only (i.e., without increasing the prestress force) has little effects on the corrosion-induced capacity reduction factor. In addition, the influence of ρ_p is slightly more important for the scenario of $a/d = 11.25$ compared with the scenario of $a/d = 2.25$ especially when the corrosion degree is large. This can be attributed to that longitudinal strands and prestress force play a more important role in flexural capacity compared with shear capacity.

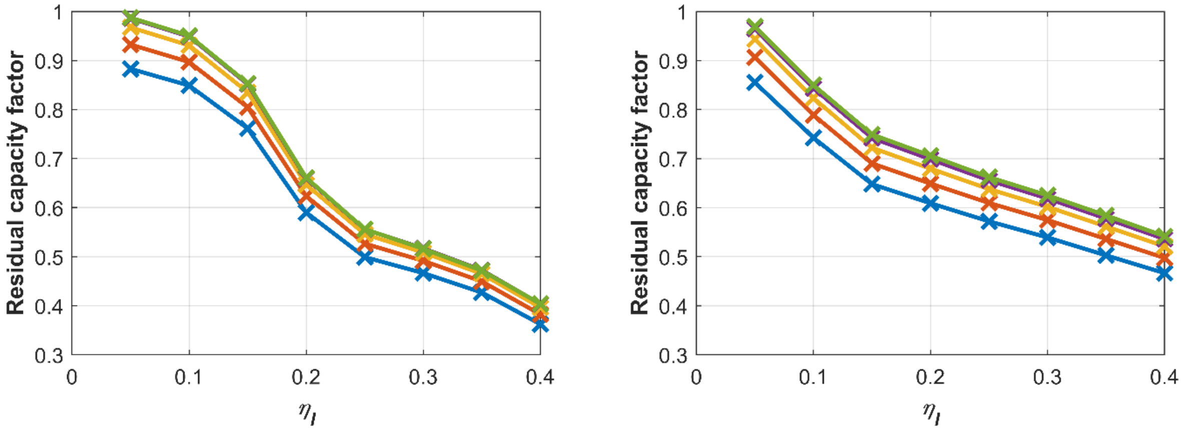

(a) (b)

Figure 7-10: The influence of tensile strands ratio ρ_p on corrosion-induced capacity reduction: (a) $a/d = 2.25$, and (b) $a/d = 11.25$

7.3.2.3 Tensile mild steel ratio

The influence of tensile mild steel ratio ρ_s is studied by varying its value from 0.1% to 1.7% with an increment of 0.4%, which covers the range of ρ_s for all virtually tested girders, i.e., from 0.145% to 1.662%. Two loading scenarios (i.e., $a/d = 2.25$ and $a/d = 11.25$) are considered to study the influence of ρ_s on the capacity reduction factor as shown in Figure 7-11 (a) ~ (b). The corrosion degrees for longitudinal steel and stirrups are considered to be the same.

It is shown that the ρ_s has a more significant influence for the scenario of $a/d = 11.25$ compared with the scenario of $a/d = 2.25$ since longitudinal steel play a more important role in flexural capacity compared with shear capacity. For the scenario of $a/d = 11.25$, the capacity reduction factor increases (i.e., less reduction) with the increase of ρ_s. This indicates again that increasing the tensile steel can reduce the corrosion-induced capacity loss for flexure-dominated loading scenarios.

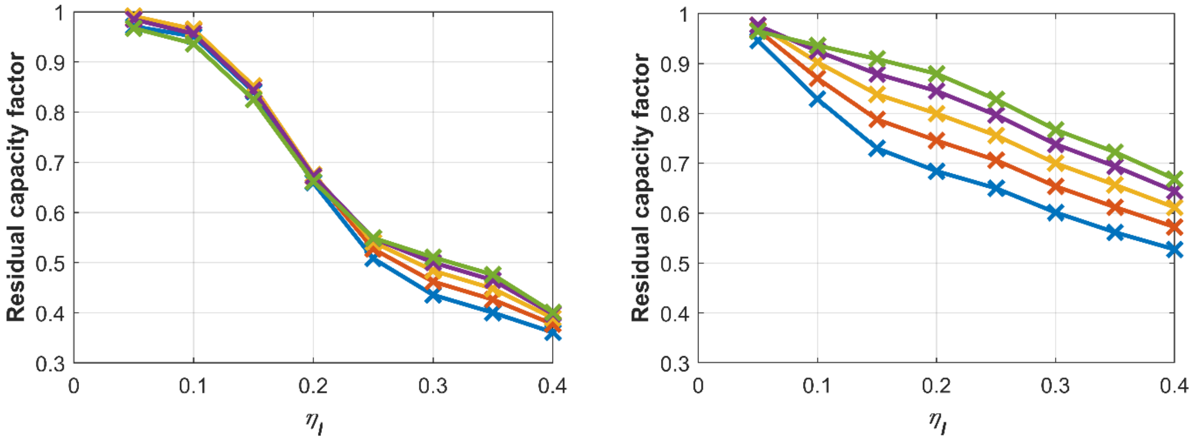

(a) (b)

Figure 7-11: The influence of tensile mild ratio ρ_s on corrosion-induced capacity reduction: (a) $a/d = 2.25$, and (b) $a/d = 11.25$

7.3.2.4 Stirrups ratio

The influence of stirrups ratio ρ_v is studied by varying its value from 0.3% to 0.7% with an increment of 0.1%, which covers the range of ρ_v for all virtually tested girders, i.e., from 0.373% to 0.654%. Two loading scenarios (i.e., $a/d = 2.25$ and $a/d = 11.25$) are considered to study the influence of ρ_v on the capacity reduction factor as shown in Figure 7-12 (a) ~ (b). The corrosion degrees for longitudinal steel and stirrups are considered to be the same. It is shown that the ρ_v has a slightly larger influence for the scenario of $a/d = 2.25$ compared with the scenario of $a/d = 11.25$ because stirrups play a more important role in shear capacity compared with flexural capacity. Despite this slight difference, the influence of ρ_v is observed to be relatively small for both the considered scenarios compared with other model parameters.

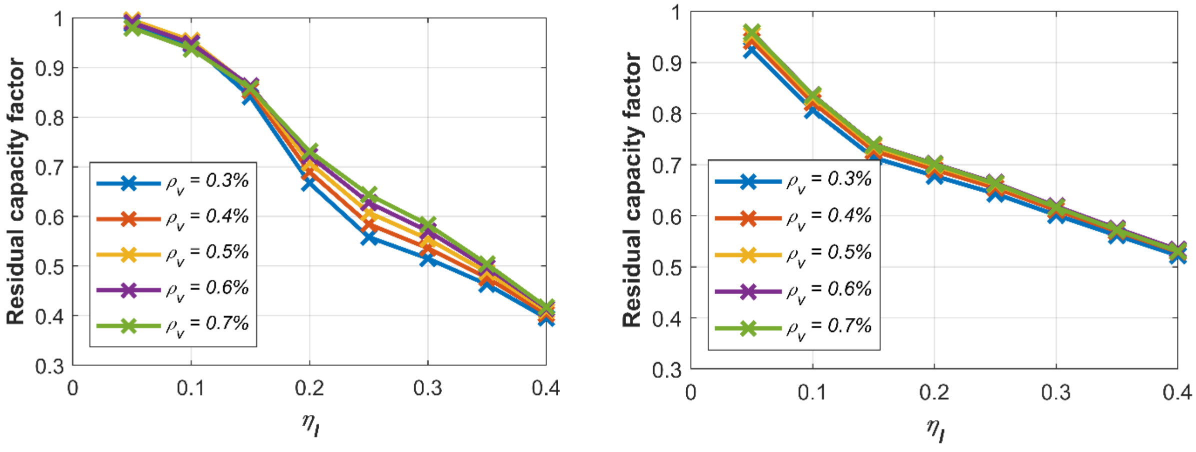

(a) (b)

Figure 7-12: The influence of tensile mild ratio ρ_v on corrosion-induced capacity reduction: (a) $a/d = 2.25$, and (b) $a/d = 11.25$

7.4 Probabilistic Load-carrying Capacity Model

7.4.1 Model Development

To facilitate reliability-based evaluation of bridge girder conditions, a model for predicting the load-carrying capacity of corroded PC girders will be needed. To this end, with the generated virtual experimental database, a probabilistic load-carrying capacity model $P(\mathbf{x})$ is developed, as shown in Eq. (7-19),

$$P(\mathbf{x}) = 0.25 f_c' b_w d \cdot C(\mathbf{x}) \tag{7-19}$$

where $C(\mathbf{x})$ is the normalized ultimate load-carrying capacity, the normalizing constant $0.25 f_c' b_w d$ is conventionally used as the upper limit of shear capacity by design codes (AASHTO 2017; CSA 2019), $\mathbf{x}$ is the vector of predictors, containing important influencing factors related to the design, corrosion and loading, i.e., $\mathbf{x} = \left\{ \eta_l, \eta_v, \frac{a}{d}, \frac{L}{h}, \rho_p, \rho_s, \rho_v, \frac{f_c'}{35}, \frac{f_{pu}}{1860}, \frac{f_y}{400} \right\}^T$. Similarly, GPR is adopted to develop a probabilistic model for the normalized load-carrying capacity of corroded PC girders as shown in Eq. (7-20).

$$C(\mathbf{x}) \sim GP\left(m(\mathbf{x}), k(\mathbf{x}, \mathbf{x}')\right) \tag{7-20}$$

The learned hyperparameter values based on the training dataset are summarized in Table 7-10.

Table 7-10: Summary of the learned hyperparameter values

Hyperparameter	σ_f	σ_{noise}	l_1	l_2	l_3	l_4	l_5	l_6	l_7	l_8	l_9	l_{10}
Value	0.168	0.009	0.092	0.883	2.738	29.19	2.506	3.414	0.881	1.116	2.245	2.396

Based on the learned GPR, the performance of the developed probabilistic load-carrying capacity model is assessed against both training and testing datasets as shown in Figure 7-13. Both the mean prediction and the 95% confidence interval prediction. It is shown that the developed model performs equally well for both training and testing datasets. The mean prediction curves successfully represent the central tendencies of the virtually tested results, while the majority of the virtually tested results fall within 95% confidence intervals. Specifically, 3164 out of 3332 points (i.e., 95.0%) and 774 out of 833 points (i.e., 92.9%) fall within the 95% confidence interval for the training and testing database, respectively. For practical use, the mean + 2 standard deviation (SD) can be used for the load-carrying capacity to be conservative. However, the probabilistic capacity model developed allows reliability analysis, or conditional reliability assessment of PC girders given a certain load level, rendering insights into the increase in probability of failure due to corrosion.

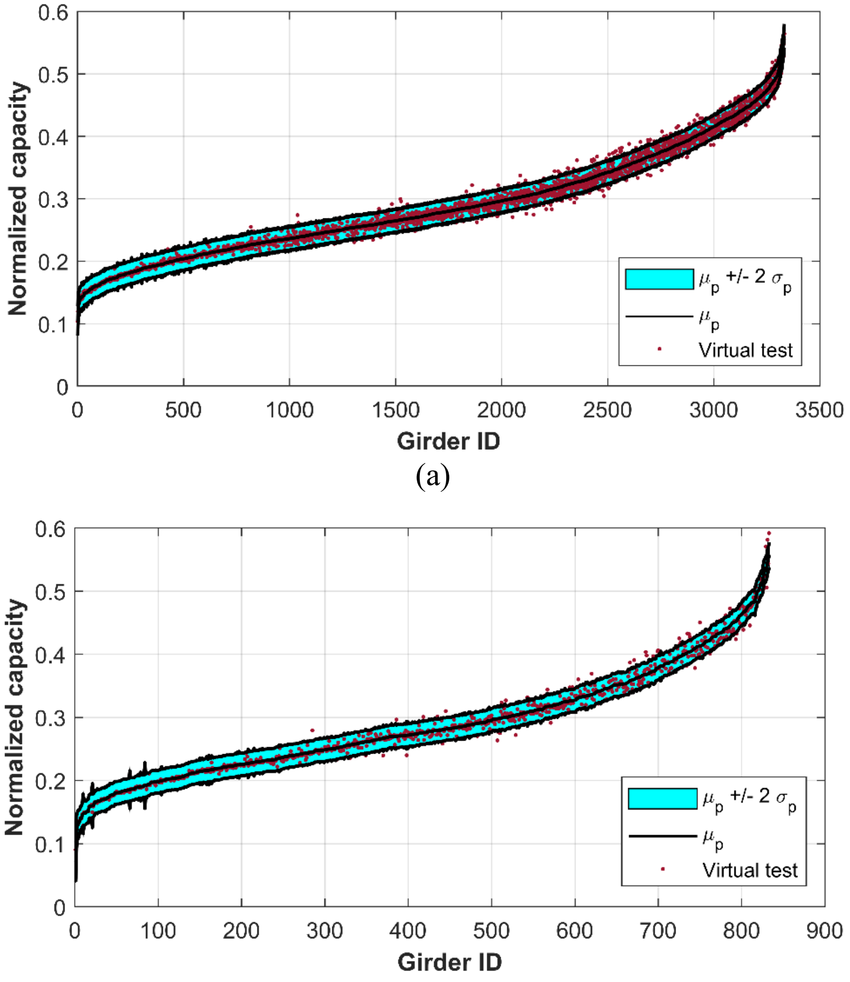

(a)

(b)

Figure 7-13: Performance of the developed load-carrying capacity model over: (a) training dataset, and (b) testing dataset

7.4.2 Application in Conditional Reliability Analysis

Based on the developed probabilistic load-carrying capacity model, the probabilistic load-carrying capacity can be calculated after considering the uncertainties in material and geometrical properties in the PC girder, in addition to the model prediction uncertainty (error). The resulted probabilistic capacity curve can be used to determine the conditional probability of attaining or exceeding a prescribed limit state for a given loading condition (Gardoni et al. 2002), i.e., conditional reliability analysis (or fragility analysis as widely used in earthquake engineering).

This application is to study the influence of corrosion on the conditional probability of failure under given (deterministic) load levels. To this end, the random variables with statistics summarized in Table 7-11 are considered. Direct Monte Carlo simulation is used with a large number of samples (i.e., 1 million) to obtain the load-carrying capacity under two loading scenarios: shear-critical and flexure-dominated loading scenarios with $a/d = 2.25$ and 11.25, respectively. Note that the large sample size of 1 million is utilized to guarantee a satisfactory accuracy when the failure probability is small, i.e., the failure probability with a mean and COV value of 10^{-4} and 0.1. The corrosion degrees for longitudinal steel and stirrups are considered to be the same.

Table 7-11: Summary of the statistic parameters

Parameter	Nominal	Mean	COV	Distribution	Reference
f'_c	35	48.3	0.12	Normal	Nowak and Szerszen (2003)
f_{pu}	1860	1943	0.025	Normal	Nowak and Szerszen (2003)
f_y	400	458	0.065	Normal	Nowak and Szerszen (2003)
b_w	–	309	0.04	Normal	Nowak and Szerszen (2003)
d	–	444.5	0.025	Normal	Nowak and Szerszen (2003)

As shown in Figure 7-14, the conditional probability of failure (i.e., fragility) curves shift to the left with the increase of corrosion degree for both shear-critical and flexure-dominated loading scenarios. This means that for a given load level, the probability of failure would increase. Based on the obtained curves, the conditional probability of failure under the ultimate limit state (ULS) loads, 298.6 kN for the shear-critical loading scenario with $a/d = 2.25$ and 233.4 kN for the flexure-dominated loading scenario with $a/d = 11.25$, are summarised in Figure 7-15 for PC grinders with different corrosion degrees. Note that when the conditional probability failure is equal to zero, it is indicated as a small value (i.e., 10^{-10}) to facilitate the plot in logarithmic scale. More details for the calculation of ULS loads can be found in Appendix G. It can be seen that with the increase of corrosion degree, the conditional probability of failure under the ULS load level (i.e., the “1 × ULS load” in Figure 7-15) increases from 0 to 0.37 and 0.15 for the shear-critical and flexure-dominated loading scenarios, respectively. When the load level is increased by a factor of 1.5 to the level of “1.5 × ULS load”, the conditional probability of failure also increases as expected. The obtained conditional failure probability curves can be used to facilitate the reliability-based safety assessment of corroded bridges with the measured corrosion degree and the designed load level in engineering practice.

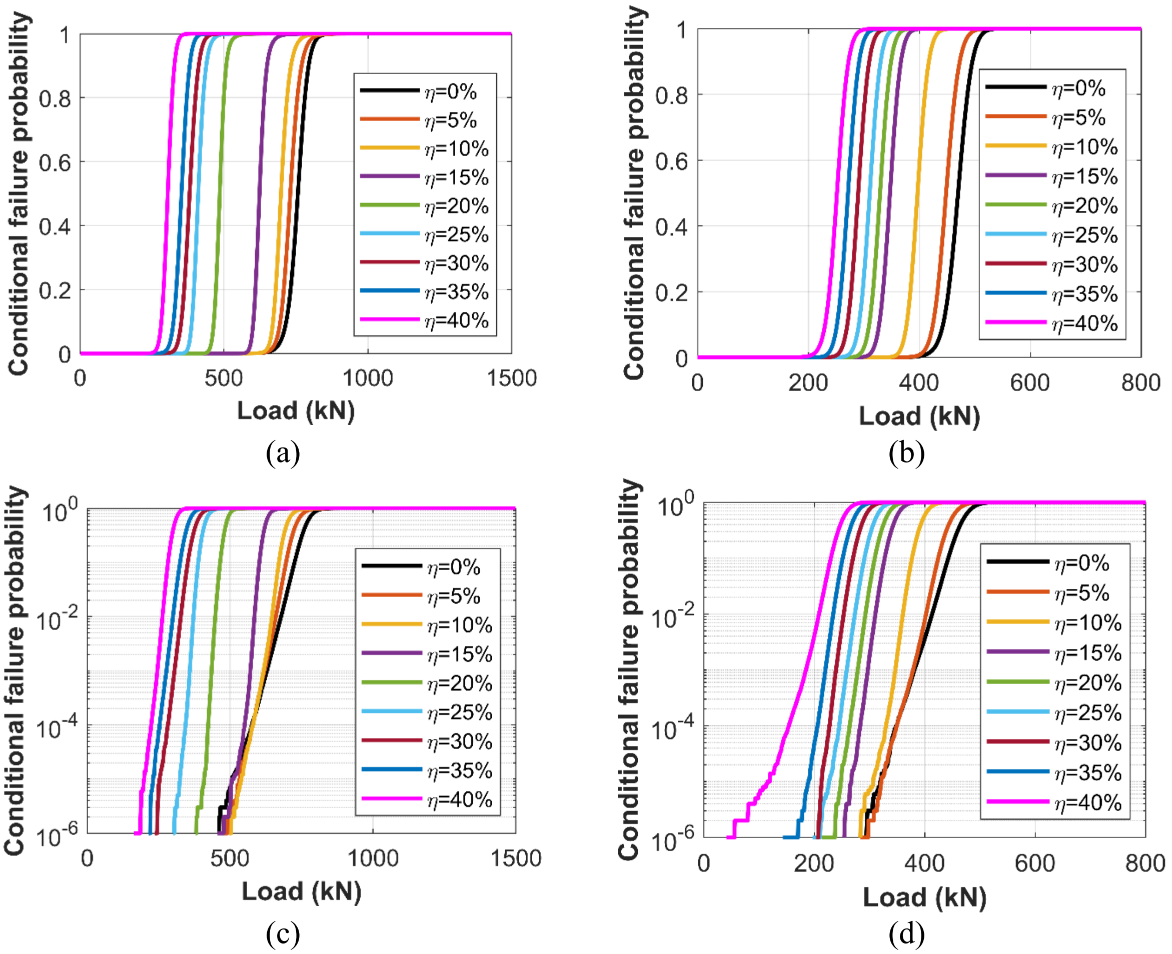

(a) (b)

(c) (d)

Figure 7-14: Fragility curves with different corrosion degrees (η): (a) a/d =2.25 with linear scale for the y-axis, (b) a/d =11.25 with linear scale for the y-axis, (c) a/d =2.25 with logarithmic scale for the y-axis, and (d) a/d =11.25 with logarithmic scale for the y-axis

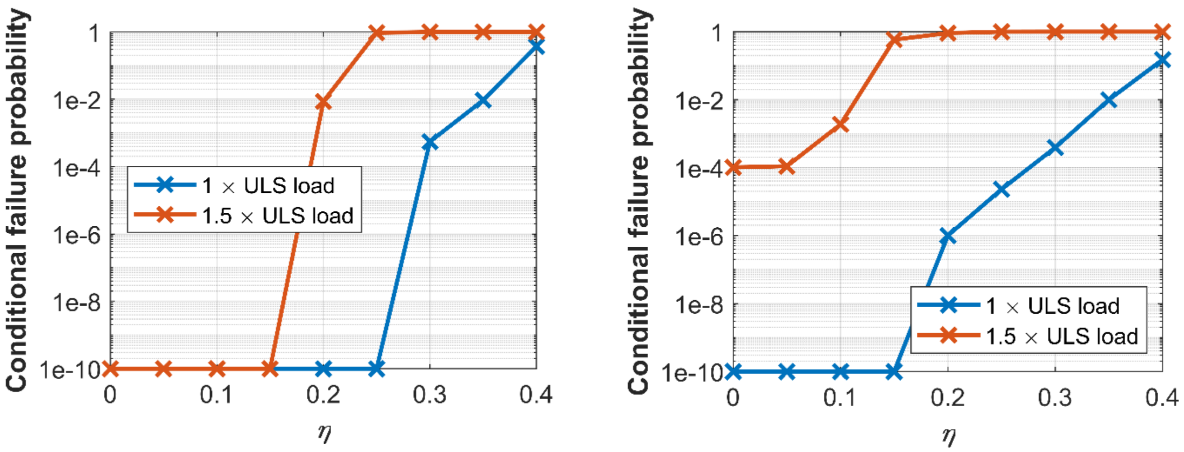

(a) (b)

Figure 7-15: Failure probability of corroded girders under ULS loads: (a) *a*/*d* =2.25, and (b) *a*/*d* =11.25

7.5 Summary

In this chapter, data-based prediction models for load-carrying capacity of corroded PC voided girders were developed to facilitate their fast screening and reliability-based evaluation. Firstly, a 2D continuum-based FE model for corroded PC girders was developed and validated by existing experimental tests. Then, a virtual experimental database of 4,165 PC girder tests considering various design, loading, and corrosion conditions was generated based on the developed FE model. With the generated virtual experimental database, the probabilistic capacity reduction factor model and the load-carrying capacity model were developed via Gaussian process regression to study the corrosion effects on capacity reduction and failure probability of corroded PC girders, respectively. Main conclusions and results in this chapter are summarised as below.

(1) Comparisons between experimental and numerical results indicated that the developed 2D FE model can serve as a reliable tool to simulate the residual behavior and failure modes of corroded PC girder, and provide satisfactory prediction results for the ultimate load carrying capacity under both shear-critical and flexure-dominated scenarios.

(2) The developed probabilistic capacity reduction model and the load-carrying capacity model showed equally well performance for both training and testing datasets. The mean prediction curves obtained from the developed model successfully represent the central tendencies of the virtually tested results with the majority of the virtually tested results falling within the mean ± 2 standard deviation (SD) intervals.

(3) Parametric study for the influence of different model parameters on the corrosion-induced load-carrying capacity reduction showed that increasing the tensile steel and the prestress force can reduce the corrosion-induced capacity loss under flexure-dominated loading scenarios, while increasing the prestress force can reduce the corrosion-induced capacity loss under shear-critical loading scenarios.

(4) Conditional reliability analysis showed that for both shear-critical and flexural-dominated loading scenarios, the failure probability of PC girders increases with the increase of corrosion degree. The obtained conditional failure probability curves can be used to guide the reliability-based bridge management with the measured corrosion degree and the designed load level in engineering practice.

CHAPTER 8: CONCLUSIONS AND RECOMMENDATIONS

8.1 Summary and Conclusions

To facilitate reliability-based safety assessment of both intact and corroded prestressed concrete (PC) bridge girders, reliable mechanics-based FE models and data-based capacity prediction models with probabilistic quantification of model uncertainty/error were developed and applied to PC bridge girders in this thesis. To this end, this thesis research was divided into three sub-objectives, namely mechanics-based shear capacity models for intact PC girders, experimental data-based shear capacity models for intact PC girders, and simulated data-based load-carrying capacity models for corroded PC girders. As such, conclusions are organized according to these three sub-objectives.

8.1.1 Sub-objective #1

In this sub-objective, a new flexure-shear coupled fibre beam element was developed based on the Timoshenko beam theory by utilizing multi-axial material constitutive models. The developed element was validated through a classic test series of shear-critical reinforced concrete (RC) beams from the literature and a PC girder recently tested under both shear-critical and flexure-dominated scenarios. Then, the developed element was applied to a representative nine-girder PC bridge in Alberta, Canada to study the bridge system behavior and load sharing of multi-girder bridges. Main conclusions and findings are summarized as follows.

(1) This thesis provides analysts and engineers with a reliable numerical tool for structural behavior analysis of RC/PC girders, as complementary to the widely used conventional fibre beam element.

(2) Compared with traditional fibre beam element, it is shown that the developed flexure-shear coupled fibre beam element is superior in predicting the load-deflection behavior of RC/PC

girders under shear-critical scenarios. Also, the developed FE model can be used to predict the shear capacity of RC/PC girders more accurately than commonly used code-based models.

(3) The bridge system behavior analysis shows that the nonlinearity (e.g., concrete cracking and connector yielding) plays an important role in internal force distribution and load sharing, while linear elastic assumption for load distribution factor can be unrealistic. It is also shown that the shear connector failure has a greater influence on the shear-connected girder system under flexure-dominated loading compared with that under shear-critical loading. One single shear connector failure out of the 40 shear connectors in the studied bridge can result in a capacity loss up to 14.32%.

8.1.2 Sub-objective #2

In this sub-objective, an experimental database containing 369 PC girders that failed in shear was compiled and utilized to probabilistically assess five widely utilized concrete structure and bridge design codes, i.e., ACI 318-19, AASHTO LRFD 2017, CSA A23.3:19, CSA S6:19 and *fib* MC 2010. In view of the fact that systematic error exists in those models, probabilistic correction terms were developed for each design code model through Bayesian linear regression and Gaussian process regression. The resulted probabilistic shear capacity prediction models were then applied to the fragility analysis of PC girders. Main conclusions and findings are summarized as follows.

(1) The assessment of shear capacity models from design codes indicates that although the detailed/general methods perform better than simplified methods, all design code models exhibit large conservative bias and prediction scatter. It is shown that the detailed method from ACI 318-19 exhibit the least conservatism, while the general procedure from AASHTO LRFD 2017 has the lowest prediction scatter.

(2) Comparisons show that the developed probabilistic model for intact PC girders outperformed the original design code model in both accuracy and precision. It is also shown that the systemic correlation between the model error and model parameters in the original design code model has been learned successfully by the developed probabilistic correction term.

(3) Fragility analysis results indicate that not considering the model error can lead to unreliable safety assessment in the design and management of PC girders and thus model error needs to be taken into account for reliability assessment, for which the probabilistic models developed in this study can be used.

8.1.3 Sub-objective #3

In this sub-objective, probabilistic prediction models for load-carrying capacity of corroded PC voided girders were developed. Firstly, a 2D continuum-based FE model for corroded PC girders was developed and validated by existing experimental tests. Then, a virtual experimental database of 4,165 PC girder tests considering various design, loading, and corrosion conditions was generated based on the developed FE model. With the generated virtual experimental database, the probabilistic capacity reduction factor model and the load-carrying capacity model were developed via Gaussian process regression to study the corrosion effects on capacity reduction and failure probability of corroded PC girders, respectively. Main conclusions and findings are summarized as follows.

(1) Comparisons between experimental and numerical results indicates that the developed 2D FE model for corroded PC girders can serve as a reliable tool to simulate the residual behavior and failure modes of corroded PC girders.

(2) Parametric study for the influence of different model parameters on the corrosion-induced load-carrying capacity reduction shows that increasing the tensile steel and the prestress

force can reduce the corrosion-induced capacity loss under flexure-dominated loading scenarios, while increasing the prestress force can reduce the corrosion-induced capacity loss under shear-critical loading scenarios.

(3) Conditional reliability analysis shows that for both shear-critical and flexural-dominated loading scenarios, the failure probability of PC girders increases with the increase of corrosion degree. The obtained conditional failure probability curves can be used to guide the reliability-based bridge management with the measured corrosion degree and the designed load level in engineering practice.

8.2 Contributions and Highlights

The contributions and highlights of the research work in this thesis are summarised as follows:

(1) A new flexure-shear coupled fibre beam element was developed in this thesis, which provides analysts and engineers with a computational efficient and accurate numerical tool for the behavior/failure analysis of PC girders.

(2) The system behavior and load-shearing of multi-girder PC bridges were studied under both flexure-dominated and shear-critical loading scenarios. The influence of losing (e.g., due to corrosion damage) and increasing (e.g., due to retrofit) shear connectors were also studied by parametric analyses. The insights gained from this study can provide guidance for future design and construction of multi-girder bridges.

(3) An experimental database containing 369 PC girders that failed in shear was compiled, based on which the model errors for shear capacity models from ACI 318-19, AASHTO LRFD 2017, CSA A23.3:19, CSA S6:19, and *fib* MC 2010 were quantified. These quantified model errors can be used as professional or corrective factors in reliability analysis or reliability-based code calibration of PC girders for analysts and engineers.

(4) Probabilistic shear capacity models for intact PC girders were developed, which can benefit shear capacity predictions with better accuracy and precision, as well as reliability/fragility analysis of PC girders with the model error considered.

(5) Probabilistic load-carrying capacity models for corroded PC girders were developed and applied to study how corrosion reduces the load-carrying capacity and increases the probability of failure for corroded PC girders. The resulted conditional failure probability curves can be used to guide the reliability-based bridge management with the measured corrosion degree and the designed load level in engineering practice.

8.3 Recommendations for Future Work

The presented work is limited in various aspects, and thus recommendations for future work are suggested as follows:

(1) The bonding between concrete and steel in the developed fibre beam element is assumed to be perfect, which limits its application to corroded RC/PC girders where the bond-slip plays an important role. The developed fibre beam element can be further enhanced in its formulation to consider bond-slip and thus applicable for corroded RC/PC girders.

(2) The developed fibre beam element only focuses on the monotonic behavior of RC/PC girders. With the adoption of cyclic MCFT material model, the developed fibre beam element can be extended to simulating the cyclic behavior of RC/PC members.

(3) The model error of developed FE models for both intact and corroded PC girders are neglected in this thesis. Although sufficient accuracy has been proved by comparison with experimental tests, systematic analysis/quantification of the model error from FE models are needed in the future to better serve FE-based reliability analysis.

(4) As an important ingredient in reliability-based safety assessment of bridges, this thesis focuses on probabilistic capacity model development. Its integration into reliability-based safety assessment framework where the uncertainty in loads is also considered and its application for reliability-based bridge evaluation will be the next step following this research project.

BIBLIOGRAPHY

ABAQUS. (2014) *ABAQUS Analysis User's Manual, Version 6.14*. Dassault Systems Simulia Corp, Providence, RI, USA.

ACI (American Concrete Institute). (2019). *Building Code Requirements for Structural Concrete*. ACI 318-19. Farmington Hills, MI: ACI

Alberta Transportation. (2019). *Bridge standard drawings*. Edmonton, AB, Canada

ASCE-ACI 426 (1973). The shear strength of reinforced concrete members. *Journal of the Structural Division*, *99*(6), 1091-1187.

ASCE. (2021). *2021 report card for American's infrastructure*. [Online] Available at: https://infrastructurereportcard.org/cat-item/bridges/

Aslani, F., & Dehestani, M. (2020). Probabilistic impacts of corrosion on structural failure and performance limits of reinforced concrete beams. *Construction and Building Materials*, *265*, 120316.

ASTM. (2014). *Standard Test Method for Compressive Strength of Cylindrical Concrete Specimens (ASTM C39/C39M-14).*

ASTM. (2016). *Standard Test Methods and Definitions for Mechanical Testing of Steel Products (ASTM A370-16)*

ASTM. (2016). *Standard Test Methods for Testing Multi-Wire Steel Prestressing Strand (ASTM A1061/1061M-16)*

ATENA. (2020). *ATENA Program Documentation, Part 1 - Theory*, Cervenka Consulting, Prague, Czech Republic

Barker, R. M., & Puckett, J. A. (2013). *Design of Highway Bridges: an LRFD Approach*. Hoboken, NJ: John Wiley & Sons, Inc.

Barr, P. J., Eberhard, M. O., & Stanton, J. F. (2001). Live-load distribution factors in prestressed concrete girder bridges. *Journal of Bridge Engineering*, *6*(5), 298-306.

Bažant, Z. P., & Oh, B. H. (1983). Crack band theory for fracture of concrete. *Matériaux et construction*, *16*(3), 155-177.

Belarbi, A., & Hsu, T. T. (1994). Constitutive laws of concrete in tension and reinforcing bars stiffened by concrete. *Structural Journal*, *91*(4), 465-474.

Belletti, B., Damoni, C., den Uijl, J. A., Hendriks, M. A., & Walraven, J. C. (2013). Shear resistance evaluation of prestressed concrete bridge beams: fib Model Code 2010 guidelines for level IV approximations. *Structural concrete*, *14*(3), 242-249.

Belletti, B., Vecchi, F., Bandini, C., Andrade, C., & Montero, J. S. (2020). Numerical evaluation of the corrosion effects in prestressed concrete beams without shear reinforcement. *Structural Concrete*, *21*(5), 1794-1809.

Bentz, E. C., Vecchio, F. J., & Collins, M. P. (2006). Simplified modified compression field theory for calculating shear strength of reinforced concrete elements. *ACI Materials Journal*, *103*(4), 614.

Bernardo, L. F. A., Lyrio, A. R. B., Silva, J. R. B., & Horowitz, B. (2018). Refined softened truss model with efficient solution procedure for prestressed concrete membranes. *Journal of Structural Engineering*, *144*(6), 04018045.

Bhargava, K., Mori, Y., & Ghosh, A. K. (2011). Time-dependent reliability of corrosion-affected RC beams—Part 1: Estimation of time-dependent strengths and associated variability. *Nuclear Engineering and Design*, *241*(5), 1371-1384.

Bitar, I., Grange, S., Kotronis, P., & Benkemoun, N. (2018). A comparison of displacement-based Timoshenko multi-fibre beams finite element formulations and elasto-plastic applications. *European Journal of Environmental and Civil Engineering*, *22*(4), 464-490.

Box, G. E., & Tiao, G. C. (1992). *Bayesian inference in statistical analysis* . John Wiley & Sons.

Bresler, B., & Scordelis, A. C. (1963). Shear strength of reinforced concrete beams. In *Journal Proceedings*, *60*(1), 51-74.

BRIME. (2001). *Research project no.: RO-97-SC.2220, The European union: transport research and technological development, final report*. Bridge management in Europe

Cairns, J., Plizzari, G. A., Du, Y., Law, D. W., & Franzoni, C. (2005). Mechanical properties of corrosion-damaged reinforcement. *ACI Materials Journal*, *102*(4), 256.

Canadian Infrastructure Report Card. (2019). *Canadian infrastructure report card 2019*. [Online] Available at: http://canadianinfrastructure.ca/downloads/canadian-infrastructure-report-card-2019.pdf

California Department of Transportation. (2014*). PC/PS concrete slab girder (without CIP deck)*. Sacramento, US

Castel, A., Coronelli, D., Vu, N. A., & François, R. (2011). Structural response of corroded, unbonded posttensioned beams. *Journal of Structural Engineering*, *137*(7), 761-771.

Ceresa, P., Petrini, L., Pinho, R., & Sousa, R. (2009). A fibre flexure–shear model for seismic analysis of RC-framed structures. *Earthquake engineering & structural dynamics*, *38*(5), 565-586.

Červenka, J., & Papanikolaou, V. K. (2008). Three dimensional combined fracture–plastic material model for concrete. *International journal of plasticity*, *24*(12), 2192-2220.

Choe, D. E., Gardoni, P., Rosowsky, D., & Haukaas, T. (2008). Probabilistic capacity models and seismic fragility estimates for RC columns subject to corrosion. *Reliability Engineering & System Safety*, *93*(3), 383-393.

Coronelli, D., & Gambarova, P. (2004). Structural assessment of corroded reinforced concrete beams: modeling guidelines. *Journal of structural engineering*, 130(8), 1214-1224.

Coronelli, D., Castel, A., François, R., & Cleland, D. (2009). Modelling the response of prestressed beams with corroded reinforcement. *European journal of environmental and civil engineering*, *13*(6), 653-669.

CSA (Canadian Standards Association). (2019a). *Design of concrete structures.* CSA A23.3:19. Ottawa, Canada: CSA

CSA (Canadian Standards Association). (2019b). *Canadian highway bridge design code.* CSA S6:19. Ottawa, Canada: CSA

Chehab, A. I., & Eamon, C. D. (2018). Regression-based adjustment factor to better estimate shear capacity for load-rating simple span PC girders. *Journal of Bridge Engineering*, *23*(5), 04018017.

Chou, J. S., Pham, T. P. T., Nguyen, T. K., Pham, A. D., & Ngo, N. T. (2020). Shear strength prediction of reinforced concrete beams by baseline, ensemble, and hybrid machine learning models. *Soft Computing*, *24*(5), 3393-3411.

Darmawan, M. S., & Stewart, M. G. (2007). Spatial time-dependent reliability analysis of corroding pretensioned prestressed concrete bridge girders. *Structural Safety*, *29*(1), 16-31.

Darmawan, M.S., (2009). Pitting corrosion model for partial prestressed concrete (PC) structures in a chloride environment. *IPTEK The Journal for Technology and Science*, *20*(3).

D'Ambrisi, A., & Filippou, F. C. (1999). Modeling of cyclic shear behavior in RC members. *Journal of Structural Engineering*, *125*(10), 1143-1150.

Del Vecchio, C., Del Zoppo, M., Di Ludovico, M., Verderame, G. M., & Prota, A. (2017). Comparison of available shear strength models for non-conforming reinforced concrete columns. *Engineering Structures*, *148*, 312-327.

DIANA. (2021). *DIANA finite element analysis user's manual release 10.5*, Delft, Netherlands

Dunker, K. F., & Rabbat, B. G. (1993). Performance of prestressed concrete bridges in the united states - the first 40 years. *PCI Journal, 37*(3), 48–64.

Du, J. S., & Au, F. T. K. (2005). Deterministic and reliability analysis of prestressed concrete bridge girders: comparison of the Chinese, Hong Kong and AASHTO LRFD Codes. *Structural safety*, *27*(3), 230-245.

Ehrlich, D., & Armero, F. (2005). Finite element methods for the analysis of softening plastic hinges in beams and frames. *Computational Mechanics*, *35*(4), 237-264.

Elghazy, M., El Refai, A., Ebead, U., & Nanni, A. (2018). Experimental results and modelling of corrosion-damaged concrete beams strengthened with externally-bonded composites". *Engineering Structures*, 172, 172-186.

Ellingwood, B.; Galambos, T. V.; MacGregor, J. G.; and Cornell, C. A. (1980). Development of a Probability Based Load Criterion for American National Standard A58, *NBS Special Report* 577, U.S. Department of Commerce, National Bureau of Standards.

Eurocode 2 (2004). *Eurcode 2: Design of concrete structures – Part 1-1: General rules for buildings*. EN 1992-1-1. Brussels, Belgium: Eurocode 2

fib (International Federation for Structural Concrete). (2013). *fib Model Code for Concrete Structures 2010*. Lausanne, Switzerland: *fib*

Feng, D. C., Wu, G., Sun, Z. Y., & Xu, J. G. (2017). A flexure-shear Timoshenko fibre beam element based on softened damage-plasticity model. *Engineering Structures*, *140*, 483-497.

Feng, D. C., & Xu, J. (2018). An efficient fibre beam-column element considering flexure–shear interaction and anchorage bond-slip effect for cyclic analysis of RC structures. *Bulletin of Earthquake Engineering*, *16*(11), 5425-5452.

Ferreira, D., Bairán, J., & Marí, A. (2015). Efficient 1D model for blind assessment of existing bridges: simulation of a full-scale loading test and comparison with higher order continuum models. *Structure and Infrastructure Engineering*, *11*(10), 1383-1397.

Filippou, F. C., & Saritas, A. (2006). A beam finite element for shear-critical RC beams. *ACI Special Publications*, *237*, 295-310.

Fu, B., & Feng, D. C. (2021). A machine learning-based time-dependent shear strength model for corroded reinforced concrete beams. *Journal of Building Engineering*, *36*, 102118.

Gardoni, P., Der Kiureghian, A., & Mosalam, K. M. (2002). Probabilistic capacity models and fragility estimates for reinforced concrete columns based on experimental observations. *Journal of Engineering Mechanics*, *128*(10), 1024-1038.

Gokkaya, B. U., Baker, J. W., & Deierlein, G. G. (2016). Quantifying the impacts of modeling uncertainties on the seismic drift demands and collapse risk of buildings with implications on seismic design checks. *Earthquake Engineering & Structural Dynamics*, *45*(10), 1661-1683.

Guo, T., Frangopol, D. M., Han, D., & Chen, Y. (2011). Probabilistic assessment of deteriorating prestressed concrete box-girder bridges under increased vehicle loads and aggressive environment. *Journal of Performance of Constructed Facilities*, *25*(6), 564-576.

Hacking, I. (1975). *The Emergence of Probability*. Cambridge University Press, Cambridge, 1975.

Harries, K.A. (2009). Structural testing of prestressed concrete girders from the Lake View Drive Bridge. *Journal of Bridge Engineering*, *14*(2), 78-92.

Hamutçuoğlu, O. M., & Scott, M. H. (2009). Finite element reliability analysis of bridge girders considering moment–shear interaction. *Structural Safety*, *31*(5), 356-362.

Hansen, J. L., Hanna, K. E., & Tadros, M. K. (2012). Simplified transverse post-tensioning construction and maintenance of adjacent box girders. *PCI journal*, *57*(2).

Hoffman, M. D., & Gelman, A. (2014). The No-U-Turn sampler: adaptively setting path lengths in Hamiltonian Monte Carlo. *J. Mach. Learn. Res.*, *15*(1), 1593-1623.

Holický, M., Retief, J. V., & Sýkora, M. (2016). Assessment of model uncertainties for structural resistance. *Probabilistic Engineering Mechanics*, *45*, 188-197.

Hossain, T., Okeil, A. M., & Cai, C. S. (2014). Field test and finite-element modeling of a three-span continuous-girder bridge. *Journal of Performance of Constructed Facilities*, *28*(1), 136-148.

Hsu, T. T. (1988). Softened truss model theory for shear and torsion. *Structural Journal*, *85*(6), 624-635.

Hsu, T. T., & Zhu, R. R. (2002). Softened membrane model for reinforced concrete elements in shear. *Structural Journal*, *99*(4), 460-469.

Hsu, T. T. C., & Mo, Y. L. (2010). *Unified theory of concrete structures*. New York: Wiley.

Huang, L. (2020). *Finite Element-based Parametric and Probabilistic Analysis of Structural Deterioration in Corroded Pre-stressed Concrete Girders* (M.Sc. thesis). University of Alberta, Edmonton, Alberta

Huang, L., Liu, J., Wu, Z., Tomlinson, D., Cruz-Noguez, C., Alexander, J., & Li, Y. (2022). Finite Element-based Parametric and Forensic Analysis of Corrosion-induced Structural Deterioration in Prestressed Concrete Bridge Girders. *Canadian Journal of Civil Engineering*.

Hughs, E., & Idriss, R. (2006). Live-load distribution factors for prestressed concrete, spread box-girder bridge. *Journal of bridge engineering*, *11*(5), 573-581.

Ian Gilbert, R. (2007). Tension stiffening in lightly reinforced concrete slabs. *Journal of Structural Engineering*, *133*(6), 899-903.

Jiang, K., Zhao, O., & Tan, K. H. (2020). Experimental and numerical study of S700 high strength steel double shear bolted connections in tension. *Engineering Structures*, **225**, 111175.

Jiang, C. S., & Liang, G. Q. (2021). Modeling shear strength of medium-to ultra-high-strength concrete beams with stirrups using SVR and genetic algorithm. *Soft Computing*, *25*(16), 10661-10675.

Jnaid, F., & Aboutaha, R. S. (2016). Residual flexural strength of corroded reinforced concrete beams. *Engineering Structures*, *119*, 198-216.

Kennedy, M. C., & O'Hagan, A. (2001). Bayesian calibration of computer models. *Journal of the Royal Statistical Society: Series B (Statistical Methodology)*, *63*(3), 425-464

Kim, T. S., & Kuwamura, H. (2007). Finite element modeling of bolted connections in thin-walled stainless steel plates under static shear. *Thin-Walled Structures*, **45**(4), 407-421.

Kioumarsi, M., Benenato, A., Ferracuti, B., & Imperatore, S. (2021). Residual flexural capacity of corroded prestressed reinforced concrete beams. *Metals*, *11*(3), 442.

Kivell, A., Palermo, A., & Scott, A. (2015). Complete model of corrosion-degraded cyclic bond performance in reinforced concrete. *Journal of Structural Engineering*, *141*(9), 04014222.

Kodur, V., Kand, S., & Khaliq, W. (2012). Effect of temperature on thermal and mechanical properties of steel bolts. *Journal of Materials in Civil Engineering*, **24**(6), 765-774.

Leng, Y., Zhang, J., Jiang, R., & Xiao, Y. (2020). Experimental Study on the System Performance of Adjacent Precast Concrete Box Beam Bridges. *Advances in Civil Engineering*, *2020*.

Li, Z. X., Gao, Y., & Zhao, Q. (2016). A 3D flexure–shear fibre element for modeling the seismic behavior of reinforced concrete columns. *Engineering Structures*, *117*, 372-383.

Liu, J., Huang, L., Wu, Z., Tomlinson, D., Cruz-Noguez, C., Alexander, J., Adeeb, S., & Li, Y. (2021). Development of enhanced fibre beam element with multi-axial material constitutive models for reinforced/prestressed concrete girders. *Engineering Structures,* 248(1), 113289

Lu, Z. H., Li, H., Li, W., Zhao, Y. G., & Dong, W. (2018). An empirical model for the shear strength of corroded reinforced concrete beam. *construction and Building materials*, *188*, 1234-1248.

Ma, Y., Zhang, J., Wang, L., & Liu, Y. (2013). Probabilistic prediction with Bayesian updating for strength degradation of RC bridge beams. *Structural Safety*, *44*, 102-109.

MacGregor, J. G., Kennedy, D. L., Bartlett, F. M., & Chernenko, D. (1997). Design criteria and load and resistance factors for the Confederation Bridge. *Canadian Journal of Civil Engineering*, *24*(6), 882.

Marini, A., & Spacone, E. (2006). Analysis of reinforced concrete elements including shear effects. *ACI Structural Journal*, *103*(5), 645-655.

Mast, R. F., Dawood, M., Rizkalla, S. H., & Zia, P. (2008). Flexural strength design of concrete beams reinforced with high-strength steel bars. *ACI Structural Journal*, *105*(5), 570.

Mathy, B., Demars, P., Roisin, F. and Wouters, M. (1996). Investigation and strengthening study of twenty damaged bridges: A Belgium case history. In *Bridge management 3. Inspection, maintenance and repair. Papers presented at the third international conference on bridge management,* University of Surrey, Guildford, UK, 14-17.

Massey Jr, F. J. (1951). The Kolmogorov-Smirnov test for goodness of fit. *Journal of the American statistical Association*, *46*(253), 68-78.

Maupin, K. A., & Swiler, L. P. (2020). Model discrepancy calibration across experimental settings. *Reliability Engineering & System Safety*, 106818.

Metwally, I. M. (2012). Evaluate the capability and accuracy of response-2000 program in prediction of the shear capacities of reinforced and prestressed concrete members. *HBRC Journal*, *8*(2), 99-106.

Mirza, S. A., Kikuchi, D. K., & MacGregor, J. G. (1980). Flexural strength reduction factor for bonded prestressed concrete beams. *Journal Proceedings, 77*(4), 237-246.

MOHURD (Ministry of Housing and Urban-Rural Development of the People's Republic of China). (2015). *Code for design of concrete structures.* GB 50010-2010. Beijing, China: MOHURD

Naderpour, H., & Mirrashid, M. (2020). Bio-inspired predictive models for shear strength of reinforced concrete beams having steel stirrups. *Soft Computing*, *24*(16), 12587-12597.

Naito, C., Brunn, G., Parent, G., & Tate, T. (2005). *Comparative performance of high early strength and self consolidating concrete for use in precast bridge beam construction* (No. 05-03). ATLSS, Lehigh University.

Nakamura, E., Avendaño, A. R., & Bayrak, O. (2013). Shear database for prestressed concrete members. *ACI Structural Journal*, *110*(6), 909.

Ning, C. L., & Li, B. (2017). Probabilistic development of shear strength model for reinforced concrete squat walls. *Earthquake Engineering & Structural Dynamics*, *46*(6), 877-897.

Ning, C. L., & Li, B. (2018). Analytical probabilistic model for shear strength prediction of reinforced concrete beams without shear reinforcement. *Advances in Structural Engineering*, *21*(2), 171-184.

Nowak, A. S., & Grouni, H. N. (1983). Development of design criteria for transit guideways. *Journal Proceedings, 80*(5), 387-395.

Nowak, A. S., & Zhou, J. (1990). System reliability models for bridges. *Structural Safety*, *7*(2-4), 247-254.

Nowak, A. S., & Szerszen, M. M. (2003). Calibration of design code for buildings (ACI 318): Part 1-Statistical models for resistance. *ACI Structural Journal*, *100*(3), 377-382

Olalusi, O. B., & Awoyera, P. O. (2021). Shear capacity prediction of slender reinforced concrete structures with steel fibres using machine learning. *Engineering Structures*, *227*, 111470.

Pang, X. B. D., & Hsu, T. T. (1996). Fixed angle softened truss model for reinforced concrete. *Structural Journal*, *93*(2), 196-208.

Potisuk, T., Higgins, C. C., Miller, T. H., & Yim, S. C. (2011). Finite element analysis of reinforced concrete beams with corrosion subjected to shear. *Advances in Civil Engineering*, *2011*.

Prayogo, D., Cheng, M. Y., Wu, Y. W., & Tran, D. H. (2020). Combining machine learning models via adaptive ensemble weighting for prediction of shear capacity of reinforced-concrete deep beams. *Engineering with Computers,* 36(3), 1135-1153.

Ramirez, J. A., & Aguilar, G. (2005). *Shear reinforcement requirements for high-strength concrete bridge girders* (No. C-36-56III). Joint Transportation Research Project, Purdue University.

Ramseyer, C., & Kang, T. H.-K. (2012). Post-damage repair of prestressed concrete girders. *International Journal of Concrete Structures and Materials*, 6(3), 199–207.

Reineck, K. H., Bentz, E. C., Fitik, B., Kuchma, D. A., & Bayrak, O. (2013). ACI-DAfStb Database of Shear Tests on Slender Reinforced Concrete Beams without Stirrups. *ACI Structural Journal,* 110(5).

Reineck, K. H., Bentz, E., Fitik, B., Kuchma, D. A., & Bayrak, O. (2014). ACI-DAfStb Databases for Shear Tests on Slender Reinforced Concrete Beams with Stirrups. *ACI Structural Journal,* 111(5).

Rericha, P. (1991). Layer model of bending-shear failure in RC plates and beams. *Journal of Structural Engineering*, *117*(10), 2865-2883.

Sadeghian, V., & Vecchio, F. J. (2018). The modified compression field theory: then and now. *ACI Struct J, Special Publication*. SP-328:3.1-3.20

Sajid, H. U., & Kiran, R. (2018). Influence of high stress triaxiality on mechanical strength of ASTM A36, ASTM A572 and ASTM A992 steels. *Construction and Building Materials*, **176**, 129-134.

Salvatier, J., Wiecki, T. V., & Fonnesbeck, C. (2016). Probabilistic programming in Python using PyMC3. *PeerJ Computer Science*, *2*, e55.

Saritas, A. (2006). *Mixed formulation frame element for shear critical steel and reinforced concrete members.* Doctoral dissertation, University of California, Berkeley.

Semendary, A. A., Steinberg, E. P., Walsh, K. K., & Barnard, E. (2017). Live-load moment-distribution factors for an adjacent precast prestressed concrete box beam bridge with reinforced UHPC shear key connections. *Journal of Bridge Engineering*, *22*(11), 04017088.

Shah, B. N., Sennah, K., Kianoush, M. R., Tu, S., & Lam, C. (2007). Experimental study on prefabricated concrete bridge girder-to-girder intermittent bolted connections system. *Journal of Bridge Engineering*, *12*(5), 570-584.

Sharma, H., Gardoni, P., & Hurlebaus, S. (2014). Probabilistic demand model and performance-based fragility estimates for RC column subject to vehicle collision. *Engineering Structures*, *74*, 86-95.

Sigrist, V. (2011). Generalized Stress Field Approach for Analysis of Beams in Shear. *ACI Structural Journal*, *108*(4).

Sigrist, V., Bentz, E., Ruiz, M. F., Foster, S., & Muttoni, A. (2013). Background to the fib Model Code 2010 shear provisions–part I: beams and slabs. *Structural Concrete*, *14*(3), 195-203.

Soltani, M., AlilooeeDolatabad, A., Akurang, E., & Abu-Abaileh, A. (2021). A Statistical Approach to Modeling the Reduced Flexural Capacity of Corrosion-Damaged Reinforced Concrete Beams. *ACI Structural Journal*, *118*(4).

Somo, S., & Hong, H. P. (2006). Modeling error analysis of shear predicting models for RC beams. *Structural safety*, *28*(3), 217-230.

Song, H. W., You, D. W., Byun, K. J., & Maekawa, K. (2002). Finite element failure analysis of reinforced concrete T-girder bridges. *Engineering Structures*, *24*(2), 151-162.

Song, J., Kang, W. H., Kim, K. S., & Jung, S. (2010). Probabilistic shear strength models for reinforced concrete beams without shear reinforcement. *Structural engineering & mechanics*, 11(1), 15.

Spacone, E., Filippou, F. C., & Taucer, F. F. (1996a). Fibre beam–column model for non-linear analysis of R/C frames: Part I. Formulation. *Earthquake Engineering & Structural Dynamics*, *25*(7), 711-725.

Spacone, E., Filippou, F. C., & Taucer, F. F. (1996b). Fibre beam–column model for non-linear analysis of R/C frames: part II. Applications. *Earthquake Engineering & Structural Dynamics*, *25*(7), 727-742.

Stevens, N. J., Uzumeri, S. M., & Will, G. T. (1991). Constitutive model for reinforced concrete finite element analysis. *Structural Journal*, *88*(1), 49-59.

Stewart, M. G., & Rosowsky, D. V. (1998). Time-dependent reliability of deteriorating reinforced concrete bridge decks. *Structural safety*, *20*(1), 91-109.

Stramandinoli, R. S., & La Rovere, H. L. (2012). FE model for nonlinear analysis of reinforced concrete beams considering shear deformation. *Engineering Structures*, *35*, 244-253.

Sýkora, M., Holický, M., & Krejsa, J. (2013). Model uncertainty for shear resistance of reinforced concrete beams with shear reinforcement according to EN 1992-1-1.

Sykora, M., Krejsa, J., Mlcoch, J., Prieto, M., & Tanner, P. (2018). Uncertainty in shear resistance models of reinforced concrete beams according to fib MC2010. *Structural Concrete*, *19*(1), 284-295.

Tabsh, S. W., & Nowak, A. S. (1991). Reliability of highway girder bridges. *Journal of structural engineering*, *117*(8), 2372-2388.

Thoft-Cristensen, P., & Baker, M. J. (2012). *Structural reliability theory and its applications*. Springer Science & Business Media.

Tošic´, N., Marinkovic´, S., & Ignjatovic´, I. (2016). A database on flexural and shear strength of reinforced recycled aggregate concrete beams and comparison to Eurocode 2 predictions. *Construction and Building Materials, 127*, 932-944

Tu, B., Dong, Y., & Fang, Z. (2019). Time-dependent reliability and redundancy of corroded prestressed concrete bridges at material, component, and system levels. *Journal of Bridge Engineering*, *24*(9), 04019085.

Vecchio, F. J., & Collins, M. P. (1986). The modified compression-field theory for reinforced concrete elements subjected to shear. *ACI J.*, *83*(2), 219-231.

Vecchio, F. J. (1989). Nonlinear finite element analysis of reinforced concrete membranes. *ACI Structural Journal*, *86*(1), 26-35.

Vecchio, F. J., & Collins, M. P. (1993). Compression response of cracked reinforced concrete. *Journal of structural engineering*, *119*(12), 3590-3610.

Vecchio, F. J. (2000). Disturbed stress field model for reinforced concrete: formulation. *Journal of structural engineering*, *126*(9), 1070-1077. https://doi.org/10.1061/(ASCE)0733-9445(2000)126:9(1070)

Vecchio, F. J., & Shim, W. (2004). Experimental and analytical reexamination of classic concrete beam tests. *Journal of Structural Engineering*, *130*(3), 460-469.

Wang, G. L., & Meng, S. P. (2008). Modified strut-and-tie model for prestressed concrete deep beams. *Engineering Structures*, *30*(12), 3489-3496.

Wang, L., Zhang, X., Zhang, J., Ma, Y., Xiang, Y., & Liu, Y. (2014). Effect of insufficient grouting and strand corrosion on flexural behavior of PC beams. *Construction and Building Materials*, *53*, 213-224.

Wang, L., Zhang, X., Zhang, J., Dai, L., & Liu, Y. (2017a). Failure analysis of corroded PC beams under flexural load considering bond degradation. *Engineering Failure Analysis*, *73*, 11-24.

Wang, L., Zhang, X., Zhang, J., Yi, J., & Liu, Y. (2017b). Simplified model for corrosion-induced bond degradation between steel strand and concrete. *Journal of Materials in Civil Engineering*, *29*(4), 04016257.

Wang, L., Hu, Z., Yi, J., Dai, L., Ma, Y., & Zhang, X. (2020). Shear Behavior of Corroded Post-Tensioned Prestressed Concrete Beams with Full/Insufficient Grouting. *KSCE Journal of Civil Engineering*, *24*(6), 1881-1892.

Wang, X., Mao, X., Frangopol, D. M., Dong, Y., Wang, H., Tao, P., ... & Tang, S. (2021). Full-scale experimental and numerical investigation on the ductility, plastic redistribution, and redundancy of deteriorated concrete bridges. *Engineering Structures*, *234*, 111930.

Williams, C. K., & Rasmussen, C. E. (2006). *Gaussian processes for machine learning*. Cambridge, MA: MIT press.

Woodward, R.J. and Williams, F.W. (1989). Collapse of Ynys-Y-Gwas Bridge, West-Glamorgan-Discussion. *Proceedings of the Institution of Civil Engineers Part 1-Design and Construction*, *86*, pp.1177-1191.

Wong, P. S., Vecchio, F. J., & Trommels, H. (2013). *Vector2 & Formworks user's manual second edition*. University of Toronto, Canada.

Wu, Z. (2021). *Flexural and Shear Response of Deteriorated Prestressed Concrete Girders Taken from a Decommissioned Bridge in Alberta* (M.Sc. thesis). University of Alberta, Edmonton, Alberta

Xu, S. Y., & Zhang, J. (2012). Axial–shear–flexure interaction hysteretic model for RC columns under combined actions. *Engineering Structures*, *34*, 548-563.

Yang, Y., Peng, J., Liu, X., Cai, S. C., & Zhang, J. (2021). Probability analysis of web cracking of corroded prestressed concrete box-girder bridges considering aleatory and epistemic uncertainties. *Engineering Structures*, *228*, 111486.

Ye, Z., Zhang, W., & Gu, X. (2018). Deterioration of shear behavior of corroded reinforced concrete beams. *Engineering Structures*, *168*, 708-720.

Yetilmezsoy, K., Sihag, P., Kıyan, E., & Doran, B. (2021). A benchmark comparison and optimization of Gaussian process regression, support vector machines, and M5P tree model in approximation of the lateral confinement coefficient for CFRP-wrapped rectangular/square RC columns. *Engineering Structures*, *246*, 113106.

Yousif, Z., & Hindi, R. (2007). AASHTO-LRFD live load distribution for beam-and-slab bridges: Limitations and applicability. *Journal of Bridge Engineering*, *12*(6), 765-773.

Yu, T., Teng, J. G., Wong, Y. L., & Dong, S. L. (2010). Finite element modeling of confined concrete-II: Plastic-damage model. *Engineering structures*, *32*(3), 680-691.

Yu, B., Liu, S., & Li, B. (2019). Probabilistic calibration for shear strength models of reinforced concrete columns. *Journal of Structural Engineering*, *145*(5), 04019026.

Yuan, J., & Graybeal, B. (2016). Full-scale testing of shear key details for precast concrete box-beam bridges. *Journal of Bridge Engineering*, *21*(9), 04016043.

Zandi Hanjari, K., Kettil, P., & Lundgren, K. (2011). Analysis of mechanical behavior of corroded reinforced concrete structures. *ACI Structural Journal*, *108*(5), 532-541.

Zhang, X., Wang, L., Zhang, J., Ma, Y., & Liu, Y. (2017a). Flexural behavior of bonded post-tensioned concrete beams under strand corrosion. *Nuclear Engineering and Design*, *313*, 414-424.

Zhang, X., Wang, L., Zhang, J., & Liu, Y. (2017b). Corrosion-induced flexural behavior degradation of locally ungrouted post-tensioned concrete beams. *Construction and Building Materials*, *134*, 7-17.

Zhang, J., Sun, Y., Li, G., Wang, Y., Sun, J., & Li, J. (2020). Machine-learning-assisted shear strength prediction of reinforced concrete beams with and without stirrups. *Engineering with Computers*, 1-15.

Zhu, R. R., Hsu, T. T., & Lee, J. Y. (2001). Rational shear modulus for smeared-crack analysis of reinforced concrete. *Structural Journal*, *98*(4), 443-450.

Zhu, D., Yuan, P., & Dong, Y. (2021). Probabilistic performance of coastal bridges under hurricane waves using experimental and 3D numerical investigations. *Engineering Structures*, *242*, 112493.

Zsutty, T. C. (1968). Beam shear strength prediction by analysis of existing data. *Journal Proceedings, 65*(11), 943-951.

APPENDIX A: IMPLEMENTATION AND VALIDATION OF THE MCFT MATERIAL MODEL IN MATLAB

In order to consider the coupling effect of shear and flexural behavior in reinforced concrete or pre-stressed concrete girders, a well-recognized material constitutive model, the modified compression field theory (MCFT), can be used. Before integrating it into the finite element formulation of the new fibre beam element, the MCFT is implemented in *MATLAB* and applied to reproduce the response of the specimen PV20 (as shown in Figure A-1(a)) from Vecchio and Collins (1986) to verify that the MCFT is well understood and implemented correctly by the author. As shown in Figure A-1(b), the predicted strain-stress curve agrees well with the prediction results from Vecchio and Collins (1986). The MCFT material model is then implemented in *OpenSees* and work together with the new flexure-shear coupled fibre beam element. The utilized *MATLAB* code is attached in this appendix.

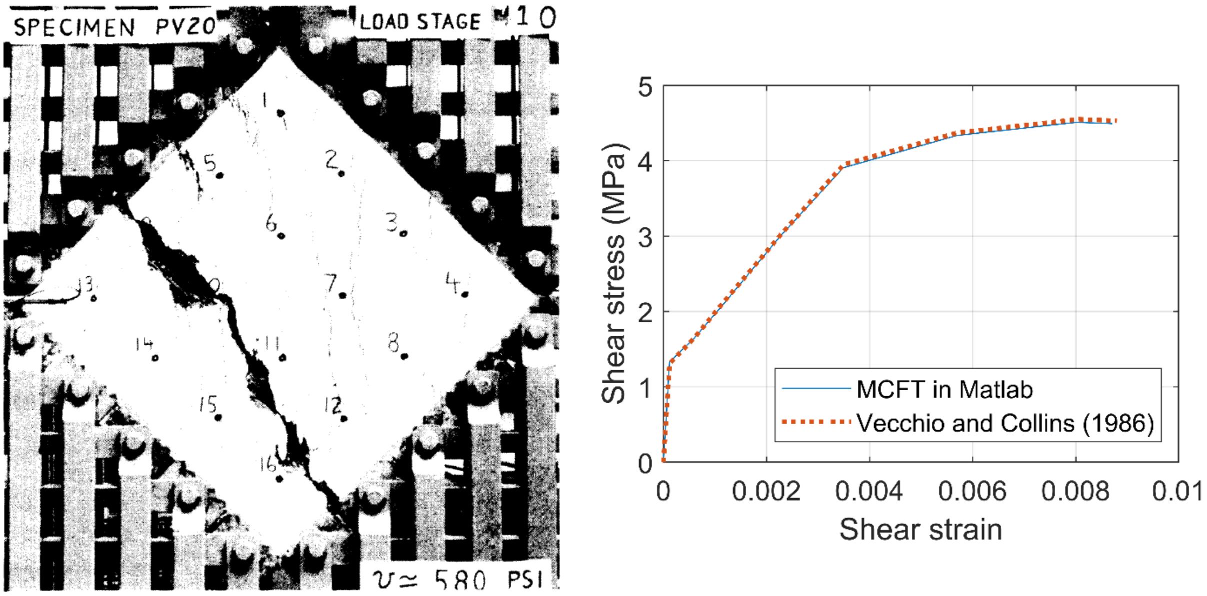

(a) (b)

Figure A-1: Reproduce of the response for the specimen PV20: (a) specimen PV20 after failure (Vecchio and Collins 1986), and (b) comparison of the predicted stress-strain curves

```
clear all
clc
%%
%From stress to strain(in mm, N and MPa, tension is positive, compression is negative)
smx=47;
smy=44; %crack control parameters, from paper in section "examples of prediction
response"
epsilon1=[0.067*10^(-3),0.5*10^(-3),1*10^(-3),1.5*10^(-3),2*10^(-3),3*10^(-
3),5*10^(-3),7*10^(-3),7.5*10^(-3)]; %from paper in Table 2
theta=[44.9,42.8,42.0,41.6,41.4,41.3,37.9,36.3,36.3]; %from paper in Table 2
fsy=[1.6,46,97,148,198,293,297,297,297]; %from paper in Table 2
fx=0;
fy=0; %pure shear
Rx=0.0179;  %from paper in Table 1
Ry=0.0089;
fyx=460;
fyy=297;
fc_prime=-19.6;
epsilonc_prime=-0.0018;
Ec=2*fc_prime/epsilonc_prime; %equation from paper
fcr=0.33*(-fc_prime)^0.5;
Es=200000; %Not found in the paper, 200GPa is assumed
Aa=6; %Maximum aggregate size, from paper in section of "experimental program"

for i=1:length(epsilon1)
    stheta=1/(sind(theta(i))/smx+cosd(theta(i))/smy);
    w(i)=epsilon1(i)*stheta;
    fc1(i)=fcr/(1+(200*epsilon1(i))^0.5);
    vcimax(i)=(-fc_prime)^0.5/(0.31+24*w(i)/(Aa+16));
    kk=1.64-1/tand(theta(i));
    if kk<0
        kk=0;
    end
    fc1_max(i)=vcimax(i)*(0.18+0.3*kk^2)*tand(theta(i))+Ry*(fyy-fsy(i));
    fcy=fy-Ry*fsy(i);
    vxy(i)=(fc1(i)-fcy)/tand(theta(i));
    fc2(i)=fc1(i)-vxy(i)*(tand(theta(i))+1/tand(theta(i)));
    Ratio(i)=fc2(i)/fc_prime;
    fc2_max(i)=fc_prime/(0.8-0.34*epsilon1(i)/epsilonc_prime);
    epsilon2(i)=epsilonc_prime*(1-(1-fc2(i)/fc2_max(i))^0.5);
    fc2_check(i)=fc2_max(i)*(2*epsilon2(i)/epsilonc_prime-
(epsilon2(i)/epsilonc_prime)^2);

epsilony(i)=(epsilon1(i)+epsilon2(i)*(tand(theta(i)))^2)/(1+(tand(theta(i)))^2);
    fsy_check(i)=Es*epsilony(i);
    if fsy_check(i)>fyy
        fsy_check(i)=fyy;
    end
    epsilonx(i)=epsilon1(i)+epsilon2(i)-epsilony(i);
    fsx(i)=Es*epsilonx(i);
    if fsx(i)>fyx
        fsx(i)=fyx;
    end
```

```
    fcx(i)=fc1(i)-vxy(i)/tand(theta(i));
    fx(i)=fcx(i)+Rx*fsx(i);
    deta_fc1=fc1(i)-Ry*(fyy-fsy(i));
    if deta_fc1<=0
        vci(i)=0;
        fci=0;
    else
        Cc=deta_fc1/tand(theta(i))-0.18*vcimax(i);
        if Cc<=0
            fci=0;
            vci(i)=deta_fc1/tand(theta(i));
        else
            AAA=0.82/vcimax(i);
            BBB=1/tand(theta(i))-1.64;
            fci=(-BBB-(BBB^2-4*AAA*Cc)^0.5)/(2*AAA);
            vci(i)=(fc1(i)+deta_fc1)/tand(theta(i));
        end
    end
    fsycr(i)=fsy(i)+(fc1(i)+fci-vci(i)*tand(theta(i)))/Ry;
    fsxcr(i)=fsx(i)+(fc1(i)+fci+vci(i)*tand(theta(i)))/Rx;
    Gamma_xy(i)=2*(epsilonx(i)-epsilon2(i))/tand(theta(i));
end

%%
%From strain to stress
for i=1:length(Gamma_xy)
    theta_prime(i)=(atan(Gamma_xy(i)/(epsilony(i)-epsilonx(i))))/2*180/pi;
    Ep1(i)=(epsilonx(i)*(tand(theta_prime(i)))^2-
epsilony(i))/((tand(theta_prime(i)))^2-1);
    Ep2(i)=epsilonx(i)+epsilony(i)-Ep1(i);
    Fc1(i)=fcr/(1+(200*Ep1(i))^0.5);
    Fc2_Max(i)=fc_prime/(0.8-0.34*Ep1(i)/epsilonc_prime);
    Fc2(i)=Fc2_Max(i)*(2*Ep2(i)/epsilonc_prime-(Ep2(i)/epsilonc_prime)^2);
    Vxy(i)=(Fc1(i)-Fc2(i))/(tand(theta_prime(i))+1/tand(theta_prime(i)));
    Fcx(i)=Fc1(i)-Vxy(i)/tand(theta_prime(i));
    Fcy(i)=Fc1(i)-Vxy(i)*tand(theta_prime(i));
    Fsx(i)=Es*epsilonx(i);
    if Fsx(i)>fyx
        Fsx(i)=fyx;
    end
    Fsy(i)=Es*epsilony(i);
    if Fsy(i)>fyy
        Fsy(i)=fyy;
    end
    Fx(i)=Fcx(i)+Rx*Fsx(i);
    Fy(i)=Fcy(i)+Ry*Fsy(i);
end

Xx=[0,0.12,0.60,1.15,1.71,2.29,3.50,5.70,8.06,8.80]*10^(-3); %MCFT from paper
Yy=[0,1.31,1.65,2.11,2.56,3.03,3.95,4.37,4.55,4.53];
Xx1=[0,Gamma_xy];
Yy1=[0,Vxy];
plot(Xx1,Yy1,'-','linewidth',0.5)
```

```
hold on
plot(Xx,Yy,':','linewidth',2)
box on; grid on;
xlabel('Shear strain', 'fontsize', 12)
ylabel('Shear stress (MPa)', 'fontsize', 12)
legend('MCFT in Matlab','Vecchio and Collins (1986)','Location','southeast')
filename = 'Jack';
W=4; H=3;
set(gca, 'fontsize', 12);
set(gcf, 'PaperUnits', 'inches');
set(gcf, 'PaperSize', [W H]);
set(gcf, 'PaperPositionMode', 'manual');
set(gcf, 'PaperPosition', [0 0 W H]);
print('-depsc','-r800',filename);
print('-dtiff','-r800',filename);
saveas(gcf, [filename,'.fig']);
```

APPENDIX B: SUMMARY OF THE COMPILED EXPERIMENTAL DATABASE

The detailed information of the 369 PC girders that failed in shear is listed in Table A-1 with the following information. The related references are also provided in the end.

Specimen I.D.: specimen's identification reported in the original references

Cross section: I means I-shaped section, T means T-shaped section, R means rectangular section

f_c' : concrete compressive tested by cylinder specimens, in MPa

a/d : shear span to depth ration

b_w/h : web width to overall depth ratio

$\rho_v f_{yt}$: shear reinforcement index $= A_v f_{yt}/b_w s$, in MPa

f_{se}/f_{pu} : percentage of effective prestress to tensile strength in tensile prestressing strands

$A_s f_y$: tensile non-prestressing steel index, in kN

$A_{ps} f_{pu}$: tensile prestressing strand index, in kN

v_{test} : normalized tested sectional shear strength $= V_{tested}/0.25 f_c' b_w d$

Table A-1: Experimental database of PC girders that failed in shear

Specimen I.D.	*Cross section*	f_c' (MPa)	a/d	b_w/h	$\rho_v f_{yt}$ (MPa)	f_{se}/f_{pu}	$A_s f_y$ (kN)	$A_{ps} f_{pu}$ (kN)	v_{test}
Brandes and Kurama 2018									
UP4-0-2	R	79.8	2.0	0.66	2.29	0.58	0	367.56	0.29
UP4-50-2	R	83.5	2.0	0.66	2.29	0.56	0	367.56	0.28
UP4-100-2	R	85.6	2.0	0.66	2.29	0.54	0	367.56	0.28
UP5-0-2	R	71.1	2.0	0.66	2.29	0.56	0	367.56	0.33
UP5-50-2	R	69.1	2.0	0.66	2.29	0.55	0	367.56	0.35
UP5-100-2	R	72	2.0	0.66	2.29	0.55	0	367.56	0.31
CT4-0-2	R	66.8	2.0	0.66	2.29	0.41	0	367.56	0.27
CT4-50-2	R	70.1	2.0	0.66	2.29	0.39	0	367.56	0.29
CT4-100-2	R	69.8	2.0	0.66	2.29	0.37	0	367.56	0.26
Chehab et al. 2018									
1-1	I	52	2.8	0.17	2.28	0.72	0	2763.25	0.59

1-2	I	54	3.4	0.17	2.28	0.72	0	2763.25	0.47
1-3	I	59	3.4	0.17	0.86	0.72	0	2763.25	0.42
2-1	I	63	2.0	0.17	0.86	0.59	0	2763.25	0.53
2-2	I	63	2.8	0.17	0.86	0.59	0	2763.25	0.46
2-3	I	63	3.5	0.17	0.86	0.59	0	2763.25	0.30
Shen et al. 2015									
S30-1A	R	35.4	3.8	0.52	0	0.58	169.95	172.98	0.25
S50-1A	R	52.6	3.8	0.52	0	0.58	169.95	172.98	0.19
S70-1A	R	68.3	3.8	0.52	0	0.58	169.95	172.98	0.16
S30-2A	R	34.9	4.0	0.52	0	0.58	339.90	172.98	0.27
S50-2A	R	57.1	4.0	0.52	0	0.58	339.90	172.98	0.23
S70-2A	R	67.3	4.0	0.52	0	0.58	339.90	172.98	0.19
S30-1B	R	36.7	3.8	0.52	0	0.58	169.95	172.98	0.30
S70-1B	R	67.3	3.8	0.52	0	0.58	169.95	172.98	0.17
Wilder et al. 2015									
B101	I	77.5	3.1	0.11	1.64	0.62	0	1894.77	0.54
B102	I	77.5	3.9	0.11	1.64	0.62	0	1894.77	0.46
B103	I	77.5	3.9	0.11	0	0.62	0	1894.77	0.38
B104	I	88.9	3.1	0.11	1.64	0.31	0	1894.77	0.35
B105	I	88.9	3.9	0.11	1.64	0.31	0	1894.77	0.32
B106	I	88.9	3.9	0.11	0	0.31	0	1894.77	0.23
B109	I	89.3	3.6	0.11	0	0.62	0	947.39	0.21
Lee et al. 2010									
C40P2S10	I	45.4	2.6	0.17	1.12	0.54	3092.93	2099.36	0.65
C40P2S13	I	45.4	2.6	0.17	1.98	0.54	3092.93	2099.36	0.71
C60P1S10	I	73.4	2.6	0.17	1.12	0.49	3092.93	1049.68	0.38
C60P2S10	I	73.4	2.6	0.17	1.12	0.54	3092.93	2099.36	0.47
C60P2S13	I	73.4	2.6	0.17	1.98	0.54	3092.93	2099.36	0.53
C80P2S10	I	84.9	2.6	0.17	1.12	0.54	3092.93	2099.36	0.38
C80P2S13	I	84.9	2.6	0.17	1.98	0.54	3092.93	2099.36	0.46
Saqan and Frosch 2009									
V-4-0	R	52.1	3.3	0.50	0	0.65	0	735.02	0.09
V-4-0.93	R	52.7	3.0	0.50	0	0.65	248.21	735.02	0.11
V-4-2.37	R	53.4	3.1	0.50	0	0.65	632.54	735.02	0.12
V-7-0	R	54.5	3.3	0.50	0	0.38	0	1286.29	0.13
V-7-1.84	R	53.1	3.1	0.50	0	0.38	491.08	1286.29	0.15
V-7-2.37	R	53.1	3.1	0.50	0	0.38	632.54	1286.29	0.14
V-10-0	R	51.7	3.3	0.50	0	0.27	0.00	1837.56	0.14
V-10-1.51	R	51.7	3.1	0.50	0	0.27	403.01	1837.56	0.14
V-10-2.37	R	51.7	3.1	0.50	0	0.27	632.54	1837.56	0.15
Heckmann and Bayrak 2008									
CB-60-1	I	84.8	2.2	0.18	0.98	0.62	0	4777.66	0.52
CB-60-2	I	87.6	2.2	0.18	0.98	0.62	0	4777.66	0.50
CB-70-1	I	83.4	2.2	0.18	0.98	0.62	0	4777.66	0.52
CB-70-4	I	85.7	2.2	0.18	0.98	0.61	0	4777.66	0.50

CB-70-5	I	86.2	2.2	0.18	0.98	0.60	0	4777.66	0.48
CB-70-6	I	88.3	2.2	0.18	0.98	0.59	0	4777.66	0.51
CC-70-1	I	73.8	2.2	0.18	0.98	0.59	0	6615.22	0.61
CC-70-2	I	73.8	2.2	0.18	0.98	0.59	0	6615.22	0.67
CC-65-3	I	73.8	2.2	0.18	0.98	0.55	0	6615.22	0.63
CC-65-4	I	73.8	2.2	0.18	0.98	0.55	0	6615.22	0.65
CC-60-1	I	73.8	2.2	0.18	0.98	0.51	0	6615.22	0.62
CC-60-2	I	73.8	2.2	0.18	0.98	0.51	0	6615.22	0.62
CD-70-1	I	73.8	2.2	0.18	0.98	0.59	0	6615.22	0.66
CD-70-2	I	73.8	2.2	0.18	0.98	0.59	0	6615.22	0.67
CD-65-3	I	73.8	2.2	0.18	0.98	0.55	0	6615.22	0.64
CD-65-4	I	73.8	2.2	0.18	0.98	0.55	0	6615.22	0.66
CD-60-1	I	73.8	2.2	0.18	0.98	0.51	0	6615.22	0.66
CD-60-2	I	73.8	2.2	0.18	0.98	0.51	0	6615.22	0.68
De Silva and Witchukreangkrai. 2006									
IPRC-1	I	41.8	3.0	0.30	1.32	0.59	1413.72	639.77	0.50
IPRC-2	I	49.3	3.0	0.30	0.73	0.59	1413.72	639.77	0.39
IPRC-3	I	45	3.0	0.30	1.06	0.59	1413.72	639.77	0.41
IPRC-4	I	43.2	3.0	0.30	1.32	0.59	2621.96	639.77	0.51
Teoh et al. 2002									
A6-8	I	93.9	2.7	0.21	0.44	0.60	593.33	1116.00	0.17
A3-8	I	88.9	2.7	0.21	0.44	0.32	593.33	1116.00	0.16
B6-4	I	42.9	2.7	0.21	0.42	0.60	593.33	1116.00	0.30
B6-12	I	99.9	2.7	0.21	0.79	0.60	593.33	1116.00	0.17
B6-8	I	92.1	2.7	0.21	0.64	0.60	593.33	1116.00	0.21
B3-8	I	84.3	2.7	0.21	0.64	0.32	593.33	1116.00	0.15
Alshegeir and Ramirez 1992									
I-3A	I	60.7	2.4	0.21	0.92	0.65	0	1638.75	0.34
I-4A	I	60.7	2.3	0.21	1.26	0.67	0	1638.75	0.47
II-1A	I	61.7	2.2	0.17	1.26	0.65	0	2458.12	0.50
Rangan 1991									
II-1	I	45	2.5	0.10	9.15	0.67	910.00	484.76	1.13
II-2	I	31.5	2.5	0.10	15.47	0.67	910.00	484.76	1.35
II-3	I	44.6	2.5	0.12	8.03	0.67	910.00	484.76	1.07
II-4	I	43	2.5	0.12	13.17	0.67	910.00	484.76	1.07
III-1	I	40	2.5	0.11	8.88	0.67	737.10	692.52	0.99
III-2	I	37	2.5	0.11	14.77	0.67	737.10	692.52	1.14
III-3	I	39	2.5	0.13	7.61	0.67	737.10	692.52	0.94
III-4	I	37	2.5	0.12	13.35	0.67	737.10	692.52	1.20
IV-1	I	37.1	2.6	0.10	15.72	0.67	150.15	1246.54	1.22
IV-2	I	33	2.6	0.10	9.15	0.67	150.15	1246.54	1.20
IV-3	I	36	2.6	0.12	13.54	0.67	150.15	1246.54	1.34
IV-4	I	28.7	2.6	0.12	8.14	0.67	150.15	1246.54	1.41
Hartman et al. 1988									
1-1	I	77.9	3.0	0.09	0	0.61	0	527.11	0.31

1-2	I	77.9	3.0	0.09	0.85	0.61	0	527.11	0.30
1-3	I	77.9	3.0	0.09	1.51	0.61	0	527.11	0.32
2-1	I	74.5	3.3	0.09	11.07	0.55	142.88	1581.34	0.97
2-2	I	74.5	3.3	0.09	13.84	0.55	142.88	1581.34	1.06
2-3	I	74.5	3.3	0.09	13.84	0.55	142.88	1581.34	1.04
Kaufman and Ramirez 1988									
I-2	I	57.5	2.4	0.21	1.04	0.65	0	1604.56	0.45
I-3	I	57.7	2.4	0.21	0.90	0.67	0	1604.56	0.31
I-4	I	57.7	2.4	0.21	1.04	0.68	0	1604.56	0.34
II-1	I	62.7	2.5	0.17	1.04	0.66	0	2406.84	0.31
Robertson and Durrani 1987									
1	T	41.6	3.5	0.15	0	0.54	0	551.27	0.54
3	T	46.1	3.5	0.15	0.95	0.51	0	551.27	0.55
4	T	44.1	3.5	0.15	0.95	0.57	0	551.27	0.62
5	T	44.6	3.5	0.15	0.90	0.57	0	551.27	0.62
6	T	41.9	3.5	0.15	0.24	0.56	0	551.27	0.62
7	T	43.0	3.5	0.15	0	0.50	0	551.27	0.54
8	T	39.4	3.5	0.15	0.72	0.57	0	551.27	0.71
10	T	42.0	3.5	0.15	0.72	0.56	0	551.27	0.68
11	T	41.8	3.5	0.15	1.43	0.56	0	551.27	0.71
12	T	41.5	3.5	0.15	0.41	0.58	0	551.27	0.63
13	T	41.3	3.5	0.15	0.41	0.56	0	551.27	0.58
Elzanaty et al. 1986									
CW1	I	76.5	2.9	0.11	0	0.47	92.48	1282.86	0.39
CW3	I	76.5	5.0	0.11	0	0.46	92.48	1282.86	0.33
CW2	I	76.5	3.8	0.11	0	0.47	92.48	1282.86	0.35
CW4	I	78.6	3.8	0.11	0	0.48	0	1282.86	0.35
CW5	I	77.9	3.8	0.11	0	0.47	504.43	1282.86	0.34
CW7	I	77.6	3.8	0.11	0	0.50	92.48	890.87	0.29
CW6	I	77.9	3.8	0.11	0	0.35	92.48	1282.86	0.31
CW9	I	61.0	3.8	0.11	0	0.35	92.48	1282.86	0.36
CW8	I	41.4	3.8	0.17	0	0.35	92.48	1282.86	0.31
CI1	T	76.5	7.8	0.21	0	0.47	92.48	1282.86	0.22
CI3	T	76.5	4.0	0.21	0	0.47	92.48	1282.86	0.34
CI2	T	76.5	5.8	0.21	0	0.47	92.48	1282.86	0.32
CI4	T	78.6	5.8	0.21	0	0.48	0	1282.86	0.30
CI5	T	77.9	5.8	0.21	0	0.47	504.43	1282.86	0.33
CI7	T	77.6	5.8	0.21	0	0.50	92.48	890.87	0.23
CI6	T	77.9	5.8	0.21	0	0.35	92.48	1282.86	0.25
CI9	T	61.0	5.8	0.21	0	0.35	92.48	1282.86	0.32
CI8	T	41.4	5.8	0.21	0	0.35	92.48	1282.86	0.46
CW10	I	73.1	3.8	0.11	4.78	0.34	92.48	1282.86	0.51
CW11	I	55.8	3.8	0.11	4.78	0.33	92.48	1282.86	0.60
CW12	I	40.0	3.8	0.11	4.78	0.34	92.48	1282.86	0.76
CW13	I	72.4	3.8	0.11	4.78	0.47	92.48	1282.86	0.54

CW14	I	73.8	3.8	0.11	6.83	0.48	92.48	1282.86	0.55
CW15	I	70.3	3.8	0.11	4.78	0.49	92.48	890.87	0.46
CW16	I	73.1	3.8	0.11	4.78	0.47	504.43	1282.86	0.55
CW17	I	69.6	3.8	0.11	2.17	0.47	92.48	1282.86	0.44
CI10	T	73.1	5.8	0.21	3.98	0.34	92.48	1282.86	0.42
CI11	T	55.8	5.8	0.21	3.98	0.34	92.48	1282.86	0.50
CI12	T	40.0	5.8	0.21	3.98	0.34	92.48	1282.86	0.67
CI13	T	72.4	5.8	0.21	3.98	0.47	92.48	1282.86	0.47
CI14	T	73.8	5.8	0.21	6.37	0.48	92.48	1282.86	0.49
CI15	T	70.3	5.8	0.21	3.98	0.49	92.48	890.87	0.37
CI16	T	73.1	5.8	0.21	3.98	0.47	504.43	1282.86	0.49
CI17	T	69.6	5.8	0.21	1.81	0.47	92.48	1282.86	0.40
Xuan 1986									
PSN 1 -0	T	36.1	2.9	0.17	0	0.70	565.50	360.95	0.62
PSN2-WD	T	38.1	2.9	0.17	1.29	0.70	565.50	360.95	0.68
PSN3-D2	T	33.3	2.9	0.17	1.65	0.70	565.50	360.95	0.92
PSN4-WDH	T	31.5	2.9	0.17	1.30	0.70	565.50	360.95	0.93
PSN5-S6M	T	32.5	2.9	0.17	1.18	0.70	565.50	360.95	0.93
PSN6-WS	T	34.3	2.9	0.17	1.37	0.70	565.50	360.95	0.88
Lyngberg 1976									
2A-3	I	32.6	2.8	0.20	4.31	0.50	408.41	1249.55	0.96
2B-3	I	33.9	2.8	0.20	3.41	0.50	407.79	1249.55	0.94
3A-2	I	31.1	2.8	0.20	3.51	0.51	822.98	833.04	0.97
3B-2	I	27.5	2.8	0.20	3.31	0.51	824.21	833.04	0.97
4A-1	I	31.5	2.8	0.20	3.39	0.52	1299.86	416.52	0.92
4B-1	I	30.4	2.8	0.20	3.49	0.50	1305.48	416.52	0.92
Mahgoub 1975									
A1	I	41.2	3.0	0.25	0	0.56	0	316.54	0.43
A5	I	44.5	2.0	0.25	0	0.55	0	316.54	0.50
A6	I	47.2	3.0	0.25	0	0.55	0	316.54	0.41
A12	I	29.2	3.5	0.25	0	0.44	0	316.54	0.42
B1	I	37.0	4.0	0.17	0	0.39	0	316.54	0.37
B3	I	46.4	2.0	0.17	0	0.45	0	316.54	0.50
B10	I	39.8	3.5	0.17	0	0.49	0	316.54	0.43
C1	I	40.0	2.0	0.25	0	0.58	0	316.54	0.63
C11	I	36.0	4.0	0.25	0	0.43	0	316.54	0.30
D3	I	42.6	3.0	0.17	0	0.43	0	316.54	0.33
D4	I	41.2	4.5	0.17	0	0.40	0	316.54	0.27
E1	I	51.3	3.0	0.25	0	0.43	0	316.54	0.30
E2	I	42.2	2.0	0.25	0	0.33	0	316.54	0.36
E3	I	44.6	2.0	0.25	0	0.51	0	316.54	0.71
E4	I	40.0	4.0	0.25	0	0.51	0	316.54	0.30
E6	I	40.0	3.0	0.25	0	0.62	0	316.54	0.47
F2	I	39.4	4.0	0.17	0	0.46	0	316.54	0.32
F4	I	39.5	2.0	0.17	0	0.58	0	316.54	0.68

F5	I	42.1	4.5	0.17	0	0.33	0	316.54	0.24
G3	R	43.6	2.0	0.67	0	0.51	0	316.54	0.27
G6	R	39.8	3.0	0.67	0	0.53	0	316.54	0.19
Bennett and Balasooriya 1971									
3A2	I	41.7	3.4	0.10	8.68	0.54	16.81	375.24	1.17
2A3	I	33.8	2.3	0.10	8.68	0.57	16.81	375.24	1.67
2B2	I	43.0	2.3	0.10	8.68	0.48	16.81	375.24	1.63
2B3	I	43.9	2.3	0.10	8.68	0.56	16.81	375.24	1.62
2B4	I	38.1	2.3	0.10	8.68	0.28	16.81	375.24	1.45
2B5	I	39.0	2.3	0.10	8.68	0.12	16.81	375.24	1.36
3C2	I	33.2	3.4	0.10	8.68	0.47	16.81	375.24	1.59
3C3	I	33.6	3.4	0.10	8.68	0.36	16.81	375.24	1.63
3C4	I	30.5	3.4	0.10	8.68	0.27	16.81	375.24	1.29
3C5	I	31.6	3.4	0.10	8.68	0.12	16.81	375.24	1.08
3D1	I	44.3	3.4	0.10	13.01	0.46	16.81	375.24	1.35
3D2	I	44.3	3.4	0.10	8.68	0.48	16.81	375.24	1.21
3D3	I	40.3	3.4	0.10	5.79	0.44	16.81	375.24	1.21
3D4	I	39.4	3.4	0.10	4.33	0.46	16.81	375.24	1.08
3E3	I	40.7	3.4	0.15	5.79	0.47	16.81	375.24	1.03
2F1	I	39.2	2.2	0.06	7.43	0.60	16.81	500.33	1.44
2F2	I	39.2	2.2	0.06	7.43	0.58	16.81	500.33	1.41
2F3	I	39.2	2.2	0.06	7.43	0.41	16.81	500.33	1.26
2F4	I	40.0	2.2	0.06	7.43	0.26	16.81	500.33	1.13
Hanson and Hulsbos 1964									
F-X1-Ist	I	45.9	3.4	0.17	0.84	0.37	0	1091.32	0.45
F-1-Ist	I	47.0	2.1	0.17	1.34	0.38	0	1091.32	0.83
F-2-Ist	I	45.2	2.8	0.17	0.84	0.35	0	1091.32	0.57
F-3-Ist	I	47.2	2.8	0.17	0.58	0.36	0	1091.32	0.55
F-4-Ist	I	43.7	3.5	0.17	0.80	0.39	0	1091.32	0.56
F-5-Ist	I	44.2	3.5	0.17	0.56	0.35	0	1091.32	0.47
F-6-Ist	I	43.0	7.1	0.17	0.32	0.36	0	1091.32	0.29
F-7-Ist	I	45.6	4.2	0.17	0.67	0.38	0	1091.32	0.41
F-8-Ist	I	47.4	4.2	0.17	0.39	0.37	0	1091.32	0.37
F-9-Ist	I	45.9	6.3	0.17	0.70	0.37	0	1091.32	0.36
F-10-Ist	I	48.6	4.9	0.17	0.33	0.37	0	1091.32	0.33
F-11-Ist	I	41.6	4.9	0.17	0.46	0.36	0	1091.32	0.41
F-12-Ist	I	44.8	5.6	0.17	0.29	0.36	0	1091.32	0.33
F-13-Ist	I	44.5	5.6	0.17	0.41	0.34	0	1091.32	0.35
F-14-Ist	I	46.6	6.3	0.17	0.26	0.37	0	1091.32	0.31
F-15-Ist	I	39.9	7.1	0.17	0.23	0.32	0	1091.32	0.28
F-16-Ist	I	46.2	7.8	0.17	0.32	0.36	0	1091.32	0.27
F-19-Ist	I	51.1	3.5	0.17	1.07	0.37	0	1091.32	0.50
F-X1-2nd	I	45.9	3.4	0.17	0.84	0.37	0	1091.32	0.53
F-1-2nd	I	47.0	2.1	0.17	1.34	0.38	0	1091.32	0.89
F-2-2nd	I	45.2	2.8	0.17	0.84	0.35	0	1091.32	0.69

F-3-2nd	I	47.2	2.8	0.17	0.58	0.36	0	1091.32	0.69
F-4-2nd	I	43.7	3.5	0.17	0.80	0.39	0	1091.32	0.59
F-5-2nd	I	44.2	3.5	0.17	0.56	0.35	0	1091.32	0.49
F-7-2nd	I	45.6	4.2	0.17	0.67	0.38	0	1091.32	0.59
F-8-2nd	I	47.4	4.2	0.17	0.39	0.37	0	1091.32	0.51
F-9-2nd	I	45.9	6.3	0.17	0.70	0.37	0	1091.32	0.32
F-10-2nd	I	48.6	4.9	0.17	0.33	0.37	0	1091.32	0.39
F-11-2nd	I	41.6	4.9	0.17	0.46	0.36	0	1091.32	0.45
F-12-2nd	I	44.8	5.6	0.17	0.29	0.36	0	1091.32	0.36
F-13-2nd	I	44.5	5.6	0.17	0.41	0.34	0	1091.32	0.34
F-14-2nd	I	46.6	6.3	0.17	0.26	0.37	0	1091.32	0.32
F-19-2nd	I	51.1	3.5	0.17	1.07	0.37	0	1091.32	0.51
Evans and Schumacher 1963									
S2	R	38.8	2.4	0.33	0	0.11	0	531.09	0.43
S3	I	37.1	4.0	0.17	0	0.19	0	294.25	0.37
S4	I	34.9	4.0	0.17	0	0.08	0	661.36	0.56
S5	I	35.2	4.0	0.17	0	0.18	0	400.74	0.49
S7	I	33.8	3.4	0.17	0	0.16	0	524.05	0.66
S8	I	28.6	5.4	0.17	0	0.32	0	401.65	0.39
S9	I	30.5	5.0	0.16	0	0.24	0	525.65	0.52
S10	I	30.5	5.5	0.11	0	0.23	0	525.25	0.53
S11	I	32.6	5.4	0.16	0	0.34	0	293.82	0.38
S12	I	32.6	5.4	0.12	0	0.25	0	400.64	0.45
S13	I	36.0	5.4	0.11	0	0.32	0	295.64	0.49
S14	I	30.3	4.5	0.17	0	0.18	0	525.65	0.51
S15	I	27.9	4.5	0.17	0	0.33	0	296.25	0.48
S16	I	34.0	4.5	0.17	0	0.25	0	400.34	0.44
S17	I	37.4	4.4	0.11	0	0.15	0	524.10	0.34
S18	I	30.0	4.5	0.11	0	0.23	0	400.64	0.46
S19	I	30.0	3.7	0.17	0	0.18	0	522.95	0.49
S20	I	28.1	4.5	0.11	0	0.35	0	295.45	0.52
S21	I	28.1	3.7	0.17	0	0.37	0	293.82	0.58
S22	I	24.0	3.6	0.11	0	0.17	0	524.10	0.54
S24	I	36.9	3.7	0.11	0	0.30	0	295.64	0.45
S25	I	36.9	3.7	0.17	0	0.23	0	401.65	0.44
S26	I	35.5	3.8	0.11	0	0.22	0	399.46	0.42
S27	I	35.4	2.8	0.17	0	0.16	0	525.65	0.58
S29	I	28.5	2.8	0.17	0	0.20	0	401.65	0.69
S30	I	35.2	2.8	0.17	0	0.36	0	293.82	0.65
S32	I	32.2	2.8	0.11	0	0.28	0	295.45	0.60
S34	I	33.9	2.8	0.10	0	0.20	0	401.65	0.73
S35	I	39.3	2.7	0.11	0	0.15	0	525.06	0.70
S36	I	35.7	2.7	0.10	0	0.50	0	129.20	0.42
S42	I	43.6	4.0	0.35	0	0.14	0	399.94	0.42
S43	I	48.3	4.2	0.37	0	0.10	0	523.45	0.35

S44	I	32.5	2.7	0.10	0	0.43	0	118.16	0.47
S46	R	33.0	4.7	0.52	0	0.45	0	117.40	0.25
S48	R	33.0	5.0	0.52	0	0.54	0	116.49	0.28
S49	I	36.3	2.8	0.11	0	0.36	0	295.45	0.47
S50	I	39.6	3.0	0.12	0	0.37	0	293.97	0.53
S51	I	36.5	2.7	0.11	0	0.37	0	295.78	0.48
S52	I	33.9	2.7	0.10	0	0.34	0	295.86	0.64
S53	I	37.9	2.8	0.10	0	0.34	0	295.45	0.51
S54	I	36.3	2.8	0.10	0	0.36	0	295.45	0.45
MacGregor et al. 1960									
B.14.34	I	18.2	3.5	0.26	0	0.45	0	205.31	0.43
B.14.41	I	19.9	3.6	0.25	0	0.45	0	274.50	0.71
BW.14.34	I	25.0	3.5	0.25	0	0.49	0	274.50	0.47
BW.14.38	I	21.4	3.6	0.25	1.15	0.45	0	287.42	0.57
BW.14.58	I	21.8	3.6	0.24	0.56	0.39	0	455.85	0.67
BW.14.60	I	20.9	3.6	0.24	0.56	0.39	0	455.85	0.67
BW.18.15S	I	52.6	7.0	0.25	0.95	0.41	0	271.99	0.13
C.13.23	I	25.7	2.6	0.15	0	0.47	0	205.31	0.59
CW.13.28	I	29.9	2.8	0.15	2.82	0.46	0	457.78	0.93
CW.14.17	I	21.6	3.4	0.15	0	0.47	0	143.71	0.54
CW.14.22	I	32.1	3.6	0.14	1.93	0.46	0	287.42	0.68
CW.14.23	I	18.5	3.4	0.15	0	0.47	0	143.71	0.65
CW.14.37	I	22.3	3.6	0.14	1.44	0.45	0	287.42	0.93
CW.14.39	I	20.8	3.6	0.15	1.15	0.45	0	287.42	0.82
CW.14.47	I	17.5	3.6	0.14	0.95	0.44	0	287.42	1.09
CW.14.50	I	16.5	3.5	0.15	1.24	0.46	0	287.42	1.14
CW.14.51	I	22.5	3.6	0.15	0.68	0.45	0	407.41	0.89
CW.14.54	I	22.8	3.6	0.15	5.74	0.42	0	407.41	0.92
Sozen et al. 1959									
B.11.20	I	31.2	5.3	0.25	0	0.47	0	209.82	0.20
B.11.29	I	28.9	5.4	0.25	0	0.49	0	266.84	0.28
B.11.40	I	31.0	5.4	0.25	0	0.47	0	400.82	0.32
B.12.10	I	38.6	3.2	0.26	0	0.48	0	137.25	0.17
B.12.12	I	31.5	3.2	0.25	0	0.49	0	137.25	0.21
B.12.14	I	26.5	3.2	0.25	0	0.48	0	137.25	0.27
B.12.19	I	19.9	3.2	0.25	0	0.48	0	137.25	0.37
B.12.26	I	30.8	3.6	0.25	0	0.44	0	259.11	0.35
B.12.29	I	28.8	3.7	0.25	0	0.46	0	280.55	0.42
B.12.34	I	33.3	3.5	0.26	0	0.43	0	388.11	0.38
B.12.35	I	22.1	3.6	0.26	0	0.46	0	280.55	0.47
B.12.50	I	20.3	3.5	0.25	0	0.46	0	333.83	0.52
B.12.61	I	20.5	3.6	0.25	0	0.46	0	400.82	0.55
B.13.16	I	38.2	2.7	0.25	0	0.50	0	199.85	0.31
B.13.26	I	31.7	2.8	0.25	0	0.49	0	266.84	0.43
B.13.41	I	29.8	2.8	0.24	0	0.47	0	400.82	0.51

B.21.26	I	30.8	5.3	0.25	0	0.24	0	280.55	0.19
B.22.09	I	43.6	3.3	0.25	0	0.24	0	140.27	0.14
B.22.23	I	35.3	3.6	0.25	0	0.21	0	280.55	0.25
B.22.30	I	19.1	3.5	0.26	0	0.23	0	194.61	0.35
B.22.41	I	18.7	3.6	0.26	0	0.20	0	259.11	0.41
B.22.65	I	12.1	3.6	0.26	0	0.24	0	259.11	0.41
B.22.68	I	18.4	3.6	0.25	0	0.24	0	400.82	0.48
C.12.09	I	44.5	3.3	0.15	0	0.49	0	137.25	0.27
C.12.18	I	36.6	3.7	0.15	0	0.46	0	206.29	0.41
C.12.19	I	41.6	3.6	0.15	0	0.44	0	259.11	0.41
C.12.32	I	25.0	3.7	0.16	0	0.43	0	248.74	0.48
C.12.33	I	37.7	3.6	0.16	0	0.47	0	411.48	0.50
C.12.40	I	16.5	3.7	0.15	0	0.47	0	206.29	0.61
C.12.44	I	19.9	3.8	0.15	0	0.41	0	274.69	0.55
C.12.50	I	20.8	3.6	0.15	0	0.46	0	333.83	0.68
C.12.57	I	21.4	3.6	0.15	0	0.47	0	400.82	0.90
C.22.29	I	17.2	3.5	0.15	0	0.25	0	123.84	0.40
C.22.31	I	18.6	3.3	0.15	0	0.24	0	205.31	0.49
C.22.36	I	22.8	3.5	0.16	0	0.24	0	273.37	0.36
C.22.39	I	14.8	3.5	0.15	0	0.23	0	187.89	0.37
C.22.40	I	31.9	3.7	0.15	0	0.36	0	411.48	0.46
C.22.46	I	21.8	3.6	0.15	0	0.23	0	333.83	0.46
C.22.62	I	14.2	4.0	0.16	0	0.23	0	248.74	0.60
C.22.73	I	20.1	3.6	0.15	0	0.22	0	467.82	0.54
Hernandez 1958									
G5	I	22.3	3.6	0.14	1.17	0.45	0	287.42	0.93
G6	I	20.8	3.6	0.15	0.97	0.45	0	287.42	0.82
G7	I	32.1	3.6	0.14	1.55	0.46	0	287.42	0.68
G10	I	17.5	3.6	0.14	1.56	0.44	0	287.42	1.09
G13	I	21.6	3.4	0.15	0.48	0.47	0	143.71	0.54
G14	I	21.4	3.6	0.25	0.58	0.45	0	287.42	0.57
G20	I	16.5	3.5	0.15	1.89	0.46	0	287.42	1.14
G21	I	18.5	3.4	0.15	0.57	0.47	0	143.71	0.65
G28	I	26.7	3.6	0.25	0.79	0.46	0	275.58	0.46
G29	I	29.9	2.8	0.15	2.28	0.46	0	275.58	0.93
G34	I	27.0	2.9	0.15	2.28	0.46	0	275.58	0.86
Zwoyer and Siess 1954									
S-1	R	25.0	4.3	0.50	0	0.04	0	187.89	0.13
S-3	R	29.6	4.2	0.50	0	0.10	0	187.89	0.12
S-4	R	21.3	4.9	0.50	0	0.48	0	469.73	0.29
S-5	R	43.2	4.7	0.50	0	0.43	0	469.73	0.20
S-6	R	55.1	4.8	0.50	0	0.46	0	469.73	0.17
S-7	R	24.5	4.6	0.50	0	0.43	0	469.73	0.31
S-8	R	42.2	4.8	0.51	0	0.02	0	406.75	0.11
S-9	R	32.8	4.8	0.50	0	0.24	0	406.75	0.20

S-10	R	39.9	4.8	0.50	0	0.30	0	406.75	0.19
S-11	R	17.8	4.4	0.50	0	0.15	0	187.89	0.16
S-12	R	32.8	4.8	0.50	0	0.13	0	406.75	0.18
S-14	R	32.1	4.8	0.50	0	0.55	0	375.79	0.24
S-15	R	19.9	4.7	0.50	0	0.37	0	187.89	0.20
S-16	R	24.3	4.8	0.50	0	0.37	0	187.89	0.17
S-18	R	28.6	4.7	0.50	0	0.25	0	249.81	0.13
S-19	R	26.5	4.7	0.50	0	0.25	0	187.89	0.14
S-20	R	36.9	4.6	0.50	0	0.26	0	187.89	0.11
S-22	R	38.8	6.7	0.50	0	0.24	0	515.18	0.13
S-23	R	30.1	6.7	0.50	0	0.50	0	411.48	0.18
S-24	R	20.0	6.4	0.50	0	0.47	0	515.18	0.26
S-25	R	20.0	6.4	0.50	0	0.46	0	274.69	0.19
S-26	R	21.6	6.0	0.50	0	0.24	0	240.49	0.13
S-27	R	23.1	6.4	0.50	0	0.25	0	172.09	0.09
S-28	R	23.9	4.4	0.50	0	0.25	0	156.93	0.15
S-29	R	22.9	3.2	0.50	0	0.47	0	343.08	0.43
S-30	R	23.1	3.2	0.50	0	0.48	0	274.69	0.37
S-31	R	16.8	3.2	0.50	0	0.48	0	308.88	0.48
S-32	R	23.1	3.2	0.50	0	0.47	0	240.49	0.34
S-33	R	23.4	4.5	0.50	0	0.44	0	343.08	0.28
S-34	R	40.0	4.5	0.50	0	0.46	0	343.08	0.18

References

Alshegeir, A., & Ramirez, J. A. 1992. “Strut-Tie Approach in Pretensioned Beams.” *Structural Journal*, *89*(3), 296-304.

Bennett, E. W., & Balasooriya, B. M. A. 1971. “Shear strength of prestressed beams with thin webs failing in inclined compression.” *Journal Proceedings 68*(3), 204-212.

Brandes, M. R., & Kurama, Y. C. 2018. “Behavior of shear-critical prestressed concrete beams with recycled concrete aggregates under ultimate loads.” *Engineering Structures*, *165*, 237-246.

Chehab, A. I., Eamon, C. D., Parra-Montesinos, G. J., & Dam, T. X. 2018. “Shear Testing and Modeling of AASHTO Type II Prestressed Concrete Bridge Girders.” *ACI Structural Journal*, *115*(3).

De Silva, S., & Witchukreangkrai, E. 2006. “Experimental study on shear cracking behavior in I-shaped partially prestressed concrete beams.” *Transactions of the Japan Concrete Institute*, *28*(2), 817-822.

De Wilder, K., Lava, P., Debruyne, D., Wang, Y., De Roeck, G., & Vandewalle, L. 2015. “Experimental investigation on the shear capacity of prestressed concrete beams using digital image correlation.” *Engineering Structures*, *82*, 82-92.

Elzanaty, A. H., & Nilson, A. H. 1986. “Shear capacity of prestressed concrete beams using high-strength concrete.” *Journal Proceedings, 83*(3), 359-368.

Evans, R. H., & Schumacher, E. G. 1963. “Shear strength of prestressed beams without web reinforcement.” *Journal Proceedings, 60*(11), 1621-1642.

Hanson, J. M., & Hulsbos, C. L. 1964. "Ultimate shear tests of prestressed concrete i-beams under concentrated and uniform loadings." *Journal of PCI*, *256*(9), 15-28.

Hartman, D. L., Breen, J. E., and Kreger, M. E., 1988. *Shear Capacity of High Strength Prestressed Concrete Girders* (No. FHW/TX-88+381-2). Center of Transportation Research, The University of Texas at Austin

Heckmann, C., & Bayrak, O. 2008. *Effects of increasing the allowable compressive stress at release on the shear strength of prestressed concrete girders* (No. FHWA/TX-09/0-5197-3). Texas. Dept. of Transportation. Research and Technology Implementation Office.

Hernandez, G. 1958. *Strength of prestressed concrete beams with web reinforcement*. University of Illinois Engineering Experiment Station. College of Engineering. University of Illinois at Urbana-Champaign.

Kaufman, M. K., & Ramirez, J. A. 1988. "Re-evaluation of the ultimate shear behavior of high-strength concrete prestressed I-beams." *Structural Journal*, *85*(3), 295-303.

Lee, S. C., Cho, J. Y., & Oh, B. H. 2010. "Shear Behavior of Large-Scale Post-Tensioned Girders with Small Shear Span-Depth Ratio." *ACI Structural Journal*, *107*(2).

Lyngberg, B. S. 1976. "Ultimate shear resistance of partially prestressed reinforced concrete I-beams." In *Journal Proceedings*, *73*(4), 214-222.

MacGregor, J. G., Sozen, M. A., & Siess, C. P. 1960. *Strength and behavior of prestressed concrete beams with web reinforcement*. University of Illinois Engineering Experiment Station. College of Engineering. University of Illinois at Urbana-Champaign.

Mahgoub, M. O. 1975. "Shear strength of prestressed concrete beams without web reinforcement." *Magazine of Concrete Research*, *27*(93), 219-228.

Rangan, B. V. 1991. "Web crushing strength of reinforced and prestressed concrete beams." *Structural Journal*, *88*(1), 12-16.

Robertson, Ian & Durrani, Ahmad. 1987. "Shear Strength of Prestressed Concrete T Beams With Welded Wire Fabric As Shear." *Pci Journal*, 32, 46-61.

Saqan, E. I., & Frosch, R. J. 2009. "Influence of flexural reinforcement on shear strength of prestressed concrete beams." *ACI Structural Journal*, *106*(1), 60.

Shen, J., Yurtdas, I., Diagana, C., & Li, A. 2015. "Experimental investigation on the shear performance of prestressed self-compacting concrete beams without stirrups." *Materials and Structures*, *48*(5), 1291-1302.

Teoh, B. K., Mansur, M. A., & Wee, T. H. 2002. "Behavior of high-strength concrete I-beams with low shear reinforcement." *Structural Journal*, *99*(3), 299-307.

Sozen, M. A., Zwoyer, E. M., & Siess, C. P. 1959. *Investigation of prestressed concrete for highway bridges: Part I strength in shear of beams without web reinforcement*. University of Illinois at Urbana Champaign, College of Engineering. Engineering Experiment Station.

Xuan, X. Y. 1986. *Effectiveness of welded wire fabric as shear reinforcement in pretensioned prestressed concrete T-beams*. MsC thesis, University of Manitoba, Winnipeg

Zwoyer, E. M., & Siess, C. P. 1954. "Ultimate strength in shear of simply-supported prestressed concrete beams without web reinforcement." *Journal Proceedings*, *51*(10), 181-200.

APPENDIX C: SUMMARY OF THE CALCULATION PROCEDURE AND THE RELATED PARAMETERS OF THE CONSIDERED SHEAR CAPACITY MODELS

The calculation procedures of considered shear capacity prediction models are summarized in Figure C-1, and the related parameters are listed in Table C-1 for the purpose of comparison. It is worth mentioning that each design code includes more than one shear capacity models with different levels of simplification. As shown in Figure C-1, ACI 318-19 contains two models with different approaches to obtain the concrete contribution V_c. As also indicated in Table C-1, ACI 318-19 is the only design code that explicitly considers different types of concrete contributions, i.e., flexure-shear capacity V_{ci} and web-shear capacity V_{cw}. AASHTO LRFD 2017, CSA A23.3:19 and CSA S6:19 contain two models each, while *fib* MC 2010 contains three models for members with shear reinforcement in addition to two models for members without shear reinforcement. Note that the general methods from CSA A23.3:19 and CSA S6:19 are essentially the same.

As can be seen in Figure C-1, the shear capacity V_d generally considers the contributions from concrete, shear reinforcement, and prestress force. Among these three components, the contribution from prestress force distinguishes the shear capacity models for RC members and those for PC members. For ACI 318-19 and *fib* MC 2010, the contribution from prestress force is considered implicitly, i.e., in the calculation of web-shear capacity V_{cw} for the detailed method of ACI 318-19, and in the calculation of longitudinal strain at mid-depth ε_x for *fib* MC 2010. Apart from similar consideration of prestress force effect in AASHTO LRFD 2017, CSA A23.3:19 and CSA S6:19, an additional contribution component from prestress force is considered explicitly in the shear capacity prediction models, by taking the vertical component of effective prestress force (e.g., $V_p = N_p \sin\alpha$) in $V_d = V_c + V_s + V_p$. Here, V_c and V_s denote the contributions from concrete and shear reinforcement, respectively.

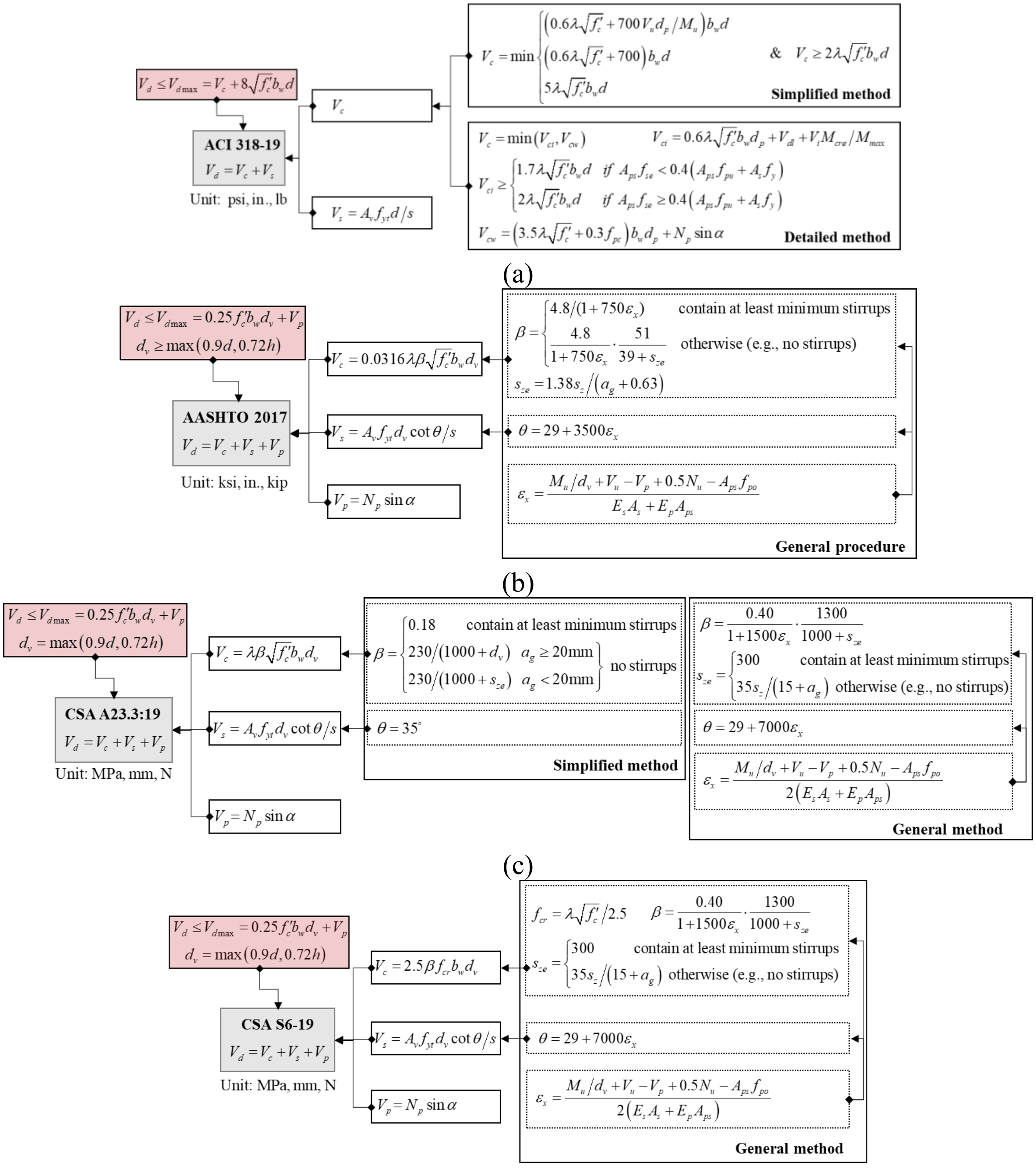

(a)

(b)

(c)

(d)

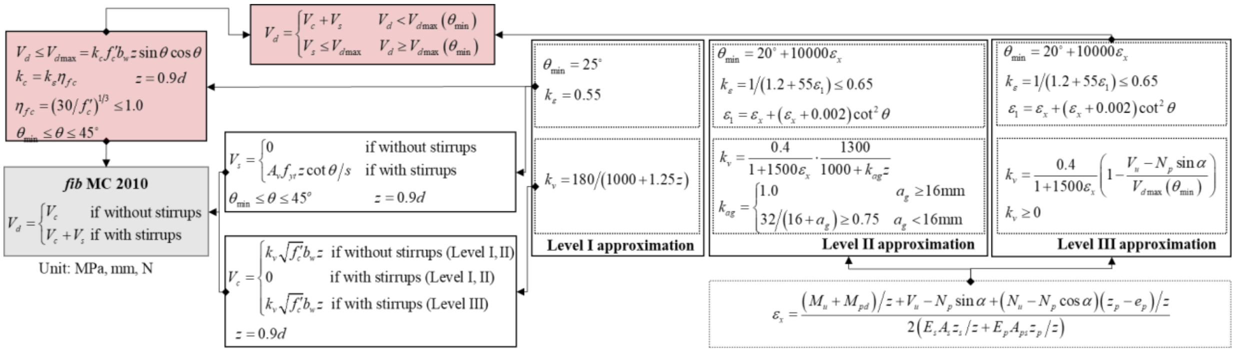

(e)

Figure C-1: Summary of the shear capacity models considered: (a) ACI 318-19, (b) AASHTO LRFD 2017, (c) CSA A23.3:19, (d) CSA S6:19, and (e) *fib* MC 2010

Table C-1: Parameters in the shear capacity models considered

Symbol	Parameter	ACI	AASHTO	CSA A23	CSA S6	*fib*
a_g	Maximum size of coarse aggregate		√	√	√	√
A_{ps}	Area of prestressed longitudinal tension reinforcement	√	√	√	√	√
A_{pv}	Area of prestressed transverse reinforcement					
A_s	Area of non-prestressed longitudinal tension reinforcement	√	√	√	√	√
A_{sb}	Area of bend-up non-prestressed reinforcement					
A_v	Area of shear reinforcement	√	√	√	√	√
b_w	Web width	√	√	√	√	√
d	Distance from extreme compression fibre to centroid of longitudinal tension reinforcement	√	√	√	√	√
d_p	Distance from extreme compression fibre to centroid of prestressed reinforcement	√				
d_v	Effective shear depth		√	√	√	
e_p	Distance from center of gravity to centroid of prestressed reinforcement					√
E_p	Modulus of elasticity of prestressed reinforcement		√	√	√	√
E_s	Modulus of elasticity of non-prestressed reinforcement		√	√	√	√
f_c’	Cylinder concrete compressive strength	√	√	√	√	√
f_{cr}	Concrete cracking strength				√	
f_{pc}	Compressive stress in concrete at centroid of cross section	√				
f_{po}	Stress in prestressed reinforcement when strain in the surrounding concrete is zero		√	√	√	
f_{pu}	Tensile strength of prestressed reinforcement	√				
f_{se}	Effective prestress in prestressed reinforcement	√				
f_y	Yield strength of non-prestressed reinforcement	√				
f_{yt}	Yield strength of shear reinforcement	√	√	√	√	√
h	Sectional height		√	√	√	
M_{cre}	Moment causing flexural cracking at section due to external loads	√				
M_{max}	Maximum moment at section due to externally applied loads	√				
M_{pd}	Bending moment at section due to prestressing					√
M_u	Bending moment at section	√	√	√	√	√
N_p	Effective prestress force	√	√	√	√	√
N_u	Axial force at section		√	√	√	√
s	Stirrups spacing	√	√	√	√	√
s_z	Crack spacing parameter		√	√	√	
V_{ci}	Flexure-shear capacity	√				
V_{cw}	Web-shear capacity	√				
V_{dl}	Shear force at section due to dead load	√				
V_i	Shear force at section due to externally applied loads	√				
V_u	Shear force at section	√	√	√	√	√

z_p	Distance from centerline of compressive chord to centroid of prestressed reinforcement					√
z_s	Distance from centerline of compressive chord to centroid of non-prestressed reinforcement					√
α	Angle between prestressed reinforcement and longitudinal axis	√	√	√	√	√
β	The factor accounting for shear resistance of cracked concrete		√	√	√	√
ε_x	Longitudinal strain at mid-depth of the member		√	√	√	√
θ	Angle of inclination of diagonal compressive stresses to longitudinal axis		√	√	√	√
λ	The factor to account for lightweight concrete	√	√	√	√	

APPENDIX D: SECTIONAL INFORMATION OF THE CONSIDERED GIRDER TYPES IN THE VIRTUAL EXPERIMENTAL DATABASE

In the generated virtual experimental database for corroded prestressed concrete voided girders, the sectional information of the considered girder types is summarized in Figure. D-1. For the steel arrangement of the archived standard PC voided girders in Alberta, a typical convention is to have two tensile mild steel bars, five compression mild steel bars, four prestressed strands located at the four corners used as longitudinal reinforcement to facilitate the stirrups placement, and more tensile mild steel and prestressed strands depending on the span length of girders. For the considered girder types with spans ranging from 6m to 11m, the tensile prestressed strand ratio $\rho_p = A_p / b_w d$ ranges from 0.573% to 1.26%, where A_p is the area of tensile prestressed strands, b_w is the web width, and d is the effective depth, while the tensile mild steel ratio $\rho_s = A_s / b_w d$ ranges from 0.145% to 1.662%, where A_s is the area of tensile mild steel. Note that the 11m SM-510 girder in the standard drawing does not contain 25M longitudinal bars, while additional four 25M bars were typically used to control long-term deformation of girders in engineering practice as observed (Liu et al. 2021; Huang et al. 2022) . Thus, 11m SM-510 girder with additional four 25M longitudinal steel bars is also considered in in the virtual experimental database. Regarding transverse reinforcement for the archived standard PC voided girders, four-legged stirrups with 10M mild steel are used as a typical convention. The considered girder types covered a representative stirrup spacing range from 150 mm to 350 mm, with the transverse reinforcement ratio $\rho_v = A_v / b_w s$ ranging from 0.373% to 0.654%, where A_v is the total area of the four-legged stirrup, s is the stirrup spacing.

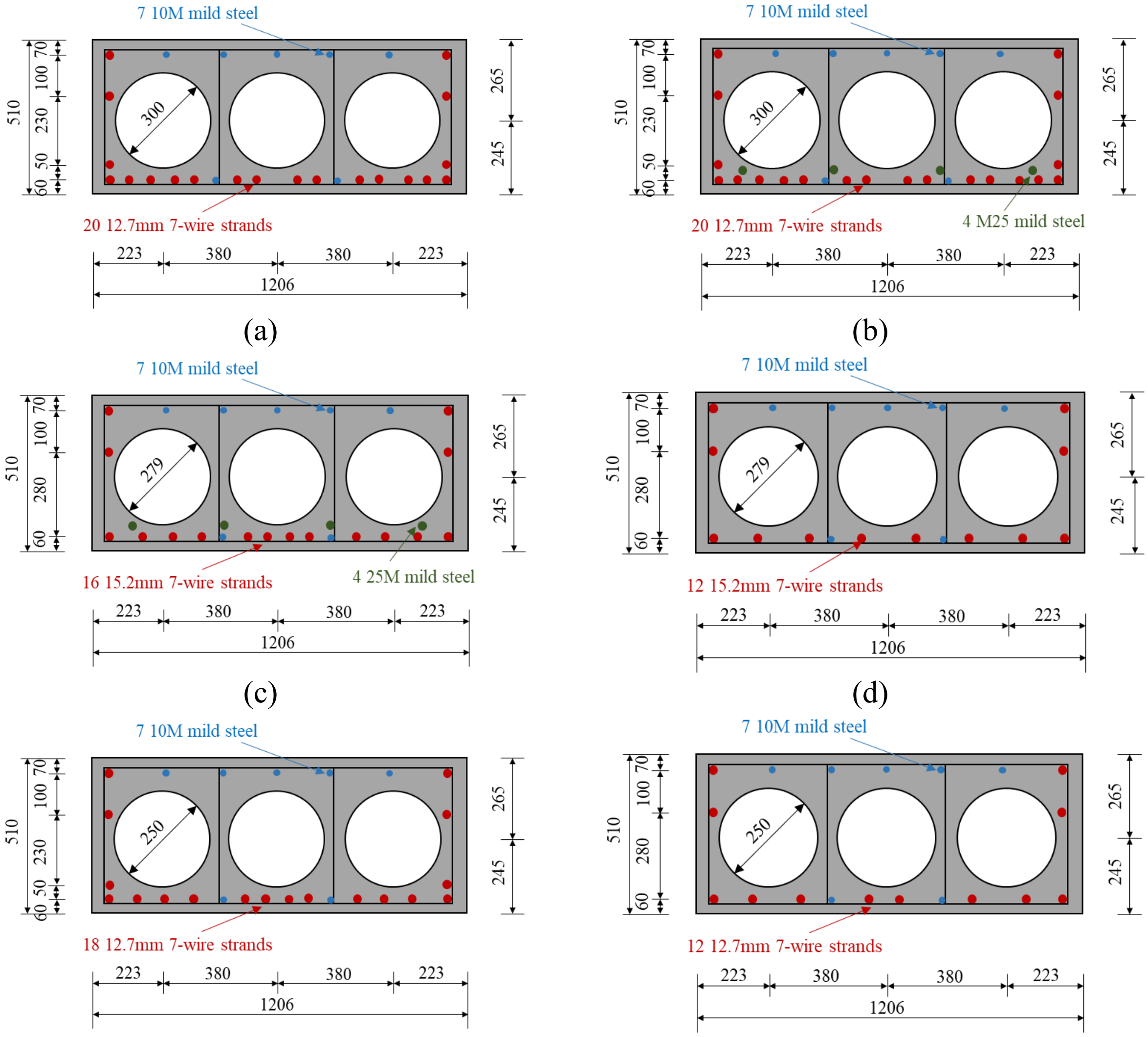

(a) (b) (c) (d) (e) (f)

Figure D-1: Girder types of the virtually tested girders: (a) 11m SM-510, (b) 11m SM-510 (with 25M), (c) 9.14m Type SL-510, (d) 6m Type SL-510, (e) 8.53m Type SC-510, and (f) 6m Type SC-510

APPENDIX E: SUMMARY OF THE GENERATED VIRTUAL EXPERIMENTAL DATABASE

A total of 4,165 virtual experimental tests on corroded prestressed concrete voided girders are obtained with various design, loading and corrosion conditions. Due to the length limitation, only a template for the input (e.g., material properties, sectional dimensions and corrosion degrees) and output (i.e., load-carrying capacity) parameters of the generated virtual experimental database is provided in this appendix, where f'_c is the concrete compressive strength in MPa, f_{pu} is the tensile strength of strands in MPa, f_{sy} is the yield strength of mild steel in MPa, b_w is the web width in mm, h is the sectional height in mm, d is the effective depth in mm, a is the shear span in mm, A_p is the tensile strands area in mm^2, A_s is the tensile mild steel area in mm^2, A_v is the stirrups area in mm^2, s is the stirrups spacing in mm, η_l is the corrosion degree for longitudinal steel, η_v is the corrosion degree for stirrups, and P is the load-carrying capacity in kN.

Table E-1: Template for the input and output parameters of the virtual experimental database

f'_c	f_{pu}	f_{sy}	b_w	h	d	a	A_p	A_s	A_v	s	η_l	η_v	P
53.2	1876	480	306	510	444	1000	1579	200	400	200	0	0	818.7
53.2	1876	480	306	510	444	1000	1579	200	400	200	0.05	0.05	775.6
53.2	1876	480	306	510	444	1000	1579	200	400	200	0.10	0.10	746.8
53.2	1876	480	306	510	444	1000	1579	200	400	200	0.15	0.15	605.2
53.2	1876	480	306	510	444	1000	1579	200	400	200	0.20	0.20	541.8
…	…	…	…	…	…	…	…	…	…	…	…	…	…
…	…	…	…	…	…	…	…	…	…	…	…	…	…
…	…	…	…	…	…	…	…	…	…	…	…	…	…
48.3	1943	458	456	510	450	3000	789.6	200	400	300	0	0.20	697.9
48.3	1943	458	456	510	450	3000	789.6	200	400	300	0.05	0.25	659.6
48.3	1943	458	456	510	450	3000	789.6	200	400	300	0.10	0.30	639.7
48.3	1943	458	456	510	450	3000	789.6	200	400	300	0.15	0.35	527.7
48.3	1943	458	456	510	450	3000	789.6	200	400	300	0.20	0.40	502.3

APPENDIX F: PARAMETRIC STUDIES ON MATERIAL PROPERTY-RELATED PARAMETERS

The influence of material property-related parameters on the capacity reduction factor is studied in this appendix. Same to the parametric study on other parameters, the influence of different model parameters is studied in the one-at-a-time manner by taking the simply supported 11m SM-510 girder under single point loading as a case study. Unless otherwise specified, when studying the effects of other parameters, the fixed values for a/d, L/h, ρ_p, ρ_s, ρ_v, $f_c'/35$, $f_{pu}/1860$, and $f_y/1860$ are 2.25, 21.569, 1.161%, 0.147%, 0.373%, 1.38, 1.045, and 1.145 respectively based on the sectional properties and the mean value of material properties for the 11m SM-510 girder.

F.1 Normalized Concrete Strength

The influence of normalized concrete strength $f_c'/35$ is studied by varying its value from 1.0 to 1.8 with an increment of 0.2. This represents varying f_c' from 35MPa to 63MPa to cover the 2 standard deviation (SD) interval of concrete strength value as summarized in Table 7-6, i.e., from 36.7MPa to 59.9MPa. Two loading scenarios (i.e., $a/d = 2.25$ and $a/d = 11.25$) are considered to study the influence of $f_c'/35$ on the capacity reduction factor as shown in Figure F-1(a) ~ F-1(b). It is shown that the $f_c'/35$ plays a significant role in the capacity reduction for all considered scenarios, while its influence is correlated with the corrosion degree (η_l, η_v) without exhibiting an obvious tendency.

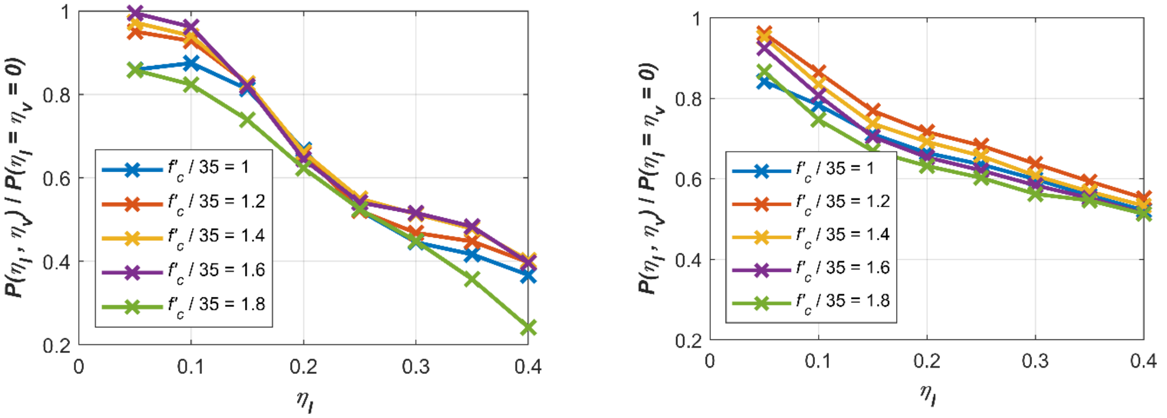

(a) (b)

Figure F-1: The influence of normalized concrete strength *f'$_c$*/35 on corrosion-induced capacity reduction: (a) *a*/*d* = 2.25, and (b) *a*/*d* = 11.25

F.2 Normalized Tensile Strength of Strands

The influence of normalized tensile strength of strands $f_{pu}/1860$ is studied by varying its value from 0.98 to 1.10 with an increment of 0.03. This represents varying f_{pu} from 1822.8MPa to 2046.0MPa to cover the 2 SD interval of tensile strength value as summarized in Table 7-6, i.e., from 1845.9MPa to 2040.2MPa. Two loading scenarios (i.e., $a/d = 2.25$ and $a/d = 11.25$) are considered to study the influence of $f_{pu}/1860$ on the capacity reduction factor as shown in Figure F-2(a) ~ F-2(b).

It is shown that compared with $f'_c/35$, the influence of $f_{pu}/1860$ is relatively smaller. This is considered to be resulted from that the varying range of $f_{pu}/1860$ (i.e., from 0.98 to 1.10) is smaller compared with that of $f'_c/35$ (i.e., from 1.00 to 1.80). It is to be expected that the influence of $f_{pu}/1860$ would increase with the increase of its varying range. However, it would be unfair for comparison purpose and unreasonable in engineering practice to increase the varying range of $f_{pu}/1860$. This is because that the 2D interval of material property values is applied to guide the varying range selection for both $f_c'/35$ and $f_{pu}/1860$, while the 2D interval represents a 95% confidence level and can be regarded as a reasonable range to consider the material property variability in engineering practice.

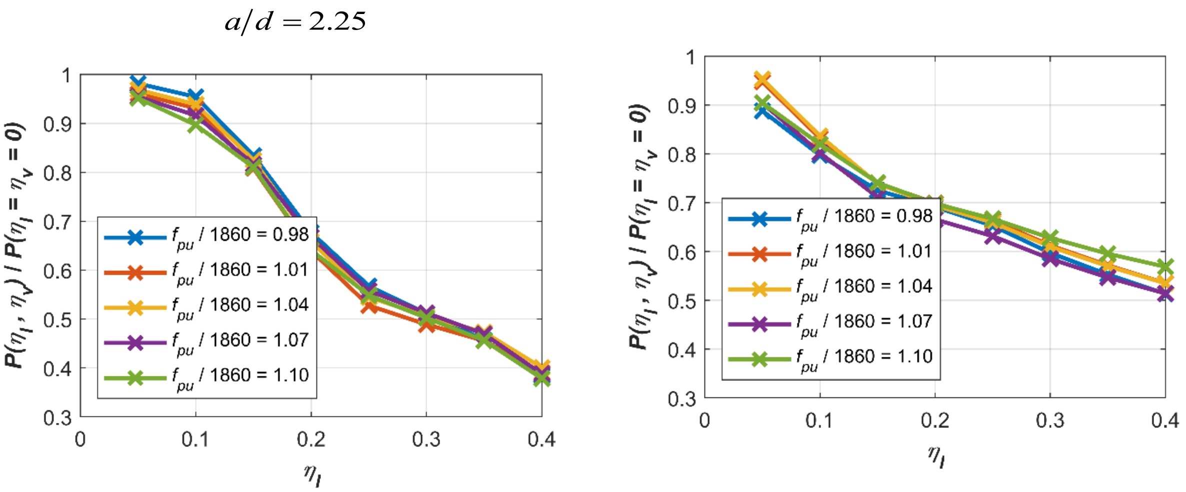

(a) (b)

Figure F-2: The influence of normalized tensile strength of strands $f_{pu}/1860$ on corrosion-induced capacity reduction: (a) $a/d = 2.25$, and (b) $a/d = 11.25$

F.3 Normalized Yield Strength of Mild Steel

The influence of normalized yield strength of mild steel $f_y/400$ is studied by varying its value from 0.9 to 1.3 with an increment of 0.1. This represents varying f_y from 360MPa to 520MPa to cover the 2 SD interval of yield strength value as summarized in Table 7-6, i.e., from 398.5MPa to 517.5MPa. Two loading scenarios (i.e., and $a/d = 11.25$) are considered to study the influence of $f_y/400$ on the capacity reduction factor as shown in Figure F-3(a) ~ F-3(b). Similarly to the preceding discussion, the influence of $f_y/400$ is relatively small compared with that of $f_c'/35$, which can be attributed to that the varying range of $f_y/400$ (i.e., from 0.9 to 1.3) is smaller compared with that of $f_c'/35$ (i.e., from 1.0 to 1.8).

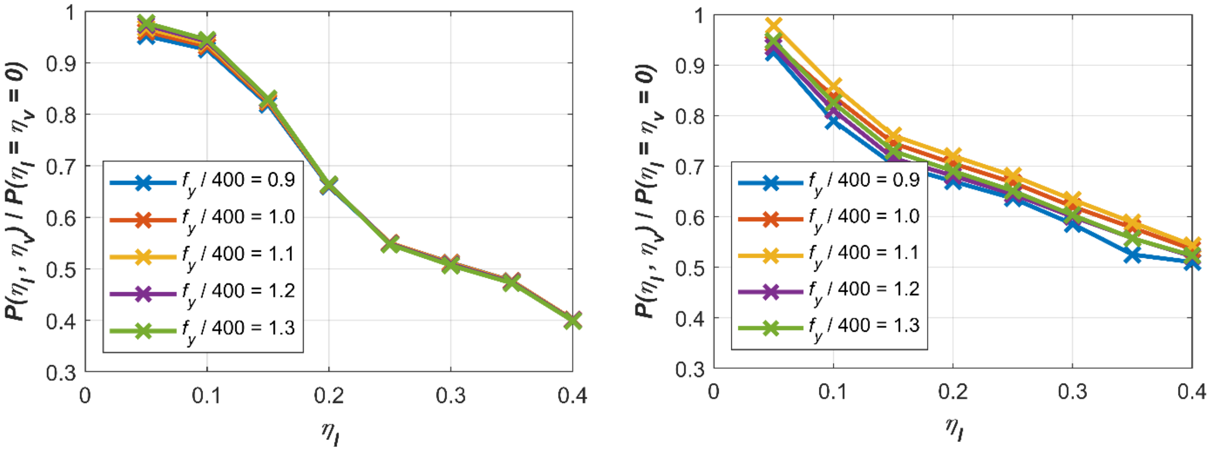

(a) (b)

Figure F-3: The influence of normalized yield strength of mild steel f_y/400 on corrosion-induced capacity reduction: (a) a/d = 2.25, and (b) a/d = 11.25

APPENDIX G: ULTIMATE LIMIT STATE (ULS) LOAD CALCULATION FOR 11M SM-510 GIRDER FROM THE TIGER LILY BRIDGE

In this appendix, the ultimate limit state (ULS) load is calculated based on the Canadian highway bridge design code CSA S6:19 (CSA 2019) by considering the ULS combination 1 of dead load and CL-625 truck load. Note that for the PC girder under the flexure-dominated loading scenario of $a/d = 11.25$, it is assumed that the moment is the dominant internal force when calculating the ULS load. The ULS moment is calculated first, then the equivalent ULS load is obtained under the single point loading with $a/d = 11.25$. While for the PC girder under shear-critical loading scenario of $a/d = 2.25$, it is assumed that the shear force is the dominant internal force.

G.1 Flexure-dominated Loading Scenario

The ULS combination 1 of dead load and CL-625 truck load from CSA S6:19 is adopted to calculate the ULS loading effects in terms of moment. The dead load is considered to be resulted from the self weight of the girder which can be simplified as uniformly distributed loading as shown in FigureG-1. The factored moment as a function of the position for the considered section (*x*) resulted from the dead load can then be calculated based on Eq. (G-1). Note that in this study, the moment is considered to be positive if the bottom side of the girder is in tension state.

$$M_D\left(x\right) = \alpha_D \frac{q\left(Lx - x^2\right)}{2} \tag{G-1}$$

Here, $M_D\left(x\right)$ is the factored moment resulted from the dead load, *x* is the distance between the left support and the considered section, $\alpha_D = 1.10$ is the dead load factor, $q = \gamma_c A_c$ is the uniformly distributed load resulted from the self-weight, γ_c = 1980 kg/m^3 is the weight density of concrete, A_c is the cross-sectional area, and L is the girder length.

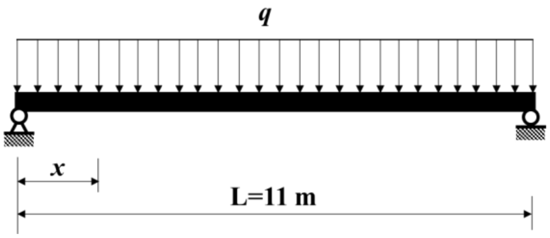

Figure G-1: Schematic view of the 11m SM-510 girder under dead load

The axle loads of CL-625 truck (i.e., whole truck load) is considered for the live load applied to the bridge as shown in Figure G-2, i.e., the Tiger Lily bridge with nine shear-connected SM-510 girders as shown in Figure 6-1 and Figure 6-2. The truck load fraction factor (also referred to as live load distribution factor in AASHTO LRDF 2017) is then applied to calculate the distributed moment for one interior 11m SM-510 girder.

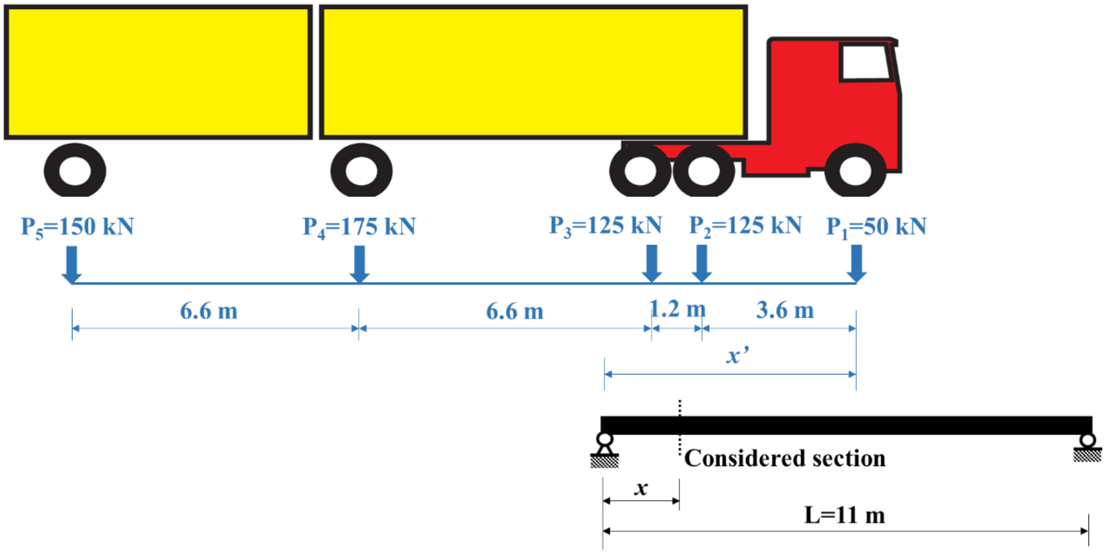

Figure G-2: Schematic view of the 11m SM-510 girder under live load

The factored moment resulted from the live load of CL-625 truck is a function of both the position of the considered section (i.e., *x*) and the longitudinal position of truck (i.e., *x'*) as shown in Figure G-2. Influence line analysis is adopted to calculate the factored moment resulted from the live load by applying a unit load as shown in Figure G-3. The moment resulted from this unit load can be obtained by Eq. (G-2),

$$M\left(x,x'\right)=\begin{cases}\dfrac{x'}{L}\left(L-x\right) & 0\le x'\le x\\ x\left(1-\dfrac{x'}{L}\right) & x\le x'\le L\end{cases} \tag{G-2}$$

where $M\left(x,x'\right)$ is the moment resulted from the applied unit load, x' is the distance between the left support and the position of loading.

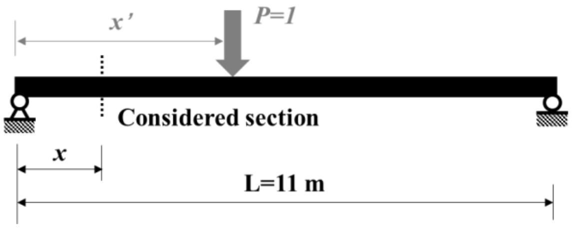

Figure G-3: Schematic view of the 11m SM-510 girder under unit single point load

The factored moment resulted from the live load can then be obtained by applying influence line analysis results as shown in Eq. (G-3) ,

$$M_L\left(x,x'\right)=\begin{cases}\alpha_L\alpha_{DLA}\alpha_M P_1 M\left(x,x'\right) & 0\le x'\le 3.6\text{m}\\ \alpha_L\alpha_{DLA}\alpha_{truck}\left[P_1M\left(x,x'\right)+P_2M\left(x,\left(x'-3.6\right)\right)\right] & 3.6\text{m}\le x'\le 4.8\text{m}\\ \alpha_L\alpha_{DLA}\alpha_{truck}\left[P_1M\left(x,x'\right)+P_2M\left(x,\left(x'-3.6\right)\right)+P_3M\left(x,\left(x'-4.8\right)\right)\right] & 4.8\text{m}\le x'\le 11\text{m}\\ \alpha_L\alpha_{DLA}\alpha_{truck}\left[P_2M\left(x,\left(x'-3.6\right)\right)+P_3M\left(x,\left(x'-4.8\right)\right)\right] & 11\text{m}\le x'\le 11.4\text{m}\\ \alpha_L\alpha_{DLA}\alpha_{truck}\left[P_2M\left(x,\left(x'-3.6\right)\right)+P_3M\left(x,\left(x'-4.8\right)\right)+P_4M\left(x,\left(x'-11.4\right)\right)\right] & 11.4\text{m}\le x'\le 14.6\text{m}\\ \alpha_L\alpha_{DLA}\alpha_{truck}\left[P_3M\left(x,\left(x'-4.8\right)\right)+P_4M\left(x,\left(x'-11.4\right)\right)\right] & 14.6\text{m}\le x'\le 15.8\text{m}\\ \alpha_L\alpha_{DLA}\alpha_{truck}P_4M\left(x,\left(x'-11.4\right)\right) & 15.8\text{m}\le x'\le 18\text{m}\\ \alpha_L\alpha_{DLA}\alpha_{truck}\left[P_4M\left(x,\left(x'-11.4\right)\right)+P_5M\left(x,\left(x'-18\right)\right)\right] & 18\text{m}\le x'\le 22.4\text{m}\\ \alpha_L\alpha_{DLA}\alpha_{truck}P_5M\left(x,\left(x'-18\right)\right) & 22.4\text{m}\le x'\le 29\text{m}\end{cases} \tag{G-3}$$

where $\alpha_L=1.7$ is the live load factor, α_{DLA} is the factor to consider dynamic load allowance, $\alpha_{truck}=0.35$ is the calculated truck load fraction factor for moment distribution, P_1, P_2, P_3, P_4, and P_5 are the axel loads of CL-625 truck as shown.

The total factored ULS moment $M_T\left(x,x'\right)$ resulted from the ULS combination 1 can then be obtained by combing $M_D\left(x\right)$ and $M_L\left(x,x'\right)$ as shown in Eq. (G-4). The 3D plot of $M_T\left(x,x'\right)$ is presented in Figure G-4. The maximum moment is observed to be 636.67 kN.m, which occurs when $x=5.46$ and $x'=9.06$. The ULS load for the 11m SM-510 girder under single point loading with $a/d=11.25$ (i.e., shear span a = 5 m) is then calculated as $P=11M_T^{\max}/30=233.44\text{kN}$.

$$M_T\left(x,x'\right)=M_D\left(x\right)+M_L\left(x,x'\right) \tag{G-4}$$

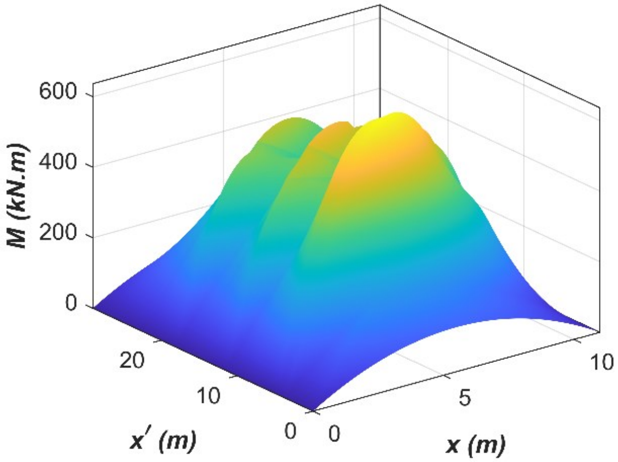

Figure G-4: 3D plot of the total factored ULS moment

G.2 Shear-critical Loading Scenario

Similarly, the factored shear force resulted from the dead load $V_D\left(x\right)$ can be obtained based on Eq. (G-5).

$$V_D\left(x\right)=\alpha_D\frac{q\left(L-2x\right)}{2} \tag{G-5}$$

The influence line analysis is then adopted to calculate the factored shear force under the live load of CL-625 truck load. The shear force resulted from the unit load can be obtained by Eq. (G-6).

$$V\left(x,x'\right)=\begin{cases}-\dfrac{x'}{L} & 0\le x'\le x\\ 1-\dfrac{x'}{L} & x\le x'\le L\end{cases} \tag{G-6}$$

Based on the influence line analysis, the factored shear force resulted from the live load can be calculated based on Eq. (G-7).

$$V_L\left(x,x'\right)=\begin{cases}\alpha_L\alpha_{DLA}\alpha_{truck}P_1V\left(x,x'\right) & 0\le x'\le 3.6\text{m}\\ \alpha_L\alpha_{DLA}\alpha_{truck}\left[P_1V\left(x,x'\right)+P_2V\left(x,\left(x'-3.6\right)\right)\right] & 3.6\text{m}\le x'\le 4.8\text{m}\\ \alpha_L\alpha_{DLA}\alpha_{truck}\left[P_1V\left(x,x'\right)+P_2V\left(x,\left(x'-3.6\right)\right)+P_3V\left(x,\left(x'-4.8\right)\right)\right] & 4.8\text{m}\le x'\le 11\text{m}\\ \alpha_L\alpha_{DLA}\alpha_{truck}\left[P_2V\left(x,\left(x'-3.6\right)\right)+P_3V\left(x,\left(x'-4.8\right)\right)\right] & 11\text{m}\le x'\le 11.4\text{m}\\ \alpha_L\alpha_{DLA}\alpha_{truck}\left[P_2V\left(x,\left(x'-3.6\right)\right)+P_3V\left(x,\left(x'-4.8\right)\right)+P_4V\left(x,\left(x'-11.4\right)\right)\right] & 11.4\text{m}\le x'\le 14.6\text{m}\\ \alpha_L\alpha_{DLA}\alpha_{truck}\left[P_3V\left(x,\left(x'-4.8\right)\right)+P_4V\left(x,\left(x'-11.4\right)\right)\right] & 14.6\text{m}\le x'\le 15.8\text{m}\\ \alpha_L\alpha_{DLA}\alpha_{truck}\left[P_4V\left(x,\left(x'-11.4\right)\right)\right] & 15.8\text{m}\le x'\le 18\text{m}\\ \alpha_L\alpha_{DLA}\alpha_{truck}\left[P_4V\left(x,\left(x'-11.4\right)\right)+P_5V\left(x,\left(x'-18\right)\right)\right] & 18\text{m}\le x'\le 22.4\text{m}\\ \alpha_L\alpha_{DLA}\alpha_{truck}P_5V\left(x,\left(x'-18\right)\right) & 22.4\text{m}\le x'\le 29\text{m}\end{cases} \tag{G-7}$$

where $\alpha_{truck}=0.37$ is the calculated truck load fraction factor for shear force distribution.

The total factored shear force $V_T\left(x,x'\right)$ resulted from the ULS combination 1 can then be obtained by combing $V_D\left(x\right)$ and $V_L\left(x,x'\right)$ as shown in Eq. (G-8). The 3D plot of $V_T\left(x,x'\right)$ is presented in Figure G-5. The maximum shear force is observed to be 270.42 kN.m, which occurs when $x=11$ and $x'=14.59$. The ULS load for the 11m SM-510 girder under single point loading with $a/d=2.25$ (i.e., shear span *a* = 1 m) is then calculated as $P=11V_T^{\max}/10=298.57\text{kN}$.

$$V_T\left(x,x'\right)=V_D\left(x\right)+V_L\left(x,x'\right) \tag{G-8}$$

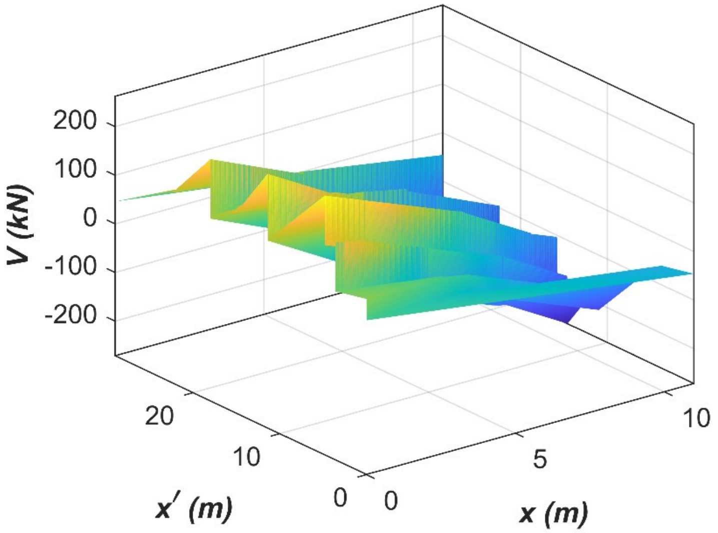

Figure G-5: 3D plot of the total factored ULS moment